17th International Symposium on Ice
Saint Petersburg, Russia, 21 - 25 June 2004
International Association of Hydraulic Engineering and Research

A QUALITATIVE ANALYSIS OF VELOCITY EFFECTS OF ICE LOAD ON NARROW CONICAL STRUCTURES

Li Feng, Yue Qianjin, Bi Xiangjum[1]

ABSTRACT

This paper first reviews different patterns of velocity effect observed from full-scale tests as well as model tests. A supposition of failure mode domination is induced according to the interrelation of amplitude vs. period of ice force, because of increment of ice force always related with alteration of breaking length. Secondly, by means of static ice force analysis, it is proved that failure load of ice sheet gets great or less under two different bending mode respectively along with decreasing breaking length. Finally, a numerical test is made by FEM which shows breaking length of ice beam monotonous decrease along with increasing impact velocity at the front end of the beam. Sum up above aspects, it conclude that velocity effect of ice force on narrow conical structures reflects transition of failure mode to a great extent.

Key words: ice load, conical structures, velocity effect, qualitative analysis

1. INTRODUCTION

Velocity effect is an important subject in ice load research for offshore structures intruded by fast moving ice. Many tests have been carried out to investigate velocity effect of ice loads on conical structures. Matskevitch (2002) presented a review on researches in this field. However different conclusions were obtained by different tests. Most of them proved that ice force increase with increasing velocity, the load increment could great than two times. But some others denied there exist velocity effect of ice force at all. And there were still some tests even observed contrary phenomena, ice force decrease with increasing velocity. Therefore, a qualitative analysis is also necessary in addition to those efforts to simulate the dynamic interaction processes. The purpose of this paper is tried to find a physical reason of velocity effect to explain above perplexity.

2. OBSERVATIONS ON VELOCITY EFFECT OF ICE FORCE

If only the peak load is considered within the ice force tests on conical structures, there are the following three scenarios associated with bending failure can be identified as velocity effect.

[1] Dalian University of Technology, China, 116023

2.1. Case I-constant ice force with velocity

During early years of ice load research, a number of tests with 45^0 cone model had carried out in which no any obvious increment of on maximum ice force had been observed (Wessels, 1984; Sodhi at al, 1985; McKenna and Jones, 1995), despite the circumferential distance gradually increased with velocity (Wessels, 1984). The narrow velocity range (low than 25cm/s) should be the main reason to explain this phenomena. Moreover， In NRC/IMD tests, when thin ice (35mm) was used, there is no velocity effect at all for the 45^0 cone, and only very small increment was showed for the 60^0 cone (Lau,2000).

2.2. Case II- ice force increase with velocity

More tests with steeper cone model were conducted at wider velocity range. They show significant velocity effect on the maximum ice load. These tests are shown in table 1 (Matskevitch, 2002).

Some typical results among above tests are shown with normalized force vs. dimensionless velocity, Froud number in Fig.1

Table 1 Model tests where ice force increase with velocity

Author	Cone type	Waterline diameter (cm)	Slope angle/shape	Speed range (cm/sec)	Number of tests
Sorensen, 1978	Up	16	45 – 65 flat	10 – 100	9
Frederking et al, 1982	Down	100	15 – 60 cone	1 – 50	21
Finn et al, 1993	Down	12	60 – 85 flat	1 – 20	17
Spencer et al, 1993	Up	95 – 120	60 cone	2 – 44	34
Ohta et al, 1996	Up	50 – 180	60 cone	0.4 – 41	Not given
JOIA, 1998	Up	50	45 – 75 cone	0.7 – 14	Not given
Timco et al, 1998	Up	22	45 – 75 flat	5 – 65	34
Lau et al, 2000	Up	94 – 123	45, 60 cone	0.5 – 50	36

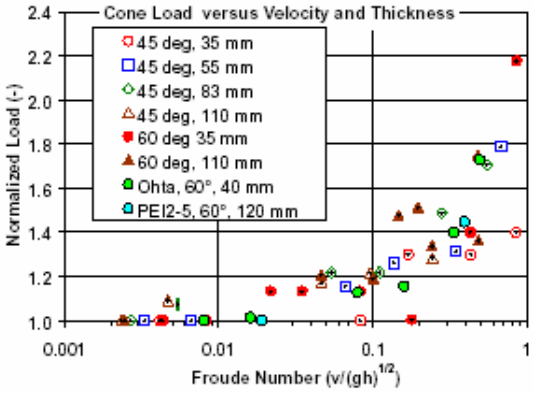

Fig.1. Velocity effect in IMD tests (Lau et al, 2000)

2.3. Case III-ice force decrease with velocity

This kind of phenomenon was first observed in CRREL tests with rough cone (μ=0.5), Ice force decreased with increasing ice velocity (Sodhi et al, 1985). Later on, the same scene

emerged in COSMAR tests under the condition of thick ice (7.2 cm) (Wessels, 1988). Wessels explained this as a transition of failure mode from bending to shearing. Moreover, the same case was also observed in the tests by NRC/IMD with 60^0 cone and 11cm thick EG/AD/S ice when velocity great than 15 cm/s (Lau, 2000) and the tests with 45^0 and 60^0 cone and 2-4 cm urea ice conducted by Tianjin University (China) at whole the velocity range.

2.4. In-field observations on prototype structure

Full-scale ice force measurements were conducted on JZ20-2, the 4-leg platform with conical collars (α =60°, D =4.6 m), during the last decade. The panels recorded the local ice forces on the cone continuously. Although it is difficult to obtain the total force, but local ice forces are still useful for a qualitative analysis. A group of data recorded in winter of 2000-2001 is used to show velocity effect of ice force (Fig.2). The normalized forces are used to show influence of velocity; they are obtained from the measured force divided by.$\sigma_f h^2$ and then normalize by the maximum number of the results. We can see from this figure that all the three cases mentioned above are displayed, they are marked by broken lines I, II, and III respectively. This result suggests that emerge of the three cases in turn are quite common if only the parameter (velocity or thickness of ice) scope is sufficient wide.

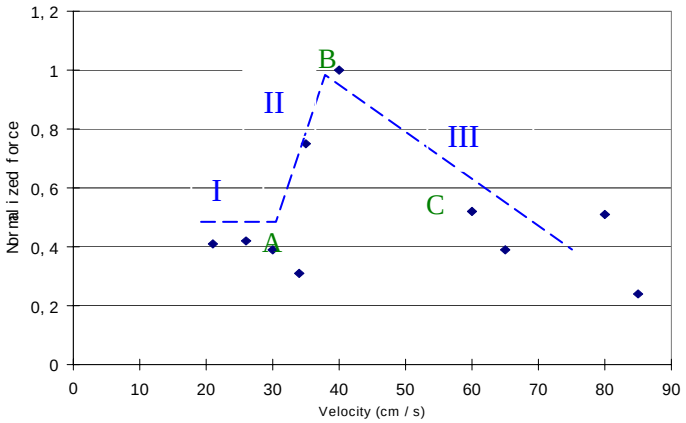

Fig.2. Velocity effect of ice force on JZ20-2

3. AN ANALYSIS FOR ESSENCE OF VELOCITY EFFECT

3.1. Interrelation between ice force amplitude and its period

In order to reveal why velocity effect exists different cases, the velocity effect is reexamined in an alternate visual angle in Fig.3 by using the same group of data. Here it shows normalized force vs. the peak force period. Period and velocity satisfy the following relationship

$$T = \frac{l_b}{v} \tag{1}$$

In which, l_b is breaking length of ice.

Fig.3 shows the above three cases of amplitude of ice force also can be regarded as a function of period. In this way, we are easily understand of the critical contribution of

failure mode to ice force in addition to velocity, if variation of the breaking pattern is regarded as a signal of transition between different bending modes. On the one hand, various failure mode correspond with different failure size for a certain ice thickness; on the other hand, various failure mode correspond with different period to enable develop corresponding limit deformation. When period is sufficient long (case I), the typical bending deformation can completely develop, the corresponding phenomenon is breaking length sufficiently long relative to thickness. Therefore ice force keeps constant without influence of velocity. For the shorter period (case II), the corresponding phenomenon is breaking length significantly gets short with increasing velocity, there's only time to develop insufficient bending deformation and greater force is needed to fail the ice sheet. When period keep on decrease to the shortest phase (case III), ice force decreases suddenly with decreasing period, it means an alternative failure mode has emerged. Of course, an analysis of dynamic deformation process is required to give a better explanation, but this is beyond the study scope of this paper. The important thing now is to examine what the alternative mode is.

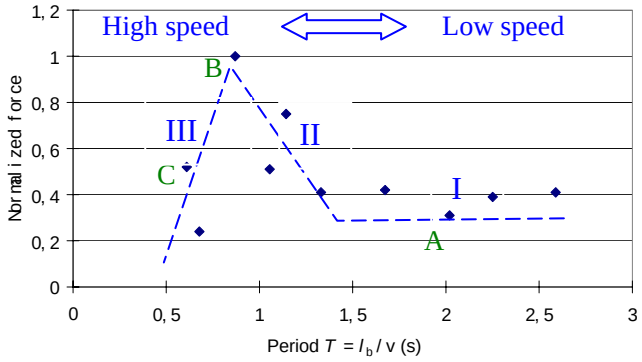

Fig.3. Interrelation between amplitude and period of ice force

3.2. Validating the alternating failure mode

It is interesting to see what was happened within the different cases of velocity effect. Three data of the ice force time series shown in Fig 4 are selected for further analysis; The corresponding data points are marked by A, B, and C in Fig. 2 and Fig. 3. Parameters of the selected data groups are shown in Table 2.

Table 2. Comparison of dynamic ice forces under different failure modes

Data group	A	B	C
Date / Time	010122 / 171500	010114 / 101531	010111 / 085700
h (cm)	10	8	10
v (cm/s)	34	40	60
F_{m3} **(t)**	1.2	2.5	1.8
F_{normal}	0.31	1.0	0.41
Period (s)	2.02	0.87	0.61
Length-thickness ratio	6.89	3.95	3.66
Dominant failure mode	Wedged beam type bending	Transition type bending	Plate type bending
Tide lever (cm)	220	230	235

The parameter F_{m3} means a mean value of the three maximum peak forces. Due to the tide lever of the three data are very close, influence of the cone diameter is neglected. Different failure mode in Table 2 is observed from the video and they are recognized according to the definition of Fig. 5 (Li, Yue, Shkhinek and Karna, 2003)

(a)

(b)

(c)

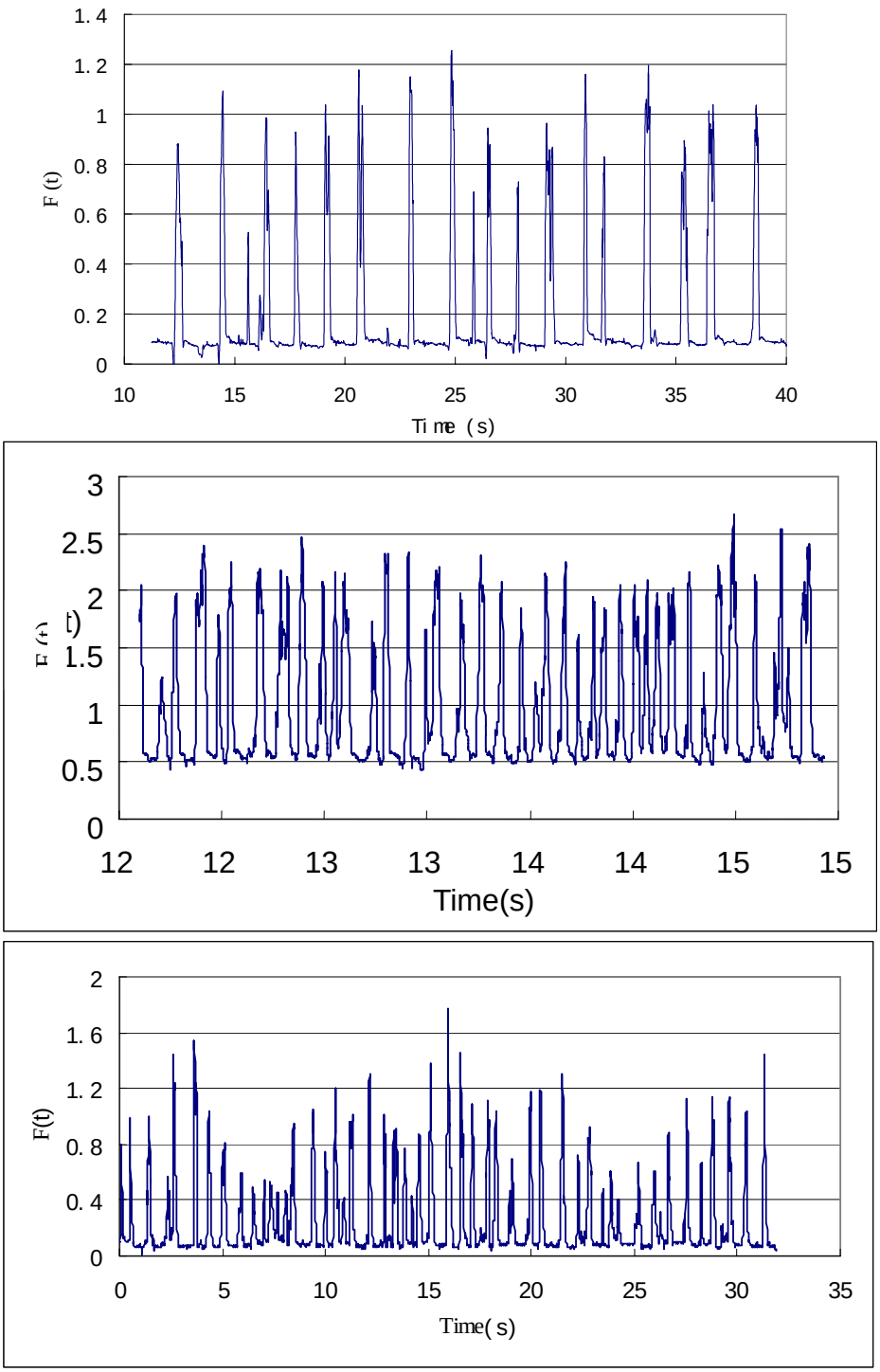

Fig.4. Comparison of ice forces with different periods

Failure modes in Fig.5 are defined with two dimensionless parameters, k_1 and k_2. In which, h is ice thickness; l_b, is breaking length, $2a$ is width of the failure area. This map is obtained analytically based on elastic plate theory. Bending of wedged beam type means that the radial cracks are developed firstly, dividing ice sheet into long and narrow pieces. Plate type bending is corresponding to failure with circumferential crack develop firstly, which leads to formation of short and wide pieces. Transition type bending means a state between the two considered above where cracks along two different directions are seams emerged simultaneously.

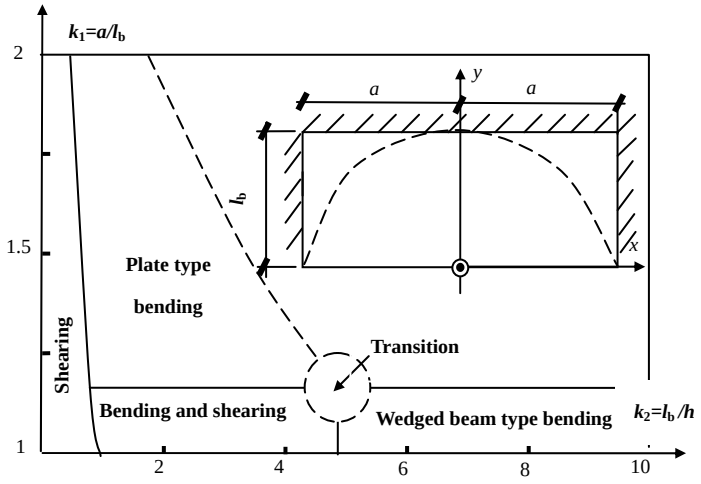

Fig.5. A definition map of failure mode for ice-cone interaction

As many researchers indicated, at the critical point of velocity effect (point B in figure 2 and 3), a transition of failure mode puts an upper limit on how much the bending load can increase with velocity. But what is the alternative failure mode? Different researchers have different opinion. Most of them consider it is shearing (Wessels, 1988; Lau, 2000; Matskevitch, 2002), the others consider it is crushing (Shkhinek, 2001). This paper presents a new viewpoint. According to data of JZ20-2, we suggest transition point of the maximum dynamic ice force do not involve other failure mode, it is only a transition between different types of the bending failure. It is important that this transition results in an essential change of failure pattern.

4. INTERRELATION BETWEEN ICE FORCE AND BREAKING SIZE UNDER TWO BENDING MODES

In order to confirm the conclusion of above analysis, it is necessary to compare the ice forces of the two modes. According to definition of Fig.5, two models are developed to predict the breaking forces respectively.

4.1. Plate type bending mode

According to an ice force model based on elastic plate theory, we can express ice force as a function of dimensionless breaking length as shown in Fig. 6. The dimensionless force is obtained from the failure load divided by $\sigma_f h^2$. In-field observations show that width of the failure area, $2a$, is merely a little greater than cone diameter and changes in a narrow range. Hence, Fig. 6 proves that ice force decreases with decreasing of breaking length. It

is especially clear demonstrated on the right part of the curve. The right end of this curve, at l_b/a=0.86, is the borderline of the two bending failure modes. This tendency is coincident with case III of Fig.3.

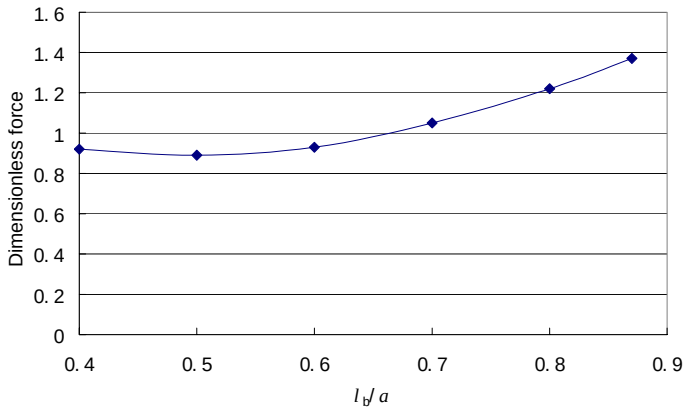

Fig.6. Ice force as a function of the ratio l_b/a under plate type bending mode

4.2. Wedged beam type bending failure

For the typical wedged beam type bending failure, we can express ice force as a function of dimensionless breaking length, $k=l_b/h$, as shown in Fig.7. It shows ice force has small change with k, for the relatively big values of k. But when k-value is less than 8, ice force increases obviously with decreasing k. This tendency is coincident with case II of Fig.3.

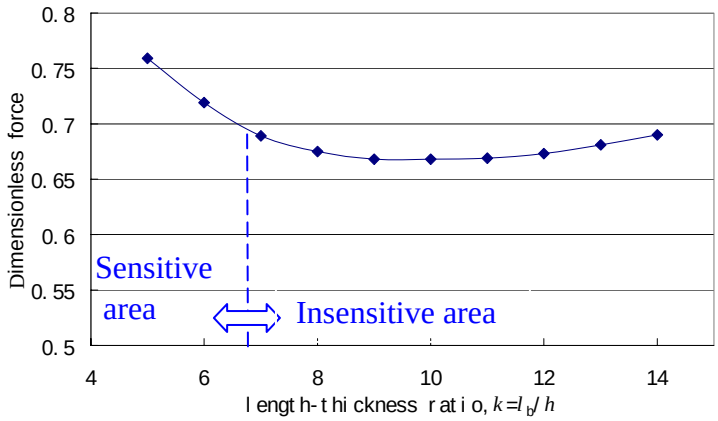

Fig.7. Ice force as a function of the ratio l_b/h under wedged beam type bending failure

According to these two models, the maximum ice force under bending failure should be emerged at a transition point between the two with a certain breaking length as shown in figure 5. In order to relate this transition phenomenon with velocity effect, it is necessary to determine the relationship between breaking length and velocity.

5. INTERRELATION BETWEEN BREAKING LENGTH AND VELOCITY

Similarly to ice force, different tendency of variation of breaking length with velocity was seen in different experiments. Many model tests display that breaking length of ice

decreases with increasing velocity (Sørensen, 1978; Kato et al, 1996; Kärnä et al, 2003). But other tests also showed opposite tendency (Wessels, 1984; Sodhi et al, 1985). Comparison of these test conditions suggests that the first phenomenon corresponds to rough cone surface which is resulted in positive velocity effect of ice force; and the latter corresponds to smooth cone surface and low to medium speed in which almost no any velocity effect on ice force. Therefore, only the first situation is important for this study.

In order to relate the normal velocity effect of ice force, as shown in phase II of Fig.2, and corresponding failure mode, as shown in Fig.7, we should adopt a beam model. Using finite element method to simulate an ice beam being impacted at the front end along vertical direction. A beam with constant cross-section is adopted for simplifying calculation. the following parameters are used for the ice beam: E=1G Pa, l=24 m, h = = 0.2 m, v =0.5 m/s, 2 m/s. Under the small deflection condition, buoyancy is simulated by an elastic foundation.

Breaking length corresponds to coordinate of the point where maximum dynamic stress reaches the bending strength of ice. Fig. 8 shows the stress distribution at a given moment. Fig. 9 shows the analysis result. Breaking length decreases with increasing velocity, but it changes very slowly at low velocity condition. This is the common developing tendency of failure pattern of ice beam under dynamic bending. We believe that under 3D condition a similar tendency exists.

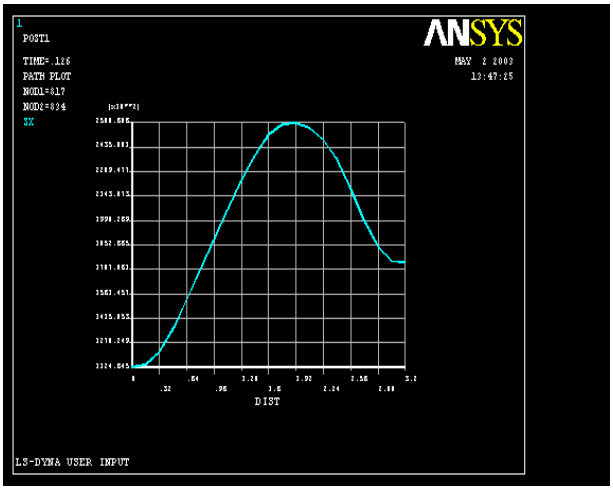

Fig. 8. Bending stress distribution along the length direction of ice beam

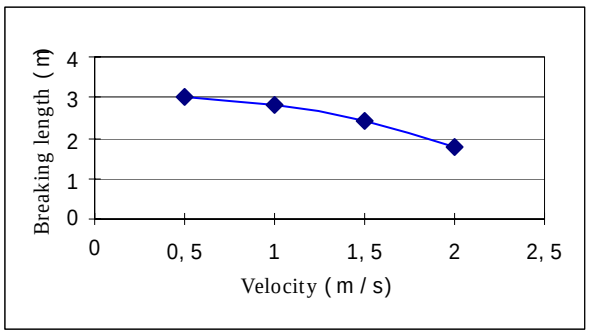

Fig. 9. Breaking length as a function of displacement velocity at the end of the ice beam

6. DISCUSSION

Based on above analysis, now we can discuss mechanism of velocity effect within the three cases respectively, we shall pay attention to differences in failure mode in different cases.

6.1. Case I-static ice force

There is no velocity effect for the long-period ice force when velocity is relatively slow. The dominant failure mode is wedged beam type bending with sufficient long breaking length under static load. In view of statics, we know that for the high-stress area, variation of bending moment along longitudinal direction of the wedged beams is very slow due to adjusting of the “elastic foundation”. Therefore, when breaking length gets short with increasing velocity, few effect of inertia can be detected, ice force under this area is not sensitive to l_b, as shown in Fig. 7.

6.2. Case II-positive velocity effect

The positive velocity effect occurs in mediate to high-speed condition. The dominant failure mode is also the wedged beam type bending but with shorter breaking length under dynamic load. In this condition, inertia of the ice sheet result in more and more ice force increment with increasing velocity. Relate Fig. 9 and 7, we may explain velocity effect with in-plane compressive stress. It is known that breaking length is roughly equal to phase velocity of the elastic wave times the loading time. Because of the loading time decreases with increasing velocity, the breaking length of ice gets shorter and shorter. When l_b is fairly short, the in-plane compressive stress at the critical section becomes very important and result in positive load increment by bigger equivalent flexural strength. Moreover, In dynamic analysis, for a bar under impacting compression, the dynamic load is inverse proportion to square root of static deformation, Δ_{st}, of the bar. A short bar results in lessΔ_{st}, and hence greater dynamic ice load. In this way, ice force is sensitive to breaking length as shown by the left part of the curve in figure 7.

6.3. Case III-negative velocity effect

The negative velocity effect occurs in high velocity conditions with short-period ice force. The dominant failure mode has been transformed into the plate type bending rather than shearing. This is because observations on JZ20-2 show that breaking length-thickness ratio fall into a range of 3~5, whereas shear would normally result in broken ice piece size of the order of one ice thickness (Matskevitch, 2002). Under this mode, insufficient bending deformation restricts radial cracking and failure of ice sheet also tends to localization. Ice force can decrease with decreasing breaking length as shown in Fig.6. This analysis is based on bending theory and it cannot be fit for thick ice situation under which shear effect must be considered.

7. CONLUSIONS

(1) Full-scale observations on JZ20-2 showed that there are three different cases of velocity effect of ice force: independent on velocity (case 1), positive load increment (case 2), and negative load increment (case 3) with increasing velocity. These cases are emerged in turn if only range of velocity and thickness of ice is sufficient wide.

(2) Wedged beam type bending is the dominant failure mode corresponding to case 1 and 2 of velocity effect of ice force. Ice force increment as result of inertia effect of ice sheet gets great with decreasing breaking length as shown in failure process of case 2.

(3) Transition of failure mode occurs when case 2 transformed into case 3 of velocity effect of ice force, the alternative mode is plate type bending other than shearing as observed. This transition results in an upper limit of the dynamic ice force increment. After that, deformation and failure of ice sheet, under high-speed bending, tends to localization.

(4) The above conclusions are valid only for the narrow conical structures. Rubble on wider cone could bring different modes.

ACKNOWLEDGEMENTS

Authors of this paper express deep gratitude to Professor K. Shkhinek and Professor Tuomo Karna for their helpful suggestions and discussions. We also thank Ms Hu Y. J. and Mr. Qu Y. for their contributions on calculation and statistic data.

This paper is funded by National Science Technology Ministry of China.

REFERENCES

Dmitri G. Matskevitch, 2002. Velocity effects on conical structure ice loads[ ]. *In Proceedings of OMAE conference* [ ]. Oslo, Norway, 2002.

Shkhinek K, Uvarova E, 2001. Dynamics of the ice sheet interaction with the sloping structure[ ]. R. Frederking, etc. *Proceedings of the 16th POAC conference* [ ]. Ottawa, Ontario, Canada: Canadian Hydraulics Center, 2001.639-648.

Li Feng, Tue Qianjin, 2003. Dynamic load effect of ice force on inclined structures (In Chinese), *Mechanics in engineering*, Vol.25, No. 2, 28-30.

Yue, Q.J., Bi, X.J, 1998. Full-scale tests and analysis of dynamic interaction between ice sheet and conical structures, In *Proceedings of 14th IAHR Symposium on Ice*, Potsdam. Vol. II.

Wessels E., Kato K., 1984. Ice force on fixed and floating conical structures, *IAHR Ice Symposium*, Sapporo.

Sodhi, D. S., Morris, C.E., Cox, G.F.N., 1985. Sheet ice forces on a conical structure: An experimental study. In *Proceedings of 8th POAC Symposium on Ice*, Narssarssuaq, Greenland.

McKenna R.F.and Jones S.J., 1995. Ice forces on conical structures. *Progress report 1994/95*. IMD Test Report TR-1995-25.

Lau M., Jones S.J., Phillips R. and Mckenna R.F., 2000. Influence of velocity on ice-cone interaction. In *Proceedings of IUTAM Symposium on Scaling Lows in ice mechanics and ice dynamics*. University of Alaska Fairbanks.

Li, Yue, Shkhinek and Karna, 2003. A qualitative analysis of breaking length of sheet ice against conical structures. In *Proceedings of POAC Symposium on Ice*.

Sørensen C., 1978. Interaction between floating ice sheets and sloping structures, *Institute of Hydrodynamics and Hydraulic engineering, Technical University of Denmark*, Series Paper No 19, 175p.

Kato K., Adachi H., Kishimoto H. and Ichikawa T., 1996. Experimental study on ice forces on conical structure using segmented models. In *Proceedings of 13th IAHR Symposium on Ice*, Beijing, Vol.1, pp.176-183.

Kärnä et al, 2003. Tests on dynamic ice-structure interaction. *Proceedings of 22th OMAE Symposium Cancun*, Mexico.

17th International Symposium on Ice
Saint Petersburg, Russia, 21 - 25 June 2004
International Association of Hydraulic Engineering and Research

SEA ICE – VERTICAL PILE INTERACTION EXPERIMENT, PART I: TEST SET-UP AND ICE PROPERTIES

P.O. Moslet[1], P. Liferov[1,2,3], R. Nilsen[1], K.V. Høyland[1], M. Bjerkås[1, 2], B. Bonnemaire[2], J. Dybdahl[1] and S. Løset[1, 2]

ABSTRACT
Two interaction experiments between a level ice sheet and a vertical pile have been conducted on Svalbard, Norway during the spring 2003. The structure consists of a vertical pile with a diameter of 0.470 m and a 20' container as a foundation for the pile. The pile was instrumented with a semi-circular load panel, which increased the diameter to 0.665 m and a turnbuckle with a gauge measuring the strain between the pile and the foundation. Salinity and temperature were measured and ice cores were taken and tested to find the unaxial strength. This paper describes the test set-up.

INTRODUCTION
Different approaches have been used to learn more about the behaviour of ice in contact with a structure and the loads the ice exerts. In the past, field measurement programs have measured loads in one way or the other, while the load contributing parameters such as ice thickness, temperature, and speed have remained unknown or unclear. A number of medium scale experiments have been conducted and the most remarkable experiments were the indentation tests where a structure was pushed into the ice cover by means of a hydraulic jack (e.g. Sodhi et al. 2001, Frederking et al. 1990).

To gain more control on the experiments, the research has been brought inside the laboratories where the parameters mentioned previously can be controlled. This caused problems with scaling the load contributing parameters and ice strength in particular. In laboratory the structure is usually mounted on a carriage, which moves through the ice cover (Sodhi 1998, Wessels and Jochmann 1991, Timco 1987). In the laboratory experiments two main types of ice have been used: model ice or freshwater ice.

The rationale for the experiment in Svea, Svalbard was to create a meeting point between the laboratory experiments and the field measurements. This was an experiment where all the load contributing parameters of the ice could be determined while conducting interaction between a structure and natural sea ice. The idea was to have a structure fixed to the seabed and apply the force to the ice, imitating the process as it happens

[1] The University Centre in Svalbard
[2] The Norwegian University of Science and Technology
[3] Barlindhaug Consult AS

in nature. As the design process advanced it became obvious that in this case, the ice should be towed against the structure rather than pushing the structure into the ice. The towing method was already tested during winter 2002 (Liferov et. al. 2002).

STRUCTURE DESIGN

A 20’ container was used as a foundation. A 5 m long steel pipe with diameter 0.47 m was installed vertical from the floor of the container through the roof (Fig. 1). The container was structurally reinforced. Focus was put on creating a stiff structure, as measurements of dynamic ice forces not were the goal of the project.

One concern during the design was the overturning moment of the structure and the sliding forces between the seabed and the container created during tests or ice break-up. At the site of installation there was a layer of very soft sediments that had to be removed before installation. A digger, standing on the ice at low tide, excavated the soft layer at 2-3 m water depth. The entire soft layer was not removed so when the container was filled with rock, the front part settled 0.4 m, which gave an inclination of the pile of 4°. The situation after installation is shown in Fig. 1.

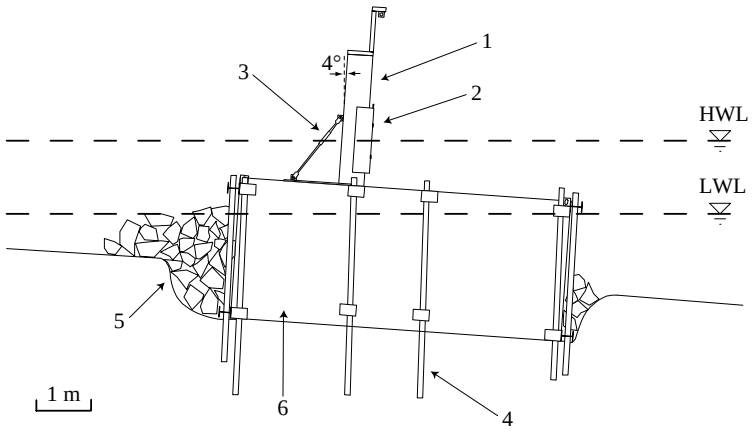

Fig. 1. Side view of the pile with the 20’ container as a foundation. The water level at high and low tide are marked with dashed lines. The arrows denote: 1. Pile, 2. Load panel, 3. Turnbuckle with strain gauge, 4. Anchor beams, 5. Rock fill, 6. Container

The structure was installed at low tide in shallow water. Then it was possible to access the roof during low tide, and conduct the experiments during high tide. The tidal amplitude varies between 1 and 2 m in the area.

TEST SET-UP AND EXECUTION

Several codes and investigations (Løset et al., 1999, Schwarz, 1994, Sodhi, 1992) were compared to establish the design force of the given structure. The empirical equation presented by Schwarz (1994) (variation of Eq. 7 in Schwarz et al. (1974)) was used to predict the ice force on a 0.665 m wide structure (110 kN with 0.2 m thick ice), even though it is based upon laboratory experiments with up to 0.1 m wide structure indented into freshwater ice sheet. The results of Schwarz were, however, validated by Wessels and Jochmann (1991), who conducted measurements on a 2.0 m wide jacket leg in Bohai Bay. The set-up was designed for 200 kN ice load, which corresponds to 0.35 m thick ice according to the Iowa formula (Wessels and Jochmann, 1991).

The goal of the experiment was to conduct natural sea ice interaction with a structure as described in the previous section. As the parent ice sheet of the fjord (up to 1.35 m thick in the end of April 2003) would yield too high forces, a thinner sheet had to be used for the experiment. A hole measuring 10 m wide and 10 m long was made in front of the structure. Blocks measuring approximately 1x1 m in the surface were cut out with a hydraulic chain saw (Stanley CS11) with a 1.50 m long sword mounted. A digger (Komatsu PW95) lifted the ice blocks out of the basin and they were transported away from the site with a tractor (Massey Ferguson MF675) as the weight of the blocks would push the parent ice cover down and flooding would occur making the site unsafe and unfit to work on. When all the ice blocks were removed the basin was left undisturbed so the ice could grow until the desired thickness was reached. The area is very prone to bad weather and snow blew into the basin just after opening so the ice was frozen out of slush.

When the wanted ice thickness was reached, the test ice floe was cut free from the parent ice sheet. 1 m wide channels were cut on each side creating a test floe 8 m wide and 10 m long. In the far end from the structure a part of the parent ice sheet was included with the test ice floe as a towing floe. In this part, anchors were frozen in to transfer the forces from the winch to the ice, and thus the ice flow was named towing ice floe. It was pulled by the winch pushing the test ice floe into the pile. The movement of the ice was measured with a displacement meter from the towing ice floe to the parent ice sheet. The velocity was deduced from the displacement measurements.

To transfer the forces between the winch and the ice, a number of steel rods and steel rope were used as shown in Fig 2. The pneumatic winch (PROFI 6T) had a pulling capacity of 60 kN and a tackle was used to increase the total pulling force to 240 kN. To transfer the forces between the tackle and the anchors in the towing ice floe, two long steel bars (Ø35 mm), which each consisted of 3 segments (6 m), giving a total length of 18 m, was used. The pulling force was measured (T20 by Waage Instruments) in the connection point (number 8 in Fig. 2) between the tackle and the two long steel bars.

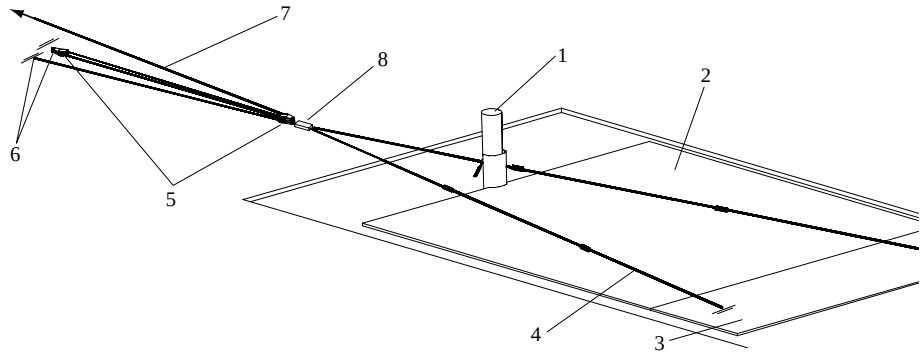

Fig. 2. Overview of the test set-up. The arrow denotes the pulling direction of the winch. The numbers denote: 1. Pile Ø470 mm, 2. Ice floe for interaction with structure, 3. Towing floe, 4. Steel bar Ø35 mm, 5. Pulleys, 6. Fixed points, 7. Chain connected to the winch, 8. T20 load cell

The tackle consisted of steel rope and pulleys. The stiffness of the steel rope turned out to be a problem as it was very elastic. This meant that when the ice was resisting (load build-up) the wire was stretched until the load was so high that the ice failed. At the moment of failure all the energy stored in the wire was released and thus forced the steel bars and the ice to move forward with high speed.

Two devices measured the exerted force from the ice onto the structure. Firstly a turnbuckle with a strain gauge was installed between the pile and the container (Figs. 1, 3 and 4). Secondly, load cells (CS2S by Waage Instruments) transferred the forces between the load panel and the pile. However as shear forces were transmitted, but not measured by these load cells, these measurements have been rendered useless. To get an idea of the force – strain relationship in the strain gauge, two calibration runs were made. These consisted of applying a known measured force onto the pile directly while measuring the strain in the turnbuckle.

Because of the highly elastic steel rope used in the tackle, the system behaviour was not as anticipated. The steel rope worked as a spring and as the winch were pulling at a nearly constant speed the steel rope elongated, while the ice were stationary until the load were equal to the failure load of the ice.

Fig. 3. Close-up of the structure. 1. Load panel Ø665 mm, 2. Turnbuckle with strain gauge, 3. Steel bar, 4. Radial crack

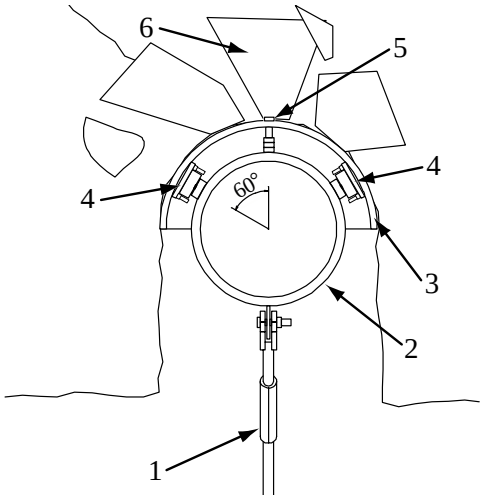

Fig. 4. Top view of the ice structure interaction. Note the radial crack in the top left corner. 1. Turnbuckle with strain gauge, 2. Pile, 3. Load panel, 4. Load cell, 5. Pretensioned bolt, 6. Ice pieces

The measurements were recorded with two Datascan 7221 data-loggers, which were connected to a laptop running Labtech data acquisition software. The sampling were done at 10 Hz. To ensure that both data-loggers were using the same time domain they were linked. The measurements for the two tests are summarised in Table 1.

Table 1. Summary of ice properties, measurements and documentation.

Test	Date	Ice properties				Measurements and documentation				
		Ice temperature	Ice salinity	Ice strength	Thin sections	Exerted force [1]	Pulling force	Ice displacement	Ice pressure	Video documentation
1	13.04.2003	X	X			X	X	X		X
2	27.04.2003	X	X	X	X	X	X	X	X	X

[1] Deduced from the strain measurements on the turnbuckle.

ICE PROPERTIES

Ice salinity and temperature were measured in–situ. Horizontal and vertical ice cores were sampled and taken back to the laboratory at UNIS for uniaxial testing. However, the ice sampled after the first test was lost, so only temperature and salinity are available for test 1. The average salinity of test 1 was 10.7 ppt and the salinity measurements of test 2 show a linear decreasing salinity (Fig. 5), from 9 ppt at the top of the ice to 6 ppt at the bottom. The ice temperature was nearly constant at –2.5°C in test 1 and almost linearly increasing from –6°C to –2°C in test 2. The air temperature at the time of testing was –1.7°C and –10.6°C for test 1 and 2 respectively.

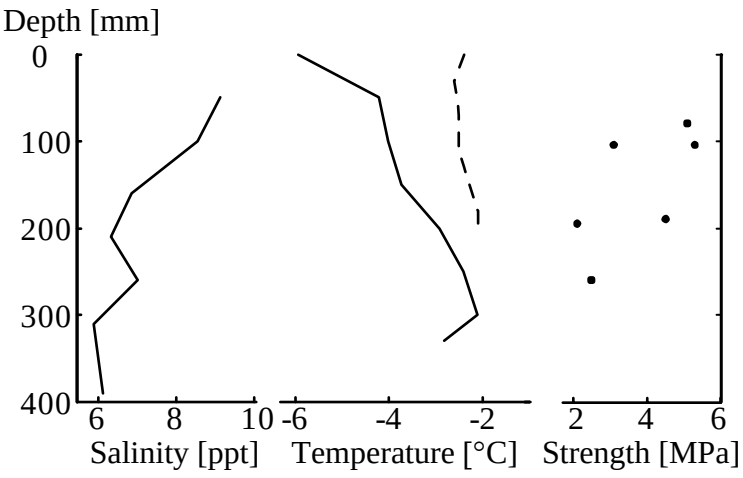

Fig. 5. Salinity, temperature and horizontal uniaxial strength as a function of depth. Test 1 with dashed line, test 2 with solid line. Strength data only for test 2

During freezing of the test ice cover in the basin, wind transported snow into the basin. At this stage the basin was not covered to prevent the snow mixing into the ice. This should have been prevented as the snow became saturated with water and froze to ice.

The samples were cored and had a cylindrical shape with diameter 70 mm and length 175 mm and were transported, stored and tested according to standardised testing methods as described by Schwarz et al. (1981). During storage and testing the ice samples were kept at a nominal temperature of –17°C. The strain rate used at the uniaxial tests was $\dot{\varepsilon} = 10^{-3}$ s^{-1}. For the vertical samples the ice strength was determined to 4.1 ± 0.5 MPa, while the horizontal uniaxial strength ranged from 2.1 MPa to 5.3 MPa with a mean of 3.8 MPa. Horizontal samples were taken at different depths in the ice and the dependency is shown in Fig. 5.

Thin sections of the sampled ice were also prepared. They showed a predominantly granular crystal structure, but columnar crystals were also found in the lower part of the ice. The granular crystals had a diameter of 1-3 mm, while the columnar crystals had a typical length of 25 – 30 mm. Bjerkås (2003) reported columnar grains more than 80 mm long for the parent ice sheet in proximity of the test site.

ACKNOWLEDGEMENTS

We would like to thank Statoil ASA and the Norwegian Research Council for financially supporting this work. Store Norske Spitsbergen Kulkompani provided much needed food, lodging and logistics. We are grateful to all the participants, contributors and especially to the Russian drilling experts Sergey Vernyayev and Rinat Kamalov. The help of Professor Lars Grande of NTNU and Professor Karl Shkhinek of SPTU was highly appreciated.

REFERENCES

Bjerkås M. (2003): Compressive Behaviour of Norwegian Arctic Sea Ice under Vertical and Horizontal Loading. In *UNIS AT-208 Students Report spring 2003*, University Centre on Svalbard, 10 p.

Frederking R., I.J. Jordaan, J.S. McCallum (1990): Field tests of ice indentation at medium scale Hobson's Choice ice island, 1989, *Proc. 10th Int. Sym. on Ice (IAHR)*, Espoo, Finland, pp. 931 – 944.

Liferov P., S. Løset, P.O. Moslet, B. Bonnemaire, and K.V. Høyland (2002): Medium scale modelling of ice ridge scouring of the seabed, Part I: Experimental set-up and basic results. *Proc. 16th Int. Sym. on Ice (IAHR)*, Dunedin, New Zealand, pp. 86 – 93.

Løset S., K. Shkhinek, E. Uvarova (1999): An overview of the influence of structure width and ice thickness on the global load. *Proc. 15th Int. Conf. on Port and Ocean Engineering under Arctic Conditions (POAC)*, Helsinki, Finland, pp. 425 – 434.

Schwarz J., K.-I. Hirayama, H. C. Wu (1974): Effect of Ice Thickness on Ice Forces. *6th Offshore Technology Conference*, Houston, USA, pp. 145-156.

Schwarz J., R. Frederking, V. Gavrillo, I.G. Petrov, K.-I. Hirayama, M. Mellor, P. Tryde, K.D. Vaudrey (1981): Standardized testing methods for measuring mechanical properties of ice. *Cold Regions Science and Technology*, Vol. 4, pp. 245 – 253.

Schwarz J. (1994): Low level ice forces. *Proc. 12th Int. Sym. on Ice (IAHR)*, Trondheim, Norway, pp. 1040 – 1050.

Sodhi D.S (1992): Ice – structure interaction with segmented indentors. *Proc. 11th Int. Sym. on Ice (IAHR)*, Banff, Canada, pp. 909 – 929.

Sodhi D.S., T. Takeuchi, M. Kawamura, N. Nakazawa, S. Akagawa (2001): Measurements of ice forces and interfacial pressure during medium-scale indentation tests in Japan. *Proc. 16th Int. Conf. on Port and Ocean Engineering under Arctic Conditions (POAC)*, Ottawa, Canada, pp. 617 – 626.

Sodhi D.S. (1998): Nonsimultaneous crushing during indentation of freshwater ice sheets. *Cold Regions Science and Technology*, Vol. 27, pp. 179 – 195.

Timco G.W. (1987): Indentation and penetration of edge-loaded freshwater ice sheets in the brittle range. Proc. *5th Int. Offshore Mechanics and Arctic (OMAE) Symposium*, Tokyo, Japan, pp. 444 – 452.

Wessels E., Jochmann P. (1991): Model/Full scale correlation of ice forces on a jacket platform in Bohai Bay. Proc. *11th Int. Conf. on Port and Ocean Engineering under Arctic Conditions (POAC)*, St. Johns, Canada, pp. 198 – 212.

17th International Symposium on Ice
Saint Petersburg, Russia, 21 - 25 June 2004
International Association of Hydraulic Engineering and Research

SEA ICE – VERTICAL PILE INTERACTION EXPERIMENT, PART II: TEST RESULTS 2003

P.O. Moslet[1], K.V. Høyland[1]

ABSTRACT
A medium scale ice – interaction experiment has been conducted at Svalbard, Norway as described in Part I. During the interaction the pulling force, the ice displacement, the ice pressure and strain on the structure was measured. A pressure sensor was installed in the ice floe ahead of the structure and the stresses in the ice floe measured in time. Two ice sheets were naturally grown and level ice between 0.16 m to 0.27 m thick was pushed against the structure. The highest force exerted by the ice on the load panel was 161 kN and the highest effective pressure was 1.5 MPa as 0.16 m thick ice was crushing against the structure. The measured internal stresses in the ice floe are compared with elastic and elasto-plastic theory. Crushing and spalling ice failure was observed and both radial cracking and splitting of the tested ice floes occurred. Test results are presented and discussed.

INTRODUCTION
Hydrocarbon field development in icy waters presents a challenge for design engineers. Sea ice introduces new aspect for the design of platforms, ships, loading facilities and evacuation systems. Surveys (Croasdale and Kennedy, 1996, Shkhinek et al., 1994, Sanderson, 1988) illustrates the scatter in the experts' opinion about the loads on offshore structures in ice-infested waters. It is clear that further research is needed to understand the processes associated with ice – structure interaction.

Part I (Moslet et al., 2004) describes the test set-up and the ice properties for the ice – structure interaction experiments conducted on Svalbard, Norway during spring 2003.

TEST RESULTS
Level ice with thickness varying from 0.16 – 0.26 m was towed towards a cylindrical structure with diameter 0.665 m. Crushing, spalling, radial cracking and splitting failure was observed. The data for the two tests are summarised in Table 1.

The first test was conducted with relatively warm ice (T_{ice} = -2.5°C). The ice was pulled against the structure with an average velocity of 8 mm/s. The exerted force, calculated from the strain measurements, and the displacement can be seen in Fig. 1.

[1] The University Centre in Svalbard

Table 1. Test data

Test	Date	$\overline{T}_{ice}$ [ºC]	T_{air} [ºC]	h_i [m]	$\overline{v}$ [m/s]	$\overline{S}$ [ppt]	$F_{\max}$ [kN]	$\overline{\sigma}_{\max}$ [MPa]
1	13.04.2003	-2.5	-1.7	0.20	$8 \cdot 10^{-3}$	10.7	23	0.173
2	27.04.2003	-4	-10.6	0.16 – 0.26	$3.5 \cdot 10^{-3}$	7.1	161	1.542

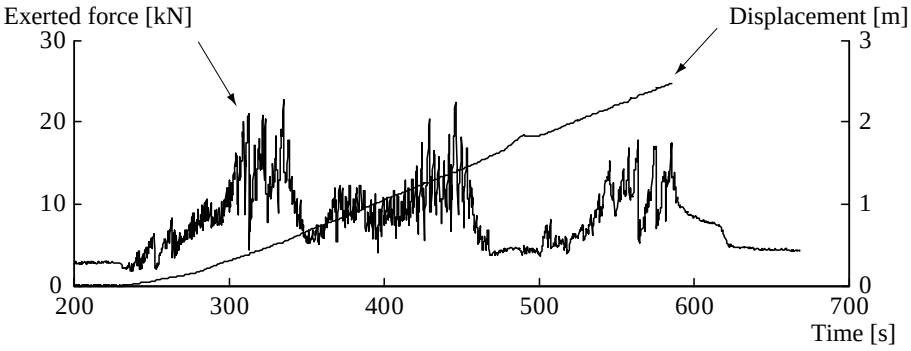

Fig. 1. Exerted force and displacement for test 1

The maximum force measured was 23 kN. The floe was 7 m wide and 8 m long, the ice thickness was 0.2 m and the ice was crushing with frequencies of 0.3 – 0.5 Hz. The failure length, measured by the displacement sensor, was 0.02 m. After 586 seconds the ice floe split after the structure had penetrated 2.44 m into the ice floe. The crushed material consisted of pulverized ice.

Fig. 2 shows the exerted force and displacement of the second test. The ice was more uneven than in the first test with an ice thickness varying between 0.16 and 0.26 m. In some parts of the ice floe the ice was up to 0.42 m thick, but these areas were never in contact with the structure. The ice below 0.3 m depth consisted of very soft pieces of high porosity ice. During the freezing of the second test floe, ice blocks slid under the ice and froze to the test floe increasing the ice thickness in certain areas making rafted ice with a soft lower rafted layer. No measurements have been conducted with this soft ice. During test 2 the ice failed in both crushing and spalling and the failure length was up to 0.15 m. The spalling failure did not occur at every failure.

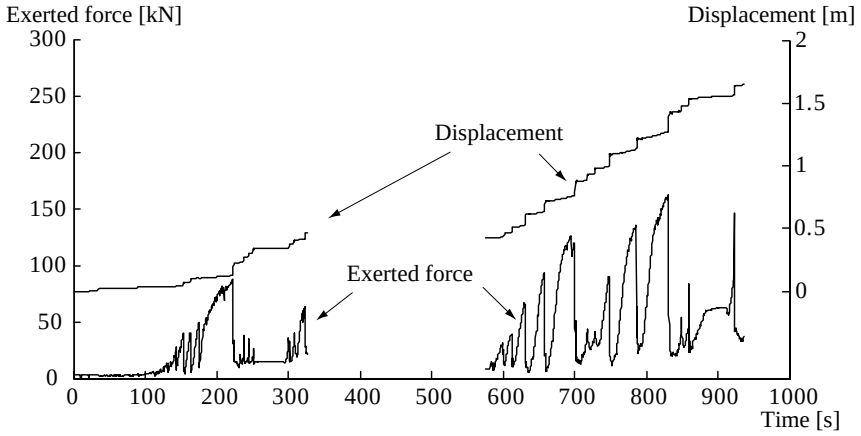

Fig. 2. Exerted force and displacement for test 2

It was full contact between the ice and the structure after 250 seconds. After 301 seconds a radial crack appeared (Fig. 4 in Moslet et al. (2004)) and the test was stopped shortly after to review the situation. It was then discovered that the ice contact surface was very smooth and seemed almost polished. As seen on Fig. 2 the frequency of the failure events were lower than of test 1 and in the order of 0.05 – 0.1 Hz. Maximum load occurred after 830 seconds and was 161 kN. Total indentation during the second test was 2.15 m, but after 1.61 m of indentation (935 seconds), the floe came in contact with the parent ice cover and only the results before contact are presented here.

DISCUSSION

The vertical uniaxial ice strength shows small variation in space, while the horizontal samples, showed however, large variations. The horizontal samples also showed variation with depth and in average the samples taken from the top part of the ice was 1.5 MPa stronger than in the lower part. The procedures can of course be questioned since the ice was quite warm during the test, while it was stored and tested at about –17°C. Vertical samples were stronger than horizontal samples, which also was the case for the parent ice sheet (Bjerkås, 2003).

In between the failures of test 2, when the ice was in contact with the structure and the load was building up, there were small movements of the ice. It is believed that these movements are the sum of the elastic deformation of the structure and the ice, and the plastic deformation of the ice in the contact zone. This displacement occurred with an average velocity of $0.75 \cdot 10^{-3}$ m/s, which is slow compared to the average velocity of the test, which was $3.5 \cdot 10^{-3}$ m/s. However because there were 10 – 30 seconds between each crushing event, the ice moved as much as 65 mm during one loading event. Using Hookes law of elasticity with an elastic modulus of 5 GPa the elastic displacement of the ice would amount to 1 mm. The deflection of the pile with the maximum exerted force was less than 1 mm based on calculations for a cantilever beam. So most of the movement seems to be plastic deformation of the ice in the contact zone. This is supported by the fact that the contact surface was very smooth and even, which would not be the case just after failure. So it seems, as it was plastic deformation in the contact zone, which increased the real contact area while the load was building up.

The high forces in test 2 compared to test 1, lead to a different system behavior. When contact was made between the ice and the structure, the ice stopped until the pulling force was high enough for failure to occur. This was an effect of the highly elastic wire in the tackle, which worked as a spring. Just after failure the ice leaped forward and velocities as high as 0.5 m/s were measured. This means that in addition to the failure length created by the original failure, the high velocity just after failure may have expanded this original failure length. However, the increment of the failure length due to the high velocity is thought to be proportional to the load drop itself as since the load just before failure will be proportional to the energy stored in the wire.

Comparing Fig. 1 and Fig. 2 the frequency of the failure events and the magnitude of the load are different in the two tests. At the first test the ice had a high salinity and was close to the melting point, while the ice of test 2 was fresher and colder. This was clearly proved by the different failure mechanisms taking place.

For test 2 it was installed two BP pressure sensors (Duckworth and Westermann, 1989) to measure the internal stress state of the ice sheet during the interaction. The pressure at

a certain distance from the structure can be modelled by a thick infinite long expanding cylinder (Hill, 1950). The elasto-plastic solution reads:

$$\sigma(r) = \sigma_r \frac{a^2}{(r+a)^2} \tag{1}$$

$$\sigma(\theta) = \sigma_\theta \frac{a^2}{(r+a)^2} \tag{2}$$

where σ_r is the radial pressure and σ_θ is the tangential pressure at $r = 0$, a is the internal radius of the cylinder and r is the distance from the cylinder. The measured pressure by the sensor is compared with Hills elasto-plastic theory in Fig. 3. The effective pressure in the test is used as the radial pressure in Eq. 1 and is only true at a certain distance from the cylinder. Hills solution is only true for an infinite space and not the finite half-space considered here. However, the pressure dissipates fast as only 0.5 % of the effective pressure is remaining at 4 m distance. Given the half-space conditions, the stress state will differ and especially the tangential solution (Eq. 2).

The term failure length is applied here to the zone where the ice has failed in such a manner that only a fractional part of the ice strength is left after failure. The failure length was measured with the displacement meter and is displayed as a function of the effective pressure in Fig. 4. The effective pressure is here the peak load just before failure divided on the contact area.

Spalling failure was also observed and progressed further than the failure length. Only a part of the ice thickness spalled away so the failure length is here defined as less than the spalling length. Assuming that the original failure length is proportional to the effective pressure, the experienced failure length during test 2 would also be proportional to the effective pressure, which is measured. The failure length was up to 153 mm long, while the spalling extended almost 500 mm away from the structure at one occasion.

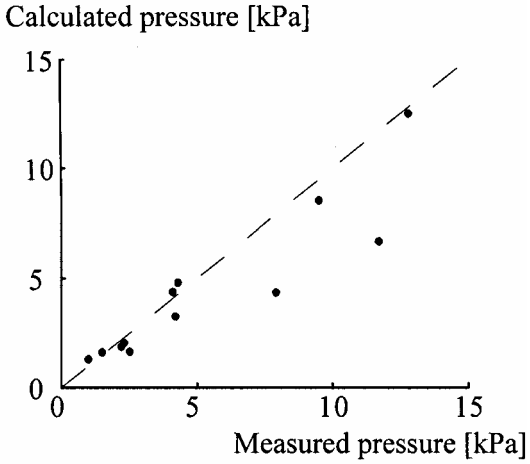

Fig. 3. Pressure calculated with elasto-plastic theory versus measured pressure by the pressure sensor

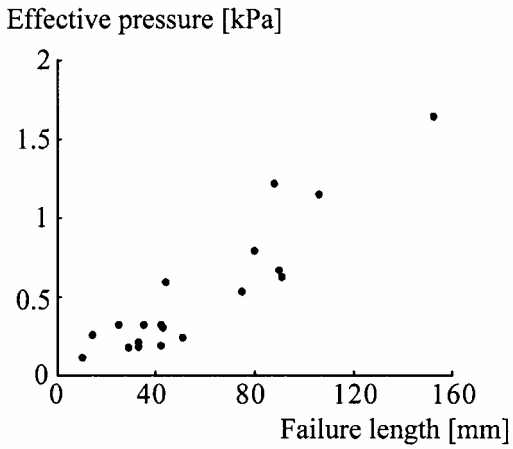

Fig. 4. Failure length as a function of the peak effective pressure

Fig. 5 shows the development of failure in test 2. First a high degree of contact was established (Fig. 5a). This led to a high force build up followed by a large failure zone and spalling failure (Fig. 5b). From an underwater camera, large pieces of ice were seen breaking off during the test. It is believed that these pieces were spalled of the bottom part of the ice sheet as it also happened on the topside.

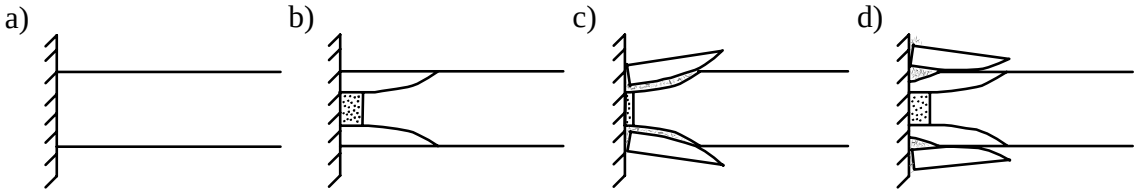

Fig. 5. a) initial conditions with a high degree of contact between ice and structure; b) high-force build-up and spalling with partly crushing occurs, large failure length; c) reduced contact area with low-force failure and small failure length; d) higher degree of contact is established, which leads to high-force build-up and large failure length

As the top part of the ice (in average 1.5 MPa stronger than the ice of the lower part as reported by Moslet et al. (2004)) had broken off, there was substantial reduced load carrying capacity of the residual ice, in addition to a reduced contact area. So then followed a series of failures with less failure load (Fig. 5c), where there was only crushing failure. When a higher degree of contact had been established again (Fig. 5d), the process repeated with a high force build-up, a large failure zone and spalling failure. It is not believed that the high forces are directly connected to the increasing contact area, but rather that colder stronger ice was in contact with the structure during these events, and thus increasing the strength of the ice at the contact surface.

CONCLUSIONS

Two ice sheets have been grown and pulled against a 0.665 m wide cylindrical structure. During test 1 a 0.2 m thick ice floe exerted up to 23 kN, while the ice of test 2, 0.16 – 0.26 m thick, exerted up to 161 kN. The ice thickness in the two tests were similar, but the ice of test 1 was close to the melting point (T_{ice} = -2.5°C) and with high salinity (10.7 ppt) compared to the ice of test 2 (T_{ice} = -4°C, 7.1 ppt). During test 1 the ice failed in crushing before the ice floe split. Crushing, spalling and radial cracking were observed for test 2.

ACKNOWLEDGEMENTS

We would like to thank Statoil ASA and the Norwegian Research Council for financially supporting this work. Store Norske Spitsbergen Kulkompani provided much needed food, lodging and logistics. We are grateful to all the participants, contributors and especially to the Russian drilling experts Sergey Vernyayev and Rinat Kamalov. The help of Professor Lars Grande of NTNU and Professor Karl Shkhinek of SPTU was highly appreciated.

REFERENCES

Bjerkås M. (2003): Compressive Behaviour of Norwegian Arctic Sea Ice under Vertical and Horizontal Loading. *In UNIS AT-208 Students Report spring 2003*, University Centre on Svalbard, 10 p.

Croasdale K.R, K.P. Kennedy (1996): Ice loads consensus study update. *Proc. 15th Int. Conf. on Offshore Mechanics and Arctic Engineering (OMAE),* Florence, Italy, Vol 4., pp. 115 – 118.

Duckworth R., P.H. Westermann (1989): Stress and Strain Instruments Developed for Field Measurements of Ice. *IEEE Journal of Oceanic Engineering,* Vol. 14, Issue 2, pp. 159 – 165.

Hill R. (1950): The mathematical theory of plasticity. Oxford, *Clarendon Press,* 355 p.

Moslet P.O., P. Liferov, R. Nilsen, K.V. Høyland, M. Bjerkås, B. Bonnemaire, J. Dybdahl, S. Løset (2004): Sea Ice – Vertical Pile Interaction Experiment, Part I: Test Set-up and Ice Properties. *Proc. 17th Int. Sym. on Ice (IAHR)*: St. Petersburg, Russia, submitted.

Sanderson T.J.O. (1988): The ice load question: Some answers. *Proc. 9th Int. Sym. on Ice (IAHR),* Sapporo, Japan, pp. 740 – 748.

Shkhinek K.N., D. Blanchet, K. Croasdale, D.G. Maskevitch, S.U. Bhat (1994): Comparison of the Russian and foreign codes and methods for global load estimations. *Proc. 13th Int. Conf. on Offshore Mechanics and Arctic Engineering (OMAE),* Houston, USA, Vol 4., pp. 75 – 82.

17th International Symposium on Ice
Saint Petersburg, Russia, 21 - 25 June 2004
International Association of Hydraulic Engineering and Research

THE SIMULATION SEA ICE PILE-UP ON INCLINED STRUCTURE

LI Chunhua[1], WANG Yongxue[2]
SUN Hequan[3] and LI Zhijun[4]

ABSTRACT

The process of sea ice pile-up on an inclined structure is simplified to a two-dimension dynamic problem. Assuming the sea ice to be viscous-elastic material, the process of sea ice pile-up is simulated by using the discrete element method, which is based on the simulation of systems of multitudinous polygonal blocks. And, the model is verified to be reasonable and feasible via the comparison with the 2D theory and physical experiments.

INTRODUCTION

Sea Ice pile-up or ride-up occurs commonly when a large ice sheet is pushed against an inclined surface such as a beach, breakwater, or offshore structure by environmental forces in cold regions. The influence induced by the ice pile-up or ride–up may damage the embankments and structures. Therefore, it is necessary to study the mechanism of ice ride-up and pile-up in order to defend the structures.

However, the dynamic interaction between the moving ice sheet and the structure is a very complex process which is governed by a number of factors including the configuration of the structure, the contact conditions at the ice-structure interface and the speed of movement of the ice sheet, etc. Large scale field-testing is full of difficulty and is also very expensive so that few programs are executed by this way. The numerical simulation method becomes one of the most effective and economic methods. The mechanism of ice ride-up and pile-up is complex because it not only involves failure of the ice sheet but also numerous individual ice blocks form and move quite considerable distances. Finite element and boundary element schemes had ever been tried to illustrate the problem, but they are only able to examine the initiation and evolution of fragmentation (Ingraffea and Saouma, 1984; Selvadurai et al., 1993; Selvadurai and Busschen, 1995). At the present time, the discrete element method is

[1] Associate Professor, National Marine Environmental Forecasting Center,Beijing 100081, China
[2] Professor, State Key Laboratory of Coastal and Offshore Engineering, DUT, Dalian 116024, China
[3] Docent, State Key Laboratory of Coastal and Offshore Engineering, DUT, Dalian 116024, China
[4] Professor, State Key Laboratory of Coastal and Offshore Engineering, DUT, Dalian 116024, China

considered a useful means to simulate the ice ride-up and pile-up process on the structure, because it can supply the gap associated with FEM and BEM in the simulation. Based on the numerical simulation of systems of multitudinous polygonal blocks (Hopkins, 1992), the paper develops a program to simulate the ice pile-up on an inclined structure process visually. And, the model is verified to be reasonable and feasible via the comparison with the 2D theory and physical experiment which is conducted with the DUT-1 non-refrigerated model ice in the State Key Laboratory of Coastal and Offshore Engineering of Dalian University of Technology.

NUMERICAL MODEL

Figure 1. describes the initial status of ice sheet, which moves toward the slope structure along *x* direction at a constant speed. When the ice sheet contacts the surface of the structure, the ice sheet rides up on the structure surface and fractures may be happened. The pile-up is formed as the fragments continue ride-up or slide down into water.

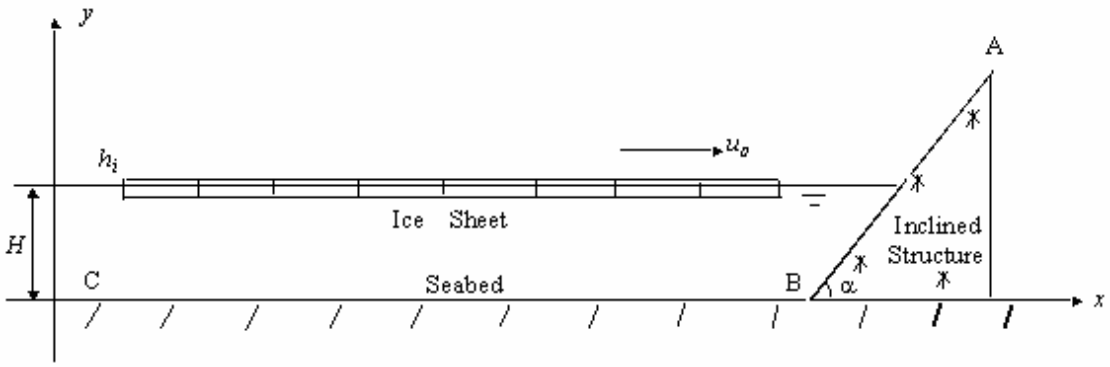

Fig. 1. Initial status of ice sheet

Shown as in Figure 1, the inclined structure and the seabed are two fixed boundaries. Assuming the ice sheet glued joint with some ice blocks and according to the Newtonian dynamic theory, the ice blocks are satisfied with the following equations when they contact the structure or interact with themselves.

$$m_i \frac{du_i}{dt} = \sum F_i^x \qquad m_i \frac{dv_i}{dt} = \sum F_i^y \qquad I_i \frac{d\omega_i}{dt} = \sum M_i^o \qquad i=1,2\ldots n \tag{1}$$

where m_i is the mass of i block and I_i is its inertia moment. u_i, v_i, ω_i are corresponded to the horizontal speed, vertical speed and angle speed of the i block respectively, and F_i^x, F_i^y, M_i^o are its horizontal force, vertical force and moment respectively.

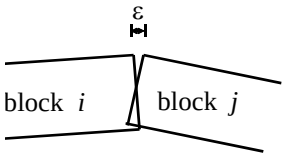

Fig. 2. Glued joint model between blocks

Figure 2 shows the glued joint model between ice blocks and a viscous-elastic force model is used. The ice sheet is fractured if the stress in a glued joint,

$\sigma_m = k_e\varepsilon + k_v\, d\varepsilon/dt$, where k_e and k_v are the elastic modulus and viscous damping of the ice sheet and ε is the strain at the end of joint, exceeds the compressive or tensile stress of the material. The ice blocks become into the discrete blocks undergoing the failures.

Assuming the discrete blocks contacting to be the viscous-elastic force model also, the normal and tangential force models between adjacent blocks are shown in Figure 3. The symbols k_{ne}, k_{te}, k_{nv} shown in the figure represent the normal and tangential elastic stiffness and the normal viscous damping respectively, and μ denotes the friction coefficient between the blocks. The normal and tangential forces, $F_{i,j}^n$ and $F_{i,j}^t$, are concerned with these parameters, and the maximum tangential force can not exceed the frictional force between adjacent blocks, and the computation expressions are as follows.

$$\begin{aligned} F_{i,j}^n &= k_{ne}\Delta Area_{i,j} + k_{nv}\Delta Area_{i,j}/\Delta t \\ F_{i,j}^t &= k_{te}V_{i/j}^t\Delta t \qquad \left|F_{i,j}^t\right| \le \mu F_{i,j}^n \end{aligned} \tag{2}$$

where the denotation $\Delta Area_{i,j}$ represents the deformation area of ice block and Δt is the calculation time step, and $V_{i/j}^t$ the relative tangential speed between *i* block and j block. Translating the forces $F_{i,j}^n$、$F_{i,j}^t$ into the component of forces $F_{i,j}^x, F_{i,j}^y$ in integer coordinate system,

$$F_{i,j}^x = n_x F_{i,j}^n - n_y F_{i,j}^t \tag{3a}$$

$$F_{i,j}^y = n_y F_{i,j}^n + n_x F_{i,j}^t \tag{3b}$$

$$M_{i,j}^o = r_{i,j}^x F_{i,j}^y - r_{i,j}^y F_{i,j}^x \tag{3c}$$

where n_x, n_y is the *x* and *y* direction components of normal vector on interface between *i* and *j* blocks, $M_{i,j}^o$ is the moment of *j* block acting on the centroid of *i* block and $r_{i,j}^x, r_{i,j}^y$ are the *x* and *y* direction components of distances from the acting point to the centroid of *i* block respectively.

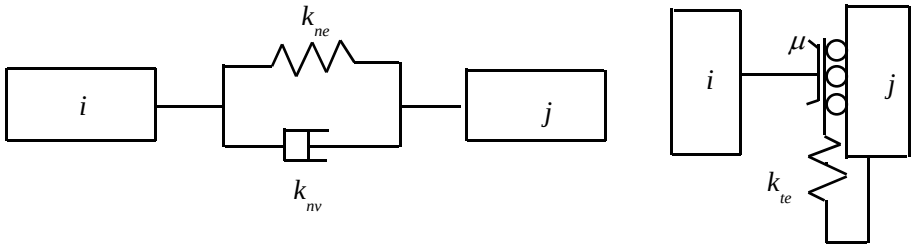

(a) Normal force model (b) Tangential force model

Fig. 3. Contact model between adjacent blocks

Besides the interaction forces, the ice block weight W_i and the buoyancy force F_i^b need to be considered, then the right terms of equations (1) can be derived as follows.

$$\sum F_i^x = \sum_{j=1}^{n} F_{i,j}^x$$

$$\sum F_i^y = \sum_{j=1}^{n} F_{i,j}^y + W_i + F_i^b \quad i \neq j \tag{4}$$

$$\sum M_i^o = \sum_{j=1}^{n} M_{i,j}^o + r_{ib}^x F_i^b$$

where r_{ib}^x is the *x* component of distance from the buoyancy center to the centroid of *i* block.

The simulating steps are as follows: The initial position and velocity of each block are given. With the motion of the blocks and discovering the blocks that are in contact with other blocks at a given time, the force between these blocks is calculated. Then the position and velocity of each block at the given time can be derived from the integration of the equation (1). Finally, the simulation program visualizes the pile-up process.

SIMULATED RESULTS

Initial ice fractured forces

Based on the elastic foundation beam assumption (Croasdale, 1994), the horizontal force F_H and vertical force F_v, which are acted on a wide inclined structure due to the ice ride-up, can be calculated by the formulas as follows.

$$F_H / F_V = \frac{\sin\alpha + \mu\cos\alpha}{\cos\alpha - \mu\sin\alpha} \tag{6a}$$

$$F_V = 0.68\sigma_f (\rho_w g h_i^5 / E)^{0.25} \tag{6b}$$

where α is the slope angle and μ is the friction coefficient between the ice and the structure, σ_f, E and h_i are the ice limited flexural stress, elastic module and the ice thickness respectively, ρ_w the water density and *g* the gravity acceleration.

Table 1. The comparison of simulated initial ice fractured force with numerical and theoretical results

α (°)	σ_f (kPa)	E (MPa)	F_H (N)		F_V (N)		F_H / F_V	
			numerical	theory	numerical	theory	numerical	theory
35	61.46	161.14	10.035	10.196	8.712	8.852	1.1518	1.1518
45	46.03	60.44	11.864	14.119	7.119	8.471	1.6667	1.6667
60	43.93	96.78	28.680	25.125	8.204	7.187	3.4958	3.4958
70	62.58	260.91	86.515	76.489	9.038	7.990	9.5726	9.5726
80	76.20	182.98	345.284	150.674	10.476	10.6321	32.9605	14.1718

Notes: $\mu = 0.25$, $h_i = 0.8$cm

Table 1 lists the results of initial fractured ice forces obtained from theoretical formulas and numerical simulation. Comparing the values of the forces F_H and F_V gained from the two ways, it is seemed that the simulated results are less than theoretical results as the slope angle α is less than 45°, which is due to the different assumption of the ice material, that is, viscous-elastic material is assumed in numerical model and elastic material in theory. When the slope angle α is more than 45°, the fracture made of ice sheet includes the compress failure due to the steep slope, so the simulated results are larger than theoretical results. Moreover, the ratio of simulated horizontal and vertical forces, F_H / F_V, are equal to the results calculated by theory as the slope angle α is less than 80°. However, they are very different when the slope angle α is equal to 80°, which shows that buckling failure of ice sheet rather than flexural failure is happened as the slope is up to the value of $\arctan(1/\mu)$, and the 2D theoretical formulas are only fit to the flexural failure of ice sheet on gentle slope, $\alpha < \arctan(1/\mu)$.

SIMULATED PROCESS OF ICE PILE-UP

The simulated ice pile-up process on a 45° inclined structure is shown in Figure 4, where the ice thickness is 0.8cm and the ice sheet speed is 5cm/s, and its limited flexural stress and elastic module are 46.03kPa and 60.44MPa respectively as listed in Table 1. The figure shows that the ice sheet is fractured when it contacts with the structure, then the blocks broken from the ice sheet slide down into water or ride up along the slope, and an ice pile-up is formed at last. During the period, the ice sheet plugging into ice pile is happened frequently.

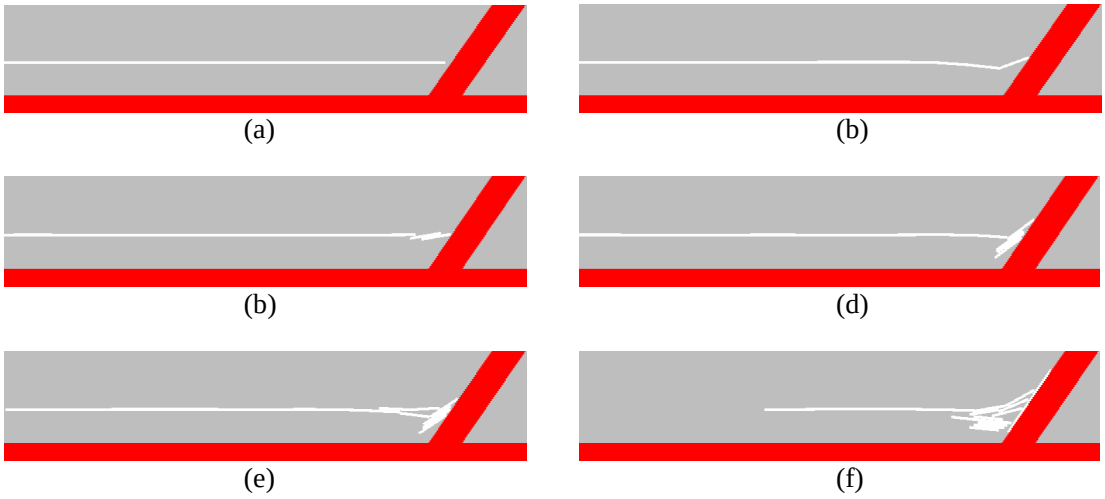

Fig. 4. Simulated ice pile-up process on 45° inclined structure

The process is quite similar to the phenomena obtained from physical experiment as shown in Figure 5 where the parameters of ice and structure are same to the numerical model. The experiments are conducted by using non-refrigerated breakable model ice developed in Dalian University of Technology.

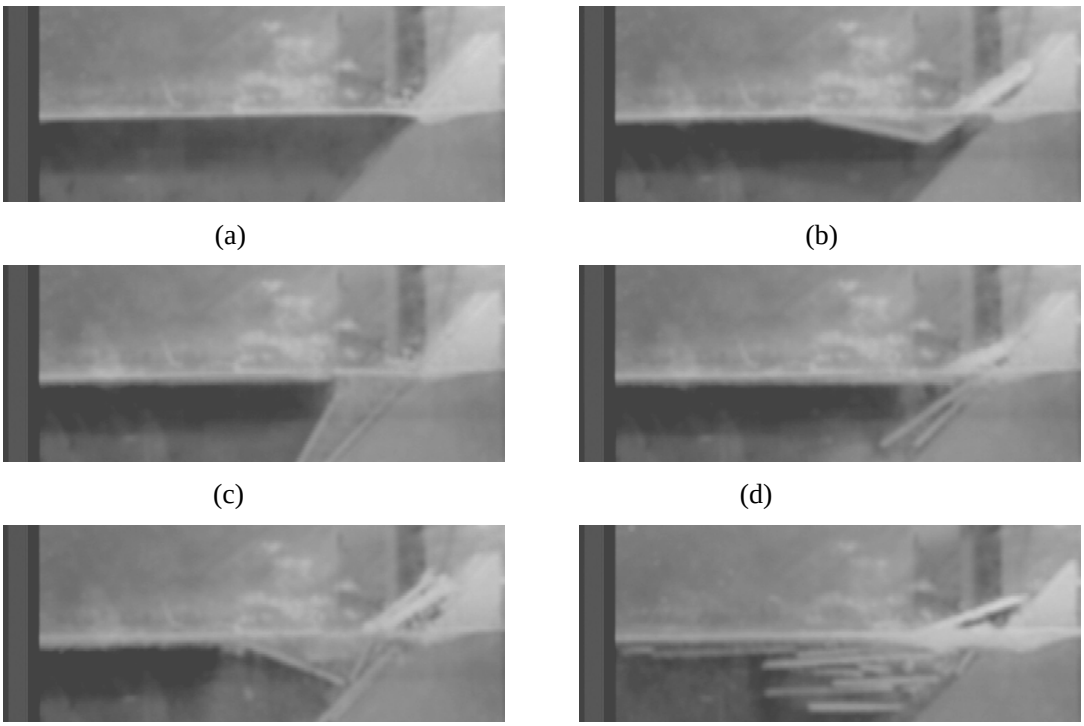

(a) (b) (c) (d) (e) (f)

Fig. 5. Experimental ice pile-up process on 45° inclined structure

HISTORIES OF ICE FORCE

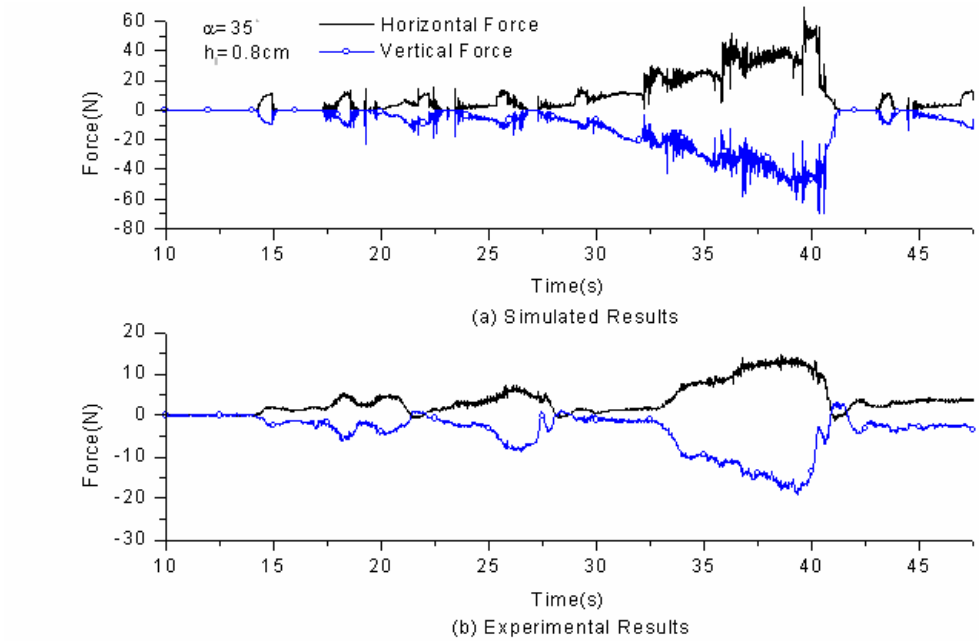

Fig. 6. The histories of ice force on 35° inclined structure

Figure 6 and Figure 7 show the histories of ice force on the inclined structure of 35° and 70° respectively, and the parameters of ice are listed in Table 1 and the ice sheet speed is 5cm/s. Comparing the simulated results and the experimental results, the trends of their histories of ice force are quite similar. The simulated forces period and the forces value are different from the experimental results, which is because the strength of model ice is not uniform and there are many randomicities when the ice sheet interacts with the structure but the ideal assumptions are used in numerical model.

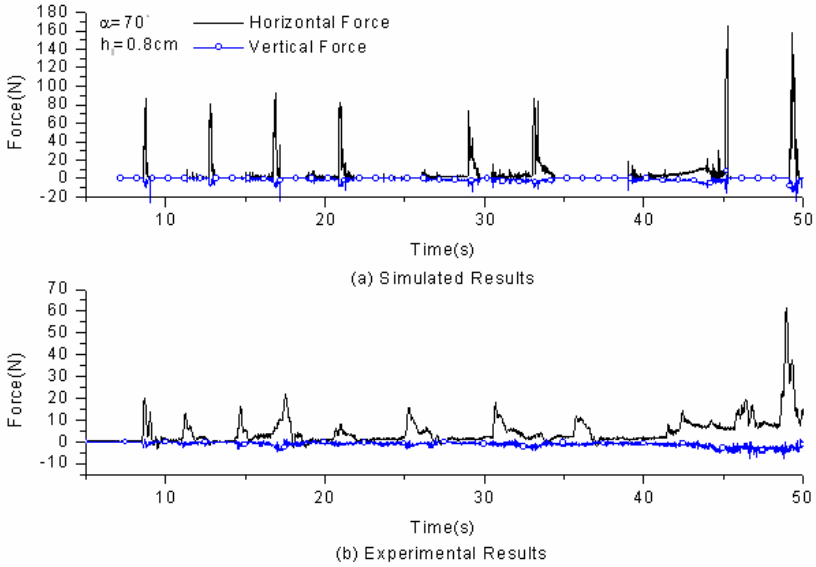

Fig. 7. The histories of ice force on 60° inclined structure

CONCLUSION

According to the results analyzed, the simulated ice pile-up process is quite similar to the phenomena obtained from physical model test, and the trends of their histories of ice force are quite analogical except that the simulated forces period and the forces value are a little different from the experimental results; Besides, the ratio of simulated horizontal and vertical force which result the first fracture of ice sheet is equal to the result calculated by theory. All the results prove that the numerical model is reasonable and feasible. Moreover, another conclusion is that buckling failure of ice sheet rather than flexural failure is happened as the slope is up to the value of $\arctan(1/\mu)$.

Due to the ideal assumptions and predigestion in the numerical model, there are some differences between the simulated ice pile-up process and the actual phenomenon. The following work will be focus on the considering the actual factors for improving the numerical model.

ACKNOWLEDGEMENTS

The authors are grateful to Prof. Hopkins, Mark A for offering the resources required and for his continued help of the work. The project was financially supported by National Natural Science Foundation of China under Grand No.50179003 and No.59725919.

REFERENCES

Croasdale, K.R., Cammaert, A.B. and Metge, M. A method for the calculation of sheet ice loads on sloping structures. *IAHR Ice Symposium.* Trondheim, Norway(1994), 874-885.

Hopkins, Mark A. Numerical simulation of systems of multitudinous polygonal blocks. *U.S Army Corps of Engineers, CRREL* Report 92-22(1992).

Ingraffea, A.R., Saouma, V. Numerical modeling of discrete crack propagation in reinforced and plain concrete, Chap. 4. In: Sih, G.C., de Tommaso, A. (Eds.), Applications of Fracture Mechanics to Concrete Structures. *Martinus Nijhoff Publishers* (1984).

Selvadurai, A.P.S., ten Busschen, A., Ernst, L.J. Computational models for fragmentation tests. In: Dijksman, J.F., Nieuwstadt, F.T.M. (Eds.), Integration of Theory and Applications in Applied Mechanics, *2nd National Mechanics Congress in Netherlands*, Topics in Applied Mechanics. Kluwer Academic Publishers, Rolduc, The Netherlands(1993), 97-110.

Selvadurai, A.P.S., ten Busschen, A.,. Mechanics of the segmentation of an embedded fibre-Part : computational modelling and comparison. *J. Apple. Mech. ASME* 62,98-107(1995).

Wang, Y.X., Li, Z.J. and Li, G.W. Technique of DUT-1 non-refrigerated breakable ice materials and its applications. *Journal of Dalian University of Technology,* 41(1):92-99(2001).

17th International Symposium on Ice
Saint Petersburg, Russia, 21 - 25 June 2004
International Association of Hydraulic Engineering and Research

A STOCHASTIC MODEL FOR THE DYNAMIC INTERACTION BETWEEN ICE AND OFFSHORE STRUCTURE

Qu Yuexia, Wang Yongxue[1]

ABSTRACT

Supposing that the ice thickness is a random variance conforming to the Logarithm Gauss distribution and taking into consideration the variation of ice rigidity, crushing length and clearance stress with ice thickness, the stochastic model for the dynamic interaction between ice and offshore structure is set up. A simplified finite element model of actual offshore platform in Bohai Sea is constructed for computing the structure response. The influence of ice velocity and ice thickness on the response displacement of the platform is discussed.

INTRODUCTION

The oiling platforms in the northern area of Bohai Sea, China will encounter ice-induced vibration in the winter, which seriously disturbs the normal operation and even threatens the safety of workers on the platform. For the safe production of platform in service and further development of offshore oil in Bohai next century, it is very important to understand the mechanism of ice-induced vibration and find some ways to mitigate the vibration to some degree.

Significant efforts have been devoted to the investigation of the dynamic interaction between ice and offshore structure since 1970's. However, because of the complicated essence, most researchers are still limited to build determinative models. For example, Matlock et al (1969,1971) proposed a mechanical model, in which the structure was represented by a spring-mass-damping system with one degree of freedom, and the ice sheet was assumed as a series of elastic-brittle cantilever beams spaced at equal distances. The action of ice on the structure was considered as the impact of cantilever beams against the structure in succession. The main drawback of the model is that the ice crushing length, the maximum elastic deformation and the maximum static ice force are presumed to be constants and no information brought out about how to determine these parameters. Many researchers have done some significant modification to the model, among them are Blenlcarn(1970), Erarti(1981), Toyama(1983), Daoud(1986), Choi(1996) and so on.

[1] The State Key Laboratory of Coastal and Offshore Engineering Dalian University of Technology, 116024 China

Xu jizu and Wang Lingyu (1988, 1993) assumed dynamic ice force as the special dynamic system and propose a theoretical model related to ice force oscillator. The dynamic interaction of ice and structure was considered as a nonlinear coupling vibration between ice force oscillator and the structure system. Yet so far, it is still difficult to estimate the energy transformation involved in the process of indentation.

Considering the random characteristics of ice material and the environments, the dynamic interaction of ice and structure is a complicated stochastic process. However, the development of stochastic model is still on the first step and lots of problems remain to be solved. Sundararajan and Reddy (1977) predicted the response of structure under artificially generated random ice force function. Ou jingping (1998) gave the power spectrum of ice force through time-series of ice pressures measured from field investigation of JZ20-2 platform. Because the influence of environment, ice feature and structure feature on the power spectrum of ice force can not be taken into account from limited data of one special platform, it is difficult to use in actual engineering design.

Assuming that the ice thickness is a stochastic variance fitted to the Logarithm Gauss distribution, a stochastic mathematical model is proposed. The simplified finite element model of JZ20-2 platform in Bohai Sea was constructed and the responses of structure displacements are given for different ice velocity and ice thickness.

Mathematical Model

Regarding the offshore structure as a spring-mass-damping system with multiple degrees of freedom, the dynamic equilibrium equation is expressed as

$$[M]\{\ddot{X}\}+[C]\{\dot{X}\}+[K_1]\{X\}=F(t) \qquad (1)$$

Where, [M], [C] and [K_1] are the mass, damping and stiffness matrixes of the structure, respectively. ice force function $F(t)$ is defined as

$$F(t)=\begin{cases}\pi Dh\sigma_d/2 & \text{if no contact}\\ K_{ice}\Delta & \text{in contact}\end{cases} \qquad (2)$$

in which, D is width or diameter of the structure; h, the ice thickness; σ_d, clearance stress; K_{ice}, the rigidity of ice. The elastic deformation of ice sheet, Δ, is expressed as

$$\Delta = V_t - X - P_i(N-1) \qquad (3)$$

in which, V is ice velocity; N, the number of broken ice pieces; P_i is defined as the crushing length during each crushing period. According to the field investigation of Tuomo et al.(1989), the crushing length P is between 0.2 0.5h. Sanderson(1988) proposed that clearance stress σ_d can be expressed as $\sigma_d = 0.5\rho_w gh$ from theoretical analysis.

Ice Thickness

During the dynamic interaction of ice and structure, the thickness of ice sheet is one of the key stochastic factors affecting ice force function. Because the formation of ice floes undergoes complicated process such as breakup, rafting, re-freezing under the action of multiple environmental factors (wind, wave, tidal current, et al.), the thickness of ice

floes takes on random characteristics in space. According to the statistic data of Bothaian Gulf (Lepparanta, 1981), ice thickness is assumed to conform to the Logarithm Gauss distribution, and the probability distribution function is expressed as

$$f_x(x) = \frac{1}{\sqrt{2\pi}\xi x}\exp\left[-\frac{1}{2}\left(\frac{\ln x - \lambda}{\xi}\right)^2\right] \tag{4}$$

the parameters of distribution λ, ξ are the means and standard deviation of $\ln x$ respectively. Assuming that μ and σ are the means and standard deviation of ice thickness, the parameters of Logarithm Gauss distribution λ and ξ can be expressed as :

$$\begin{aligned} \xi^2 &= \ln\left(1+\frac{\sigma^2}{\mu^2}\right) \\ \lambda &= \ln\mu\left(1+\frac{\sigma^2}{\mu^2}\right)^{-\frac{1}{2}} \end{aligned} \tag{5}$$

Ice Rigidity

Ice rigidity is influenced by many factors such as ice strength, contacting area, the characteristic size of structure and ice thickness. In addition, ice rigidity is also related to the relative velocity between ice and structures. The stiffness parameter K_{ice} will be approximated by the static stiffness of a semi-infinite ice sheet loaded by a flat indentor (Bezukhow,1953) and given by

$$K_{ice} = \frac{\pi E_{ice} h}{2\ln(2d/D) + (1-\gamma)} \tag{6}$$

where, E_{ice} is the Young's modulus of ice; γ, Poisson's ratio of ice; h, thickness of the ice floe; D, width of the indentor. The parameter d is a representative length in which the load is effectively carried, and d =20D is assumed in subsequent computations.

Numerical Results of the Platform Response

The proposed stochastic model was used to simulated the response of the platform JZ20-2, which is a jacket platform with three-legs in Bohai Sea. The sketch of platform in aerial view is shown in Figure 1.

The computation model of the platform showed in Figure 2 is composed of 158 spatial beam elements with 98 nodes. From dynamic mode analysis, the natural frequency of structure model is 1.30Hz, which is a good approximation to the actual platform. The prime parameters of the structure model are chosen as E = 200 GPa(Young's modulus), ρ = 7.8×10^3 kg/m^3 (Material density) and ξ= 0.022 (Damping ratio). The prime parameters for ice force function are E_{ice} = 0.2 GPa (Young's modulus), γ = 0.3 (Poisson's ratio) and D = 1.2 m (Width of structure).

Figure 3(a) shows the computed response displacement on the top of platform leg A2 in north-south direction with ice velocity *v* = 0.4 m/s, and Figure 3(b) shows the part of response displacement from *t* = 60 s to 100s. Ice thickness is assumed to fit the Logarithm Gauss distribution, in which the means of ice thickness μ is 0.1m, and standard deviation σ is 0.05.

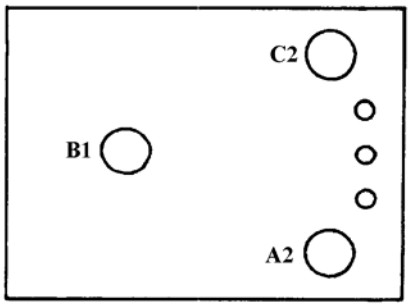

Fig.1. Sketch of platform in aerial view

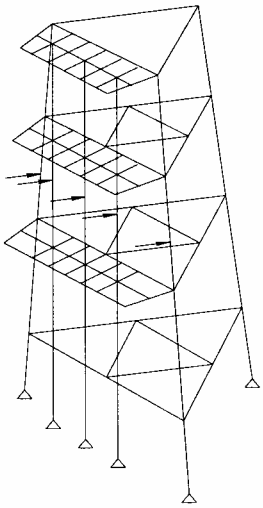

Fig.2. The finite element model of the platform

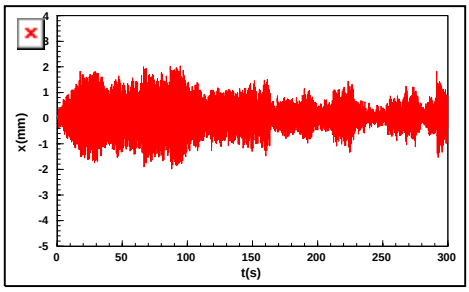

(a)

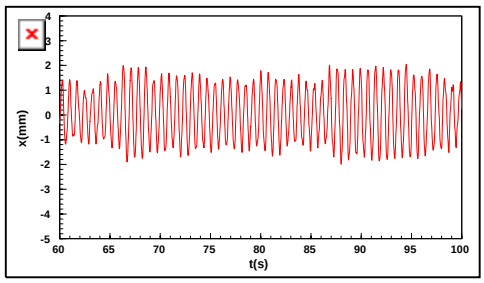

(b)

Fig.3. Computed response displacement on top of leg A2 (v = 0.4 m/s, μ = 0.1m)

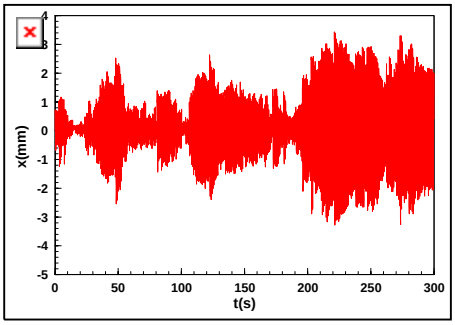

Fig.4. Computed response displacement on top of leg A2(v=0.1m/s, μ=0.1m)

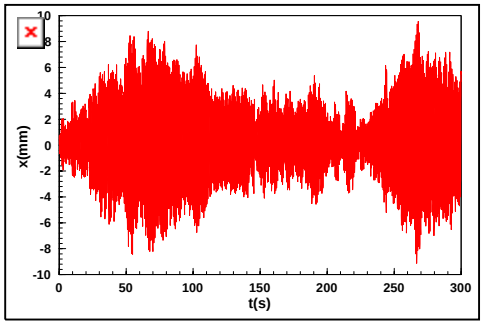

Fig.5. Computed response displacement on top of leg A2 (v=0.4m/s, μ=0.2m)

Figure 4 shows the computed response displacement on the top of platform leg A2 in north-south direction under ice velocity v= 0.1 m/s and means of ice thickness μ = 0.1m. For ice velocity v = 0.4 m/s and means of ice thickness μ = 0.2 m, the computed response displacement is showed in Figure 5. By comparison, it is indicated that for the same ice thickness, the response of structure displacement decreases with the increases

of ice velocity, the phenomena that can be observed in the field investigation. While for the same ice velocity, the response of structure displacement increases significantly with the increases of ice thickness.

CONCLUSION

The stochastic model for ice force function was given at the first step. In the model, ice thickness, one of the key random factors of ice-structure interaction, is assumed to fit the Logarithm Gauss distribution. The computed response displacements of actual platform show that at the same ice velocity, the response of structure displacement is obviously amplified with the increases of ice thickness. For the same ice thickness, the response displacement decreases with the increases of ice velocity. Due to the fact that the dynamic interaction of ice and structure is a very complicated stochastic process, further research work is needed to improve and verify the stochastic model of ice-structure interaction.

ACKNOWLEDGE

The authors gratefully acknowledged the assistance from Professor Yue Qianjin and Yu xuebing, the Department of Mechanical Engineering, Dalian University of Technology.

REFERENCES

Blenkarn, K.A. Measurement and analysis of ice forces on cook inlet structures. In *Proceedings of the second Offshore Technology Conference.* OTC 1261, Houston, USA(1970). Vol.II:365-378.

Choi, K. & Rim, C.W. A numerical technique in calculation of dynamic interaction forces between ice floe and arctic offshore structure. In *Proceedings of the Sixth Int. Offshore and Polar Engineering Conference(ISOPE)*, Los Angeles, USA(1996).

Daoud, N. & Lee, F.C. Ice-induced dynamic loads on offshore structures. In *Proceedings of the fifth Int. Offshore Mechanics and Arctic Engineering (OMAE) Symposium*. Tokyo, Japan(1986). Vol.IV:212-218.

Eranti, E., Haynes, F.D., Maattanen, M. & Soong, T.T. Dynamic ice-structure interaction analysis for narrow vertical structures. In *Proceedings of the sixth Int. Conference on Port and Ocean Engineering under Arctic Conditions(POAC).* Quebec, Canada(1981). Vol.I:472-479.

Lepparanta, M. On the structure and mechanics of pack ice in the Bothnian Bay. *Dissertation, In Finnish Marine Research.* No.248. Helsinki(1981).

Matlock, H., Dawkins, W. P. & Panak, J.J. 1969. A model for the prediction of ice-structure interaction. In *Proceedings of the first Offshore Technology Conference.* OTC1066, Houston, USA(1969). Vol.I:687-694.

Matlock, H., Dawkins, W. P. & Panak, J.J. Analytical model for ice-structure interaction. *Journal of the Engineering Mechanics Division.* ASCE, EM4: 1083-1092(1971).

Ou J.P.& Duan Z.D. Stochastic model of ice force and its parameters for jacket platform in Bohai Sea. *Acta Oceanologica Sinica of China.* 20(3): 110-118(1998).

Sanderson, T.J.O. Ice mechanics-Risks to offshore structure. BP Petroleum Development Ltd, London(1998).

Sundararajan, C. & Reddy, D.V. Probabilistic analysis of ice-offshore structure interaction using enveloping step function power spectral densities. *Canadian Journal of Civil Engineering.* 4(4): 455-461(1977).

Toyama,Y., Sensu,T., Minami,M. & Yashima, N. Model tests on ice-induced self-excited vibration of cylindrical structures. In *Proceedings of the seventh Int. Conference on Port and Ocean Engineering under Arctic Conditions(POAC).*. Helsinki, Finland(1983), Vol.II:834-844.

Tuomo K. & Risto T. Dynamic response of narrow structure to ice crushing. *Cold Region Science and Technology.* Vol.17: 173-187(1989).

Wang L.Y. & Xu J.Z. Theoretical model for dynamic interaction of ice and structure. *Acta Oceanologica Sinica of China.* 15(3): 140-146(1993).

Xu J.Z. & Wang L.Y. 1988. Ice force oscillator model and its numerical solution, *in Proceedings of the seventh Int. Offshore Mechanics and Arctic Engineering Symposium (OMAE).* Houston, USA(1988), Vol.IV: 171-176.

17th International Symposium on Ice
Saint Petersburg, Russia, 21 - 25 June 2004
International Association of Hydraulic Engineering and Research

LOCAL ICE PRESSURE DISTRIBUTION ACTING ON OFFSHORE STRUCTURE

Takahiro Takeuchi[1], Satoshi Akagawa[2], Naoki Nakazawa[3], Sinji Kioka[4] and Hiroshi Saeki[*2]

ABSTRACT

The distribution of local ice pressure acting on an offshore structure in an ice-infested sea area is investigated through data obtained by a plane pressure panel sensor in an in-situ ice/structure indentation test using sea ice. The local ice pressure is characterized into two types depending on the indentation velocity (V) divided by ice thickness (h). Thus, the ice failure pattern depends on (V/h). In this paper, an approximation curve of the ice pressure distribution is proposed as a multiple of uni-axial compressive strength (σ_c) of sea ice.

INTRODUCTION

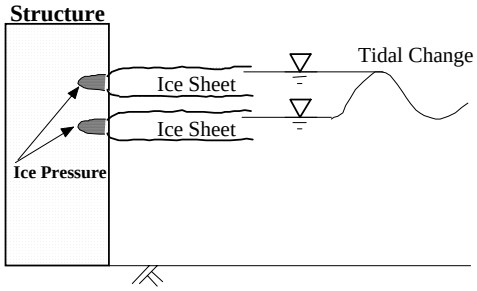

Fig.1. Ice pressure acting on structure

The distribution of local ice pressure as well as global ice force on an offshore structure in an ice-infested sea area is important for the design of the structure's members and abrasion of structural materials. Local ice pressure acts on a certain area of a structural wall depending on water level due to tidal change (Fig.1). Saeki et al. (1983) reported that local ice pressure in the middle of the ice thickness reached 4 to 6 times larger than the uni-axial compressive strength of sea ice over a small area, and the ice pressure distribution changed depending on the combination of structure width (W), indentation velocity (V) and ice thickness (h), using sea ice at Saroma lagoon connected to the sea of Okhotsk, Japan. The measurement was obtained from 16 pressure transducers of 1cm diameter embedded in the surface of an indentor. The plane pressure

[1] Hachinohe Institute of Tech., Japan. No.88-1, Oobiraki, Myo, Hachinohe, Aomori, JAPAN
TEL:+81-178-25-8196, FAX:+81-178-25-0722, E-MAIL:take@hi-tech.ac.jp
[2] Hokkaido University, Japan
[3] Systems Engineering Associates Inc., Tokyo, Japan
[4] Civil Engineering Research Institute of Hokkaido, Japan

panel sensor is a powerful tool that enables real time display of a pressure distribution on 1936 –grid points inside 238mm*238mm area. It was first used for ice pressure measurements by Wako and Izumiyama (1997) and also for measurements of local ice pressure in medium-scale field indentation tests in the JOIA project (Sodhi et al.,1998; Takeuchi et al.,1998; Nakazawa et al.,1999). It yielded new findings for ice failure patterns depending on indentation speed (V) through change in ice pressure distribution with time. Since there has been no way to determine an ice pressure distribution, an approximation curve of the ice pressure distribution is proposed for estimating the distribution for design purpose.

TESTS

Data obtained from medium scale field indentation tests carried out in the JOIA project (Takeuchi et al.,1998) are used here. The model structure and measuring instruments are shown in Fig.2.

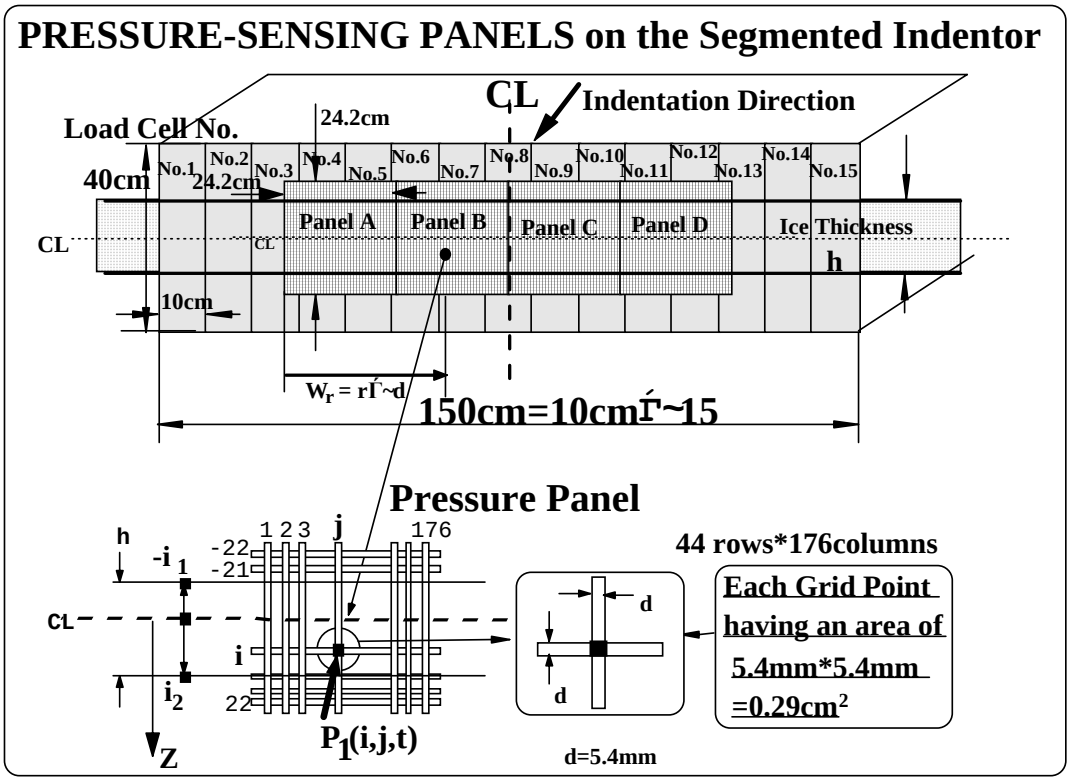

Fig.2. Model structure and measuring instruments

Fifteen load cells were attached to a 10cm-wide segment panel. Four plane pressure panel sensors (A-D) were also used and determine ice pressures of 7744 grid points with time. Calibration was conducted by comparing a force obtained from a load cell to one obtained by integration of pressure panel data over the same reference area (Takeuchi et al.;1998). The test conditions and physical properties of the test ice sheet are listed in (Table1). The uni-axial compressive strength (σ_c) of sea ice was measured in all tests at a strain rate in the order of 10^{-3} (1/s).

Table 1. Test condition and properties of ice

CASE	Ice Thickness (h) cm	Velocity (V) (cm/s)	V/h (1/s)	Strength σ_c (MPa)	Density ρ (g /cm^3)	Salinity (ppt)	Ice Temp.	Ice Type
1	24.1	0.3	0.012448	1.265	0.843	6.2	-2.7	#1
2	24.1	0.03	0.001245	1.265	0.843	6.2	-2.5	#1
3	24.1	0.03	0.001245	1.265	0.843	6.2	-2.5	#1
4	24.1	3	0.124481	1.265	0.843	6.2	-2.6	#1
5	18.6	0.03	0.001613	1.4	0.879	5.9	-1.7	#2
6	23.8	0.3	0.012605	1.52	0.895	5.4	-2.7	#2

#1:Ice sheet composed of snow ice at the top and columnar ice at the bottom.
#2: Ice sheet composed of columnar ice.

TEST RESULTS AND DISCUSSION

Calculation of Local Ice Pressure

First, the pressure over a grid area (*d*d*) at time (*t*), row (*i*) and column (*j*) (See Fig.-2) is taken as $P_1(i,j,t)$. Next, the pressure acting on an area *r*d* (=W_r) is calculated from equation-(1).

$$P_2^{\,r}(i,t) = \frac{1}{r}\sum_{j=1}^{r} P_1(i,j,t) \tag{1}$$

In the following three equations-(2),(3) and (4), a mean, an extreme, and a maximum pressure from $t=t_1$ to $t=t_2$ are calculated.

$$P_2^{\,r}(i)_{ave} = \frac{1}{(t_2 - t_1 + 1)}\sum_{t=t_1}^{t_2} P_2^{\,r}(i,t) \tag{2}$$

$$P_2^{\,r}(i)_{ext} = P_2^{\,r}(i)_{ave} + 3\times\left[\frac{1}{(t_2 - t_1)}\sum_{t=t_1}^{t_2}\left\{P_2^{\,r}(i,t) - P_2^{\,r}(i)_{ave}\right\}^2\right]^{1/2} \tag{3}$$

$$P_2^{\,r}(i)_{\max} = MAX\left(P_2^{\,r}(i,t) : t_1 \le t \le t_2\right) \tag{4}$$

To evaluate the pressure distribution in the vertical (ice thickness) direction *z*, the distance *z* as shown in Fig.2 normalized by *h* is taken as $\frac{z}{h} = i$. Further, equations-(2),(3) and (4) are normalized by (σ_c) as equations-(5),(6) and (7).

$$k(i)_{ave} = \frac{P_2^{\,r}(i)_{ave}}{\sigma_c} \tag{5}$$

$$k(i)_{ext} = \frac{P_2^{\,r}(i)_{ext}}{\sigma_c} \tag{6}$$

$$k(i)_{\max} = \frac{P_2^{\,r}(i)_{\max}}{\sigma_c} \tag{7}$$

Ice deformation can be divided into two types depending on (*V/h*). For $V/h>3*10^{-3}$ *(1/s)*, ice behaves as a brittle material, and For $V/h<3*10^{-3}$ *(1/s)*, ice behaves as a ductile material. Therefore, the relationship between *z/h* and *k(z/h)* is investigated for both brittle and ductile cases.

EFFECT OF (V/H) ON ICE PRESSURE DISTRIBUTION

For $V/h>3*10^{-3}$ *(1/s)* in the ice /structure interaction, ice fails nonsimultaneously, and an area of single failure has a scatter in size of about *h*h*. Therefore, for a reference area *h*h* (i.e., W_r=h), ice force and an image of ice pressure by plane pressure panel sensors are shown in Fig.3).

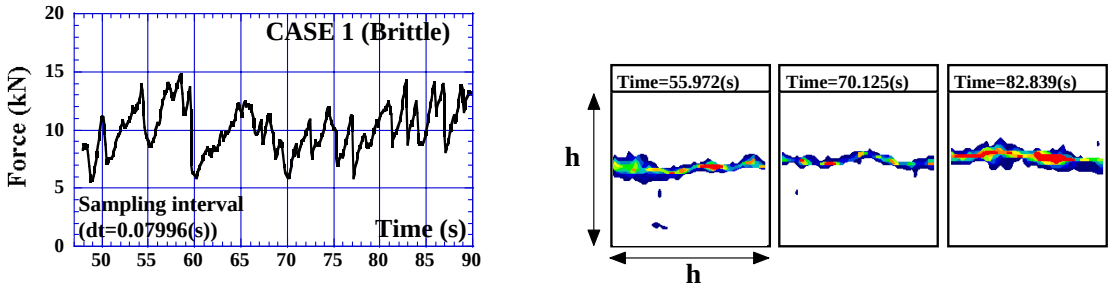

Fig.3. Ice force and image of ice pressure CASE-1

The relationships between *z/h* and *k(z/h)* for an area of *h*h* are shown in Fig.4, Fig.5 and Fig.6. Contact between ice and structure is concentrated in the middle of the ice thickness. The maximum ice pressure for an area of *h*h* becomes 3.5 times larger than σ_c. However, for $V/h<3*10^{-3}$ *(1/s)* in ice/structure interaction, ice fails all over the structure simultaneously. In the same manner, for a reference area *h*h* (i.e., W_r = h), ice force and image of ice pressure by plane pressure panel sensors are shown in Fig.7. The relationships between *z/h* and *k(z/h)* for an area of *h*h* are shown in Fig.8, and Fig.9. The contact occurs over a wider area, but the maximum ice pressure for an area of *h*h* is less than twice σ_c.

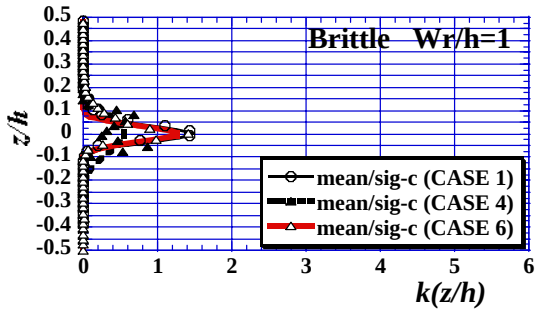

Fig.4. (z/h) vs. k(z/h) Brittle(mean)

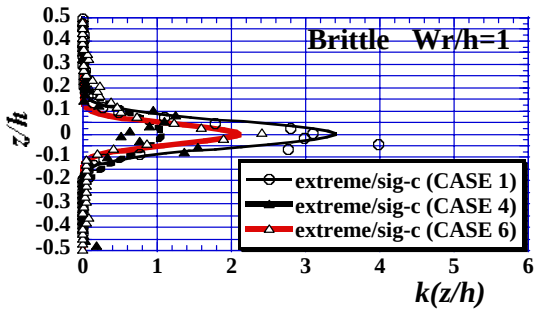

Fig.5. (z/h) vs. k(z/h) Brittle(extreme)

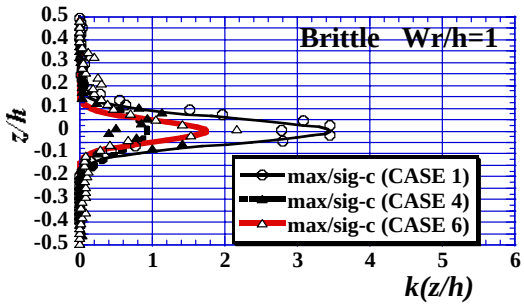

Fig. 6. (z/h) vs. k(z/h) Brittle(maximum)

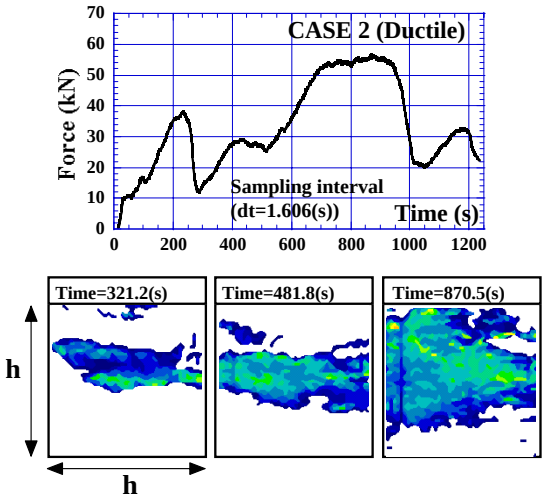

Fig. 7. Ice force and image of ice pressure CASE-2

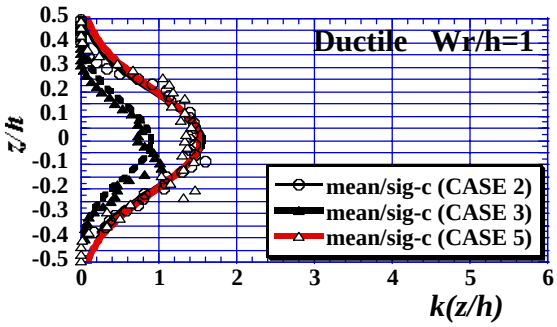

Fig. 8. (z/h) vs. k(z/h) Ductile(mean)

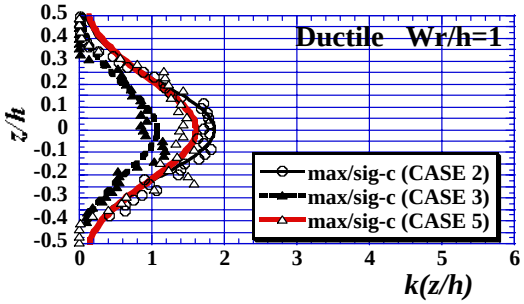

Fig. 9. (z/h) vs. k(z/h) Ductile(maximum)

EFFECT OF (W_r) ON ICE PRESSURE DISTRIBUTION

For $V/h>3*10^{-3}$ *(1/s)*, the ice failure pattern depends on the distance (W_r) due to nonsimultaneous pressure transmission. Therefore, the normalized value of (W_r/h) is considered as a parameter to investigate the change of ice pressure distribution. The plots for the brittle and ductile cases are shown in Fig.10 and Fig.11, respectively. For the brittle case, a larger (W_r/h) gives a smaller peak in the middle of the ice thickness, and ice pressure acts over the range from (z/h = – 0.2) to (z/h = 0.2). For the ductile case, ice pressure is independent of (W_r/h), and acts over the range from (z/h = – 0.45) to (z/h = 0.45).

APPROXIMATION CURVE FOR ICE PRESSURE DISTRIBUTION

Based on test data, an approximation curve for ice pressure distribution is given by equations-(8) for both brittle and ductile cases.

$$k(z/h) = m_1 \times \exp\left\{- m_2 (z/h)^2\right\} \qquad (8)$$

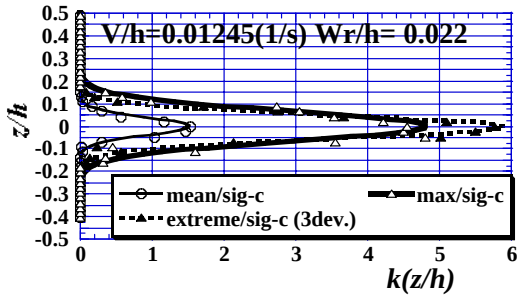

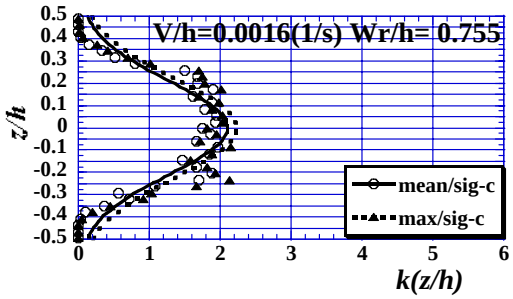

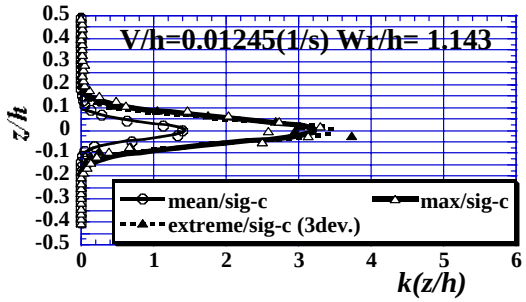

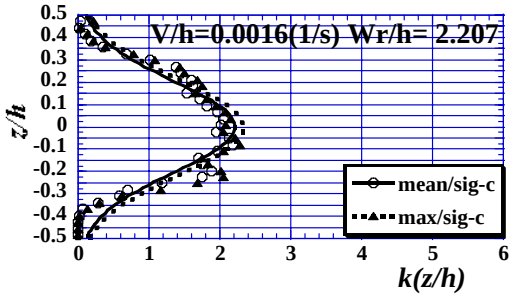

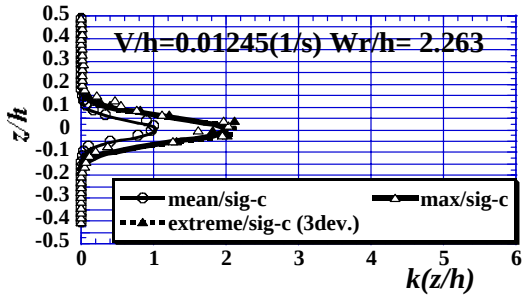

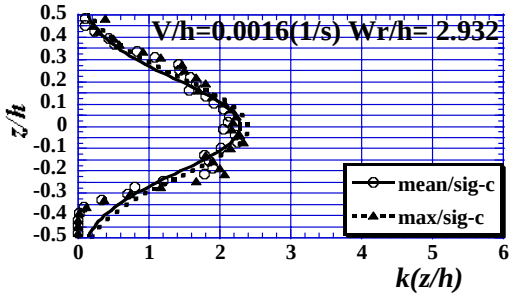

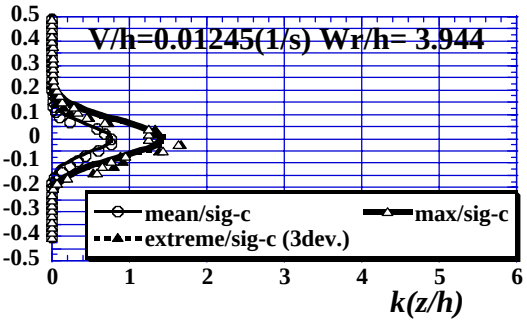

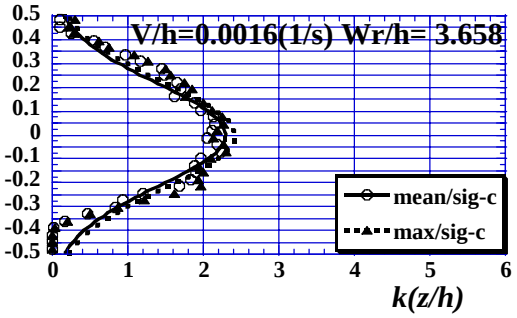

Fig.10. (z/h) vs. k(i) $v/h>10^{-3}$(1/s)

Fig.11. (z/h) vs. k(i) $v/h<10^{-3}$(1/s)

Constants in the curve are m_1 and m_2. Constant m_1 is related to peak pressure in the middle of the ice thickness (i.e., at z/h=0), and constant m_2 is related to contact ratio (i.e., in the range over which ice pressure is acting). For the brittle case, constant m_1 depends on (W_r/h) as shown in Fig. 12, and constant m_2 is taken as 100. For the ductile case, constant m_1 is independent of (W_r/h), as shown in Fig. 13, and constant m_2 is taken as 15. Therefore, from equation (8), Fig. 12 and Fig.13, ice pressure distribution

can be generated if a uni-axial compressive strength (σ_c) of sea ice in the considered sea area is given. Note that (σ_c) is measured at a strain rate in the order of 10^{-3} (1/s), which gives a maximum value. Examples of ice pressure distributions are shown in Fig.14.

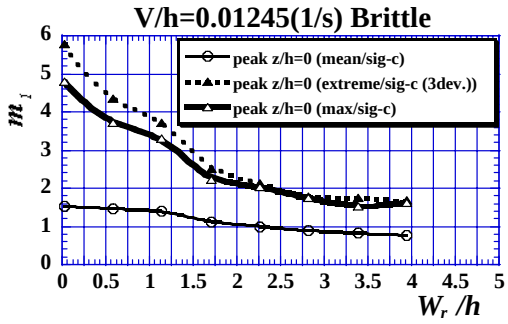

Fig. 12. (W_r/h)vs. (m_1) Brittle

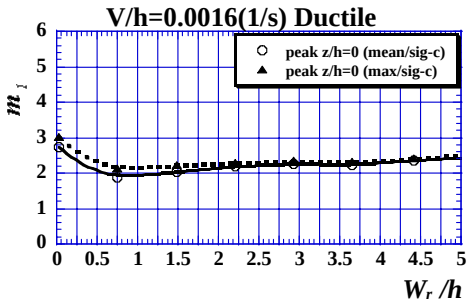

Fig. 13. (W_r/h)vs. (m_1) Ductile

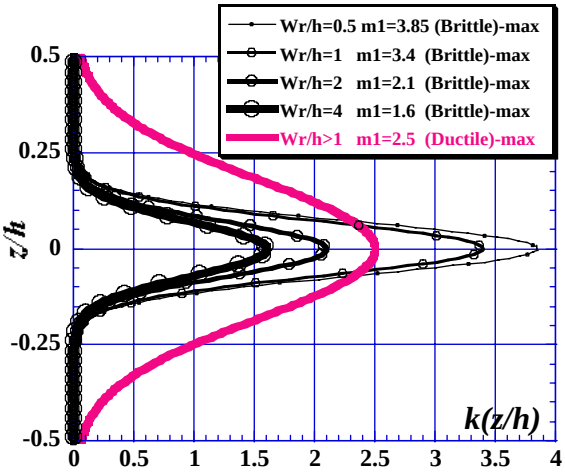

Fig. 14. Approximation Curve (example)

Further, integration of equation-(8) over an indentation area W*h gives a global ice force on the structure as equation-(9).

$$
\begin{aligned}
F_{\max}{}^{r} &= \sum_{i=-i_1}^{i_2} \{k(i)_{\max}\sigma_c\} r d^2 \\
&\approx \int_{-0.5}^{0.5} \left\{ m_1 \times \exp\{-m_2 (z/h)^2\} \right\} d(z/h) \times Wh\sigma_c \\
&= m_1 \times \left[\frac{2}{\sqrt{m_2}} \int_0^{0.5\sqrt{m_2}} \{\exp(-t^2)\} dt \right] \times Wh\sigma_c \\
&= m_1 \times m_2{}' \times Wh\sigma_c
\end{aligned}
\qquad (9)
$$

An equation for estimating the global ice force on a structure has been proposed as equation-(10) (Takeuchi, et al.; 2002).

$$F_{\max}{}^{r} = f_1 \times f_2 \times Wh\sigma_c \qquad w/h \geq 1 \qquad (10)$$

Factor f_1 depends on contact ratio, ice thickness restraint, and end effect. Factor f_2 depends on (W/h) for the brittle case and is independent of (W/h) for the ductile case. Test conditions here allow the ice thickness restraint and end effect to be omitted, and this implies that m_2' is related to f_1 and becomes constant because f_1 is constant. However, constant m_1 is related to factor f_2 and depends on (W/h) for the brittle case and is independent of (W/h) for the ductile case. This corresponds to Fig.12 and Fig.13.

CONCLUDING REMARKS

1) An approximation curve for ice pressure distribution is proposed depending on (V/h). Given a uni-axial compressive strength (σ_c) of sea ice, ice pressure distribution can be estimated.
2) For $V/h>3*10^{-3}$ *(1/s)* (brittle case), a larger (W_r/h) gives a smaller peak in the middle of the ice thickness, and ice pressure acts in the range from ($z/h = -0.2$) to ($z/h = 0.2$). Ice pressure becomes five times larger than the uni-axial compressive strength (σ_c) of sea ice.
3) For $V/h<3*10^{-3}$ *(1/s)* (ductile case), ice pressure is independent of (W_r/h), and acts in the range from ($z/h = -0.45$) to ($z/h = 0.45$).

ACKNOWLEDGEMENTS

The data used here were obtained from part of the JOIA project sponsored by the Ministry of International Trade and Industry (M.I.T.I.).

REFERENCES

Nakazawa, N., Akagawa, S., Kawamura,M., Sakai,M., Matsushita,H., Terashima,T., Takeuchi,T., Saeki,H. and Hirayama,K. , "Medium Scale Field Indentation Tests (MSFIT) –Results of 1998 winter Tests-," *Proc. of 9th Int. Offshore and Polar Eng.(ISOPE99)* ,Vol.2.,pp.498-504, 1999

Saeki,H.,"Kaigan-Kaiyoukouzoubutsu-no-Taihyousekkeihou (in Japanese)," Doctor of Engineering Thesis, p.1-336, 1983

Sodhi, D., Takeuchi T., Akagawa S., Nakazawa N. and Saeki, H.; "Medium-scale indentation tests on sea ice at various speeds," *Journal of Cold Regions Science & Technology 28*, pp.161-182, 1998

Takeuchi,T., Akagawa,S., Kawamura,M., Sakai, M., Matsushita H., Terashima T., Nakazawa N., Hirayama K. and Saeki H., "On the ice/structure in medium scale field indentation tests (part3), *Proc. of Civil Engieering in the Ocean*, Vol. 14, pp. 423-428, 1998.

Wako,D. and Izumiyama, K., " Ice Load Distribution on a Flat Indentor (in Japanese)," *Proc. of 97' Cold Region Technology Congerence*, Vol.13, pp.412-417.1997.

17th International Symposium on Ice
Saint Petersburg, Russia, 21 - 25 June 2004
International Association of Hydraulic Engineering and Research

IN-SITU ICE RIDGE SCOUR TESTS

P. Liferov[1,2,3], P.O. Moslet[3], R. Nilsen[1,3], K. Høyland[3] and S. Løset[1,3]

ABSTRACT
A second part of the in-situ program was carried out in the Van Mijen fjord at Spitsbergen during the year 2003 to investigate the ice ridge scour process. One ice scour test and one shear off test were performed. Ice ridges with dimensions of up to 3.9 × 3.9 × 2.65 m were artificially made by cutting the level ice into pieces to produce ice rubble. The ridges were left to consolidate for up to 4 weeks and then pulled towards the beach scouring the seabed that consisted of clayey sediments (ice scour tests). The ice ridge for the shear off test was built up in the pre-excavated trench in hard moraine. During pulling the keel of the ice ridge was sheared off by the sidewall of the trench. The pulling force, displacements, failure of the keel and resulting plough marks were measured. This paper provides a description of the test arrangement and the basic experimental results.

INTRODUCTION
First-year ice ridges are one of the major obstacles to offshore operations in ice-infested waters. They can scour the seafloor in relatively shallow waters. This has significant implication on the design of pipelines and other subsea facilities. The phenomenon of interaction between the ice features and the ocean floor is named ice scouring. It has been quite extensively studied for the last 30 years particularly in respect to the iceberg and multi-year ridge scouring. Icebergs and multi-year ice ridges have been treated as solid bodies that are not destroyed while scouring the seabed. First-year ice ridges and particularly their keels are much looser and weaker which makes it reasonable to assume that they may be partly destroyed during the contact with the seabed soil. This has motivated to conduct an in-situ program to study the ice ridge – soil interaction process.

During the spring 2002 one pilot test was done as described by Liferov et al. (2002) and Høyland et al. (2002). Having the experience from the first experiment, two more tests were conducted during the winter/spring 2003.

[1] Norwegian University of Science and Technology (NTNU), Trondheim, Norway, pavel.liferov@barlindhaug.no
[2] Barlindhaug Consult AS, Tromsø, Norway
[3] University Centre on Svalbard (UNIS), Longyearbyen, Norway

EXPERIMENTAL

General

The experiments were conducted in the Van Mijen fjord a few kilometres away from the coal mining community Svea on Spitsbergen (78°N 16°E). The ice conditions are fairly stable during winter and spring thus posing no danger for the ice ridge to drift away. Two tests were conducted: one scour tests R2 and one shear-off test R3. The principal difference between the scour test and the shear-off test was the following:

- the ice ridge for the scour tests was built at such water depth that there always was a gap between the keel and the seabed at low tide. Then the ridge was towed towards the shore in the open channel scouring the seabed, which consisted of relatively soft clayey sediments;
- the ice ridge for the shear-off test was built in more shallow area where the ice stands on the seabed at low tide. It was built in the trench excavated in very stiff and hard moraine. The depth of the trench was sufficient to prevent grounding of the ridge at low tide. The wall of the trench has further provided the boundary against which the ice ridge was sheared-off. The main goal of the shear-off test was to estimate the strength of the keel.

A description of the basic actions performed throughout the test program is given in the following sections.

Ice Ridge Production

The ice ridges were artificially produced from the parent level ice. They were produced in mid/late March when the ice thickness reached about 90 cm. The production of the ice ridges was essentially similar regardless of the type of test. The practical procedure included the following operations. Primarily, the snow was removed from the testing area (approximately 100 m by 70 m). In the year 2002 the team experienced severe difficulties with flooding of the ice (negative freeboard up to 40 cm) from the beginning of April caused by the snow drift. Therefore in the year 2003 it was decided to clean the snow from the testing area on a regular basis.

The initial openings in the ice with dimensions of up to 3.7 × 3.7 m were made where the ice ridge had to be built. Large ice blocks (approx. 1 m^3) were chain-sawed into smaller blocks with dimensions of about 15 cm × 25 cm × 45 cm. These small blocks were then manually thrown into the opening. However, many of these blocks broke in two-three parts during this operation. After the ridges were produced they were left to consolidate. The consolidation time was two to four weeks for the different ridges.

Channel opening and ridge towing

Channels in the ice cover were made in the same way as the openings for ridge production. Towing of the ridges was done by pushing them from behind by the parent ice sheet called the towing floe. The towing floe and the ice ridge were merged together on the day of ridge production. Ice anchors installed into the towing floe were connected by chain links to the main pulling chain that was powered by the pneumatic winch. Average towing velocity was 2 cm/s. Figs. 1 and 2 show the general plan views of the R2 and R3 tests respectively. The ridges were manually towed back to their original position after the tests at high tide.

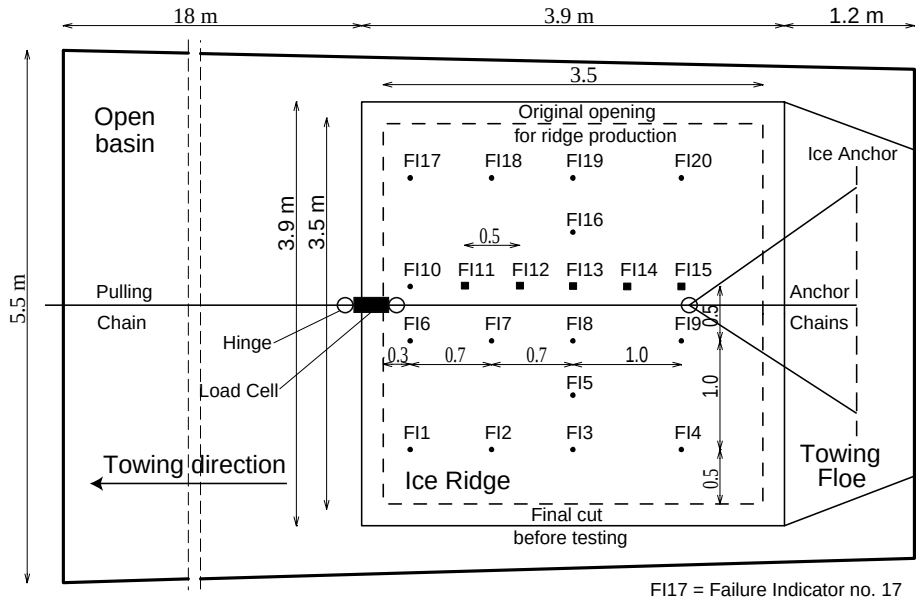

Fig. 1. Plan view of the R2 test

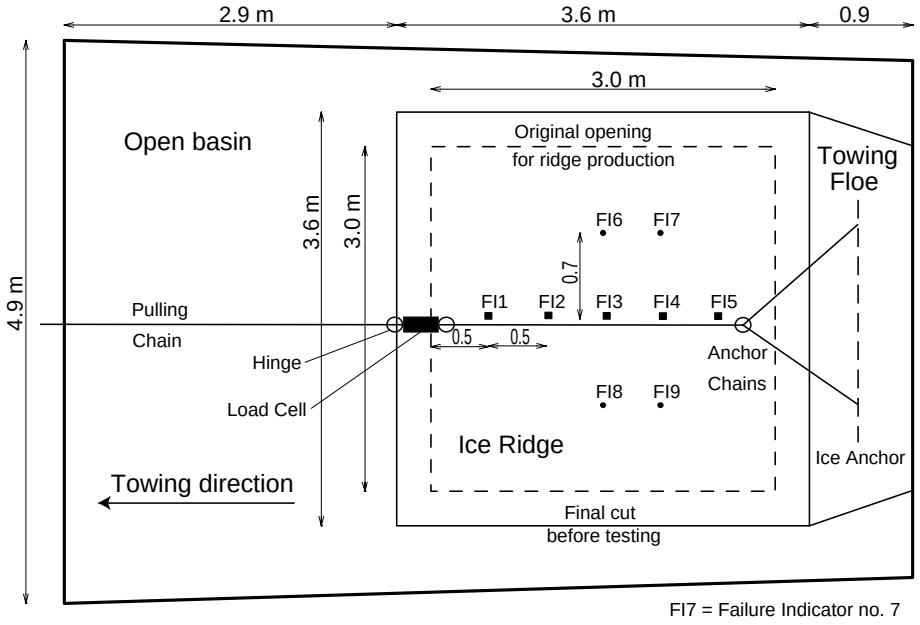

Fig. 2. Plan view of the R3 test

Instrumentation and measurements

One of the key objectives in these experiments was to study failure of the keel during scour process. For this purpose the failure indicators (FI) were designed. The resolution of the FI was 25 cm, i.e. they were able to indicate the region where the major failure slip took place inside the keel of the ice ridge. The plan of the FI installed in the ridges is given in Figs. 1 and 2 for R2 and R3 tests respectively. Only five FI were used as dynamic indicators (shown with squares), i.e. recording the keel failure in the time domain during the test. They could indicate keel failure up to 50 cm from the bottom of the keel. The amount of the dynamic indicators as well as their resolution was limited

by available number of channels on the data acquisition device. The remaining failure indicators could characterize the failure that took place inside the ridge during the experiment by residual reading from them after the test. A summary of the measurements and observations conducted before, during and after the tests is given in Table 1.

Table 1. Summary of measurements and observations

No.	Description
	Before testing
1	Temperature, salinity and hardness of the ice
2	Temperatures in the ice ridge (thermistor string)
3	Mechanical drilling (thickness of the consolidated layer, initial keel profile, porosity and consistency of the keel)
4	Underwater (UW) video of the ridge
5	Initial seabed profile along the scouring path
6	Seabed sounding (depth to the moraine)
7	Soil sampling and subsequent testing
	During testing
1	Pulling force by 20-t load cell at 3Hz
2	Horizontal and vertical displacements of the ridge at 3Hz
3	Failure of the ridge (five dynamic FI) at 3Hz
4	Overview, side view and UW video (UW video for scouring test only)
	After testing
1	Residual seabed profile along the scouring path
2	Residual ice ridge profile by means of mechanical drilling
3	Residual reading from all failure indicators
4	UW video of the scouring path

RESULTS

Basic measurements and observation

The basic results of the experiments are outlined in this section. Figs. 3 and 4 show the pulling force (10 moving average), the vertical displacement (10 moving average) and the failure in the keel recorded by the dynamic failure indicators versus the horizontal displacement for the R2 and R3 tests respectively. Failure indicators are denoted as FI#, where # and corresponding location are given in Figs. 1 and 2 and failure depth is measured from the bottom of the keel upwards.

At the beginning of each test, the ice ridge was free-floating. After the first contact with the seabed the ridge R2 began to heave slowly. A number of very shallow plough marks were observed on the seabed in this area. Initial compaction of the ice rubble in the keel could have taken place at this stage of the scour process. As the water depth decreased, the pulling force increased. The magnitude of the heave of the ridge and the scour depth did not, however, increase accordingly. The ice ridge began to slightly pitch and the so-called “galloping” behaviour was observed, similar to as described by Barker and Timco (2002). The failure of the keel began to propagate from its front bulldozing face. In the final stage of the test when the ice ridge moved into even more shallow area, the scour magnitude increased, the keel continued to fail and significant heave of the ice ridge as well as increase in the pulling force was observed. After the ridge was towed back at high tide, a few ice blocks were seen stuck in the seabed.

The R3 test behaved quite differently. As the ice ridge contacted the wall of the trench it began to pitch such that the front edge of the ridge was lower than the back edge of the towing floe. Significant “galloping” behaviour was observed throughout the entire test. No scouring took place in the area where the ice ridge interacted with soil. After the test significant amount of ice rubble from the keel was observed in the water around the ice ridge.

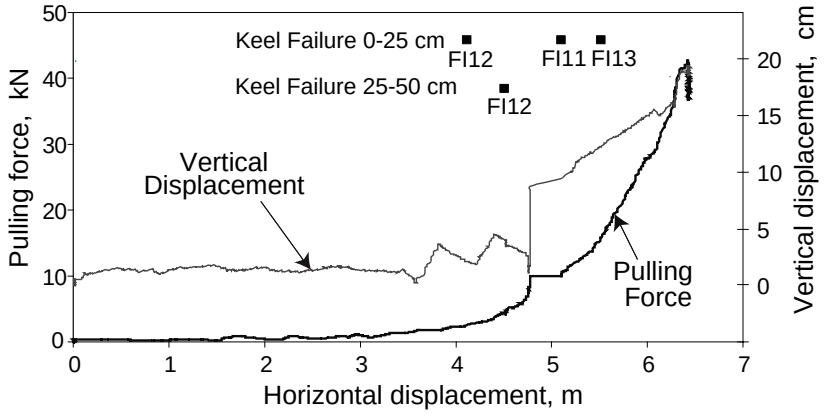

Fig. 3. Pulling force and heave of the ridge, test R2

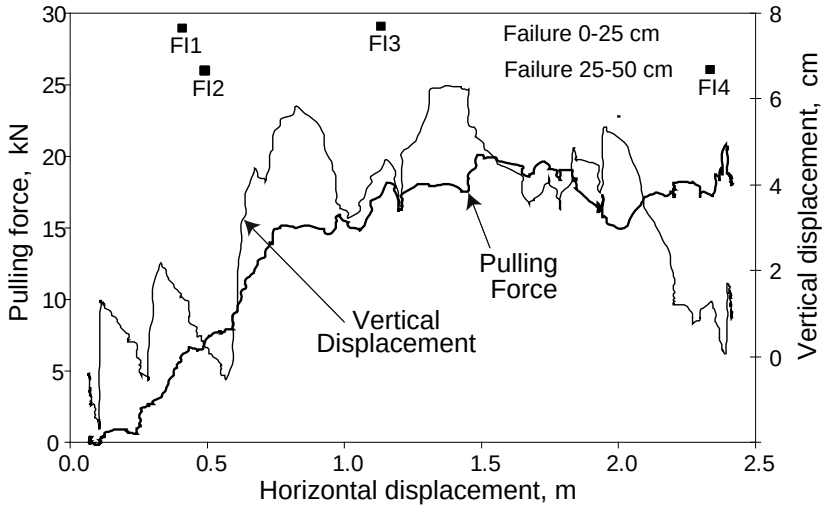

Fig. 4. Pulling force and heave of the ridge, test R3

Keel failure and keel strength

Failure of the lower part of the keel was observed in both tests. Initial and residual ice ridge profiles for tests R2 and R3 are shown in Figs. 5 and 6 respectively. Results from the residual mechanical drilling and the residual reading from all failure indicators correlated well for all tests in the front part of the ridge. In the back part of the ridge the mechanical drilling seems to underestimate the magnitude of keel destruction, which is particularly valid for test R3.

Failure of the keel was observed to be not simultaneous, but progressive, occurring while the ice ridge translated forward. In addition to the ultimate global failure plane

there could form several secondary local failure planes as the ice ridge moved forward. Analysis of the entire data set (heave of the ridge, keel destruction and scour depth) from test R2 has also shown that the keel of ice ridge was permanently compacted (volumetric plastic deformations). The magnitude of the volumetric deformations was about one third of the maximum keel destruction.

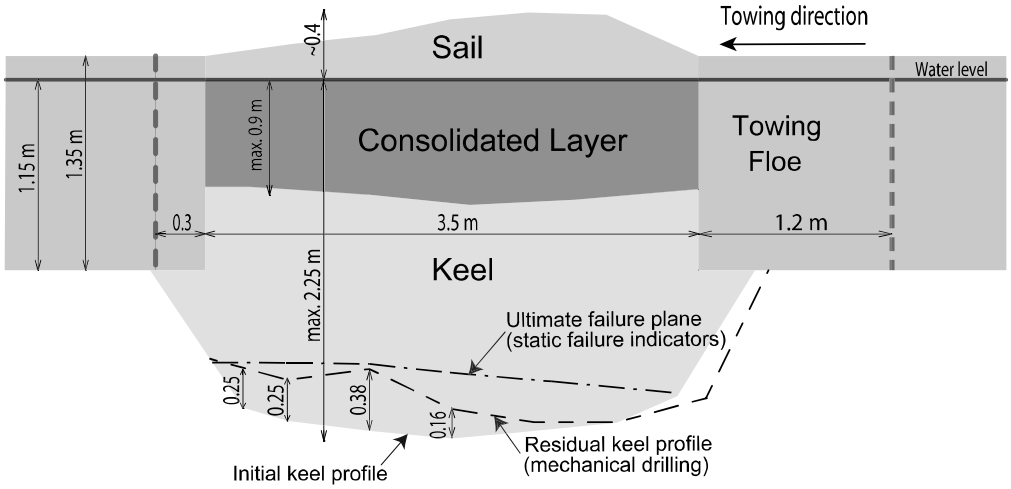

Fig. 5. Cross-section of the ice ridge (along centreline), test R2

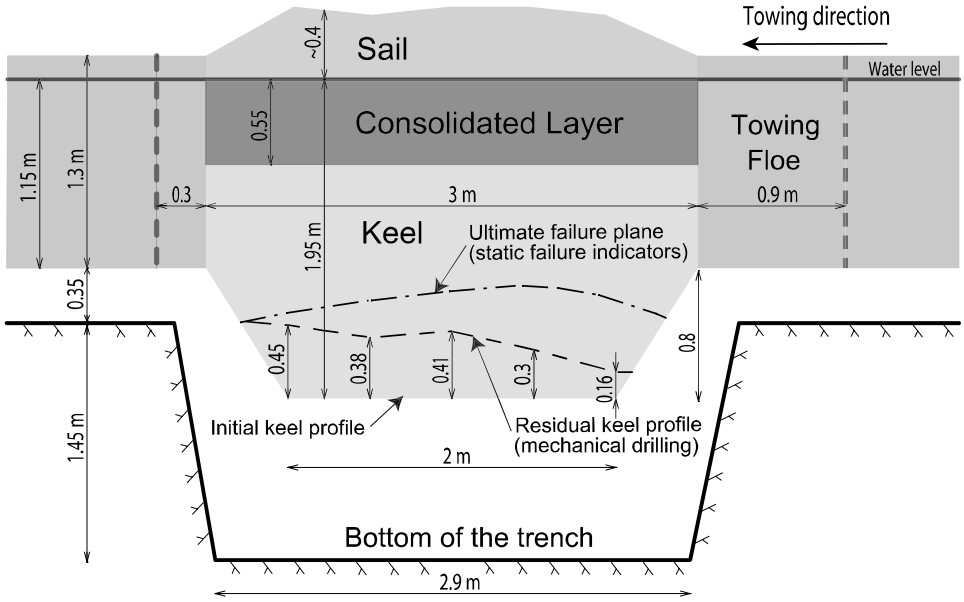

Fig. 6. Cross-section of the ice ridge (along centreline), test R3

Scour profiles

The seabed profile was measured before and after the test. The density of survey was 1 m in longitudinal direction (parallel to towing direction) and 0.5 m in transversal direction (perpendicular to towing direction). Profiling was done manually by a long meter-stick and the accuracy of measurements was not high. It was estimated to be ± 2 cm after the raw data was processed. Visual observations of the plough marks in seabed

were also done. From the place of first contact between the ice ridge and seabed a number of “scratch” looking plough marks was observed. As the scouring continued and ice ridge moved into shallower waters, the plough marks became wider and deeper. At the end of scour the plough marks more or less merged together forming one plough mark of trapezoidal shape. The longitudinal initial and residual seabed profiles from test R2 taken along the centreline of the channel are shown in Fig. 7. In case of the R3 test no significant permanent deformations in the soil was neither observed nor measured.

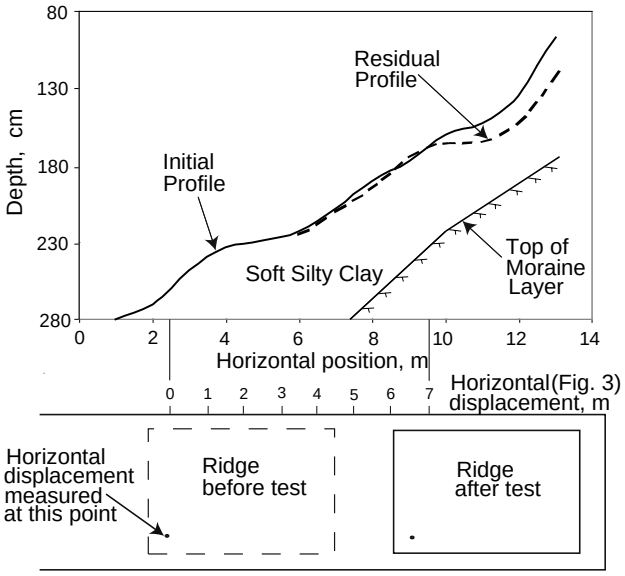

Fig. 7. Longitudinal seabed profile (along centreline of the channel), test R2

CONCLUSIONS

A field program has been performed to examine the ice ridge scouring process. In both tests a clear evidence of the keel destruction during the scour process was observed. The magnitude of the keel destruction was in the order of the scour depth and the heave of the ridge. The failure of the keel was observed to be not simultaneous, but progressive, occurring while the ice ridge translated forward.

The ice ridge in test R2 moved in such a manner so as to reduce the overall scouring force. This observation is similar to the one done by Kioka and Saeki (1995) and Barker and Timco (2002) in their laboratory experiments on ice scouring.

The major conclusion from the conducted field program is an evidence of the second component in addition to heave of the ridge, e.g. keel destruction that makes an ice ridge to follow by the way of the least resistance while scouring the seabed. There is no doubt that the conducted experiments cannot be directly compared to the full-scale conditions. The present results suggest that this aspect of ice ridge scouring shall be evaluated and simulations of the full scale ice ridge scouring are needed based on the carefully evaluated material parameters for the full-scale ice ridges.

ACKNOWLEDGEMENTS

The authors would like to thank Sergey Vernyaev and Rinat Kamalov for their crucial assistance during the field operations. The encouragement and help from Karl Shkhinek

are also greatly appreciated. We are thankful to Anatoly Alekseev for design and manufacturing of failure indicators and displacement sensors. Particular acknowledgement is given to the Store Norske Spitsbergen Gruvekompani (SNSG) and Leonhard Nilsen Store Norske for their help with the heavy machines and logistics. And finally we would like to thank those who have financially supported the project, namely: Statoil ASA, the Norwegian Research Council, the Norwegian Polar Institute and the University Centre on Svalbard.

REFERENCES

Barker, A and Timco, G., 2002. Laboratory experiments of ice scour processes: buoyant ice model. *Journal of Cold Regions Science and Technology*, 36: 103-114.

Høyland, K.V., Liferov, P., Moslet, P.O., Løset, S. and Bonnemaire, B., 2002. Medium scale modelling of ice ridge scouring of the seabed, Part II: Consolidation and physical properties. In *Proceedings of the 16th International Symposium on Ice*, Dunnedin, New Zealand, Vol. 2, pp. 94–100.

Kioka, S. and Saeki, H., 1995. Mechanisms of ice gouging. In *Proceedings of the 5th International Offshore and Polar Engineering Conference*. The Hague, Netherlands, pp. 398–402.

Liferov, P., Løset, S., Moslet, P.O., Bonnemaire, B. and Høyland, K.V., 2002. Medium scale modelling of ice ridge scouring of the seabed, Part I: Experimental set-up and basic results. In *Proceedings of the 16th International International Symposium on Ice*. Dunnedin, New Zealand, Vol. 2, pp. 86–93.

17th International Symposium on Ice
Saint Petersburg, Russia, 21 - 25 June 2004
International Association of Hydraulic Engineering and Research

MECHANICAL PROPERTIES OF UNCONSOLIDATED LAYER MODEL OF ICE RIDGE UNDER VARIOUS CONDITIONS

Shinji Kioka[1], Yuko Matuo[2], Hirofumi Kondo[3]
Yasuji Yamamoto[1] and Hiroshi Saeki[3]

ABSTRACT
A simplified unconsolidated layer model was produced, and a series of experiments was carried out under the various conditions in addition to our past experiments. Shear strength satisfied the Coulomb failure criterion without exception in our experiment. We found that although an initial porosity and failure mode of a specimen (unconsolidated layer model) depended on shape of ice block/piece which constitutes a specimen, the shear strength (strength parameters) depended not on block shape but on block volume. There is a tendency for the strength parameters such as internal friction angle and cohesion to increase as the block size increased. However, the increase in internal friction angle deceases as the block size increases, and the internal friction angle seems to approach a constant value over time. The strength parameters are not thought to depend much on whether blocks are submerged. This means that it is possible to perform experiments under easier setup of dry conditions. We also found that the shear strength depended largely on the shear rate.

INTRODUCTION
Unconsolidated layer, which is one of the categories of ice ridge structures, is composed mostly of loosely accumulated broken ice pieces. Although its strength is low, it may impose large load on offshore structure when it forms in sufficient size or has high strength because of high confining stress. Also it may effect on buried structures due to ice scour event with high confining stress. Since the unconsolidated layer is a threat to many structures in the actual cold sea, it is important to know strength of the unconsolidated layer. Unconsolidated layer has been treated by many researchers as a Mohr-Coulomb material to describe its mechanical behavior, and many experiments on the strength of unconsolidated layer have been conducted under various conditions both in the laboratory [e.g., Prodanovic et.al.,1979, Weiss et.al.,1981, Wong et.al.,1987, Heinonen et.al.,2000] and in the field [e.g., Lapparanta et.al,1989, Bruneau et al. 1998].

[1]Port and harbor eng. division, Civil Engineering Research Institute of Hokkaido, Hiragishi 1-3-1-34, Toyohira-ku, Sapporo, 062-8602, Japan
[2]City Office of Sapporo, N-1,W-2, Sapporo,060-8611, Japan
[3]Division of Environmental Resources Eng. Hokkaido University, N-13 W-8, Sapporo 060-8628, Japan

The results of which have revealed various qualitative strength parameters, such as apparent cohesion and internal friction angle. However, there are many discrepancies in published results, and there is still no established method for determining the strength of unconsolidated layer. This paper will report on the mechanical properties of shear strength under various conditions in addition to our past research [Yasunaga et al.,2002].

EXPERIMENTS

Experimental method

Although the method has been already reported by Yasunaga et al. [2002], we show the method once again, as follows.

1) A mesh-type square frames with a borehole at the bottom of each mesh were placed in a container with 30‰ saline water. After freezing the water up to a certain thickness of ice, cubic ice blocks were produced, and they were removed from the frame and used as model of broken ice pieces constituting an unconsolidated layer.
2) To make the temperature of each ice block and experimental apparatus constant, the ice blocks were left on a sheet for one day.
3) The ice blocks were put into the shear box that constituted of an upper part (500mm×500mm×200^{h}mm) and a lower part (500mm×500mm×250^{h}mm). And then, the ice blocks were randomly arranged. The apparatus is shown in Fig.1.
4) The some steel plates (497mm×497mm×250^{h}mm) were placed on the ice blocks to apply confining force to ice blocks.
5) The upper part of the shear box was moved horizontally at a constant rate by a hydraulic ram, and the shear force, horizontal deformation of the upper part of the box and vertical deformation of the steel plate were measured during the movement of the upper part of the shear box. The contact face between the upper and lower parts was smeared with grease in order to reduce the sliding resistance. We carried out the test right after the ice blocks were put into the shear box so that the ice blocks did not adhere to each other.
6) The ice blocks were removed from the shear box after the completion of each test, and new ice blocks were added to the shear box.

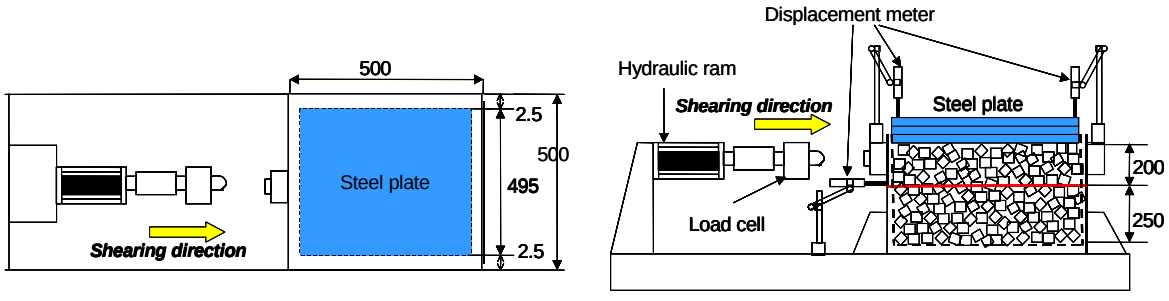

Fig. 1. Direct shear test machine [Yasunaga et al., 2001]

Experimental conditions

The tests were conducted in a cold room at -3°C. The experimental conditions are shown in Table 1. In producing our unconsolidated layer model, we used ice blocks of six different sizes and shapes (Table 2). Each run was performed four or five times. The shear strength is thought to depend greatly on the degree of interlocking, and on the degree of fracture of each block within the specimen. It also depends on various factors such as

shear rate, initial porosity, shape and size of broken ice piece within the specimen, and adhesion condition of each block (surface condition of each ice block). To investigate the effect of the abovementioned factors on the shear strength of an unconsolidated layer, we arranged the following test conditions.

Table 1. Experimental conditions

	CASE 1	CASE 2	CASE 3	CASE 4	CASE 5	CASE 6	CASE 7
Block type	Uniform (a1,a2,a3)	Mixed (a1,a2,a3)	Uniform (a2)	Uniform (a2,a4,a5)	Uniform (a6)	Uniform (a5,a6)	Uniform (a5)
Normal stress (kPa)	1.88 - 11.29	1.88 - 11.29	5.8	1.88 - 11.29	11.29 - 11.29	5.8	1.88 - 7.53
Shear rate (mm/s)	1.6	1.6	0.1-24	1.6	1.6	0.1-24	1.6

Room temperature: 3

Table 2. Types of ice block

		a1	a2	a3	a4	a5	a6
Shape		cube	cube	cube	Rectangular solid	Rectangu-lar solid	Rectangu-lar solid
Length of each side (mm)	a	22.5	42.5	65	42.5	42.5	120
	b	22.5	42.5	65	42.5	42.5	65
	h	22.5	42.5	65	15	25	33
Initial porosity		0.31	0.34	0.37	0.49	0.45	0.46

In Table 1, “uniform” means an unconsolidated layer model consisting using ice blocks of the same size (single block type), and “mixed” means an unconsolidated layer model consisting of blocks of three different types with an equal weight ratio. We regard representative size of the blocks in the “mixed” case as the mean grain size, and this size is 42.5 mm (mean porosity is 0.29). Normal stress was divided into five categories, in the range of 1.88 to 11.29 kPa.

CASE 1

Considers how the size of cubical ice blocks affects the shear strength (block type a1, a2 and a3).

CASE 2

Investigates the strength properties of “mixed” blocks of different sizes with an equal weight ratio (block type a1, a2 and a3). The results are compared with those of CASE 1.

CASE 3

Considers how shear rate affects the shear strength (block type a2).

CASE 4

Considers how block shape affects shear strength. Different shapes are produced by changing the length of one side of cubical blocks of type a2. The strength was compared between specimens consisting of block type a2, a4 and a5.

CASE 5

Compares the strength of specimens consisting of type a2 cubical blocks and that of type-a6 rectangular blocks under identical block volume.

CASE6

Considers the effect of shear rate on shear strength (block type a5 and a6).

CASE 7

Examines whether the shear strength depends on the submergence condition of block (wet vs. dry), using block type a5.

Although blocks in situ could partly adhere (broken ice pieces within unconsolidated layer), we did not consider such a situation in this study. The results of CASES 1 to 3 have been reported in Yasunaga et al. [2002]. This paper will report on the results of CASES 4 to 7. These test conditions (CASES 1 - 6) are dry (i.e., blocks are not submerged), because of the simplicity of experiment and the assumption that the surface condition of blocks (dry or wet) does not affect the shear strength. CASE 7 was conducted to validate the effect of water on the shear strength. As for its test method, we conducted the test right after antifreeze liquid at the same temperature as the cold room (-3°C) was injected into the shear box.

RESULTS AND DISSCUSSION

As mentioned above, an unconsolidated layer can be regarded as Mohr-Coulomb material. Our experiments assume that failure conditions follow the Coulomb failure criterion.

$$\tau = \sigma_N \tan\phi + C$$

Where: τ, shear strength; ϕ, internal friction angle; σ_N , normal stress; C, cohesion.
Most of the results of past experiments conformed to the Coulomb failure criterion [Yasunaga et al., 2002]. The test results herein were also found to follow that criterion, as described later.

Porosity

As mentioned above, porosity of the specimen is thought to be a factor in shear strength, in light of dilatancy effect. Table 2 shows the initial porosity of specimen for each block type when the blocks are randomly arranged in the shear box. The porosity increased with block size in the case of types a1, a2 and a3. The porosity of “mixed type” was slightly smaller than that of “uniform type” From the results for type a4, a5 and a6, we see that the porosity seems to become smaller as the block shape approaches a cube. Thus, we found that porosity depended on block size and shape even for identical initial arrangement of blocks. Therefore, although we did not intentionally control the porosity, we could indirectly consider the effect of porosity, since the porosity changed according to block size or shape. We may be able to change only porosity while maintaining the block size and shape. However,

1) This would be difficult.
2) The effect of block shape or size is assumed to exceed that of porosity.
3) Although vertical deformation and shear stress due to horizontal deformation at the initial stage would be affected by porosity, we assumed that there was no significant difference in shear strength, as discussed later.

Behavior of shear stress and vertical deformation due to horizontal deformation

Horizontal deformation was measured up to 75 mm. However, shear strength was assumed to be the maximum shear stress occurring within the range of horizontal displacement of 0 to 40 mm in this study, for the following reasons

1. The shear area becomes smaller as horizontal deformations increases. Thus, the distribution of shear stress becomes uneven when the displacement becomes large

2. As shown in Figure 2, shear stress has a maximum value or approaches a constant value for horizontal deformation between 0 and 40 mm in most cases.

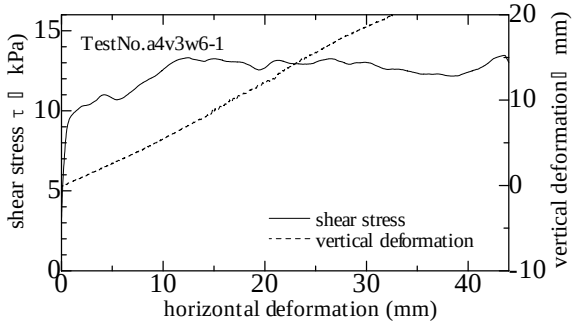

Fig. 2. Behavior of shear stress and vertical deformation

Figure 2 shows example of shear stress and vertical deformation due to horizontal deformation. Regarding vertical deformation, although repeated expansion and contraction of the test specimen occurred, most of the failures occurred when the specimen was expanded. This is because expansion from block upheaval tended to exceed subsidence from block compaction.

Effects of block size and shape on shear strength

Figure 3 shows the shear strength versus the normal stress for CASE 4 using types a2, a4 and a5. As described above, each block of type a4 and a5 is produced by changing the length of one side of the type-a2 cubical block. Each run of the experiment was repeated several times under the same condition, and the mean values were shown in the figure. We can see that the results plot as a fairly straight line and satisfy the Coulomb failure criterion. Figure 4 shows the strength parameters, such as apparent cohesion and internal friction angle (C,ϕ), estimated from the results. Here, the horizontal axis shows the ratio between the block height and length (type a2). The figure shows that the internal friction angle seems to become smaller as the block becomes thinner (as the ratio becomes smaller), while there is no significant difference in cohesion. This may be attributed to the following.

1) The effect of initial porosity: Initial porosity increases as the blocks become thinner.
2) Degree of block fracture: Block fracture after each shear test seems to be more prominent the thinner the blocks are.
3) Relatively small interlocking effect: When a rectangular block is converted to a cubical block of the same volume, the thinner is the block, the smaller are the dimensions of the converted cubical block.

Interlocking depends on the block size, block shape and initial arrangement of blocks in the shear box. In this case, however, the effect of block shape on strength was not clear, since each block size or volume converted to mean size was not the same among test cases (types a2, a4 and a5). So we compared the two shear strengths corresponding to two

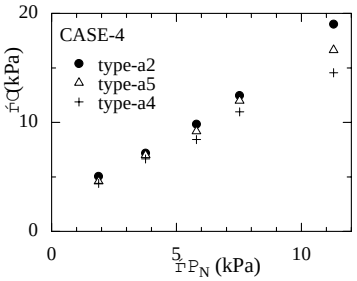

Fig. 3. σ_N vs. τ (CASE 4)

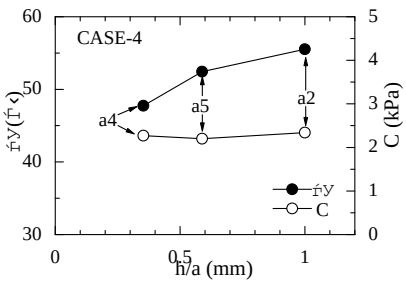

Fig. 4. Effect of block shape on C, ϕ (CASE 4)

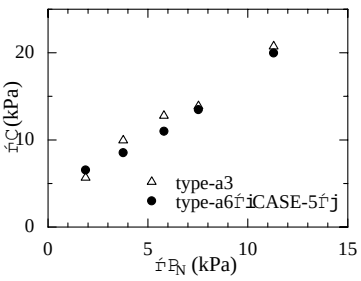

Fig. 5. σ_N vs. τ (CASE 5)

types of blocks (types a3 and a6) with different shape but with the same volume (CASE 5). The shape (ratio of the length of each side) of type a6 is based on a survey of ice pieces at ice ridges in the Sakhalin area [Surkov et al., 1996]. Figure 5 shows the relationship between normal stress and shear stress for CASE 5. A comparison of the degree of block fracture for cubical (type a3) blocks with that for rectangular blocks (type a6) shows that, after each shear test, the blocks of type a6 seem to fracture more easily than those of type a3, and the initial porosity of block type a3 and a6 was 0.37 and 0.46, respectively. This figure shows that the two strengths seem almost the same. Therefore, roughly speaking, it could be assumed that the shear strength depends not on ice block shape but on the volume or size. Thus, if we convert the size of blocks of various shapes in an unconsolidated layer to cubical size (mean grain size), we can perform a shear test under simple conditions.

The results, including those of CASE 1, are summarized in Figs. 6 (a) and (b), which show the relationships between block volume and strength parameter. From Figures 6(a) and 6(b), we can see that relationship between block volume and strength for CASES 4 and 5 plots as a fairly straight line in CASE 1 using the three types of cubical blocks (a1, a2, a3). Therefore, strength parameters seem to depend only on the block volume. This means that strength increases with block size. This may be caused by the increase in interlocking or by the dilatancy effect; that is to say, the shear strength increases since the energy used in expansion of a specimen during shear becomes larger as the block size increases. However, the rate of increase of strength parameters is thought to slow as the block size increase, and the strength parameters may approach a constant value over time. This may be because the strength of block decreases as the block size increases. When for larger block size, the blocks fail more due to the size effect, which slows the rate of increase of strength parameter. We can also assume

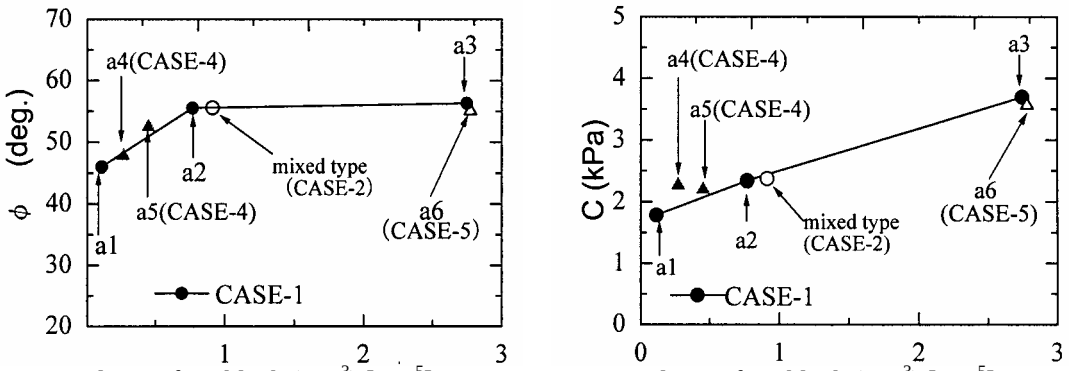

Fig. 6. Effect of block volume on strength parameters

that the strength parameter approaches a constant value. In our experiment, only the internal friction angle shows abovementioned trend. These results are similar to those reported previously by other researchers (e.g., Prodanovic et al., 1979, Weiss et al., 1981). Also, the white circles in Figures 6 (a) and (b) show the results for "mixed type." The strength parameters of mixed type were almost the same as those of uniform type (a2). Here, the size of mixed type converted to mean size corresponds to that of type a2.
Thus, it seems that the strength parameters depend only on block size or volume, whereas the initial porosity and failure mode of block depend on the block shape. Furthermore, the

rate of increase of strength parameters is thought to slow as the block size increases to approach a constant value. It seems reasonable to perform an experiment using cubical blocks that are similar in strength to those in the sea and that are big enough to mitigate the “size effect” of the strength of block.

Shear strength under the different test conditions: wet (submerged) vs. dry (CASE 7)

Ice blocks in an unconsolidated layer in situ are mostly submerged. Therefore, it is desirable to perform shear tests under submerged condition. The abovementioned experiments (CASES 1 to 6) were performed under dry condition, i.e., the blocks were not submerged. We used dry condition for its experimental simplicity and based on the assumption that the block surface condition (dry or wet) would not affect the shear strength. Here, we compare the shear strengths under the different test conditions (wet and dry) using blocks of type a5 (Fig.7). Although the shear strengths under submerged condition seem slightly larger than those under dry condition, the figure suggests that there are no significant differences in the internal friction angles for the two conditions, and there seems to be no reason for submerged shear to be greater. In this case, excess pore water pressure within the specimen obviously could not occur. Thus, because it seems reasonable to believe that the strength parameters do not depend greatly on whether the blocks are submerged, the experiment may be performed under the easier setup of dry condition.

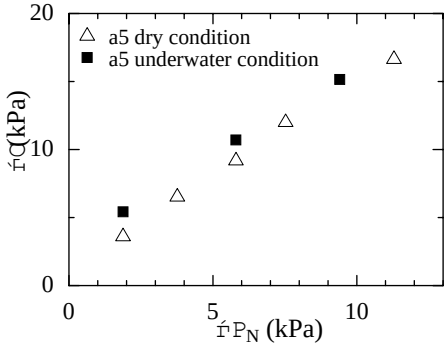

Fig. 7. Shear strength: submerged blocks and dry blocks

Effect of shear rate on shear strength

Figure 8 shows the relationship between shear strength and shear deformation rate. In this figure, normal stress remains constant at 5.8 kPa. We previously reported the results for type a2 [Yasunaga et al., 2002], and the results for types a5 and a6 have been added to those results. The shear strength decreases as the shear rate increases, and it seems to approach a constant value over time. Weiss et al. [1981] reported similar results. This may be attributed to the fracturing of blocks without rearrangement (or expansion) during shear test when the shear rate increases. Indeed, the vertical deformation decreased as the shear rate increased. Although it is possible that the shear strength has a maximum value at a certain shear rate (0.1 mm/s – 0.2 mm/s, in this case), this must be tested with a greater number of samples. We confirmed that the effect of shear rate on shear strength is also an important factor.

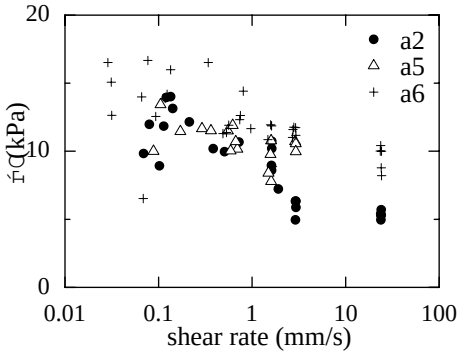

Fig. 8. Effect of shear rate on shear strength

CONCLUSIONS

- This study was not able to clarify how block shape alone affects shear strength. However, we did find that the shear parameters seem to depend not on block shape but on block volume or size, and that initial porosity and failure mode depend on block shape.
- There is a tendency for the strength parameters to increase as the block size increased. However, the increase in internal friction angle deceases as the block size increases, and the internal friction angle seems to approach a constant value over time.
- The strength parameters are not thought to depend much on whether blocks are submerged. This means that it is possible to perform experiments under dry conditions.
- The shear strength depends largely on the shear rate. Shear strength decreases as shear rate increases, and it seems to approach a constant value over time. It is possible to assume that shear strength has a maximum value at a certain shear rate (0.1 mm/s – 0.2 mm/s, in this case).

We will repeat this experiment with a larger number of samples under various conditions, considering the range of normal stress and the block strength. We also need to determine whether the shear strength takes a maximum value at a certain shear rate. Furthermore, we need to examine how the shear box size relative to block size affects the shear strength.

REFERENCES

Bruneau, S. E., et al.: Development of Techniques for Measuring In Situ Ice Rubble Shear Strength, *Proc.of 14th International Symposium On Ice (IAHR), Preprint of Papers to be Included in Volume 2 of the Proceedings*. (1998)

Heinonen, J. et al.: Ridge-Loading Experiments – Analysis of Rubble Strength in Ridge Keel Punch Test, *Proc. of the 15th International Symposium on Ice*, Vol. 1, (2000) 63 - 72.

Lepparanta, M and Hakala, R.: Field measurement of the structure and strength of first-year ice ridges in the Baltic Sea, *Proc. of the 8th International Conference on Offshore Mechanics and Arctic Eng.*, Vol. 4, (1989) 169 - 174.

Prodanovic, A.: Model Test of Ice Rubble Strength, *Proc. of the 5th International Conference on Port and Ocean Engineering under Arctic Conditions*, (1979) 89 - 105.

Surkov, G. A., Astafiev, S. V. and Polomoshnov, A. M.: Hummock Porosity Tests, *12th Internal Symposium on Okhotsk Sea and Sea ice*, (1997) 49 - 52.

Weiss, R. T., et al.: Determination of Ice Rubble Shear Properties, *Proc. of the 5th International Symposium on Ice*, (1981) 860 - 870.

Wong, T. T., et al.: Shear box tests on broken ice, *Proc. of Port and Ocean Engineering Under Arctic Condition (POAC)*, Vol. 3, (1987) 97 - 107.

Yasunaga, Y., Kioka, S., Matsuo, Y., Furuya, A. and Saeki, H.: Strength of Unconsolidated Layer Model of Ice Ridge, *Proc.of the 16th International Symposium on Ice*, Vol. 2, (2002) 62 - 68.

17th International Symposium on Ice
Saint Petersburg, Russia, 21 - 25 June 2004
International Association of Hydraulic Engineering and Research

NEW SCHEMES OF ACCOUNTING ICE RIDGING IN MODELS OF SEA ICE COVER DYNAMICS

Alexandr Makshtas[1, 3], Aleksey Marchenko[1] and Sergey Shutilin[2]

ABSTRACT
The method of estimation the number of sea ice ridges is formulated and tested using dynamic-thermodynamic model sea ice model. The influence of space orientation of ice ridges on wind drag force is studied.

INTRODUCTION
Ridged ice is formed under the compression of ice floes due to push out broken ice on floes surface and bottom. Its area occupies up to 40% of ice-covered part of the Arctic Ocean. As a rule ridged ice is organized into ice ridges separated more or less by level ice floes. Each ice ridge extends in some horizontal direction and it is possible to perform the ridge as the line on the horizontal plane (Hibler and Ackley, 1973). The length of ridgelines can be larger several kilometers and some of them are curved. Davis and Wadhams (1995) found bimodal space orientation of ridge crests in different regions of the Arctic Ocean. The shape of the ice ridge can be characterized by the shape of the ridgeline and the shape of ridge cross-section in vertical plane. Figure 1a shows typical shapes of ridgeline l_r and vertical cross-section U_r. Field studies show that averaged shape of vertical cross-section of ice ridges can be approximated by two isosceles triangles (Fig. 1b) (Timco and Burden, 1997).

Main influence of ridged ice on sea ice cover is stipulated by increasing of the roughness of the upper and bottom ice surfaces and changes of thermodynamic and rheological properties of the ice cover. Practically all ice with thickness greater than 5 meters is formed as a result of the ridging. The influence of ice ridging on large-scale rheological properties of sea ice continuum is most investigated. The first papers of Rothrock (1975) and Hibler (1979) introduced critical pressure p_* necessary for the irreversible compression of continuous ice as a function of averaged ice thickness. The increasing of drag forces applied to the ice by the wind and ocean currents has been roughly estimated by Doronin and Heisin (1975). Field studies of Garbrecht et al.

[1] Arctic and Antarctic Research Institute, Beringa str. 38, 199397 St.-Petersbutg, Russia
[2] Hokkaido University, Sapporo, Japan
[3] International Arctic Research Center, University of Alaska, Fairbanks, USA

(1999) have shown that the ridge form drag can contribute up to 50% of the total drag applied to ice surface. Kawai et al. (1999) estimated the form drag coefficient of the ice bottom with irregularities of different shapes from laboratory experiments. Marchenko et al. (2003a,b) have shown the increasing of heat flux from ice-covered ocean to atmosphere during first several days after the ridge buildup due to water freezing between ice blocks, composing the ridge.

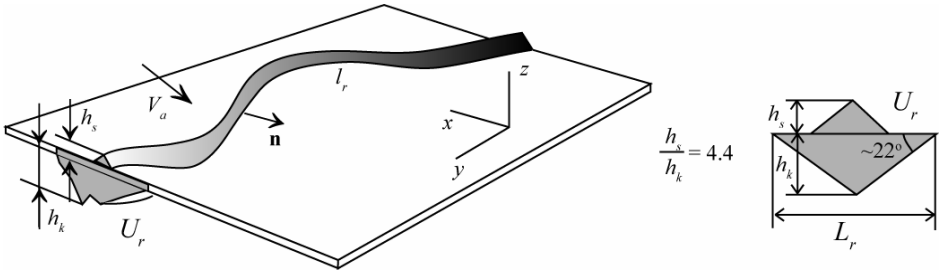

a) b)

Fig. 1. Geometry of ice ridge: spatial distribution (a) and triangular approximation of the vertical cross-section (b): l_r - ridgeline; U_r - area of vertical cross-section of the ridge, h_s - sail height, h_k - keel draft, L_r - ridge width

Most of the existing models of ice cover dynamics operate with averaged ice thickness, or with several categories of ice thickness, or with the function of thickness distribution (Pritchard, 2001). Makshtas et al. (2003 a, b) and Marchenko (2002) introduced new class of three layer models taking into account the fraction of ridged ice and giving possibility to calculate vertical sizes of ridges and ridge spacing. The calculation of these parameters is very important for the Arctic navigation since the ice ridges create large difficulties for ship operations. In the present paper we develop this class of models, improve parameterization of drag forces, taking into account the form drag applied to the surfaces of ridges ice, and demonstrate some results of numerical calculations of the number of ridges in the Arctic.

EQUATIONS OF MASS BALANCE

General form of mass balance equation in the models of sea ice dynamics is:

$$\frac{dM}{dt} + M\nabla\cdot\mathbf{v} = S_M\,, \quad \frac{d}{dt} = \frac{\partial}{\partial t} + \mathbf{v}\cdot\nabla\,, \ \nabla = \left(\frac{\partial}{\partial x}, \frac{\partial}{\partial y}\right), \tag{1}$$

where M is the mass of sea ice floating on unity area of sea surface (surface density of ice cover), $\mathbf{v} = (v_x, v_y)$ is ice drift velocity, x and y are horizontal coordinates, t is the time, and S_M is the term describing ice freezing and melting. In this section we consider only mechanical processes and assume that $S_M = 0$. Mass M is defined using some space scale L of the averaging. Lagrangian element of ice cover with diameter L is considered as material point of ice continuum. Typically in the large-scale sea ice models the length L is changed from 10 km to 100 km. In that case the material point of ice continuum includes many floes, and ice continuum has properties closed to granular materials.

Sea ice compactness A is introduced by formula $M = \rho_i A\langle h\rangle$, where ρ_i is ice density and $\langle h\rangle$ is ice thickness averaged over the representative area. In our approach we use

function $A_w = 1 - A$ describing the relative area of open water on the surface of ice-covered ocean that satisfies to equation

$$\frac{dA_w}{dt} + (A_w - 1)\nabla \cdot \mathbf{v} = 0 . \qquad (2)$$

Most common scheme of ice compression is shown on Fig. 2a. Actually, the increasing of ice thickness is related to the buildup of sea ice ridges from level ice. The scheme of ice compression taken into account this process is shown on Fig. 2b. Following this scheme the compression of level ice is occurred due to the push out of broken ice on the surface of flat ice and to the bottom.

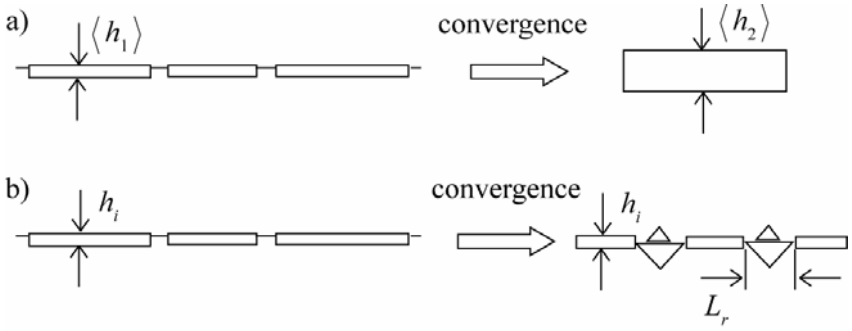

Fig. 2. Schemes of ice cover compression without ridged ice fraction (a) and with ridged ice fraction (b)

Averaged shape of vertical cross-sections of ridges, shown on Fig. 1b, closes to two isosceles triangles which slope angles α about 22°, keel draft to sail height ratio κ is about 4.4, and the values of ridge cross-section area U_r changes from 100 m^2 to 250 m^2 (Timco and Burden, 1997). Using this approximation the height of ridge sail h_s and ridge width L_r are expressed as:

$$h_s = \sqrt{U_r \tan\alpha / (1+\kappa^2)} , \quad L_r = 2\kappa\sqrt{U_r / (\tan\alpha (1+\kappa^2))} . \qquad (3)$$

It is assumed that the ridges have isotropic angular distribution and representative length of the ridges is much smaller the scale L of the averaging. We denote the mean area of vertical cross-section of ridges (the area of dashed triangles at Fig. 1b) located in a material point of ice continuum as U_r and introduce linear density of the number of ridges n_r measured in m^{-1}. The number of ridges over the length L of continuous ice is equal to $n_r L$. The number of ridges located in dS is equal to $n_r^2 dS$. Evidently that total length of all ridges in area dS is equal to $n_r^2 l_r dS$ and total mass of all ridges in the area is equal to $\rho_i n_r^2 U_r l_r dS$.

Basic relation between the fractional areas is

$$A_w + A_i + A_r = 1, \qquad (4)$$

where A_i and A_r are level and ridged ice compactness. Ridged ice compactness is equal to $A_r = n_r^2 l_r L_r$, where L_r is mean ridge width (Fig. 1b). The surface density of the ice cover can be written as

$$M = \rho_i A_i h_i + \rho_i A_r U_r L_r^{-1} . \qquad (5)$$

Level ice thickness is not changing under the ridging, therefore we set $dh_i / dt = 0$.

Representative time of single ice ridge buildup is estimated as several tens minutes (Marchenko and Makshtas, 2001). Representative time scale of large-scale sea ice models has the order of one day. During this time many ridges can be formed in Lagrangian cell of ice continuum. This is a reason to introduce the mean value $U_r = U_r(h_i)$ of the area of vertical cross-section of ridges and the mean value of ridge length $l_r = \text{const}$. Linear density of ridges is defined as $n_r = \sqrt{A_r /(l_r L_r)}$. Equations (1), (2) and (4) together with formula (5) represent closed system equations for the finding of A_i, A_w and A_r.

SIMULATIONS OF RIDGES NUMBER IN THE ARCTIC OCEAN

Above considered scheme of the parameterization of ice ridging was incorporated in dynamic-thermodynamic sea ice model (Makshtas et al., 2003a). The main equations of the model are based on the laws of mass and momentum balance. Equations of mass balance follow from equations (1), (2,) and (4), and include source terms responsible for the description of thermodynamic growth or melting of flat ice, lateral melting of level and ridged ice in leads, and melting of the upper and lower surfaces of ridges. Equation of momentum balance includes a parameterization of internal ice stresses in the framework of a cavitating fluid (Flato and Hibler, 1992). It is assumed that the mean value of the area of vertical cross-section of the ridges is $U_r = 190\,\text{m}^2$ and the mean length of ridges is $l_r = 1\,\text{km}$. The values of sail height, keel draft and the width of ridge are calculated using formulas (3) as $h_s \approx 1.9\,\text{m}$, $h_k \approx 8.5\,\text{m}$ and $L_r \approx 42.3\,\text{m}$ respectively.

Some results of numerical simulations are shown on Fig. 3. According to Fig. 3a, b the number of ridges per 1 km is varied from 2 to 4, therefore averaged distance between two neighbor ridges is varied from 250 m near the northern Greenland coast to 500 m to the north of the Barents Sea. The number of ridges in May is greater than in September due to summer melting. Figures 3c, d demonstrate the decreasing of the ridges number in 1989-1991 relatively 1985-1988. This results support the conclusion by Walsh et al (1996) that dominant cyclonic geostrophic winds well developed in the polar atmosphere in early 1990s tend to increase divergent ice motion in contrast to dominant anticyclonic winds. Figures 3e, f show partial recover of modeled number of ridges in the Canadian region in (1999-2001). It corresponds to change of atmospheric circulation from cyclonic to anticyclonic after 1996 (Polyakov and Johnson 2000). Taken into account, that the main changes of ice volume are due to ridged ice (Makshtas et al, 2003), our results support Rothrock et al (2003) conclusion about absence of any convincing argument that the decline of sea ice thickness through 1996 should be extrapolated as a prediction of its future behavior.

INFLUENCE OF ICE RIDGES ON DRAG FORCES

Wind and water drag forces are the main reasons for ice drift. Total drag force is the sum of the skin drag and the form drag. Ridges can introduce significant perturbations in the boundary layers causing the increasing of the form drag force. The most commonly used parameterization of isotropic skin drag force (stress) applied to unity surface of the ice in large-scale models of sea ice dynamics has form

$$\mathbf{F}_{i,a} = \rho_a C_{i,a} |\mathbf{V}_a| \mathbf{V}_a, \quad \mathbf{F}_{i,w} = \rho_w C_{i,w} |\mathbf{v}_w - \mathbf{v}| (\mathbf{v}_w - \mathbf{v}), \tag{6}$$

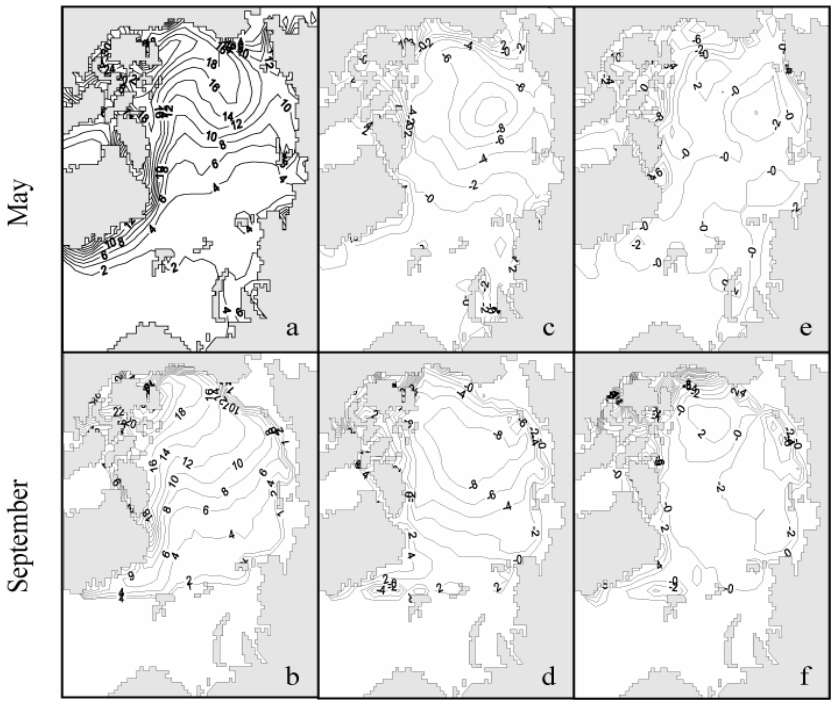

Fig. 3. The number of ridges per km^2 in May (a) and in September (b) averaged over 1984-1988; difference between the numbers of ridges per km^2 averaged over 1989-1993 and averaged over 1984-1988 in May (c) and in September (d); difference between the numbers of ridges per km^2 averaged over 1999-2001 and averaged over 1984-1988 in May (e) and in September (f)

where ρ_a and ρ_w are air and water densities, $C_{i,a} \approx 2 \cdot 10^{-3}$ and $C_{i,w} \approx 5 \cdot 10^{-3}$ are drag coefficients, $\mathbf{V}_a$ and $\mathbf{v}_w$ are the velocities of the wind at height 10 m and ocean current at 1 m distance below ice bottom.

When wind velocity and ocean current are normally directed to the ridgeline, the absolute values of the form drag forces are defined as

$$|\mathbf{F}_{r,a}| = \rho_a C_{r,a} h_s |\mathbf{V}_a|^2 / 2, \quad |\mathbf{F}_{r,w}| = \rho_w h_k C_{r,w} |\mathbf{v}_w - \mathbf{v}|^2 / 2, \tag{7}$$

where $C_{r,a}$ and $C_{r,w}$ are form drag coefficients. Coefficient $C_{r,a}$ is estimated as $C_{r,a} = 0.68\left[\ln(h_s / z_0) \ln^{-1}(10 / z_0)\right]^2$, where $z_0 = 5 \cdot 10^{-4}$ m (Garbrecht et al.,1999). Absolute value of the form drag force applied to n_r ridges of unity length by the wind is equal to $F_{n,r,a} = \rho_a n_r C_{r,a} h_s |\mathbf{V}_a|^2 / 2$. The ratio of wind drag force defined by formulas (6) to the form drag force (7) is $R_a = 2C_{i,a}\left(n_r h_s C_{r,a}\right)^{-1}$. Laboratory experiments (Kawai et al., 1999) show that $C_{r,w} \sim 1$. The ratio of water drag force defined by formulas (6) to the form drag force (7) is $R_w = 2C_{i,w}\left(n_r h_k C_{r,w}\right)^{-1}$. Assuming 3 ridges with $h_s = 2$ m and $h_k = 10$ m over 1 km length we have $R_a \approx 1.4$ and $R_w \approx 0.33$. Thus, the form drag has the order of the skin drag in the atmosphere. In the ocean the form drag is three times larger the skin drag.

Let us calculate the form drag applied to a ridge, which space configuration is characterized by ridgeline l_r. Since the form drags are related to the action of air and water pressure on ridge surfaces they must depend on the normal projections of wind and ocean current velocities on the ridgeline. Therefore total form drag applied to the ridgeline on Fig. 1a is calculated as $\mathbf{F}_{l_r} = \mathbf{F}_{l_r,a} + \mathbf{F}_{l_r,w}$, where $\mathbf{F}_{l_r,a}$ and $\mathbf{F}_{l_r,w}$ are the form drags by wind and ocean current:

$$\mathbf{F}_{l_r,a} = 0.5\rho_a \int_{l_r} C_{r,a} h_s (\mathbf{V}_a \cdot \mathbf{n})^2 \operatorname{sign}(\mathbf{V}_a \cdot \mathbf{n}) \mathbf{n} dl_r \,, \tag{8}$$

$$\mathbf{F}_{l_r,w} = 0.5\rho_w \int_{l_r} C_{r,w} h_k ((\mathbf{v}_w - \mathbf{v}) \cdot \mathbf{n})^2 \operatorname{sign}((\mathbf{v}_w - \mathbf{v}) \cdot \mathbf{n}) \mathbf{n} dl_r \,.$$

Let us consider unity surface of ice cover with n_r^2 ridges, having rectilinear ridgelines. Space orientation of each ridge is defined by unit vector normal to the ridgeline $\mathbf{n} = (-\sin\theta, \cos\theta)$, where $-\pi/2 \le \theta \le \pi/2$. Space distribution of the ridges is defined by function $f(\theta) \ge 0$, satisfying to the condition $\int_{-\pi/2}^{\pi/2} f(\theta) d\theta = 1$. The number of ridges with $\theta \in (\theta_1, \theta_2)$ is equal to $n_r^2 \int_{\theta_1}^{\theta_2} f(\theta) d\theta$. Total form drag force applied to ice cover of unity surface is calculated as $\mathbf{F}_{t,f} = \mathbf{F}_{t,f,a} + \mathbf{F}_{t,f,w}$, where

$$\mathbf{F}_{f,a} = 0.5\rho_a C_{r,a} h_s l_r n_r^2 \int_{-\pi/2}^{\pi/2} (\mathbf{V}_a \cdot \mathbf{n})^2 \operatorname{sign}(\mathbf{V}_a \cdot \mathbf{n}) \mathbf{n} f(\theta) d\theta \,, \tag{9}$$

$$\mathbf{F}_{l_r,w} = 0.5\rho_w C_{r,w} h_k l_r n_r^2 \int_{-\pi/2}^{\pi/2} ((\mathbf{v}_w - \mathbf{v}) \cdot \mathbf{n})^2 \operatorname{sign}((\mathbf{v}_w - \mathbf{v}) \cdot \mathbf{n}) \mathbf{n} f(\theta) d\theta \,.$$

The analysis of aerial photograph, carried out by Davis and Wadhams (1995) revealed the bimodal orientations of sea ice ridges to the north of Greenland with probability of space orientation of sea ice ridges shown on Fig. 4a by stems, where angle θ shows the deviation from latitude. We approximate this dependence by function $f(\theta) = 0.158 + 0.102\theta + 0.415\theta^2 - 0.088\theta^3 - 0.148\theta^4 + 0.02\theta^5$, shown at Fig. 4a by continuous line.

For the estimation of anisotropic properties of wind drag stresses we set $\mathbf{V}_a = V_a(\cos\varphi, \sin\varphi)$, where $V_a = \text{const}$. From the formulas (8) and (9) the wind drag stress is expressed as follows

$$\mathbf{F}_{f,a} = \Omega_a \int_{-\pi/2}^{\pi/2} \sin^2(\varphi - \theta) \operatorname{sign}(\sin(\varphi - \theta)) \mathbf{n} f(\theta) d\theta \,, \tag{10}$$

where $2\Omega_a = \rho_a C_{r,a} h_s l_r n_r^2 V_a^2$. Absolute value of the drag force is defined as $\left|\mathbf{F}_{f,a}\right| = \Omega_a g(\varphi)$, where $g(\varphi)$ is calculated from (10). Calculated function $g(\varphi)$ is shown on Fig. 4b. One can see that $g(\varphi)$ is changed in two times depending on the wind direction. This graph demonstrates that sea ice to the north of Greenland, region 3

in Davis and Wadhams, (1995) notations, is subjected to the west-east winds stronger than to the north-south winds.

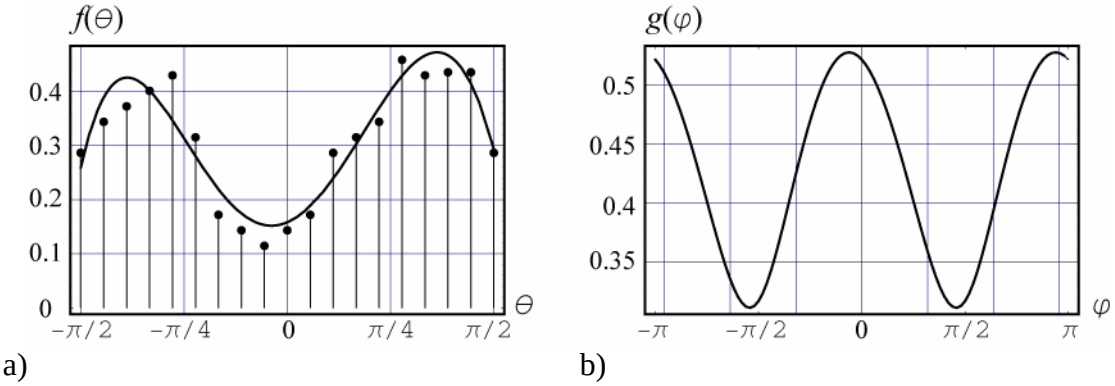

a) b)

Fig. 4. Functions *f(θ) and g(φ)* for region to the north of Greenland: a - space orientation of sea ice ridges (points) from Davis and Wadhams (1995) and its polynomial approximation *f*(θ); b - function $g(\theta)$ calculated from (10) with function $f(\theta)$ shown on Fig. 4a

DISCUSSION AND CONCLUSIONS

In present paper we consider the method of calculation of the number of ridges in large-scale modeling of sea ice cover dynamics. The method is based on the introducing in the model the fraction of ridged ice which is characterized by the compactness of ridged ice, mean ridge length, mean area of vertical ridge cross-section and number of ridges per unity length. The mean estimated number of ridges per 1 km near the northern Greenland coast is about 4 and mean ridge spacing is about 250 m. Davis and Wadhams (1995) reported about the distribution of ridge spacing from 20 to 240 m. This difference can be related to the assumptions that all ridges in our model have the same geometry and they are formed under the compression only. The improving of this scheme can be reached by introducing the function of open water production in the equation (2) (Gray and Killworth, 1996) and the equation describing the changing of n_r: $dn_r / dt + n_r \nabla \cdot \mathbf{v} = \psi_n$, where the source term $\psi_n \geq 0$ describes the rate of production of new ridgelines. This equation together with (1), (2) and (4) represent closed system equations for the finding of A_i, A_w, A_r and n_r. Here we don't consider possible parameterizations of function ψ_n assuming only that it should depend in isotropic models from principal values of strain rates and n_r. The mean ridge width is calculated as $L_r = A_r /(n_r^2 l_r)$, where the mean ridge length l_r is given. Thus, in this method ridge sizes are increasing during the ice convergence.

The influence of bimodal space orientation of ridges on the form drag is studied using data of Davis and Wadhams (1995). It is shown that the form drag can introduce up to 50% of the total drag depending on the number of ridges per unit of length. In our estimations for the case of bimodal orientation of ridges the form drag changes 2 times depending on wind direction. Application of this effect to the northern Greenland coast means that sea ice is more subjected to the east-west then north-south winds in the region.

ACKNOWLEDGEMENTS

This work has been supported by the Russian Foundation for Basic Research (Project code 03-05-64833), the Arctic and Antarctic Research Institute (Russia) and the International Arctic Research Center, University of Alaska Fairbanks.

REFERENCES

Davis, N.R. and Wadhams, P. A statistical analysis of Arctic pressure ridge morphology. *Journal of Geophysical Research* 100: 10915-10925 (1995).

Garbrecht,T., Lupkes,C., Augstein,E., and Wamser,C. Influence of a sea ice ridge on low-level airflow. *Journal of Geophysical Research* 104: 24499-24507 (1999).

Gray, J.M.T.M. and Killworth, P.D. Sea ice ridging schemes. *Journal of Physical Oceanography* 26: 2420-2428 (1996).

Doronin, Yu.P. and Heisin, D.E., 1975. Sea ice. *Gidrometeoizdat*, Leningrad (1975) 319 p. (in Russian)

Hibler, W.D.III and Ackley, S.F., 1973. Height variation along sea ice pressure ridges and the probability of finding "holes" for vehicle crossings. *CRREL Report* 197, Hanover, New Hampshire.

Hibler, W.D.III. A dynamic thermodynamic sea ice model. *Journal of Physical Oceanography* 9: 817-846 (1979).

Kawai, T., Makita, A., Saeki, H., Hara, F., and Ohtsuka, N. Experiments on the fluid resistance of rubble field of ice. *Ice in Surface Waters*, Shen (ed), Balkema, Rotterdam, 883-888 (1999).

Makshtas, A., Shoutilin, S., and Andreas, E. Possible dynamic and thermal causes for the recent decrease in sea ice in the Arctic. *Journal of Geophysical Research* 108: 25-1-25-13 (2003a).

Makshtas, A.P., Shoutilin, S.V., Marchenko, A.V., and Bekryaev, R.V. Dynamic-thermodynamic sea ice model: application to climate study and navigation. In *Proceedings of the International Workshop on Frontier Technology in Ship and Ocean Engineering*, Seoul National University, 149-157 (2003b).

Marchenko, A. and Makshtas, A. Ice ridging over various space scales. In *Proceedings of the IUTAM Symposium on Scaling Laws in Ice Mechanics and Ice Dynamics*. J.P.Dempsey and H.H.Shen eds., Kluwer Academic Publishers, (2001) 103-114.

Marchenko, A. Models of sea ice ridging. *Advances in Mechanics* 3: 67-129 (2002). (in Russian)

Marchenko, A. The influence of ice ridge consolidation on atmosphere-ocean heat fluxes, *In Proceedings of the Arctic and Antarctic Research Institute* 446, G. Alekseev ed. Gidrometeoizdat, St.-Petersbugr, 150-164 (2003a). (in Russian)

Marchenko, A., Kim, H., Gudoshnokov, Yu., Zubakin, G., and Makshtas, A. Buildup and consolidation of sea ice ridges. In *Proceedingd of the International Workshop on Frontier Technology in Ship and Ocean Engineering*, Seoul National University, Seoul 131-139 (2003b)

Polyakov, I., and Johnson, M. Decadal and interdecadal Arctic Ocean variability, *Geophysical Research Letters* 27: 4097-4100 (2000).

Pritchard, R.S., 2001. Sea ice dynamics models. In *Proceedings of the IUTAM Symposium on Scaling Laws in Ice Mechanics and Ice Dynamics*. J.P.Dempsey and H.H.Shen eds., Kluwer Academic Publishers, 265-288 (2001).

Rothrock, D.A. The energetic of the plastic deformation of pack ice by ridging. *Journal of Geophisical Research* 80: 4514-4519 (1975).

Rothrock, D.A., Zhang,, J., and Yu, Y. The arctic ice thickness anomaly of the 1990s: A consistent view from observations and models, *Journal of Geophisical Research* 108:.28-1 – 28-10 (2003).

Timco, G.M., Burden, R.P. An analysis of the shapes of sea ice ridges. *Cold Regions Science and Technology* 25: 65-77 (1997).

17th International Symposium on Ice
Saint Petersburg, Russia, 21 - 25 June 2004
International Association of Hydraulic Engineering and Research

MECHANICAL PROPERTIES OF ICE RIDGES AND LEVEL ICE, IN-SITU AND LABORATORY TESTING 2003

Knut V. Høyland[1], Morten Bjerkås[2] and Sergey Vernyayev[3],

ABSTRACT
Ice has been sampled from firstyear sea ice ridges and level ice both in the Van Mijen fjord in Svalbard and in the Northwestern Barents Sea. Insitu drop ball test and unconfined compression tests in the laboratory were conducted on horizontal and vertical samples of ice from the consolidated layer, the rubble and the level ice. The salinity, density and the ice texture was also examined. The average unconfined strength for vertical samples was 6.0 MPa for the level ice, 5.0 MPa for the consolidated layer and 3.3 MPa for the rubble. The hardness was clearly dependent on the temperature, and it varied from 11 to 37 MPa and $H_i \approx H_c > H_r$.

INTRODUCTION
Sea ice ridges are formed by compression or shear in the ice cover. In many Arctic and sub-Arctic areas ice ridges give the design forces for marine structures. However, the forces and deformations mechanisms involved in an ice ridge-structure interaction are not clear. When estimating the forces from first year ridges on structures one needs the thickness of the consolidated layer (h_c) and some mechanical properties as input (Blanchet, 1998). Mechanical properties of first year ice ridges are not well known. The consolidated layer is often assumed to behave similar to level ice, that is crush against a vertical structure and flexure against an inclined structure. Small scale samples from the consolidated layer has been tested by Frederking and Wright (1982), Høyland et al. (2000, 2002), Høyland et al. (2003) and by Veitch et al. (1991), see Høyland et al. (2003) for a summary of the results. The strength of individual blocks of rubble may of importance when modelling the mechanical behaviour of rubble (Liferov and Høyland, 2004) but is difficult to test and poorly known.

SITE AND EXPERIMENTAL SETUP
Ice was sampled from two artificially produced ice ridges and the surrounding level ice in the Van Mijen fjord between February and April 2003 (Liferov and Høyland, 2004), and from one ice ridge and the neighboring level ice in the Barents Sea close to Hopen

[1]The University Centre in Svalbard, Norway
[2]Norwegian University of Science and Technology, Trondheim, Norway
[3]St.Peterburg State Polytechnical University

(N76°16' E23°07') in May 2003. Dynamic hardness tests were performed in-situ and ice was sampled and uniaxial compression strength, salinity, density and ice texture were examined in the cold lab at UNIS. The hardness tests were performed on vertical and horizontal surfaces as described in Bonnemaire et al. (2003) and Vatne (2003). The vertical samples were cored directly with a core drill that gives ice cores with a diameter of 70 mm, but the horizontal ones were first cored with a large core drill and the recored with the small core. All the samples for unconfined compression tests then became cylindrical, with dimensions of about 175 mm and 70 mm and they were compressed with a constant speed corresponding to a nominal strain rate of $\dot{\varepsilon} = 10^{-3}s^{-1}$, see Sinha (1981) for a discussion on real and nominal strain rates. The capacity of the compression machine is 100 kN and the ice temperature was between -15°C and -20°C for all tests except when warm ice was tested (T ≈ -2 and -5°C). The ice for these tests were was also kept in the freezer at UNIS and carefully heated before testing. The temperature of each sample was measured directly after each test.

RESULTS AND ISCUSSION

Main results

Table 1 sums up all the main results. The unconfined compressive strength is given as $\sigma = F_{max}/A_0$

The samples from the ridge were in general a bit weaker than the ones from the level ice. Firstly, the level ice was basically sampled from colder ice (earlier in the season) than the ridges, so the ridged ice may have been more porous. But no relevant differences can be found in the salinity and the density measurements. Secondly it may be that cracks and other defects are introduced in the ice during the ridging process making the ridged ice weaker than the level ice, most of our level ice samples were from the landfast ice in the Van Mijen fjord, whereas most of our ridge samples were from the drift ice in the Barents Sea and this may also contribute to the differences.

It also is seen that the strength of the horizontal samples was less than that of the vertical ones. This has also been found by Frederking and Timco (1989) for level ice and by Frederking and Wright (1982) for ridges. They both found $\sigma^{vert} \approx 3\ \sigma^{hor}$, but did their tests with lower velocity. The difference for the level ice can be explained by the anisotropic nature of S2 (or S3) sea ice, but this should not apply for ridges. The lower strength of the horizontal samples may in our case be related to the sampling technique as cracks may have been created in the cold ice by the large core drill. The salinity of the horizontal samples was less than that of the vertical ones and this may also be due to the sampling technique. On the other hand there may be real effects related to the orientation of the brine channels, as these are more prone to be vertical than horizontal.

Fig. 1 shows the average salinity and strength of vertical samples to the depth for ice from the Barents Sea. As can be seen the strength varies with depth. The upper part was probably weak because the melting season had begun and the top ice was warm an porous. The consolidated layer was stronger than the ice from the rubble even if the testing was done in laboratory with the same ice temperature. So the rubble ice must have been more porous than the consolidated layer.

Table 1: Summary of results

	Barents Sea							Van Mijen fjord			
	Level ice		Cons. l		Rubble		Sail	Level ice		Cons. l	
	Vert	Hor	Vert	Hor	Vert	Hor	Vert	Vert	Hor	Vert	Hor
Unconfined compressive strength, T=(-15°C -20°C) (MPa)											
σ_{av}	6.0	3.4	5.0	2.4	3.3	3.8	4.0	5.9	4.3	4.4	-
st. dev	1.5	0.9	1.6	1.0	1.3	1.4	1.7	2.8	1.3	0.9	-
n	7	8	40	22	25	7	11	83	25	12	-
Salinity (ppt)											
S_{av}	4.6	3.9	4.7	3.9	3.9	2.9	2.14	vmli		3.6	
st. dev	1.5	0.9	1.4	1.1	0.9	0.5	0.6	vmli		0.4	
n	7	8	40	22	25	7	11	vmli		12	

Density (kg/m^3)					
ρ_{av}	883	928	964	1002	vmri
st. dev	49	31	74	53	vmri
n	9	29	3	4	vmri

Properties of the warm Van Mijen level ice, vertical cores

$\sigma_{av}/\sigma_{st.\ dev}$ (MPa)	$S_{av}/S_{st.\ dev}$ (ppt)	$T_{av}/T_{st.\ dev}/T_{range}$ (°C)	n (-)
6.2/3.4	4.6/1.6	-5.1/0.7/(-4.2, -6.4)	10
3.4/1.7	4.3/1.3	-2.0/0.2/(-1.6, -2.5)	11

This was also found by Høyland et al. (2000) with ice from the Gulf of Bothnia. There is a larger difference on the in-situ strength, but the authors are not aware of any published results of small scale in-situ tests of rubble strength. Warm sea ice is weaker because the temperature itself affects the behaviour of pure ice and because the temperature strongly affects the porosity of sea ice. The unconfined strength of the –2° C-ice was 57% of that of the cold ice, whereas the -6° C-ice was slightly stronger.

However, we believe that our -2° C-ice was in the stronger range of what can be

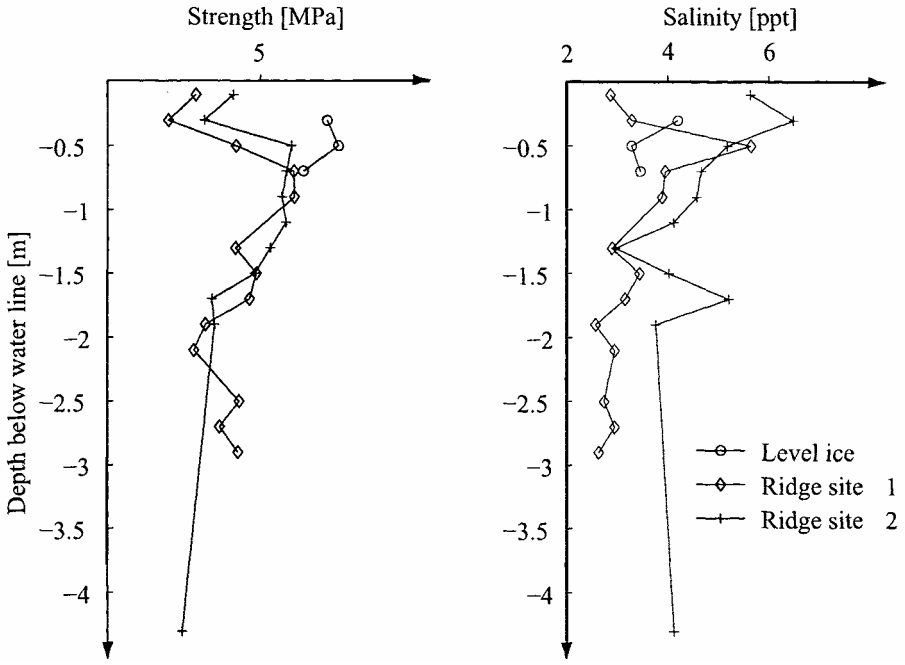

Fig. 1. The average strength and the salinity of the level ice and the ridge in the Barents Sea

expected for rubble in-situ. Firstly because when ice approaches its freezing point the temperature alone is no longer sufficient to describe the internal energy of the ice as substantial phase transfer goes on. Our ice had only been at -2°C for a few hours and was not exposed to any eroding currents. Secondly, our ice had been stored in the freezer for some months and brine had drained. Lower salinity means that less brine is created as the ice is heated and the porosity becomes less than that of in-situ rubble.

As can be seen the strength varies with depth. The upper part was probably weak because the melting season had begun and the top ice was warm an porous. The consolidated layer was stronger than the ice from the rubble even if the testing was done in laboratory with the same ice temperature. So the rubble ice must have been more porous than the consolidated layer. This was also found by Høyland et al. (2000) with ice from the Gulf of Bothnia. There is a larger difference on the in-situ strength, but the authors are not aware of any published results of small scale in-situ tests of rubble strength. Warm sea ice is weaker because the temperature itself affects the behaviour of pure ice and because the temperature strongly affects the porosity of sea ice. The unconfined strength of the 2°C C-ice was 57% of that of the cold ice, whereas the 6° C ice was slightly stronger. However, we believe that our -2° C-ice was in the stronger range of what can be expected for rubble in-situ. Firstly because when ice approaches its freezing point the temperature alone is no longer sufficient to describe the internal energy of the ice as substantial phase transfer goes on. Our ice had only been at -2°C for a few hours and was not exposed to any eroding currents. Secondly, our ice had been stored in the freezer for some months and brine had drained. Lower salinity means that less brine is created as the ice is heated and the porosity becomes less than that of in-situ

rubble.

Fig. 2a presents the strength plotted against the average stress-rate of resistance for 84 vertical samples from different depths in the level ice and 68 samples from the consolidated layer in the ice ridge. The stress-rate of resistance is defined as $\dot{\sigma} = \sigma_{max} / t$, where t is the time to failure and σ is the strength. The three failure mode explained by Kendall (1978) were all observed, but for samples loaded with $\dot{\sigma} > 0{,}4$ the failure was predominantly brittle (or premature in the terminology of Sinha (1982)). An increasing trend of strength with average stress-rate is seen, also for brittle samples.

We do not have the equipment to make a careful sample end preparation so that all the sample ends were not completely parallel. This means that end effects were probably present and this may have lowered the strength of our samples. The stiffness of the test machine is not yet measured but as the capacity is 100 kN it probably gives strain rates less than the desired 10^{-3} 1/s, and this could have affected both the failure mode and the strength (Sinha and Frederking, 1979).

The results from the hardness tests in 2002 and 2003 are given in Fig 2b. The hardness tests gave a nice dependence on the ice temperature both in 2002 (Bonnemaire et al., 2003) and in 2003 (Vatne, 2003), but the obtained hardness values were not comparable. It seems as if more work have to be put down in specifying the procedures, especially we believe that it the measurements of the footprint diameter may be person dependent. The surface preparation (manual or chain saw) was also of importance for the obtained hardness and the requirements for sample size are neither clear. The results are described more closely in Vatne (2003).

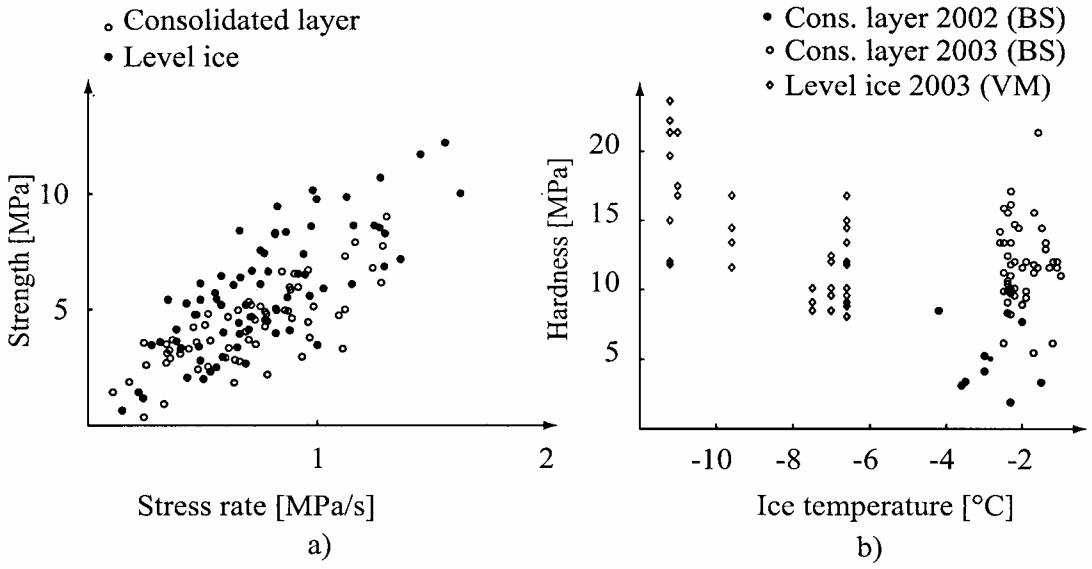

Fig. 2. a) resistance versus rate of resistance, b) hardness versus the ice temperature

CONCLUSIONS

Different types of ice has been sampled and tested in unconfined compressive tests in the UNIS laboratory and in-situ hardness tests have been performed. The main conclusions are:

- the average unconfined strength of vertical samples from the consolidated layer was 5.0 MPa and 6.0 MPa for vertical samples of level ice;
- the level ice was stronger than the ridged ice;
- the vertical samples were in general stronger than the horizontal samples. We do not know if this was due to our sampling technique or if the orientation of the brine channels makes the horizontal samples weaker;
- the average strength of ice tested at T = -2°C was 3.4 MPa, and we believe this in upper range of what may be expected in the rubble in-situ;
- the hardness of the consolidated layer was similar to that of the level ice, and stronger than the rubble. In general the the hardness had a clear dependency on the ice temperature, but the obtained value seems to depend on the person testing.

ACKNOWLEDGEMENT

We would like to thank the Arctic Technology students at UNIS the spring of 2003, especially Bjørn Dettwiler, Rinat Kamalov and the PhD students Per Olav Moslet and Pavel Liferov. We would also like to thank the mining company on Svalbard; Store Norske Spitsbergen Kulkompani (SNSK) who let us eat and sleep in Svea and helped us with logistics. Statoil provided additional money and the Norwegian Research Council through the Eastern European program made it possible for Sergey Vernyayev to study one year at UNIS, this is much appreciated.

REFERENCES

Blanchet, D. (1998). Ice loads from firstyear ice ridges and rubble fields. *Canadian Journal of Civil Eng.*, (25). 206-219.

Bonnemaire, B., Høyland, K. V., Liferov, P., and Moslet, P. (2003). An ice ridge in the Barents Sea, Part I: Morphology and physical parameters. In *Proc. of the 17th Int. Conf. on Port and Ocean Eng. under Arctic Conditions (POAC)*, NTNU, Trondheim, Norway, 2: pp. 559-568.

Frederking, R. and Timco, G. (1989). Compressive behaviour of Beaufort sea ice under vertical and horizontal loading. In *3rd Symp. on Offshore Mechanics and Arctic Eng. (OMAE)*, New Orelans, USA, 3: pp. 145-149.

Frederking, R. and Wright, B. (1982). Characteristics and stability of an ice rubble field Issugnak, February-March 1980. *Technical Report 134, National Research Centre of Canada*. p. 230-247.

Høyland, K. V., Kjestveit, G., Heinonen, J., and Määttänen, M. (2000). Loleif ridge experiments at Marjanimi; The size and strength of the consolidated layer. In *Proc. of the 15th Int. Symp. on Ice (IAHR)*, Gdansk, Poland, 1: pp. 45-52.

Høyland, K. V., Liferov, P., Moslet, P. O., Løset, S., and Bonnemaire, B. (2002). Medium scale modelling of ice ridge scouring of the sea bed, Part II: Consolidation and physical properties. In *Proc. of the 16th Int. Symp. on Ice (IAHR)*, Dunedin, New Zealand, 2: pp. 94-100.

Høyland, K. V., Valkonen, J., and Dettwiler, B. (2003). An ice ridge in the Barents Sea Part II: Laboratory investigations. In *Proc. of the 17th Int. Conf. on Port and Ocean Eng. under Arctic Conditions (POAC), NTNU*, Trondheim, Norway, 2: pp. 569-576.

Kendall, K. (1978). Complexity of compression failure. *Proc. of Roy Soc.*, (361). pp. 245-263.

Liferov, P. and Høyland, K. V. (2004). Ice ridge scouring experiments, part I: Experimental set up and

basic results. *Submitted to Cold Regions Science and Technology*.

Sinha, N. K. (1981). Rate sensitivity of compressive strength of columnar-grained ice. *Experimental Mechannics*, (26,6), pp. 209-218.

Sinha, N. K. and Frederking, R. M. (1979). Effect of test system stiffness on strength of ice. In *Proc. of the 5th Int. Conf. on Port and Ocean Eng. under Arctic Conditions (POAC),* Trondheim, Norway, Vol. 1, pp. 708-717.

Vatne, L. (2003). Interaction between a riser armour and ice rubble. Master's thesis, The University Courses in Svalbard, UNIS / Department of Marine Engineering, NTNU. 97 p.

Veitch, B., Lensu, M., Riska, K., Koslof, P., Keiley, P., and Kujala, P. (1991). Field observations of ridges in the northern Baltic Sea. In *Proc. of the 11th Int. Conf. on Port and Ocean Eng. under Arctic Conditions (POAC), St.Johns, Canada*, pp. 381-438.

17th International Symposium on Ice
Saint Petersburg, Russia, 21 - 25 June 2004
International Association of Hydraulic Engineering and Research

EXPERIMENTAL INVESTIGATION OF INTERACTION OF MOORED PLATFORMS WITH DRIFTING ICE FEATURES

Oleg N. Bezzubik[1], Alexander V. Bitsulya[1], Eugene B. Karulin[1], Marina M. Karulina[1], Nataliya Y. Klementyeva[1], Kirill E. Sazonov[1], Vladimir A. Chernetsov[2], Alexander V. Kulakov[2], Viacheslav V. Kupreev[2]

ABSTRACT

The paper presents results of experimental research on level and ridged ice interactions of two moored floating platforms tested at the Krylov Ice Model Tank. The platforms were designed for the Shtokmanovskoye deepwater gas condensate field. Both platforms cut the ice by downward breaking with their tapered sections whereas principal differences between the designs were in cone waterline diameters, underwater shapes and in the mooring systems. The tests were conducted both under inverted-motion conditions (Phase I) when rigidly fixed model were towed through the ice and under direct-motion conditions (Phase II) when the ice was pushed against models fixed with taut lines. The obtained results included global ice loads for both design options, kinematic and dynamic responses of the platform to loads inflicted by different ice features and the associated forces in mooring lines. The exercise was the first ever opportunity to compare model platform global ice loads as measured under inverted-motion conditions with indirect measurements of mooring-line forces under direct-motion conditions. The authors review differences in the ice behaviour of the two platform design options.

INTRODUCTION

Taut-moored platforms represent one of the most promising engineering solutions for the deeper part of freezing offshore waters. Crucial tasks in the design of such platforms are to estimate ice load levels and to predict the behaviour of the structures in drifting ice. These were the goals of model tests performed at the Krylov Institute Ice Model Tank for two design options of a production platform suggested by the Rubin Design Bureau for the Shtokmanovskoye deepwater gas condensate field in the Barents Sea.
Model tests conducted under this experimental research project consisted of two phases. At the first phase, the researchers used the so-called inverted-motion mode: the model was rigidly fixed to the towing carriage via a dynamometer and then towed through an immobile ice sheet.

[1] KSRI, 44, Moskovskoe shosse, St.Petersburg, Russia 196158. E-mail: e&m@jk3687.spb.edu
[2] CDB for Marine Engineering RUBIN, 90, Marata str., St. Petersburg, Russia 191119

The targets of those tests were:

to investigate major regularities of interactions between the subject platforms and different ice features;

to estimate global ice loads applied to the platforms;

to assess dimensions and depths of rubble ice accumulations in front of the platforms.

Under the second phase of the programme, the tests were conducted under direct-motion conditions: the platform was fixed to a solid immobile frame with the help of a model mooring system whereas the ice sheet was pushed against the model by the towing carriage. The aims of these experiments were:

to investigate interactions between taut-moored platforms with different ice features;

to find forces arising in the mooring lines;

to find kinematic motion parameters of the platforms as solid bodies;

to estimate global ice loads applied to taut-moored platforms;

to assess dimensions and depths of rubble ice accumulations in front of the platforms.

TEST OBJECTS & CHARACTERISTICS OF MODEL ICE FEATURES

For the purposes of these tests in the Ice Tank, the Krylov Institute has built models of two tension-leg platform (TLP) design options, which for the sake of convenience were refereed as TLP-SD (shallow draught) and TLP-DD (deep draught). Their mooring systems may be seen in Fig.1. The ice-cutting portion of either platform was designed as a cone intended to break the ice by downward bending. Principal parameters of the platform and their mooring systems are available in Table 1.

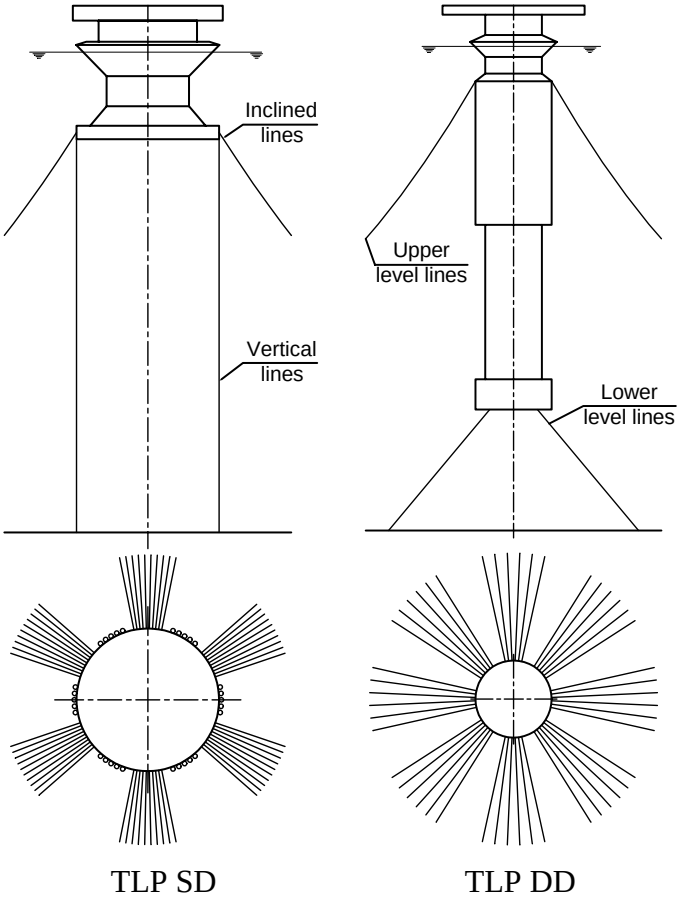

Fig. 1. The two design options of a production platform or the Shtokmanovskoye field

The model ice conditions represented 100-years events at the Shtokmanovskoye field: level ice of up to 1.5m in thickness and pressure ridges with 3m-thick consolidated layers, keel draughts of up to 18m. The relevant range of ice drift velocities was 0.3~1.2m/s.

Table 1. Main parameters of the platforms and mooring systems

Platform Geometry				
Platform option	TLP SD		TLP DD	
Diameter at waterline, m	86.1		52.0	
Diameter of submerged cylinder, m	55.0		38.0	
Cone angle, degree	46		45	
Draught, m	58.0		240.0	
Mooring System Geometry				
Lines	Inclined	Vertical	Upper level	Lower level
Number of lines (bundles of lines)	6	6	8	8
Length of lines, m	870.0	266.5	705.0	116.6
Distance between mooring point and vertical axis of platform, m	47.5	47.5	25.5	17.5
Applicate of mooring point (from waterline), m	53.5	53.5	40.0	240.0
Water depth (applicate of anchor point), m	320	320	320	320

ICE MODEL TANK & MODELS

The dimensions of the Krylov Institute Ice Model Tank (ice sheet) are as follows: 35m in length and 6m in width. The Basin is 1.8m deep. Besides, it has a deepwater zone (3.5m) of 8m length extending across the entire width of the tank.

Model scale ratios under different phases of the project had to be different because making a correct choice of the scale required considering a variety of factors, including the aims of particular tests. Therefore, the research project involved building four models: two 1:50 (for Phase I tests) and two 1:80 (for Phase II tests). The surface/ice dynamic friction coefficient was 0.15 in all cases.

The inverted-motion tests for global ice loads required geometric similarity only where one could expect any contact with ice features. Therefore, all other parts of the platforms, including the mooring systems, were discarded. Besides, there were not attempts to achieve any dynamic similarity between the models and the full-scale platforms.

The scale ratio of 1:80 chosen for the second phase of the tests was necessary for proper modelling of the water depth, ice characteristics, geometric, inertial and weight parameters of the platforms, and the mooring system parameters. In this case, it was necessary to consider the geometric dimensions of the Model Tank on one hand and the capabilities of the test equipment on the other one.

Since the limited width of the Tank (6m) would never allow directly modelling the involved three-dimensional mooring systems with their long lines, it was necessary to formulate dedicated methodological approaches to research on dynamics and kinematics of moored structures based on physically justified assumptions and numerical simulations of equivalent mooring systems.

The major assumptions made in the development of methodological approaches associated with mooring system schematic modelling were as follows:

- each bundle of mooring lines (Fig. 1) was substituted with a single equivalent line that represented the entire bundle in terms of the stiffness parameters;

- equivalent lines of the lower levels (for TLP DD) and of vertical lines (for TLP SD) of the mooring system were represented by model lines observing their true layout geometry and stiffness characteristics (that was possible thanks to the availability of the deepwater zone);

- equivalent lines of the upper levels (for TLP DD) and of inclined lines (for TLP SD) of the mooring system were represented by truncated model lines with stiffness characteristics specified for the full-length lines.

Prior to the physical modelling, the truncated mooring lines had to be simulated numerically based on a tentative set of elastic details (wire cables, springs) that could physically model the necessary stiffness. The final choice of the elastic detail was made with the help of numerical simulation optimisation methods. The priority characteristics of individual lines and entire mooring systems were those that required the best possible modelling accuracy in the view of the model test goals.

Under this project, it was decided to model two characteristics of the mooring system: the restoring capability of the system and the total tension at the mooring point. Modelling the *restoring capability* ensures specified horizontal-plane motions of the platform and enables to find the natural frequency of the moored platform based on the test data. Modelling the *total tension at the mooring point* makes it possible to get a valid estimation of forces arising in the mooring line due to mooring point excursions.

INVERTED-MOTION TESTS

The 1:50 model platforms were rigidly fixed to the towing carriage via a dynamometer and pulled through immobile ice sheets. The involved six-component dynamometer with an analogue-to-digital converter enabled to record all six components of ice load. Besides, the measurements included the speed of the carriage.

Dimensions of the underwater rubble ice accumulations were estimated based on video records taped during the tests. To make this task easier, there were marks placed on the underwater portion of the model.

Physical and mechanical properties of the model ice sheets (level or ridged) were measured directly before the tests.

A matrix describing the performed tests is available in Table 2. All the parameters are referred to full-scale sizes.

The results of the inverted-motion tests served to construct regression models for numerical evaluations of all components of the global ice loads as functions of the level ice thickness, strength and drift velocity (Alexeev et al., 1998). The regression models enabled to correct test results for the inevitable deviations of the achieved level ice and ridge consolidated layer properties from values, which were specified in accordance with the modelling laws. The same models helped to perform full-scale extrapolations.

Table 4 offers extrapolated full-scale estimates of the maximum global ice load for the tested platform design options in ice ridges of various geometric parameters.

Table 2. Tests matrix in inverted-motion mode

Sheet #	TLP option	Ice feature	Thickness of level ice or of consolidated layer of ridge, m	Ridge keel depth/width, m	Ice drift velocity, m/s
1	SD	level ice	1.2	-	0.3; 1.0: 1.2
2	SD	level ice	0.9	-	0.3; 1.0: 1.2
3	SD	level ice	1.3	-	0.3; 1.0: 1.2
4	SD	ridge	3.2	16.7 / 87.5	0.3
5	SD	ridge	4.0	18.2 / 95.0	1.0
6	SD	ridge	4.0	18.0 / 150.0	1.2
7	DD	level ice	1.7	-	0.3; 0.7: 1.2
8	DD	level ice	1.0	-	0.3; 0.7: 1.1
9	DD	level ice	1.5	-	0.3; 0.7: 1.1
10	DD	ridge	3.5	18.2 / 87.5	1.1
11	DD	ridge	4.6	18.2 / 150.0	1.2

DIRECT-MOTION TESTS

These tests were performed with the 1:80 models. The test set-up has required designing and fabricating a welded metallic frame that was placed on the basin floor. The frame served to attach pulleys of the equivalent mooring system. The necessary heights of the pulleys above the basin floor were found by computations. The inclined taut lines were calibrated and then passed through the pulleys leaving one end of each line free for running it up out of the water. These free ends served to apply the required pre-tension. The other ends of each line went via dynamometers to the mooring points of the model platform. The necessary pre-tension of the TLP-DD vertical lines was achieved with the help of purpose-designed fastening system.

Measurement performed prior to testing provided data on the stiffness of the moored model. Fig. 2 shows full-scale horizontal stiffness curves of the modelled platforms as measured in the Model Tank and as computed taking into account the parameters of the actual taut mooring lines.

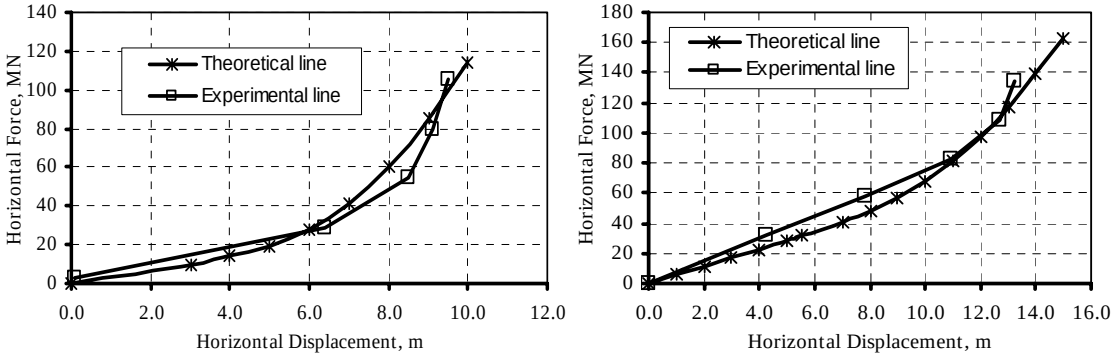

TLP SD TLP DD

Fig. 2. Full-scale horizontal stiffness curves of the modelled platforms: measured in the Model Tank and computed taking into account the stiffness of the actual mooring lines

The towing carriage pushed the ice against the model with the help of a bulldozer blade. The measurements included the carriage speed, data from mooring-line force sensors, from gyroscopes, from devices that enabled to register motions of chosen points on the

model along three mutually perpendicular axes, as well as platform heel, trim and yaw angles.

A matrix of Phase II tests is available in Table 3.

The maximum measured mooring-line tensions due to platform interactions with ice ridges may be seen in Fig. 3.

Table 3. Tests matrix in direct-motion mode

Sheet #	TLP option	Ice feature	Thickness of level ice or of consolidated layer of ridge, m	Ridge keel depth/width, m	Ice drift velocity, m/s
12	SD	level ice	1.5	-	0.3; 0.7; 1.1
13	SD	ridge	2.7	20.0 / 129.0	0.3
14	SD	ridge	3.0	19.2 / 120.0	1.2
15	DD	ridge	2.9	17.6 / 120.0	0.3
16	DD	ridge	2.9	18.0 / 120.0	1.2
17	DD without lower level line	ridge	2.7	17.2 / 100.0	1.2

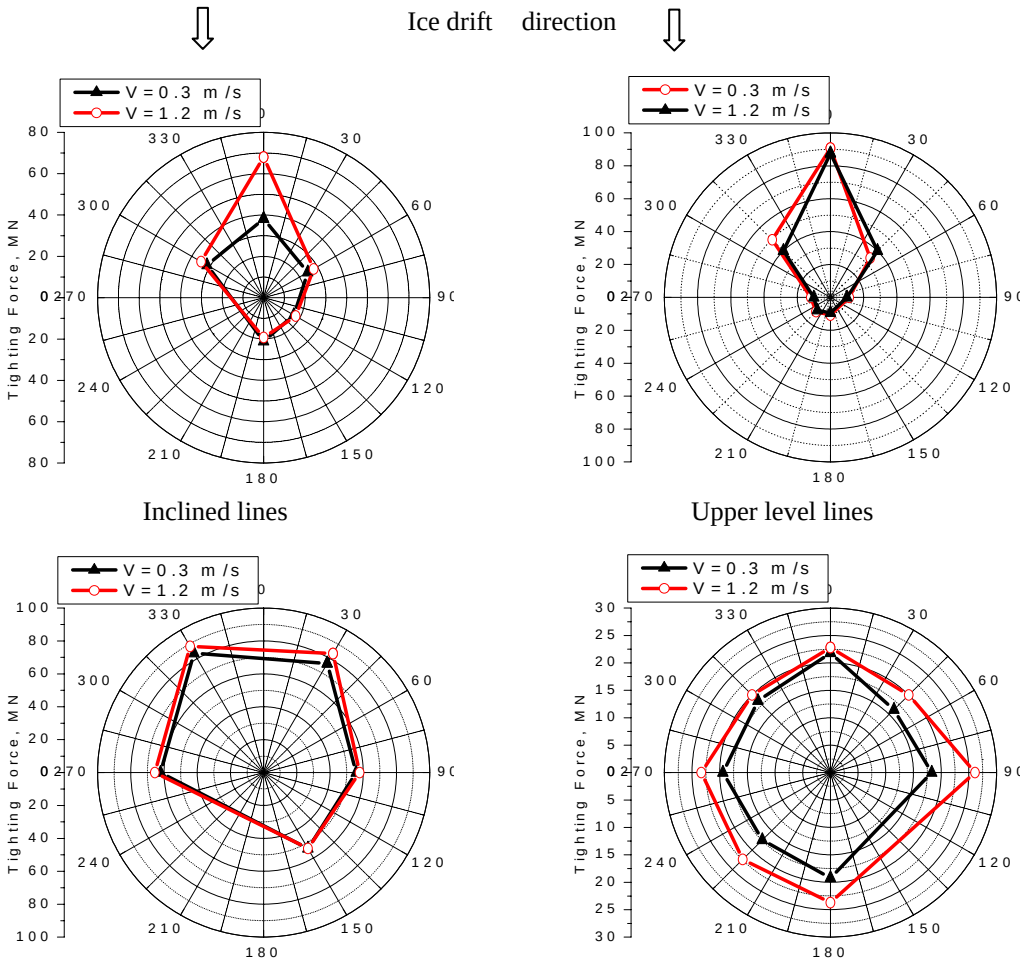

Fig. 3. Maximum measured mooring-line tensions due to platform interactions with ice ridges (full-scale size)

One of the test scenarios chosen for the deep-draught platform was testing without the lower level lines. The initial draught was in that case maintained by placing additional weights in the model. Visual observations of model/ice interactions demonstrated that without the lower level mooring lines the behaviour of the platform became more dynamic: both the linear excursions and the heel and trim angles were significantly higher than before.

The mathematical model of taut-moored platform motions in ice that was developed in association with the same project (Karulin et al., 2004) enabled to reconstruct global ice loads from the measured kinematic parameters of model motions and mooring-line tensions. Full-scale extrapolations of the results obtained at this phase of the project are available in Table 4.

Table 4. Assessments of ice loads onto the platforms obtained at the tests (full-scale size)

Sheet #	TLP option	Longitudinal force, MN	Transversal force, MN	Vertical force, MN	Trim moment, MNm	Heeling moment, MNm	Yawing moment, MNm
Measured valued (inverted-motion mode)							
4	SD	68	13	53	1250	500	50
5	SD	89	8	56	1500	344	103
6	SD	137	31	81	2188	875	213
10	DD	71	24	24	250	450	49
11	DD	74	11	25	294	188	47
Recovered valued (direct-motion mode)							
13	SD	70	11	146	1433	1638	1065
14	SD	113	12	138	1516	2375	860
15	DD	99	11	60	2334	1352	377
16	DD	138	13	70	3891	1556	307
17	DD without lower level lines	97	25	43	4751	1229	225

TEST RESULTS

(1) The inverted-motion model tests in level ice have demonstrated quite good qualitative (ice cracking and breaking patterns) and quantitative (maximum ice loads) agreement with the well-known Nevel's (1992) theoretical model of level ice interactions with conical structures.

In the direct-motion tests, the pattern of SD platform interactions with level ice was affected by the motions of the model that enjoyed six degrees of freedom. Full-scale extrapolations of the reconstructed global ice forces are shown in Fig. 4. The same Figures contain the results of global ice forces predictions based on towed test results and on calculations using the constructed regression models.

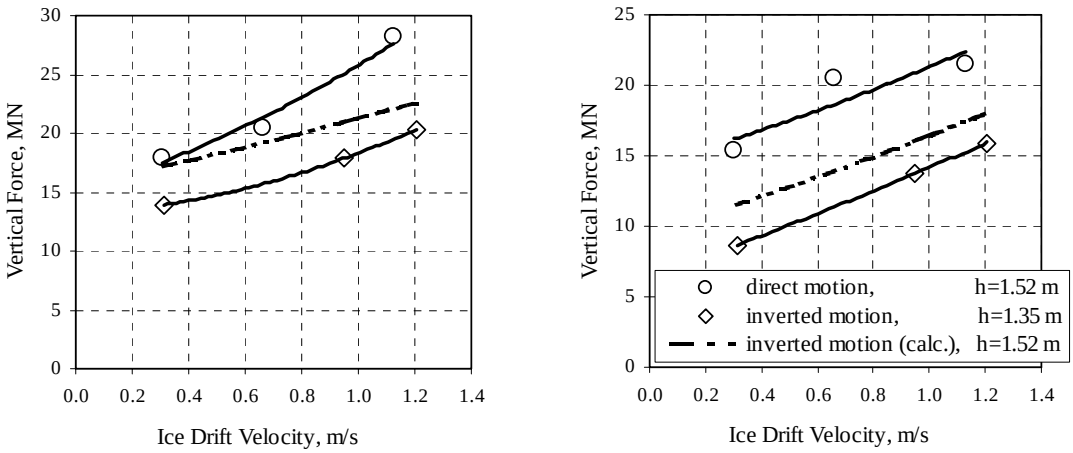

Fig. 4. Global ice forces onto the TLP SD platform interacting with level ice vs. ice drift velocity

(2) Though the involved ridges were approximately similar in terms of their geometric parameters (width and keel depth extrapolated to full-scale sizes), it is rather difficult to compare the ice loads (see Table 4) because of uncertainties in estimations of the ridge strength parameters, which are important for the global ice load.

Nevertheless, one may see that the levels of ridge-inflicted horizontal forces are in a rather good accord considering ridge geometry differences. At the same time, the vertical loads applied to the platform under the direct-motion scenario appear to exceed those measured during the towing tests. There are at least two factors that may explain these observations:

- judging by underwater videotapes, rubble ice accumulations in front of the platforms reached deeper under the direct-motion scenario than during the towing tests because the formed set-up did not produced relative fluid motions at the underwater portion of the model whereas in the latter case, those flows eroded some of the rubble pile-down;

- unlike the rigidly fixed models in the towing tests, the moored platforms were free to exercise vertical motions. This causes a noticeable increase in the vertical force: the ridge is punched along the vertical axis and that is associated with a peak of the vertical force. Actually, this is the same phenomenon that we have in the traditional punch test. This effect was not observed in the inverted-motion towing tests.

(3) The two tested platform design options have demonstrated definitely different behaviour patterns under ice loading. The TLP-SD model with its taut vertical lines and the centre of gravity close to the effective waterline responded to ice loading by plane-parallel motions nearly without any trimming (the highest logged trim angle was 0.65°). At the same time, the ice made the model to exercise torsional motions about the vertical axis. The highest measured yaw angle was 3.5°. Horizontal excursions of the platform at the waterline level reached 11.0m.

The TLP-DD model, which had its centre of gravity much deeper than the effective waterline and was rather stiffly fixed at the keel point with the lower mooring lines, demonstrated noticeable trim angles of up to 2.5°. At the same time, keel point excursions

never exceeded 1.7m whereas the maximum offset at the waterline level amounted to 9.8m.

TLP-DD tests without the lower level lines have produced the following results: maximum offsets at the waterline level were 11.1m, maximum offsets of the keel point were 18.0m and the maximum trim angles reached 7°.

PRINCIPAL CONCLUSIONS

Experiments carried out at the Ice Model Tank have demonstrated the significance of dynamic effects involved in offshore platform interactions with different ice features. Three-dimensional motions of the platform introduce changes in both the interaction pattern and the quantitative estimates of global ice load levels as compared to rigidly fixed models.

REFERENCES

Alexeev, Y., Karulina, M., Karulin, E. and Sutulo, S. A method for predicting ice loads on structures based on model test data. In *Proc. IAHR Ice Symposium*, Potsdam, New York (1998) 497-502.

Karulin, E., Karulina, M., Sazonov, K. and Chernetsov, V. Mathematical model for motion of moored platform interacting with ice. In *Proc. IAHR Ice Symposium*, St. Petersburg, Russia (2004) (Paper on this Symposium)

Nevel, D. Ice Forces on Cones from Floes. In *Proc. IAHR Ice Symposium*, Banff, Alberta, (1992).

17th International Symposium on Ice
Saint Petersburg, Russia, 21 - 25 June 2004
International Association of Hydraulic Engineering and Research

MATHEMATICAL MODEL FOR MOTION OF MOORED PLATFORM INTERACTING WITH ICE

Eugene B. Karulin[1], Marina M. Karulina[1], Kirill E. Sazonov[1], Vladimir A. Chernetsov[2]

ABSTRACT

A mathematical model for motion of moored platform interacting with drifting ice feature was developed using equations of spatial motion of solid body (Euler equations). Besides ice loads acting on the platform other factors of external action that are determining platform's behaviour were considered, such as: hydrostatic and hydrodynamic forces and moments, tightening forces in the mooring lines and inertial loads. The elaborated model was applied to reconstruction ice loads acting onto the moored platform model from drifting ice feature using measured values of tightening forces in the mooring lines and kinematic and dynamic parameters of the platform motion. The model tests were carried out in the Ice Tank at the KSRI. The influence of spatial motion of the moored platform on values of ice load components was considered in the paper. It was shown that the mathematical model might be used for assessment of ice loads on moored platforms both in model and field tests.

INTRODUCTION

Designing of ice-resisting moored structures that are intended for offshore exploitation in ice-covered seas, requires comprehensive study of behavior of those objects under ice conditions. Analysis of the moored platform dynamics may be performed both by analytical method and experimentally with the help of model tests in Ice Model Tank. Both of these ways are connected with considerable difficulties. Thus, for analytical study it is necessary to know the laws of variations of external actions, particularly, ice forces, onto the structure, as well as the mooring lines reactions. These loads are associated in a complicated manner with the platform displacements in all of six degrees of freedom. As to experiments in Ice Tank, the model tests aimed at study of the moored structure dynamics differ considerably from simulation of static or quasi-static processes that take place during interaction of fixed platform models with ice features. In the latter case a simulation of geometrical parameters both of ice features and structures, as well as mechanical properties of ice is obeyed. However, for simulation of

[1] KSRI, 44, Moskovskoe shosse, St.Petersburg, Russia 196158. E-mail: e&m@jk3687.spb.edu
[2] CDB for Marine Engineering RUBIN, 90, Marata str., St. Petersburg, Russia 191119

a moored platform dynamic behavior it is necessary to ensure a similarity of the masses, dimensions and inertial parameters both for the whole system and for its structural members (platform and mooring lines), and also to ensure a similarity of rigidity for each mooring line. Such complex experiment cannot be realised because of technical limitations.

The rational combination of analytical methods and model experiment allows to investigate more closely compound behavior of moored structure interacting with ice. The mathematical model of moored platform dynamics described below was designed with reference to the model tests of the particular moored structures, and it was used for reconstruction global ice loads on them, i.e. for the inverse problem solution.

As the mathematical model is built on the most common differential equations of spatial motion of a solid, it may be adapted for other buoyant objects.

PROBLEM STATEMENT. COORDINATE SYSTEM

A motion of buoyant moored object under effect of drifting ice features is investigated in the problem. It is assumed that wind, current and wave are not acting onto the structure. The later factor is eliminated automatically by a presence of level ice.

Two rectangular coordinate systems are used in this problem: fixed $O\xi\eta\zeta$ is used for definition of platform displacement in all six degrees of freedom relative to the initial position, and moving coordinate system $O'xyz$ rigidly bound with the platform. The horizontal plane $O\xi\eta$ is placed at a level of the waterline, the axis $O\xi$ is directed towards the opposite vector of ice drift, the axis $O\zeta$ is directed vertically downwards, and the direction of the axis $O\eta$ is determined from a condition of formation of the right coordinate system. The both coordinate systems coincide at the initial time in equilibrium condition. In ship's terminology, the plane $O'xz$ of the bound coordinate system coincides with the center line of the platform, the axis $O'x$ is directed to the platform bow, and axis $O'y$ is directed to starboard. The axis $O'z$ passes through center of gravity of the platform.

At any point of time the platform position characterized by six coordinates: by linear coordinates of the pole, point O', in fixed coordinate system $(\xi_{O'}, \eta_{O'}, \zeta_{O'})$, and by the three ship angles (Euler angles), ψ, θ, φ. Angles ψ, θ and φ determine yaw of the platform, its trim difference roll accordingly.

The transition from bound coordinate system to fixed one may be carried out using transition matrix Π:

$$\begin{pmatrix} \xi \\ \eta \\ \zeta \end{pmatrix} = \begin{pmatrix} \xi_{O'} \\ \eta_{O'} \\ \zeta_{O'} \end{pmatrix} + \Pi \begin{pmatrix} x \\ y \\ z \end{pmatrix}. \qquad (1)$$

The motion of the moored structure as solid body under drifting ice action may be described by the Euler equations, that have the following vectorial form in the coordinate system rigidly bound with the body:

$$m[\dot{\vec{V}} + \vec{\Omega} \times \vec{V} + \dot{\vec{\Omega}} \times \vec{r}_G + \vec{\Omega} \times (\vec{\Omega} \times \vec{r}_G)] = \vec{F};$$

$$\Theta^0 \cdot \dot{\vec{\Omega}} + \vec{\Omega} \times \Theta^0 \cdot \vec{\Omega} + m\vec{r}_G \times (\dot{\vec{V}} + \vec{\Omega} \times \vec{V}) = \vec{M}, \quad (2)$$

where: m is the body mass, r_G is radius-vector of center of gravity of the platform in bound coordinate system,

$\Theta^0 = \begin{pmatrix} I_{xx} & -I_{xy} & -I_{xz} \\ -I_{yx} & I_{yy} & -I_{yz} \\ -I_{zx} & -I_{zy} & I_{zz} \end{pmatrix}$ is tensor of inertia of the platform as solid, $\vec{V}$ is linear velocity vector of the point O', the pole of bound coordinate system, $\vec{\Omega}$ is angular velocity vector of the pole of bound coordinate system, $\vec{F}$ is resultant vector of external forces, $\vec{M}$ is resultant moment of external forces relative to the pole of bound coordinate system.

The resultant vectors of external force and moment acting onto the platform are determined by the applicable vectorial sums:

$$\vec{F} = \vec{F}_{HS} + \vec{F}_{HD} + \vec{F}_{ML} + \vec{F}_{ICE};$$

$$\vec{M} = \vec{M}_{HS} + \vec{M}_{HD} + \vec{M}_{ML} + \vec{M}_{ICE}, \quad (3)$$

where: $\vec{F}_{HS}, \vec{M}_{HS}$ are resultant vectors of hydrostatic forces and moments accordingly acting onto the platform, $\vec{F}_{HD}, \vec{M}_{HD}$ are resultant vectors of hydrodynamic forces and moments accordingly acting onto the platform, $\vec{F}_{ML}, \vec{M}_{ML}$ are resultant vectors of the mooring lines forces and of moments of these forces relative to the pole of bound coordinate system, $\vec{F}_{ICE}, \vec{M}_{ICE}$ are vectors of total ice force and of ice moment accordingly acting onto the platform from the drifting ice feature.

EXTERNAL LOADS ONTO THE PLATFORM

The external actions onto the platform have a different nature and may be both time-constant loads (as gravity force) and time-variable ones that are dependent on displacement of the platform and on its position in the time point, as well as on kinematic parameters of the motion.

The hydrostatic forces and moments are determined by balance of constant gravity force and buoyant force that is calculated on parameters of instantaneous trim of the platform using its geometry. The platform trim is defined by six coordinates: by linear coordinates of the pole of bound coordinate system in the fixed system and by three ship angles.

The hydrodynamic loads represent forces and moments of hydrodynamic resistance (damping) of the moored system both to linear displacement and to rotation of the structure around principal axes. As a rule, for definition of resistance forces and moments one should use dimensionless factors permitting to present hydrodynamic loads as

$$R_{HD} = c_R \cdot f(\dot{X}, A, L^n), \quad (4)$$

where: R_{HD} is one of the projections of hydrodynamic resistance force $\vec{F}_{HD}$ or of moment $\vec{M}_{HD}$ on the axes of bound coordinate system, $\dot{X}$ is either characteristic linear velocity of center of gravity of the platform (in case of force definition) or angular one, A is characteristic area, and L is characteristic linear size. In case of force calculation the exponent $n = 0$, and in case of moment definition $n = 1$. The dimensionless factors c_R are determined experimentally in hydrodynamic laboratories.

The mooring lines forces can be calculated using quasistatic method. Their quantities depend on the mooring lines rigidity as well as on instantaneous location of the mooring points. The coordinates of mooring points in fixed system are determined on their known coordinates in bound system and on coordinates of the pole of bound coordinate system. The resultant vector of mooring lines forces in bound coordinate system is defined by the sum of projections of each mooring line force on the axes of bound coordinate system. The resultant vector of moment of these forces is the sum of vector products of the radius-vectors of mooring points in bound coordinate system $\vec{r}^{n}$ and the corresponding vectors of mooring line forces $\vec{F}^{n}_{ML}$:

$$\vec{M}_{ML} = \sum_{n=1}^{k} \vec{M}^{n}_{ML} = \sum_{n=1}^{k} \vec{r}^{n} \times \vec{F}^{n}_{ML}, \qquad (5)$$

where: k is total number of mooring points (mooring lines), n is order number of mooring line.

The mathematical formulation of external ice loads onto the structure is considerable complex even in case of fixed gravitational platform due to random nature of ice failure and to some uncertainties in assignment of mechanical properties of ice features. The dynamic problems of interaction of moored structures with drifting ice are studied even less. The variation of instantaneous interaction rate of the platform with ice and changing of its spatial orientation may result in modification of ice failure mode and, consequently, in change of quantity and frequency of the maximum ice loads. The quasistatic approach for calculation of ice loads is one of the ways for solution this problem (Bolshev and Frolov, 2001).

EXAMPLE OF APPLICATION OF THE MATHEMATICAL MODEL

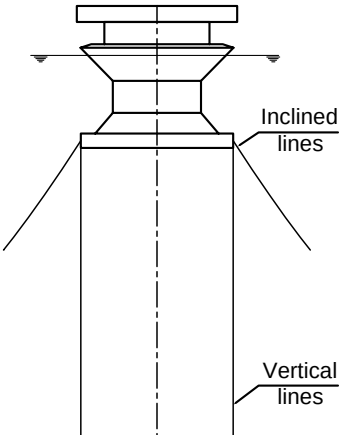

Fig. 1. Moored platform model

The mathematical model of dynamics of moored structure described above was applied for inverse problem solution, namely, for reconstruction ice loads on moored platform model through measured values of tightening forces of mooring lines and kinematic parameters of motion of the model at simulation the interaction of the platform with drifting ice features in the Ice Model Tank of KSRI.

The tested model represented a body of revolution around vertical axis (Fig. 1). Icebreaking part of the model was manufactured as a down-breaking cone with 1.08m diameter at waterline and 46° cone angle.

More detailed description of the experiments conducted in Ice Tank of KSRI as well as experimental technique used is given in Bezzubik et al. (2004).

The model motion as applied to the experimental conditions may be described by equations obtained from the system above (2). In view of added masses of water and symmetry of the platform the equations have the following scalar form:

$$
\begin{aligned}
&(m+\mu_{11})\dot{u}+(mz_g+\mu_{15})\dot{q}-mvr+mz_g pr+mwq=X\ ;\\
&(m+\mu_{22})\dot{v}-(mz_g+\mu_{24})\dot{p}+mur-mwp+mz_g qr=Y\ ;\\
&(m+\mu_{33})\dot{w}-muq-mz_g q^2+mvp-mz_g p^2=Z\ ;\\
&(I_{xx}+\mu_{44})\dot{p}-(mz_g-\mu_{24})\dot{v}+mz_g wp+(I_{zz}-I_{yy})qr+mz_g ur=K\ ;\\
&(I_{yy}+\mu_{55})\dot{q}+(mz_g+\mu_{15})\dot{u}+mz_g wq+(I_{xx}-I_{zz})pr+mz_g vr=M\ ;\\
&I_{zz}\dot{r}+(I_{yy}-I_{xx})pq=N\ ,
\end{aligned}
\qquad (6)
$$

where: $\mu_{11},\mu_{22},\mu_{33}$ are added masses of water, μ_{44},μ_{55} are inertia moments and μ_{15},μ_{24} are statical moments of the added masses of water, u,v,w and p,q,r are projection of vectors of linear $\vec{V}$ and angular $\vec{\Omega}$ velocities of the pole accordingly on the axes of bound coordinate system, z_g is applicate of the model center of gravity in bound coordinate system, X,Y,Z and K,M,N are projections of the resultant vectors of external force $\vec{F}$ and moment $\vec{M}$ on the axes of bound coordinate system.

The external loadings on the platform model during experiment were caused by combined action of hydrostatic, hydrodynamic, ice loads and by reactions of the mooring lines. Therefore, for reconstruction global ice loads on the model using the set of equations (6), it is necessary to know all the parameters that are included into the left part of the equations (namely, mass-inertia characteristics of the model and kinematic parameters of the motion) and also the remaining components of the external loading.

Mass-inertia characteristics of the model including the quantities of the added masses and moments of water were obtained with usage of the special equipment prior to the carrying out experimental researches in the Ice Tank.

During the experiments in the Ice Tank the measurements of linear and angular displacements of a fixed point of the model were performed. These measured values allowed to restore a trim of the model at any time-point and to determine a time-history position of the pole of bound coordinate system. Projections of linear and angular velocities and accelerations of the pole included in the left part of the equations (6) were calculated using numerical differentiation of the corresponding records of linear and angular displacements of the pole.

The projections of both hydrostatic forces and moments on the axes of bound coordinate system were determined using the formulas below (under condition of a smallness of the angles φ and θ):

$$
\begin{aligned}
X_{HS} &= (\rho_w g V_0 - mg)\sin\theta;\\
Y_{HS} &= (mg - \rho_w g V_0)\cos\theta\sin\varphi;\\
Z_{HS} &= (mg - \rho_w g V_0)\cos\theta\cos\varphi - \rho_w g A_{WL}\Delta h;\\
K_{HS} &= -mgh_0\varphi;\\
M_{HS} &= -mgh_0\theta;\\
N_{HS} &= 0,
\end{aligned}
\qquad (7)
$$

where: ρ_w is water density, g is acceleration of gravity, V_0 is volume of displacement of the model in initial state, h_0 is initial metacentric height, A_{WL} is sectional area of the model at waterline level in initial state, Δh is vertical displacement of the pole.

The forces and moments of hydrodynamic resistance acting onto the model when its spatial moving were computed using the values of corresponding dimensionless factors of resistance to oscillations of the object in still open water. Those factors were obtained at tests of the moored structure model in the Seakeeping Tank of KSRI.

The tightening forces acting onto the model from the mooring lines were determined by direct measurements of those values in the experiment. When calculating the moments of the tightening relative to the pole, it was supposed that the forces were directed along the straight line connecting the corresponding mooring and anchor points. The time-histories of two most loaded mooring lines during interaction with ridge are presented on Fig. 2.

Thus, it was possible to restore values of global ice loads onto the platform in bound coordinate system using the set of equations (6) and having following input information:

- the mass-inertia characteristics of the model (including the added masses of water and added both inertia and statical moments);
- the geometry of the moored system in an initial state (including coordinate of the center of gravity, coordinates of the anchor and mooring points and of a fixed point on the platform model where the linear and angular displacement were measured);
- components of the damping matrix (of hydrodynamic resistance factors) of the moored system;
- time-history records of three coordinates and ship angles (roll, trim, yaw) of the fixed point on the model;
- time-history records of tightening forces of the mooring lines.
-

Components of the global ice load in fixed coordinate system were calculated using the transition matrix Π.

The reconstructed ice loads onto the platform model when interacting with ridge are presented in Fig. 3. Moreover, these diagrams contain time-histories, which were obtained during towing tests of the fixed platform model interacting with ridge (Bezzubik et al., 2004). The two considered models, those are the moored model and the fixed one, were manufactured in various scales – 1/80 and1/50 accordingly. Due to that the ridge geometry was reduced to the one scale (1/80) for correct comparison of the loads. The ridge geometry is given in Table 1.

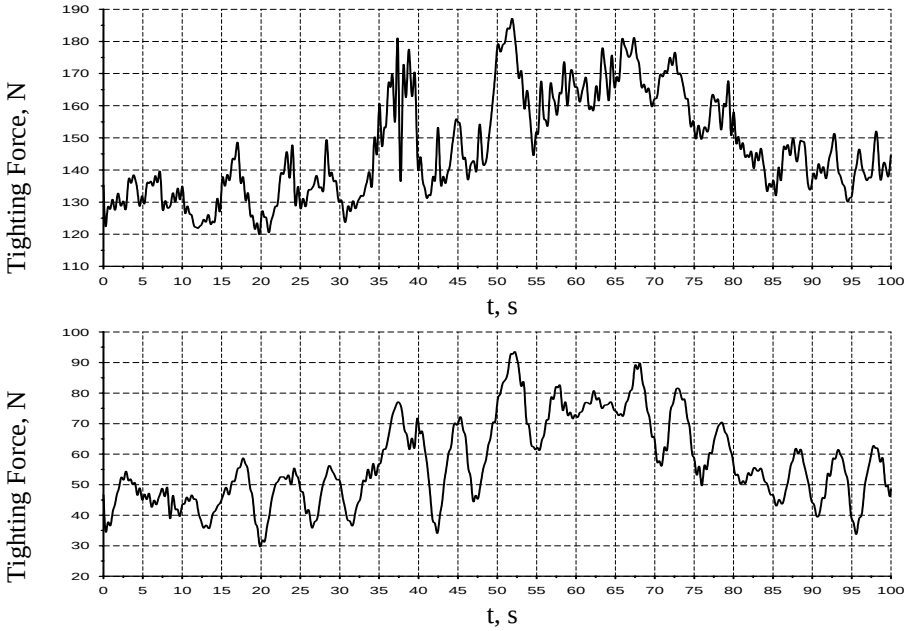

Fig. 2. Time-histories of two most loaded mooring lines during interaction with ridge

Table 1. Ridge geometries for comparison of ice loads

Model type	Consolidated layer thickness, m	Keel depth, m	Keel width, m	Ice drift velocity, m/s
Moored	0.034	0.25	1.61	0.034
Fixed	0.040	0.21	1.10	0.034

CONCLUSIONS

The presented mathematical model allows to solve the inverse problem of moored platform dynamics when interacting with ice feature, namely, to assess the ice loads using the measured values of tightening forces in the mooring lines and the measured kinemaric parameters of motion of the moored platform. The approach described above may be used for monitoring of ice loads onto the full-scale moored structures of similar type.

According to the comparison of the ice loads exerting onto the fixed and moored platforms from the similar ridges, the horizontal forces (both the longitudinal force and transverse one) coincide rather well. At the same time, the essential discrepancy in quantities of other components of the ice load (vertical force, heeling and yawing moments). In authors' opinion, this discrepancy is due to spatial motion of the moored platform, first of all, to the vertical motion and yaw.

The moored structure has effect on frequency of the ice loads as a low-frequency filter. The reconstructed time-histories of ice loads onto the moored model appear more smoothed than the initial time dependences of the ice loads onto the fixed platform model.

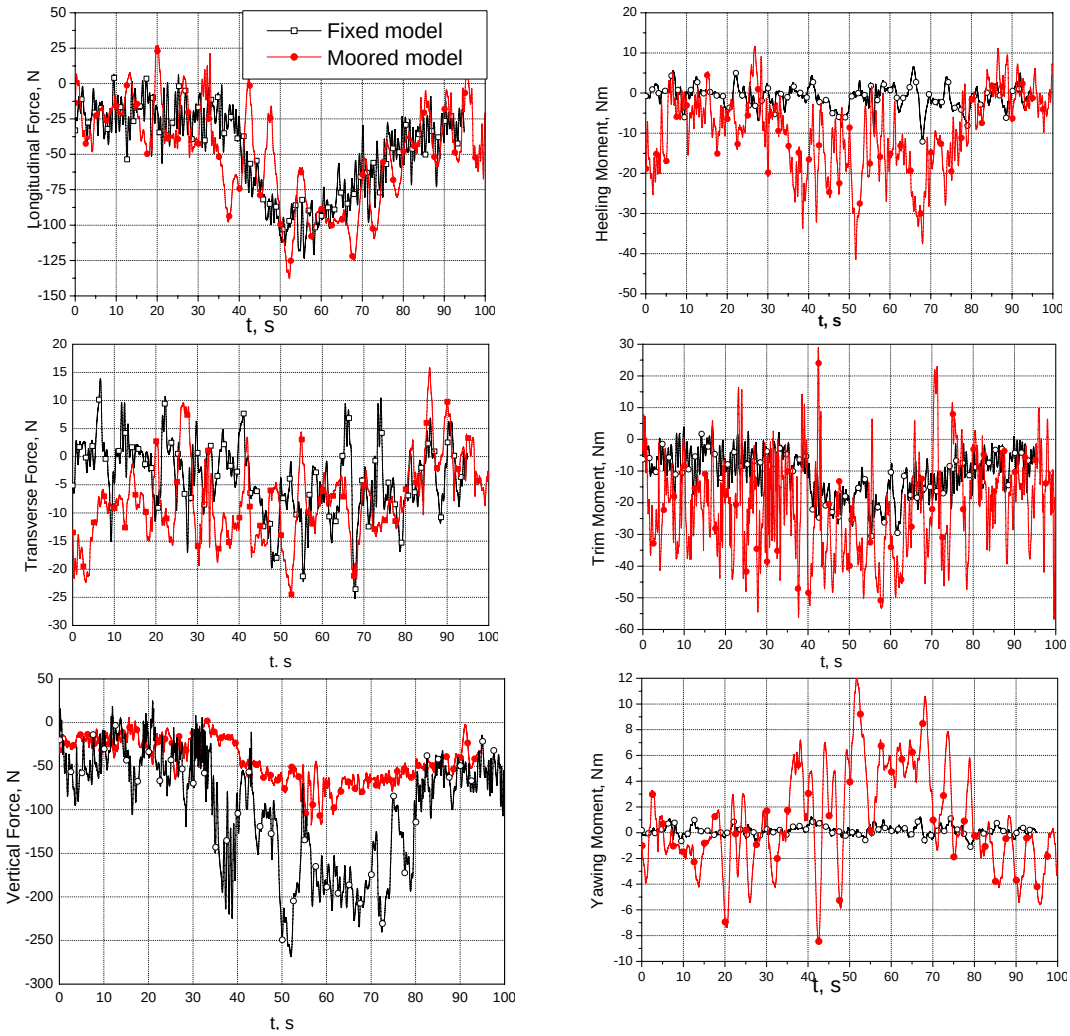

Fig. 3. Time-histories of ice loads onto the platform model interacting with modeled ridge as reconstructed values for the moored model and as measured values for fixed one

REFERENCES

Bezzubik, O., Bitsulya, A., Karulin, E., Karulina, M., Klementyeva, N., Sazonov, K., Chernetsov, V., Kulakov, A. and Kupreev, V. Experimental investigation of interaction of moored platforms with drifting ice features. In *Proc. IAHR Ice Symposium*, St. Petersburg, Russia (2004) (Paper on this Symposium)

Bolshev, A. and Frolov, S. Math modeling of floating anchored structures behavior for Russian Offshore. In *Proc. 5th International Conference RAO-01*, St. Petersburg, Russia (2001) 416-423.

17th International Symposium on Ice
Saint Petersburg, Russia, 21 - 25 June 2004
International Association of Hydraulic Engineering and Research

PRELIMINARY RESULTS OF ICE INDENTATION TEST USING CONSOLIDATED LAYER MODEL OF FRESHWATER ICE

Takahiro Takeuchi[1], Mikio Sasaki[1],Kazuo Miura[1], Sinji Kioka[2] and Hiroshi Saeki[3]

ABSTRACT

Ice load acting on hydraulic structures in ice-covered areas is of great importance for their design. Deformed ice such as an ice ridge with a consolidated layer of ice may impart a larger load because of its larger thickness. However, ice indentation tests have mainly been conducted using level sheet ice (un-deformed ice). To make a consolidated layer model as a test sheet in a cold room, ice blocks of variable size were made and mixed with water close to its freezing temperature. The ice sheet was kept to a planed thickness (h), and used for an indentation test. Indentation velocity (V) and cubic ice block size (a) were varied as parameters, and their effects on the ice load were investigated by comparing the results with those of un-deformed ice. This paper examines the effects of (a/h) and (V/h) on ice load and ice failure pattern, and compares them with those of a multi-crack model under a compressive loading presented by Coosley (1984).

INTRODUCTION

Deformed ice such as ice ridges and hummocked ice constitutes a menace to offshore structures in ice covered sea areas. Although such ice has large thickness, there is little information available for determining loads imparted by deformed ice. An ice ridge consists of a sail, a keel, and a consolidated part. The consolidated part is considered to be stronger than the other parts, and ice blocks and sea water refreeze after shear and compressive deformation. The ridge building mechanism is discussed by Parameter and Coon (1972). It is reported by Timco and Goodrich (1988) that the thickness of the consolidated layer is about twice that of the surrounding level ice sheet. From long-term field observations on hummocked ice in the northern Sakhalin offshore, Truskov et al. (1993) and Beketsky et al. (1997) report design parameters based on its dimensions, strength and so on. Kioka et. al. (2000) report on the physical properties of the consolidated layer using model ice made in a cold room. Its compressive strength is

[1] Hachinohe Institute of Tech., Japan
[2] Civil Engineering Research Institute of Hokkaido
[3] Hokkaido University

found to be lightly smaller than that of the surrounding level ice sheet. In this study, an indentation test is conducted to investigate the ice load on a model structure using a consolidated layer model made in a cold room. The effects on ice load of ice block size (a), indentation velocity (V), and failure mode of model ice are examined and the results are compared to those for level sheet ice.

TESTS

The test ice sheet specimen of the consolidated layer was made by referring to the method by Kioka et al. (2000). In this study, however, we used freshwater ice instead of sea water ice because its transparency enabled us to observe the ice behaviour during an indentation. First, freshwater was put into a mesh-type frame having cubic spaces with bore-holes at its bottom, and after the water was frozen enough a lot of cubic ice blocks were made. Several frames of different sizes were used. Second, the freshwater was kept in a tank until the temperature reached freezing point. Third, the ice blocks were put into a different tank (1000mm*900mm*450mm) with insulated bottom and sides, and also freshwater close to the freezing point was put in to a planed depth of the tank. Fourth, a test ice sheet was taken out of the tank after an intermixed specimen was sufficiently consolidated. It was moved to the indentation device shown in Fig.1, and fixed on three sides. Fifth, to measure the ice temperature in the thickness direction, a k-type thermocouple was embedded into the ice sheet. These steps were repeated depending on the planned test conditions. Ice load and displacement with time were measured. A plane pressure panel (Fig.2) was attached to the model structure and imparted ice pressure distribution with time. A video was also used for analysis of ice failure during the indentation test. The test conditions are listed in Table 1. Although Truskov et al. (1993) have reported that porosity inside consolidated ice greatly influences ice strength, it was taken to be zero in all tests because of the difficulty in assessing it. Thus, water between ice blocks is assumed to be frozen.

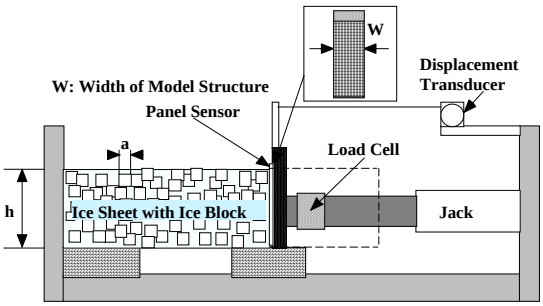

Fig. 1. Indentation Test Device

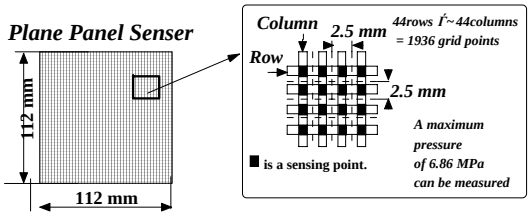

Fig.2. Plane Pressure Panel Sensor

TEST RESULTS AND DISCUSSION

Ice Load Time Series

A time series of indentation pressure and displacement are plotted in Fig.3, Fig.4 and Fig.5. Under constant V=0.2 cm/s (V/h>3*10^{-3} (1/s)), the ice pressure showed some peaks and fluctuated due to brittle flaking caused by the ice blocks. However, the ice pressure didn't fluctuate under constant V=0.02 cm/s (V/h<3*10^{-3} (1/s)) due to ductile failure caused by micro-cracks. Furthermore, the time/displacement relation shows that the model structure moved at a constant velocity.

Table 1. Test Conditions

CASE no.	Width of Structure W (cm)	Ice Thickness h (cm)	Indentation Velosity V (cm/s)	Block size a (cm)	Ice Temp. T(°C)
F1	15	7.4	0.20	no	-4.5
F2	15	10.8	0.20	3	-4.5
F3	15	10.9	0.20	3	-4.5
F4	15	10.4	2.00	3	-4.5
F5	15	10.1	2.00	3	-4.4
F6	15	9.4	0.02	3	-4.4
F7	15	11.0	0.02	3	-4.9
F8	15	10.8	0.20	6	-5.0
F9	15	11.1	0.20	6	-4.5

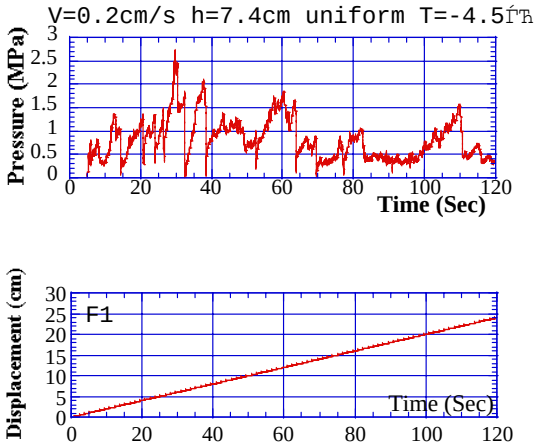

Fig. 3. Pressure and Displacement (F1)

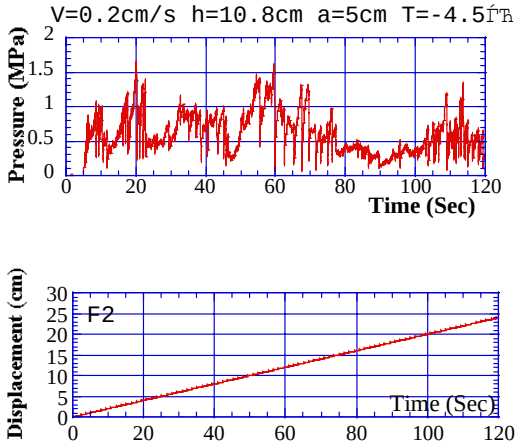

Fig. 4. Pressure and Displacement (F2)

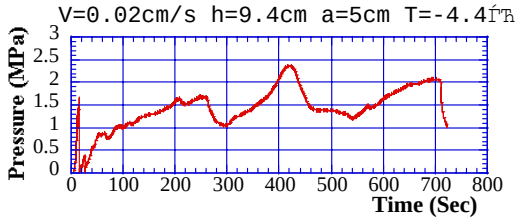

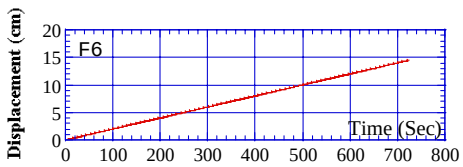

Fig. 5. Pressure and Displacement (F6)

Damage to Ice Sheet and Ice fragment Sizes

Fig.6 (a) shows damage to the ice sheet with ice blocks just after the indentation test. The damage pattern can be divided into two modes: brittle and ductile. For brittle damage under the condition of V=0.2 cm/s, ice failure with ice blocks is characterized by a few brittle flakings, a small area of micro-cracks and horizontal cracks in front of the model structure. Contact of the model structure with the ice leading edge is small and occurs on a so-called line-like area. For ductile damage under the condition of V=0.02 cm/s, ice failure is characterized by a large area of micro-cracks and vertical expansion with horizontal cracks in front of the model structure. Contact of the model structure with the ice leading edge is large and occurs on a plane-like area. Fig. 6 (b)

shows the ice fragment sizes and the damaged area of the ice sheet with ice blocks. For constant (a), the relations between these sizes and V/h are plotted in Fig.7 (a),(b),(c). As V/h becomes smaller, the length (L_m) of the micro-cracks in the indentation direction and the contact ratio (h_c/h) become larger. This implies that a larger ice load requires a smaller (V/h). Next, for constant (V=0.2 cm/s), the relations between these sizes and (a/h) are plotted in Fig. 8 (a),(b). For a larger (a/h), the lengths (L_t, L_b,) of flakings in the indentation direction are slightly smaller. This makes the ice load smaller. Further, pictures at the ice sheet leading edge just after an indentation are shown in Fig. 9 (a),(b), (c), (d). For $V/h>3*10^{-3}$ (1/s), Fig. 9 (a),(b) indicates flakings and a small area of micro-cracks, and in addition Fig.- (d) shows line-like contact. The flaking plane in Fig.9 (b) seems to be rougher than that in Fig.9 (a), as is also shown in Fig.6 (a). This may be influenced by the existence of the ice blocks. However, it is difficult to judge which flaking failure occurs: at the ice between the ice blocks or inside the ice blocks. For $V/h<3*10^{-3}$ (1/s), Fig.9 (c) shows a large area of micro-cracks (milky area) with sounds during indentation. Contact between ice and model structure is large.

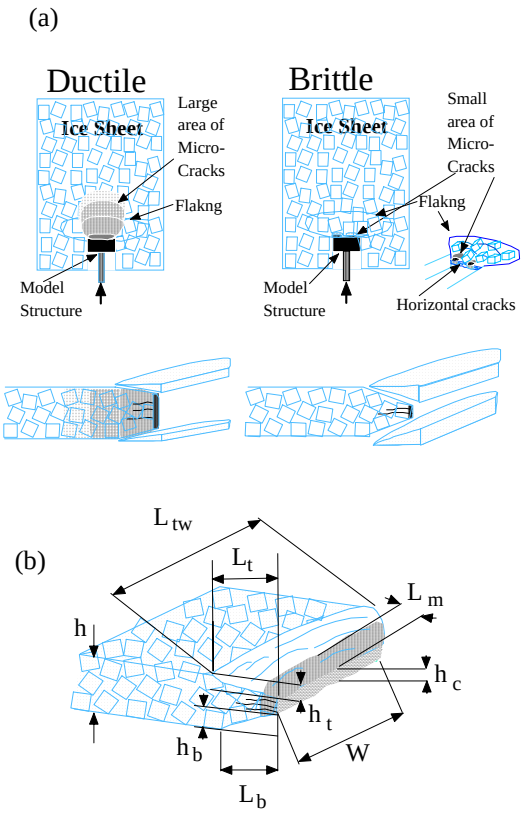

Fig. 6. Schemartics of Ice Failure Pattern and Size

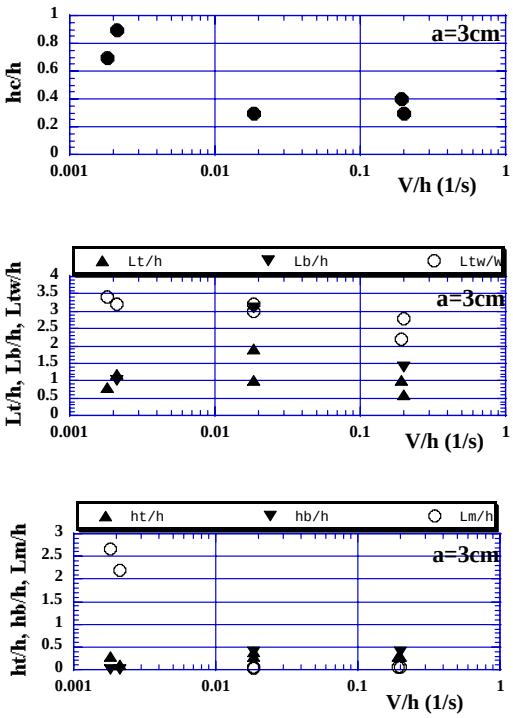

Fig. 7. Ice Failure Size vs. V/h (under constant a)

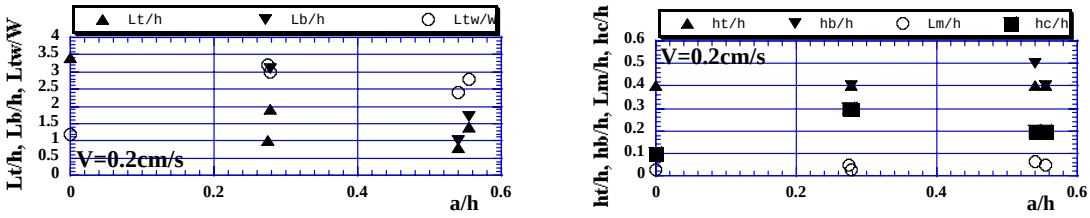

Fig. 8. Ice Failure Size vs. a/h (under constant V)

Fig. 9 (a). Ice Failure uniform (F1)

Fig. 9 (b). Ice Failure *a=3cm V=0.2cm/s* (F3)

Fig. 9. (c) Ice Failure *a=3cm V=0.02cm/s* (F6)

Fig. 9 (d). Ice Failure *a=3cm V=2cm/s* (F4)

Pressure Distribution by Panel

The pressure distributions depending on (*V*), as measured by the panel sensors, are shown in Fig.10 (a) & (b), with a time series of load (expressed by raw sum of output data). Fig.10 (a) corresponds to that in Fig.9(d), and from the change in pressure by some images it shows flaking failure, which gives a peak load. The flaking failure width varies depending on the contact condition during indentation. However, Fig.10 (b) corresponds to that in Fig.9 (c). Although the contact pressure at each grid point is smaller than that in Fig.10 (a), a wider contact area is observed through the pressure distribution measured by the panel sensor.

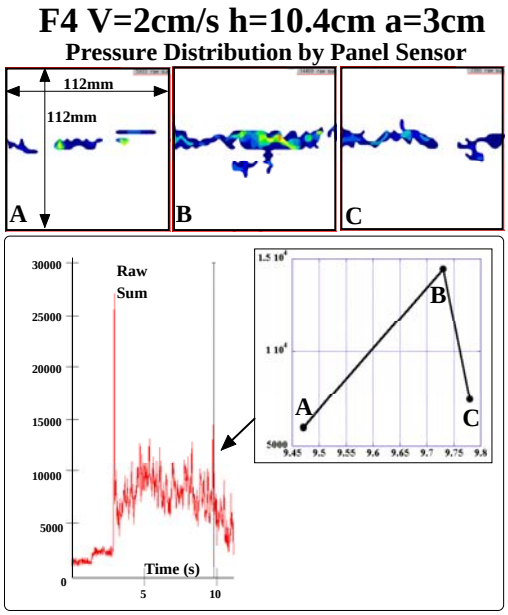

Fig. 10 (a). Contact Pressure

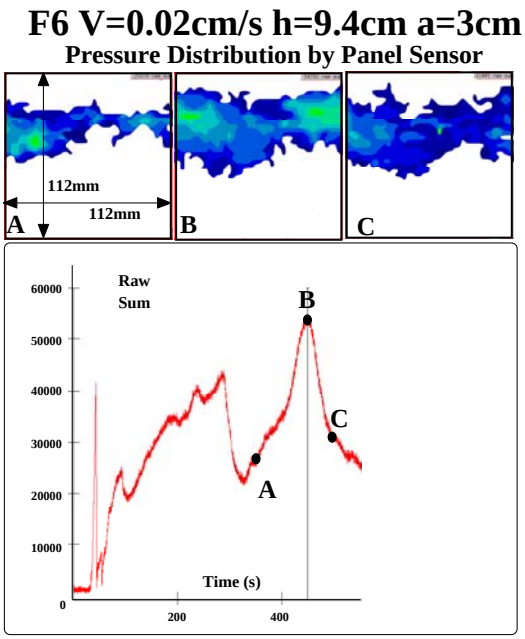

Fig. 10 (b). Contact Pressure

Therefore, the force in Fig.10 (b) becomes larger than that in Fig.10 (a). This pressure pattern depending on (*V*, or *V/h*) for ice with ice blocks is the same as that for level ice reported by e.g.Takeuchi et al.(2000).

Effect of (*V/h*) on Indentation Pressure

For constant (*a*), the indentation pressure is plotted versus (*V/h*) in Fig.11. When (*V/h*) increases, the indentation pressure decreases. This is why the load is related to the size of the micro-crack area and plane-like contact, and a larger load is required for a smaller (*V/h*). This trend is the same as that for the level ice sheet.

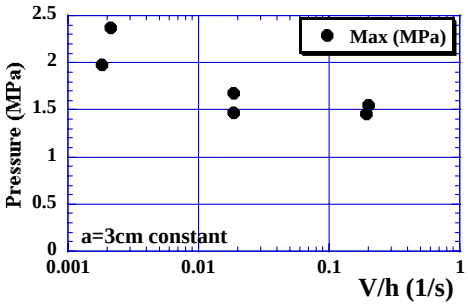

Fig. 11. Pressure vs. *V/h* constant *a*

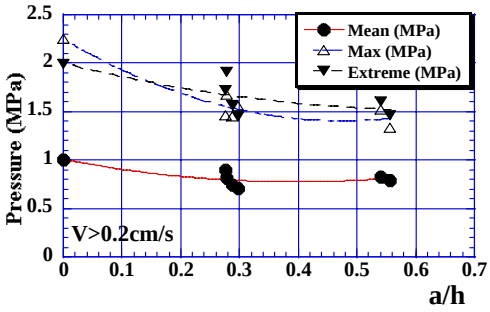

Fig. 12. Pressure vs. *a/h* larger *V/h*

Effect of (*a/h*) on Indentation Pressure

For constant (*V*) giving brittle failure, the indentation pressure is plotted versus (*a/h*) in Fig.12 in order to examine the size of the ice block. As (*a/h*) increases, the average, extreme, and maximum values of indentation pressure decrease, corresponding to the fact that the lengths (L_t , L_b) of flaking in the indentation direction become smaller, as shown in Fig.8(a). Coolsley(1984) developed a theory for several wing cracks to propagate under compressive loading for the brittle condition, as described in Fig.13, and gives an equation for strength of ice, which can be calculated from Eq.(1) when the distance (d_f) between flaws, flaw size (*a*), and fracture toughness (K_{ic}) are known.

$$\sigma \approx 3.5 \frac{K_{ic}}{a} \sqrt{\frac{d_f}{2}} \qquad (1)$$

Further, the relations of ($a=0.65d$) and ($d_f=d$, where d is ice grain size) are reported for S2-type ice by Cole (1986). These conditons are used for level ice as d=0.01m. Assuming that the size (*a*) of the ice block is a flaw size, this is applied to tests here as follows. Under the assumptions of constant (K_{ic}) and the same flaw size to the size of ice block, two conditions, (1) $d_f=1.54a$ and (2) $d_f=a$, for the tests here allow us to calculate the ratio (*r*) of strength under a unit load for strength of level ice. For increaing (*a*), the ratio (*r*) of strength gradually decreases, as shown in Fig.14. The reduction in (*r*) is larger than that shown in Fig.12. Several causes may be considered: bonding strength between ice block and surrounding ice, and difference in density and orientation of the ice block. It is natural to think that the reduction in ice load for the same (*W*) and about the same (*h*) causes the decrease in strength itself of a mass of ice sheet.

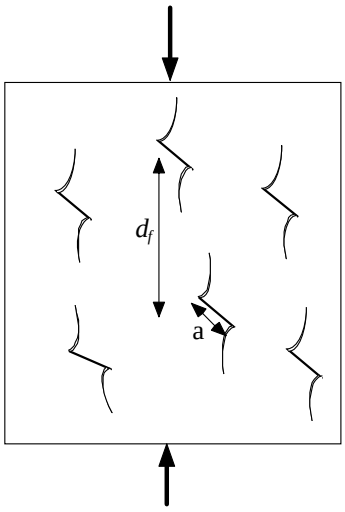

Fig. 13. Flaw model under compressive loading By Cooksley(1984)

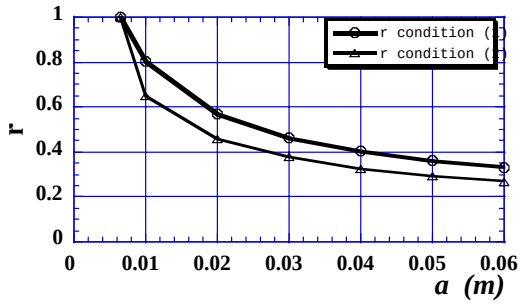

Fig. 14. Pressure Ratio *r* vs. *a*

Concluding Remarks

Indentation tests using an ice model of a consolidated layer show that the ice faliure pattern is fundamentally the same as that for level ice, and that it depends on indentation velocity. Larger (*V/h*) gives brittle failure with line-line contact and flaking, and increasing (*a/h*) provides smaller ice pressure. However, smaller (*V/h*) gives ductile deformation with a larger area of micro-cracks and in turn a larger ice load. Therefore, the creep properies of ice of a consolidated layer will be important for estimation of ice load. The existence of ice blocks contributes to the reduction in ice strength.

REFERENCES

Beketsky, S.P., Astafiev, V.N. and Truskov, P.A., Design Parameters for Hummocks and Grounded Hummocks in the Sea of Okhotsk, *Proc. of ISOPE*, Vol.2, pp.487-493, 1997.

Cooksley, S.D. , Yield and fracture surfaces of brittle solids under multi-axial loading, Ph.D. Thesis, Cambridge University, 1984.

Kioka, S., Yasunaga,Y., Matsuo, Y. and Saeki, H., Experimental Study on the Mechanical Properties of Consolidated Parts of Ice Ridge, *Proc. of Cold Region Technology Conference*, 183-190, 2000.

Parameter, R.R. and Coon, M.D., Model of pressure ridge formation in sea ice, *Journal of Geophysical Research* 77 (33), pp.6565-6575, 1972.

Sanderson, T.J.O., Ice Mechanics risks to offshore structures, Graham&Trotman, 1988.

Takeuchi, T., Sakai, M., Akagawa,S., Nakazawa, N. and Saeki,H., On the factors Influencing the Scaling of ice Forces, IUTAM *Symposium on Scaling Laws in Ice Mechanics and Ice Dynamics*, pp.149-160, 2000.

Timco, G.W. and Goodrich, L.E., Ice Rubble Consolidation, *Proc. of IAHR Ice Symposium*, pp.427-438, Sapporo, 1988.

Truskov, P.A., Surkov, G.A. and Beketsky, S.P., Strength Parameters of Hummocks: Field Observations and Laboratory Tests, *Proc. of 8th* Int. Symp. on OKHOTSK SEA &SEA ICE, pp.82-95, 1993.

17th International Symposium on Ice
Saint Petersburg, Russia, 21 - 25 June 2004
International Association of Hydraulic Engineering and Research

EVALUATION OF LOADS DUE TO PARTIAL FREEZING OF SEAWATER TRAPPED IN ENCLOSED CAVITIES

Nicolay V.Koubyshkin[1], Kirill E. Sazonov[2]

ABSTRACT

Ice formation in enclosed cavities is possible both under natural conditions and due to water freezing inside engineering structures. A specific feature of this restrained freezing is that it causes an increase in the hydrostatic pressure because of an abrupt drop of the water density associated with the transition from the liquid phase into the solid one. This rise in the pressure of the water core deforms or breaks natural or artificial walls of the cavity. Physical properties of the sea ice, including the density, are pronouncedly different from fresh ice properties because the sea ice contains a liquid phase: the brine. the salinity of the ice directly affects its density, and therefore the water core hydrostatic pressure in case the entrapped seawater freezes. This paper presents a theoretical study of the process and the aim of this investigation was to see whether accounting for the salt could refine results obtained in (Pekhovich, 1983).

INTRODUCTION

Ice formation in enclosed cavities is possible both under natural conditions and due to water freezing inside engineering structures. A specific feature of this restrained freezing is that it causes an increase in the hydrostatic pressure because of an abrupt drop of the water density associated with the transition from the liquid phase into the solid one. This rise in the pressure of the water core deforms or breaks natural or artificial walls of the cavity. The issue of loads due to fresh water freezing in rigid (non-deformable) cavities has been already considered quite thoroughly (Pekhovich, 1983). Using a simplistic calculation model, the author has demonstrated that freezing 60~70% of water in a fully flooded enclosed space makes the pressure 2000 times higher and its value reaches 209 MPa (the freezing temperature associated with this pressure is -22°C). After that, the ice transforms from Modification I into Modification II, and the density of the latter is higher than of the water.

Physical properties of the sea ice, including the density, are pronouncedly different from fresh ice properties because the sea ice contains a liquid phase: the brine. The amount of the brine depends on the ice temperature and salinity. That is why the sea ice, unless it contains entrapped air, has a higher density than the solid fresh-water ice. Besides,

[1] AARI,38 Bering street, St.Petersburg, Russia, 199397.
[2] KSRI, 44, Moskovskoe shosse, St.Petersburg, Russia 196158.

temperature-induced variations in the sea-ice density (thermal expansion) follow a different pattern than in the fresh-water ice case. With the fresh-water ice, the density grows when the temperature decreases. With the sea ice, density variations are under the influence of two contradictory processes. On one hand, cooling brings an increase in the density because it elevates the density of the fresh-water ice fraction, which is present in the sea ice. On the other hand, cooling means decreasing the density of the salt-water ice fraction because some of the denser water present in the brine turns into the less dense fresh-water ice. Individual contributions of these two processes into the resulting density variations depend on the salinity of the ice. Particularly, when the sea ice salinity is 2‰, the density reduction effect prevails at temperatures above –8.2°C because of partial freezing-out of the brine. Below that temperature point, the amount of the brine drastically reduces in association with the beginning of the $Na_2SO_4 \cdot 10H_2O$ sedimentation. When the temperature drops below –8.2°C, the fresh-water ice hardening becomes the dominant factor and the resulting density of the sea ice grows. With the ice salinity of 10‰, the density decreases together with the temperature within the entire variation range relevant for our purposes (i.e. starting from the -22°C freezing point). Thus, the salinity of the ice directly affects its density, and therefore the water core hydrostatic pressure in case the entrapped seawater freezes. This paper presents a theoretical study of the process and the aim of this investigation was to see whether accounting for the salt could refine results obtained in (Pekhovich, 1983).

ICE FORMATION IN ENCLOSED CAVITIES

Let us similarly to (Pekhovich, 1983) consider the case when the involved enclosed space has absolutely rigid walls and let us select the most simplistic shape of the cavity: a flat crack. Initially, the cavity is fully flooded with water that has a salinity of S_W and is within the entire volume cooled down to a freezing point Θ. The ice formation inside the cavity starts because the heat escapes outside from one of the cavity walls (the F_0 flux). Same as in (Pekhovich, 1983), let us assume that the volume increase associated with the freezing is compensated by the compaction of the ice ΔV_I and of the water ΔV_W. The total ice + water volume remains unchanged and equal to the volume of the cavity. Then, freezing water volume variation along the crystallisation front ΔV_F is:

$$\Delta V_F = \frac{\rho_W - \rho_I}{\rho_W} V_I = \Delta V_W + \Delta V_I , \qquad (1)$$

where: ρ_W – water density; ρ_I – ice density; V_I – ice volume.

Summands of the right-hand term in (1) should be found taking into account water and ice compression under the effect of the hydrostatic pressure P existing in the cavity:

$$\Delta V_W = \frac{P - P_0}{E_W} \left(V_0 - V_I \right); \qquad (2)$$

$$\Delta V_I = \frac{P - P_0}{E_I} V_0 \, f , \qquad (3)$$

where: P_0 – initial pressure in the cavity, i.e. before the freezing process starts; V_0 – cavity volume; E_W – water elasticity factor, which is opposite to the isothermal compression factor; E_I – ice elasticity modulus; $f = 1 - \frac{2\mu^2}{1-\mu}$ – ice compressive deformation function; μ – Poisson ratio.

With equations (1)~(3), we may derive a formula for P, which describes the static condition of the system (ice volume – pressure):

$$P = P_0 \cdot [1 + A]; \qquad A = \frac{\frac{\rho_W - \rho_I}{\rho_W} \cdot \frac{E_W}{P_0} \cdot k}{1 - k + \frac{E_W}{E_I} f}; \qquad k = V_I / V_0 . \tag{4}$$

The set of equations (1)~(4) is actually the problem considered in (Pekhovich, 1983) only simplified by assuming that the cavity contains no air. This simplification is essential for getting a clear-cut definition of water and ice salinity contributions as compared to the fresh-water model results.

The salinity of the seawater ice depends on the seawater salinity and on the ice growth rate. The higher are both these parameters, the greater is the resulting salinity of the ice. The factor that limits the ice salinity is the salinity of the water before it freezes. However, in real life the ice salinity never reaches that value and always stays much lower. There is a variety of empirical and semi-empirical formulae available for finding the ice salinity but for the purposes of this study, the most suitable option appears to the one suggested by Tsourikov (Tsourikov, 1976):

$$S_I = S_W \frac{7\sqrt{d\,h_I / d\,t}}{7\sqrt{d\,h_I / d\,t} + 10.3}, \tag{5}$$

where dh_I/dt is the ice growth rate in mm per hour.

The advantage of Tsourikov's formula compared to other one is that all its coefficients come from laboratory experiments in a small volume encompassed with ice walls and an ice "lid" frozen to the walls. For first approximation purposes, we may say that such conditions are similar to freezing in an enclosed cavity. Now, let us assume that the quantitative dependence of the ice salinity upon the water salinity and the ice growth rate as described in formula (5) stays unchanged even at the high hydrostatic pressure of the water core in our rigid-shell cavity.

Let us consider a situation when the ice grows uniformly on one of the walls of our cavity and the outgoing heat flux F_0 is constant. Then, on a wall with an area of $1m^2$, the ice growth rate is:

$$\frac{d\,h_I}{d\,t} = \frac{F_0}{L_{ef} \cdot \rho_I}, \tag{6}$$

where L_{ef} is the effective heat of the phase transformations.

Freezing an ice layer that has a thickness of h_I and a salinity of S_I of water that has an initial salinity of S_{W0} ($S_{W0} > S_I$) results in increasing the water salinity to:

$$S_W = \frac{H_0 \cdot S_{W0} \cdot \rho_W - h_I \cdot S_I \cdot \rho_I}{H_0 \cdot \rho_W - h_I \cdot \rho_I}, \tag{7}$$

where H_0 is the distance between the walls of the crack.
In formula (7), the ρ_W value should be the initial water density and ρ_I should be the density of the ice that has formed of that water.

In his computations for the water core hydrostatic pressure, A.I.Pekhovich (Pekhovich, 1983) assumed water and ice density values of 1000 kg/m^3 and 920 kg/m^3 respectively. For the sea ice and the seawater, it would be better to use these characteristics as functions of the condition parameters: temperature, salinity and pressure (for the water). For the seawater density, we may apply a simple equation suggested by Mamaev (Ocean Physics, 1978):

$$\rho_W = 1000 + 0.01\left[2815.2 - 7.35\cdot\Theta - 0.469\cdot\Theta^2 + (80.2 - 0.2\cdot\Theta)(S_W - 35)\right] + \\ + 4.6\cdot 10^{-7}\left[P - P_0\right]. \quad (8)$$

The seawater freezing temperature depends on the salinity and on the pressure, and it may be found as:

$$\Theta = -0.02831 - 0.0499\cdot S_W - 0.000112\cdot S_W^2 - 0.00759\cdot(P - P_0), \quad (9)$$

units in formulae (8) and (9) are °C for the temperature, ‰ for the salinity and Pa for the pressure.

To compute the sea ice density, we may utilise the available formulae (Nazintsev et al., 1980; Sea Ice, 1997):

$$\rho_I = \frac{\rho_{PI}\cdot\rho_B\cdot(s+p)}{-S_I\cdot(\rho_B - \rho_{PI})\cdot(1+s) + \rho_B\cdot(s+p)}. \quad (10)$$

Salinity values in formula (10) have to be substituted in relative units. The fresh-water ice density ρ_{PI}, the brine density ρ_B and the dimensionless factors s and p are functions of the ice temperature T:

$$s = \begin{cases} -1.848\cdot T\times 10^{-2} & 0 \ge T \ge -7.5\ ^{o}C \\ (5.670 - 1.077\cdot T)\times 10^{-2} & -7.5 \ge T \ge -22.4\ ^{o}C \\ (16.770 - 0.532\cdot T)\times 10^{-2} & -22.4\ ^{o}C \ge T \end{cases}; \quad (11)$$

$$s + p = \begin{cases} -1.848\cdot T\times 10^{-2} & 0 \ge T \ge -7.5\ ^{o}C \\ (3.32 - 1.387\cdot T)\times 10^{-2} & -7.5 \ge T \ge -22.4\ ^{o}C \\ (-199.20 - 10.567\cdot T)\times 10^{-2} & -22.4\ ^{o}C \ge T \end{cases}; \quad (12)$$

$$\rho_{PI} = \frac{916.8}{1 + (158\cdot T + 0.54\cdot T^2)\cdot 10^{-6}}; \quad (13)$$

$$\rho_B = \left(1 + \frac{0.8\,s}{1+s}\right)\cdot 10^3. \quad (14)$$

The average temperature across the considered ice layer is found as:

$$T = 0.5\cdot(\Theta + T_0), \quad (15)$$

where: $T_0 = \Theta - \frac{F_0\cdot h_I}{\lambda_I}$ – is the temperature at the ice interface with the rigid wall; λ_I – sea ice heat conductivity.

The heat conductivity is a function of the ice temperature and salinity:

$$\lambda_I = \lambda_P + \frac{0.1172\,S_I}{T}, \quad (16)$$

where $\lambda_P = 2.22(1 - 0.0048 \cdot T)$ is the freshwater ice heat conductivity in W/m·°C.
The effective phase transformation heat necessary for formula (6) is found as:

$$L_{ef} = L_0\left(1 - \frac{S_I}{S_B}\right) + \Theta\left(\frac{\rho_W}{\rho_I} \cdot C_W - C_I\right), \tag{17}$$

where:L_0=333500 J/kg – freshwater ice specific melting heat; $S_B = \frac{s}{1+s} \cdot 10^3$ – brine salinity, ‰; C_W = 4010 J/kg·°C – water heat capacity; C_I =2100 J/kg·°C – ice heat capacity.

For the E_W coefficient, we may assume 21277 Bar, and for the ice elasticity modulus, there is an empirical formula:

$$E_I = (10.0 - 0.0351 \cdot S_I) \cdot 10^4. \tag{18}$$

The set of equations (4)~(18) was at first applied to compute freshwater freezing (S_W=0=const) in a vessel of H_0=1m. A comparison of the thus found partial-freezing pressures with the results published in (Pekhovich, 1983) is available in Fig.1. With the same ice volumes, the difference in pressures amounts to about 20%. The reason is that our formulae are more accurate in considering the effects of the pressure upon the water density. In (Pekhovich, 1983), the assumed values of ρ_I =920 kg/m^3 and ρ_W = =1000 kg/m^3 are constant regardless of the ice volume. This ensures that the $\frac{\rho_W - \rho_I}{\rho_W}$ parameter in formula (4) is always 0.8. In our computations, accounting for the pressure effect on the water density means that at the 2000-bar pressure in the cavity, that parameter becomes 2 times higher. Fig.2 offers a plot of $\frac{\rho_W - \rho_I}{\rho_W}$ versus pressure. The same Figure shows such parameters for zero-salinity water densities at 600 bar and 1°C measured by Wilson and Bradley and published in (Popov et al., 1979). Points calculated with empirical formulae quite well agree with the curve based on the water density found with Mamaev's equation.

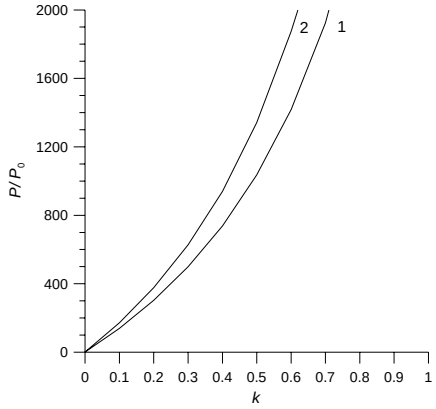

Fig.1. Enclosed-cavity pressures versus relative volumes of the frozen entrapped water: 1 – as computed by A.I.Pekhovich (Pekhovich, 1983); 2 – as computed with equations (4)~(18)

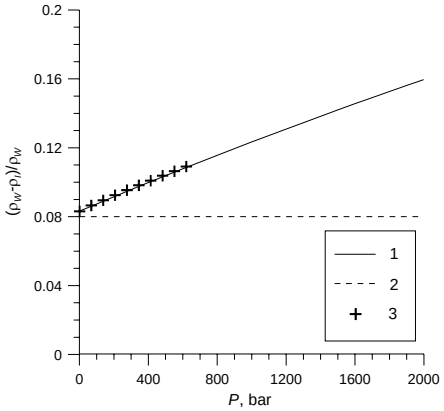

Fig.2. Density variations at the water to ice phase transformation as functions of the pressure (S_W=0): 1 – with the variable water density as Mamaev's equation; 2 – with a constant water density of 1000 kg/m^3; 3 – with water density values as measure by Wilson and Bradley (Wilson, Bradley)

In order to find out how the water salinity influences the pressure associated with ice freezing in an enclosed cavity, we have carried out a numerical experiment that included solving the (4)~(18) set of equations. For equation (6), we have applied the Runge – Kutta method finding all relevant ice and water characteristics by iterations at every integration step. As has been already mentioned before, in the entrapped case, ice and water salinity values are functions of the initial water salinity and the ice growth rate. In our computations, the ice growth rate was fixed by assuming a constant F_0 value of 50 W/m^2 and the only variable was the initial water salinity. Its values were 0, 10, 20 and 30‰. Figs.3 and 4 show water and ice salinity variations with different relative ice volumes in the flat-crack cavity. The water salinity grows because the growing ice rejects some of the salt. The ice salinity increases at the constant ice growth rate because the water salinity becomes higher.

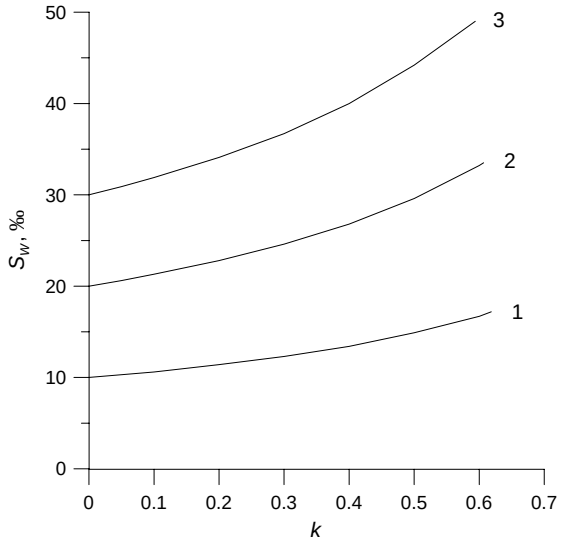

Fig.3. Entrapped water salinity variations associated with partial freezing with different initial salinity values: 1 - 10‰; 2 - 20‰; 3 - 30‰

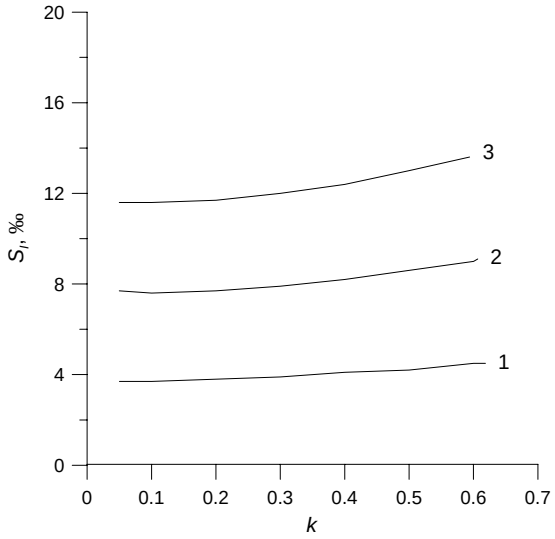

Fig.4. Ice salinity variations associated with partial freezing of entrapped water with different initial salinity values: 1 - 10‰; 2 - 20‰; 3 - 30‰

Fig.5 shows variations of the $\frac{\rho_W - \rho_I}{\rho_W}$, which defines water volume changes at the water to ice phase transformation, with the cavity pressure growth at four initial water salinity values. At first, when the pressure in the cavity is still low and the ice temperature is close to the freezing point, density variations due to saline water freezing are less than those that are due to fresh water freezing because of the large amount of the brine available in the ice. While the ice continues growing, the average temperature of its thickness profile reduces whereas the pressure increases. Therefore, the density of the ice reduces (approaches the fresh-water ice density) and the water density increases because of the growing pressure and salinity. These effects result is significant increases in $\frac{\rho_W - \rho_I}{\rho_W}$ ratios at higher values of the initial water salinity. It should be noted that the increase in phase-transformation density jump, which is associated with the fact that the initial water salinity escalates from 0 to 30‰, is less than its "method-induced"

increase due to refined density definitions in equations (4)~(18) as compared to computations presented in (Pekhovich, 1983).

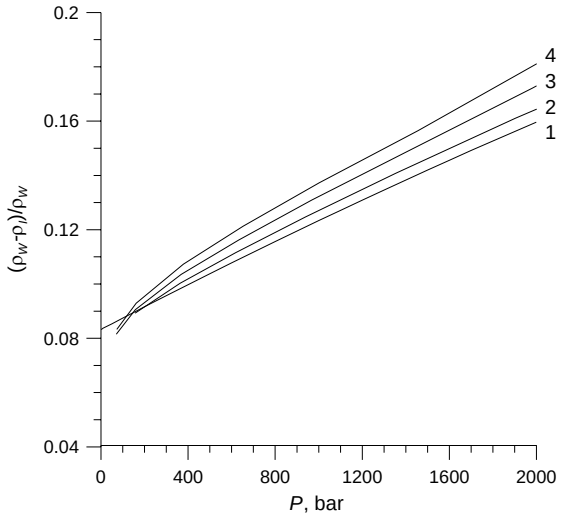

Fig.5. Density variations associated with the water to ice phase transformation versus pressures due to the freezing of entrapped water with different initial salinity values: 1 - 0‰; 2 - 10‰; 3 - 20‰; 4 - 30‰

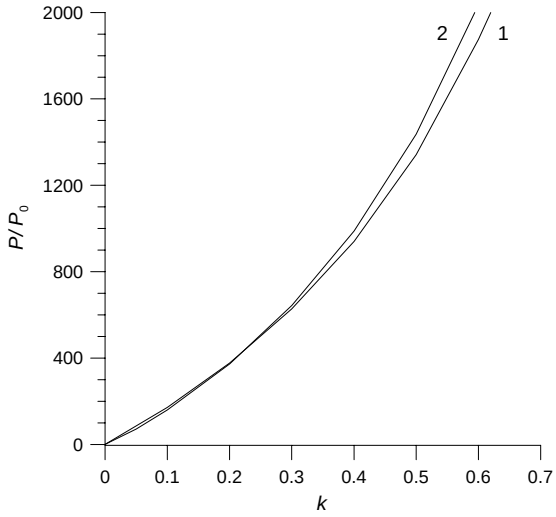

Fig.6. Entrapped water pressures versus frozen volumes with different initial water salinity values: 1 – S_W=0‰; 2 – S_W=30‰

Fig.6 shows cavity pressure variations with different frozen-water amounts for fresh water and for 30‰ initial-salinity water. With up to 20% of the volume frozen (k = 0.2), we may see that the pressure in the cavity filled with saline water is slightly less than in the cavity with fresh water. However, this pressure difference is minor and reaches just 7% at k = 0.1. With 20% to 30% of the water frozen (k = 0.2-0.3), both cavities suffer approximately equal pressures. With more than 30% of the volume frozen (k>0.3), the pressure in the saline-water cavity exceeds that in the fresh-water one. With 50% of the volume frozen (k = 0.5), the pressure difference is only 6.6%. However, by that time the absolute values are so high that this slight difference means a noticeable figure of 95 bar.

PRINCIPAL CONCLUSIONS

Thus, the results of our numerical exercises demonstrate that the presence of dissolved salts affects the pressure growth pattern associated with entrapped water freezing. As long as the frozen volume is below 20%, the entrapped seawater produces less pressure than fresh water. After more than 30% of the entrapped water turns into ice, the seawater provokes a more intensive pressure growth than fresh water. The pressure difference due to the salinity difference is rather small and rests within 7%. Comparing these results with earlier publications (Pekhovich, 1983) shows that even with the same task formulation, neglecting water and ice density variations results in up to 20% underestimation of the pressure.

REFERENCES

Ocean Physics. 1978. *Girdometeoizdat Publishers*, Leningrad, USSR (in Russian).

Nazintsev Y.L., Dmitrazh Zh.A., Moiseev V.I. 1988. Thermo-physical Properties of the Sea Ice. *Leningrad State University*, Leningrad, USSR (in Russian).

Nazintsev Y.L., Panov V.V. 1997. Phase Ratios, Chemical Composition and Thermo-physical Properties of the Sea Ice // Sea Ice: Observation Data Acquisition and Analysis, Physical Properties and the Prediction of Ice Conditions (reference book). *Girdometeoizdat Publishers*, St.Petersburg, Russia (in Russian)

Pekhovich A.I. 1983. Fundamentals of Hydroicethermics. *Energoatomizdat Publishers*, Leningrad, USSR (in Russian).

Popov N.I., Fedorov K.N., Orlov V.M. 1979. Sea Water. *Nauka Publishers*, Moscow, USSR (in Russian).

Tsourikov V.L. 1976. The Liquid Phase in the Sea Ice. *Nauka Publishers*, Moscow, USSR (in Russian).

17th International Symposium on Ice
Saint Petersburg, Russia, 21 - 25 June 2004
International Association of Hydraulic Engineering and Research

DETERMINATION OF PACK ICE STRESS FROM FLATJACK STRESS SENSORS

Max D. Coon[1], Douglas C. Echert[2] and Gerald S. Knoke[3]

ABSTRACT

This paper describes a methodology to determine pack-ice stress from local sea-ice stress measurements made with flatjack sensors. The methodology was developed from, and applied to, measurements taken during the U.S. Navy Office of Naval Research Sea Ice Mechanics Initiative field program. The gauges used were automatically able to test the ice/sensor contact at intervals during the long, unattended measurement period. On-site calibrations conducted in the local ice sheet were used as input for the calculation procedure. The most significant steps of the process are corrections for the time-dependent behavior of the ice and corrections for thermally-induced stress. The procedure is explained and illustrated with data. A three-month time history of pack ice stress is presented.

INTRODUCTION

This paper reports on the interpretation of sea ice stress measurements obtained during the U.S. Navy's Office of Naval Research (ONR) Sea Ice Mechanics Initiative (SIMI) field program. The field work took place during the winter of 1993-1994 in the Beaufort Sea. The autumn, 1993, segment of the SIMI field program is described in Coon et al. (1994). Coon et al. (1989) describe the stress sensors and the installation of the sensors in rosettes to measure the stress state in the ice. This paper describes the procedure developed for processing the measured flatjack sensor pressures to produce geophysical sea-ice stress. More than forty *in situ* calibration tests were conducted. These tests made it clear that the time-dependent behavior of the ice must be accounted for in determining the geophysical stress. The primary steps in the data processing are illustrated with examples.

ICE STRESS MEASUREMENTS

Stress sensors were deployed in an autonomous station configuration at each of four locations during the SIMI field program. At each buoy location, a rosette of four

[1] NorthWest Research Associates, Inc., Bellevue, WA USA
[2] Skip Echert Web Associates, Renton, WA USA
[3] Energy International, Inc., Bellevue, WA USA

sensors was installed at mid-ice depth, at 45° compass intervals (the fourth sensor was for redundancy). Three rosettes were installed in the autumn in roughly 70-cm thick ice; one was moved in the spring to a fourth site where the ice was 1.6 m thick. Each buoy was installed near the middle of a large expanse of smooth, first-year ice that was contained within the perimeter of a large multiyear floe. Installation in this uniform ice avoided the complex geometry and resulting complex stress state of the surrounding multi-year ice, yet still represented the regional stress state of the pack ice (Coon et al 1998). Additional details of the use of these gauges during the SIMI Program are found in Coon et al. (1995a) and Coon et al. (1995b).

At prescribed intervals a small quantity of fluid was injected from the fluid reservoir into the stress sensors to evaluate the ice/sensor contact. If the sensor pressure increased by at least 50 kPa, the sensor was considered to be in good contact with the ice. Figure 1 shows six-hour samples of the raw stress-sensor oil-pressure data transmitted via Argos satellite for the full life of the buoy 2. The data are from the three stress sensors that provided continuous data during this time. It includes spikes resulting from the auto-pressurization cycles, which took place at the times noted by the triangles at the bottom of the figure. There were no major stress events after mid-May, and the ice apparently melted away from the sensors in early July, relieving all ice stress around the sensors.

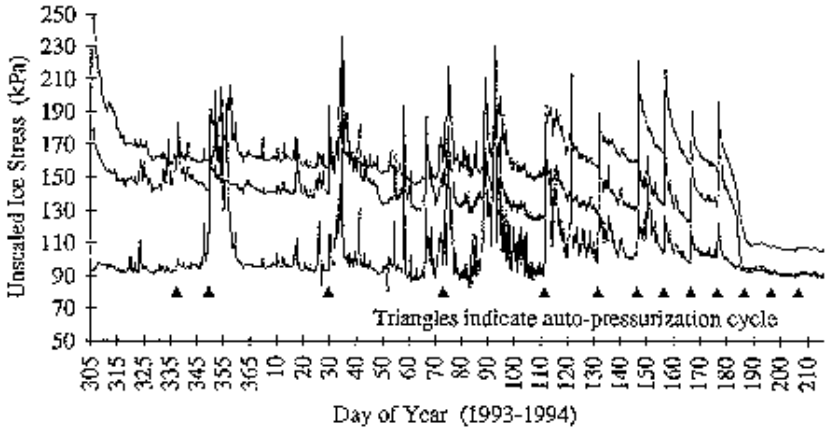

Fig. 1. Raw ice stress sensor fluid pressures from Buoy 2 (on SIMI Floe 4). The data span the period Nov. 1, 93 through Aug. 3, 94

STRESS DATA PROCESSING

The procedure to convert stress sensor fluid pressure readings to ice stress involved four primary steps:

Step 1 removes the spikes caused by automatic pressurization cycles (see Figure 1);
Step 2 corrected for the time-dependent behavior of the sea ice;
Step 3 corrects for the effect of thermal changes on the stress measurements; and
Step 4 derives geophysical stress components in a north-south-east-west system, accounting for flow rotation and the changing thickness of the ice cover.

Other possible sources of data error: gauge errors due to thermal expansion and the effects of temperature changes on the system electronics, the pressure transducer, and stress gauge stiffness were found to be minor.

Step 1 Removal of pressurization cycle

The stress caused by the pressurization cycle seen in Figure 1 clearly decays away in time. This process was modeled as the sum of a fast and a slow exponential decay. Each pressurization cycle was fitted with a double exponential curve from the oil pressure. The two exponential time constants were three hours and fourteen days. The shape of the decay curve did not vary significantly during the fall to spring deployment period - so that these time constants are applicable for the entire data set.

Step 2 Time-dependent behavior

In-situ calibration tests were made at each stress sensor deployment site. Large, flat air jacks were used to compress the ice containing the stress sensor. The stress sensor compression calibrations were made at two speeds: rapid loading (around 100 kPa/min), which produced a square-wave pressure history, and slow loading (around 1 kPa/min), which produced a ramp pressure history. The load rate of the ramp tests more closely matched geophysical load rates, while the rapid load rate of the square-wave test is fast enough to measure the elastic response of the ice-sensor system. During the ramp tests the air pressure was increased to a target value, held for a designated period, (ranging from 15 to 30 seconds) and then released. The test was repeated multiple times, each spaced by the same designated period as above. Figure 2 is a scatter diagram of the results of one such test.

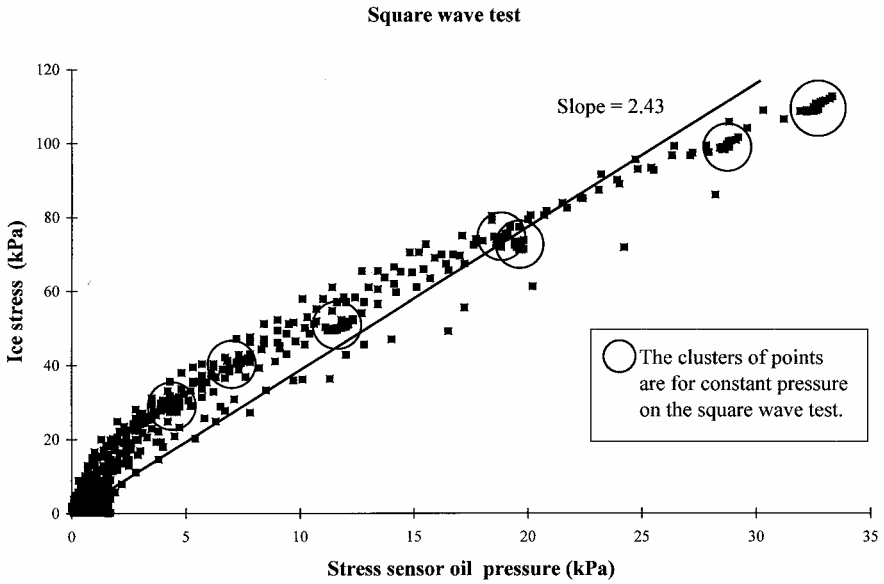

Fig. 2. Scatter diagram of an example square wave test. The vertical scale is the applied stress provided by the air jack. The horizontal scale is the fluid pressure in the stress sensor

Based on the test results, the response of the sensor to ice stress was modeled with a dynamic (time-dependent) inclusion factor of the form

$$\sigma = -AP - \int_{t-\tau_0}^{t} BPd\tau \,, \qquad (1)$$

where s is the ice stress normal to the sensor or the air pressure in the air jack, P is the oil pressure in the sensor (with pressure positive), and A, B, and t_o are constants. With values A = 2.43, B = -0.037 min^{-1}, and τ_o = 20 min, whenever the remaining oil pressure

was less than 20 kPa, the data were dropped. Hamza and Blanchet (1984) used an incremental analysis for the viscoelastic bridging response of a pressure sensor embedded in an ice sheet. Their approach is similar to what is being done here.

Step 3 Corrections for modulus and temperature variations

The ice stress measured by the sensor is our best estimate of the ice stress at the depth of the sensor in the ice sheet, but what is sought is the geophysical ice stress. For this, one must account for the following parameters: ice thickness, elastic modulus variations through the ice thickness, thermal stress, and bending stress. The ice thickness determined from drilling holes and from thermistors installed with the stress rosette was consistent at the first three sites; growth in ice thickness was interpolated in proportion to the square root of time. Cox and Weeks (1988) give estimates for the distribution of the elastic modulus through the ice thickness for various thicknesses of first-year sheet ice. We approximated their results with a constant elastic modulus for the top 80% of thickness and zero for the bottom 20%. A theory for the stresses due to temperature gradients in an unconfined, thick, elastic plate of uniform thickness in which the temperatures and the properties are a function only of depth is given by Timoshenko and Goodier (1951):

$$\sigma_{xx} = \sigma_{yy} = -\frac{\alpha E \Delta T}{1-\nu} + \frac{1}{h(1-\nu)} \int_{-h/2}^{h/2} \alpha E \Delta T dz - \frac{12y}{h^3(1-\nu)} \int_{-h/2}^{h/2} \alpha E \Delta T z dz, \qquad (3)$$

where x and y are the coordinates in the plane of the plate, z is the coordinate down from the mid-depth of the plate, σ is the stress at z, α is the thermal expansion coefficient, E is the elastic modulus, ΔT is the temperature change from a uniform temperature as a function of z, ν is the Poisson's ratio for the material, and h is the plate thickness. To determine the thermal stress on the stress sensor, we use the temperature change at the sensor depth to evaluate the first term on the right side of Equation (3). For sea-ice, α is essentially constant, and E is zero for the bottom 20% of the depth. The thermal stress in sea ice is thus

$$\sigma_{xx} = \sigma_{yy} = \frac{\alpha E}{1-\nu} \left\{ -\Delta T + \frac{1}{h} \int_{-0.3h}^{0.5h} \Delta T dz - \frac{12y}{h^3} \int_{-0.3h}^{0.5h} \Delta T z dz \right\}, \qquad (4)$$

The ice temperatures were measured with thermistors at several depths. To account for the creep out of the thermal stress, the temperature change was calculated not from an initial uniform temperature, but from a reference temperature calculated by smoothing the measured temperatures with a low-pass filter. The filter has a 14-day time constant, which is the same time constant as the slow creep found in the pressurization decay. Constant values of 1 GPa for the effective elastic modulus, 0.3 for Poisson's ratio, and 5.1 x 10^{-5} per °C for the thermal expansion coefficient were found to make the calculated thermal stress, which is the same in all (horizontal) directions, consistent with the ice stress measured with all four sensors in the rosettes. These values are similar to those used by Lewis (1993) in his calculations of thermal stress in sea ice. Lewis, however, uses a variable elastic modulus, a different definition for a reference temperature, and creep strain in his model. The maximum value of the thermal stress during this period, 38 kPa, is more an order of magnitude lower than the maximum measured ice stress, 436 kPa. However, for many periods in this data set, the average

stress is in the range of 20 to 40 kPa. Here the thermal stress correction can be larger than the geophysical stress.

Step 4 Corrections for sheet thickness and floe rotation

The geophysical stress resultant is the integral of the geophysical stress through the thickness of the ice sheet. Since the elastic modulus is taken as constant for the top 80% of the thickness, the difference between the ice stress and the thermal stress is the geophysical stress for that layer. The bottom 20% must have no stress since the assumed elastic modulus is zero, so the geophysical stress resultant is 0.8h times the difference between the ice stress and thermal stress. During our field measurements, the first year ice at buoys 2 and 3 was 76 cm thick on Day -35 and 115 cm thick on Day +57. The effect of flow rotation was accounted for in determining the north-south-east-west stress components. The total rotation for the time period considered was 45 degrees. The north stress resultant component in the north-south-east-west coordinates is shown in Figure 3a. An expansion of the time scale for a three-day period to illustrate the typical variations that cannot be seen in Figure 3b.

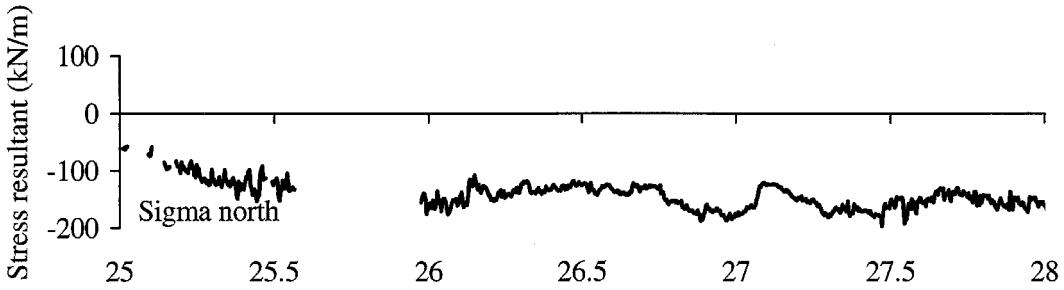

Fig. 3a. The north stress resultant component from Buoy 3

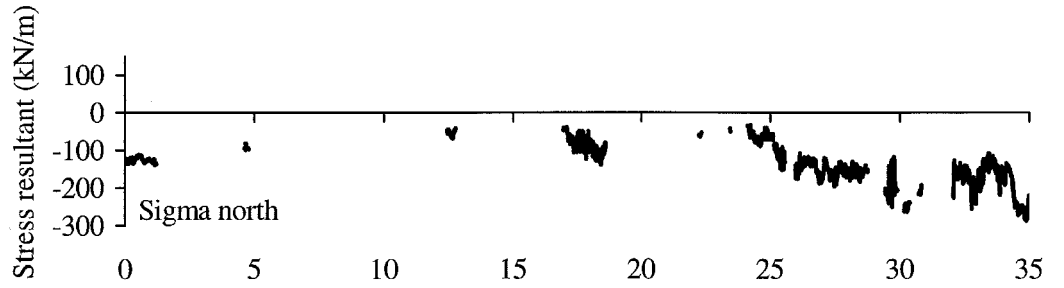

Fig. 3b. North stress resultant components from Buoy 3 for the period Jan. 25 through 27, 1994. The east, north, and east, north stress resultant components are shown

DISCUSSION

The sea-ice stress data shown in this paper indicate the difficulty in making reliable measurements of geophysical sea-ice stress. However, by accounting for the time-dependent behavior of the ice as well as its thermal history, it is possible to take measurements of the geophysical stress. The stresses shown in this paper can be used to verify sea ice dynamics models.

ACKNOWLEDGMENTS

The authors gratefully acknowledge the Office of Naval Research (under Contract Numbers N00014-92-C-0027 and N00014-96-C-0096) for funding this work. Our thanks to Drs. Thomas Curtin and Michael Van Woert for their guidance and support during this effort.

REFERENCES

Coon, M. D., P. A. Lau, S. H. Bailey, and B. J. Taylor, 1989. Observations of ice floe stress in the eastern Arctic. Proc. *POAC '89, The 10th International Conference on Port and Ocean Engineering under Arctic Conditions*, Luleå, Sweden, March 1989, 1.

Coon, M. D., G. S. Knoke, and D. C. Echert, 1994. The Sea Ice Mechanics Initiative (SIMI). *Proc. 26th Annual OTC Conference*, Houston, TX, May, 1994.

Coon, M. D., D. C. Echert, G. S. Knoke, J. E. Overland, S. Salo, R. S. Pritchard, D. A. Rothrock, and H. L. Stern, 1995a. Sea ice deformation and stress, a comparison across space scales. *Proc. Sea Ice Mechanics and Arctic Modeling Workshop*, Anchorage, AK, April 25-28, 2.

Coon, M. D., D. C. Echert, and G. S. Knoke, 1995b. Sea ice mechanics research. *Proc. Sea Ice Mechanics and Arctic Modeling Workshop*, Anchorage, AK, April 25-28, 1995, 1: 151-159.

Coon, M. D., D. C. Echert, and G. S. Knoke, 1998. Stress validation of a failure yield surface for pack ice. *Proc. 14th International Symposium on Ice*, Potsdam, NY, July 27-31, 1998.

Cox, G. F. N., and W. F. Weeks, 1988. Numerical simulations of the profile properties of underformed first-year sea ice during the growth season. *Journal of Geophysical Research*, 93: (C10), 12,449-12,460.

Hamza, H., and D. Blanchet, 1984. A study of the creep effect upon the response of a pressure sensor embedded in an ice sheet. *Cold Regions Science and Technology*, 9: 97-107.

Lewis, J. K., 1993. A model for thermally-induced stresses in multi-year sea ice. *Cold Regions Science and Technology*, 21: 337-348.

Timoshenko, S., and J. N. Goodier, 1951. Theory of Elasticity, *McGraw-Hill*, New York, NY.

17th International Symposium on Ice
Saint Petersburg, Russia, 21 - 25 June 2004
International Association of Hydraulic Engineering and Research

ICE RIDGE-STRUCTURE INTERACTION, PART I: GEOMETRY AND FAILURE MODES OF ICE RIDGES

Basile Bonnemaire[1] and Morten Bjerkås[1]

ABSTRACT

This paper addresses the interaction between first-year ice ridges and an instrumented lighthouse in brackish water. Altogether 33 interactions with relatively small ice ridges were selected and studied in detail. The deepest keel was 3.34 m and the highest sail 1.65 m. From 12 of the 33 selected ridges, the thickness of the consolidated layer was predicted based on loads on a vertically segmented panel. A ridge factor representing the thickness ratio between the consolidated layer and the parent ice sheet is found to be on average 1.45. Ice ridge – structure interaction is a complex process; it presents several failure modes such as crushing, bending, splitting and failure on rubble wedges. Snow cover does not seem to influence the ice loads significantly. Crushing failure seems to give the highest loads during interaction with ice ridges. Rubble wedge build-ups tend to save the structure from the highest ice loads.

INTRODUCTION

This is Part I of a series of two papers based on analyses of 33 interaction events including first-year ice ridges and the lighthouse Norströmsgrund in the Gulf of Bothnia. Offshore structures have to be designed to withstand environmental loads. In a milieu where only annual ice is present, loads from consolidated first year ice ridges or floating rubble fields often corresponds to the design criteria. As shown by recent surveys from e.g. Kärnä and Rim (1996) and Krankala and Määttänen (1984), the range of loads from first year ice ridges or rubble fields on Arctic structures is wide.

A ridge is an extended pile of broken ice blocks with a sail and a keel extending above and below the water line with a triangular-shaped cross section (Blanchet, 1998; see e.g. Timco and Burden (1997) for a general introduction to the shape of first-year ice ridges). Studies of ice ridges in the Baltic Sea were first conducted by Palosuo (1975). More recently, several studies of the shape and the density of Baltic ice ridges are reported e.g. by Kankaanpää (1997), Leppäranta and Hakala (1992) and Veitch et al. (1991). Among others, Hoikanen (1984) and Määttänen (1986) report on loads from Baltic ice ridges on the KEMI I lighthouse. Recently, Timco et al. (2000) gives an insight to the state of knowledge about loads on structures from first-year ice ridges.

[1] Norwegian University of Science and Technology Trondheim, Norway

Wright and Timco (2001) reports on ice ridge-structure interactions with the Molikpaq in the Beaufort Sea.

The contemporary work is based on analyses of full-scale data from the lighthouse Norströmsgrund in the Gulf of Bothnia, Sweden. From 19 February to 11 April 2002, loads and environmental measurements were conducted for 52 days. About 90 % of the monitored interactions between the lighthouse and single ice ridges were selected. Characteristics of the 33 involved ridges are given followed by a presentation of the observed failure modes. Part II of this paper addresses topics associated to the loads from the selected ridges and their surrounding ice sheets.

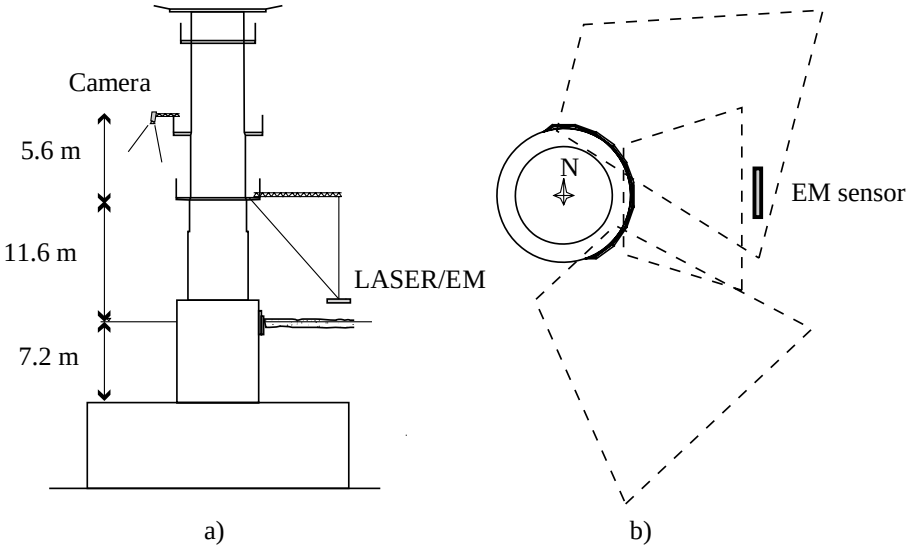

Fig. 1. a) Lighthouse Norströmsgrund with its experimental setup; b) camera coverage of the ice-structure interaction zone

EXPERIMENTAL SETUP

The lighthouse Norströmsgrund is a Gravity Based Structure (GBS) located 60 km offshore Luleå, Sweden, in the drifting ice zone. The foundation of the lighthouse is a sand filled concrete caisson resting on the seabed. This lighthouse was designed to withstand 50 MN plus safety margins loads from drifting ice features (Engelbrektson, 1977). The diameter is 7.6 m at the waterline and 23 m for the underwater caisson. The distance from the mean water level to the top of the caisson is 7.2 m (Fig. 1). The sides of the structure are vertical in the waterline.

Within the framework of the STRICE (Measurements of STRuctures in ICE) and LOLEIF (LOw LEvel Ice Forces) projects, the lighthouse Norströmsgrund was instrumented in order to measure the ice forces simultaneously with environmental parameters. A complete description of the experimental setup at the lighthouse Norströmsgrund during the STRICE/LOLEIF projects is given by Jochmann and Schwarz (1999, 2000) and Haas and Jochmann (2003).

RIDGE EVENTS CHARACTERISTICS

In 2002, continuous measurements were performed over a 52 day period. Upon visualization of records (video, load and thickness records; logbook), 33 interaction events with ice ridges were selected. These events are believed to be most of the ice

ridge interactions monitored in 2002. Some very small interacting ice ridges were not selected.

Geometry

Generally only small ridges were observed during the 2002 measurements, and the deepest observed keel was 3.3 m. Table 1 gives an overview of the mean geometrical properties of the ridges. Symbols h_k, h_s, h_c and h_i refer respectively to the keel, sail, consolidated layer and parent ice sheet thicknesses. The ridge factor is defined as $\psi_c = h_c/h_i$. Fig. 2a shows the measured sail height versus keel depth of the selected ridge events. The measured keel depths at Norströmsgrund seem to be shallower than the tendency described by the regression lines specified by Timco and Burden (1997) and Evers and Jochmann (1998). The sail heights found in the current study are in the range of those reported by Leppäranta and Hakala (1991). Nevertheless, the keel depths are notably shallower than reported by Leppäranta and Hakala (1991) and by Palosuo (1975). This tendency is especially true for the higher sail heights. The bottom profile of the ice formations was measured using an EM sensor. From measurements with both EM and Sonar devices, it was indicated that the deepest ridge keels get underestimated by the EM device. That could be the reason for the different trends in Fig. 2a.

Table 1. Geometrical characteristics of the ridges from the 33 selected events (h_c and Ψ_c were calculated for only 12 events).

	h_k [m]	h_s [m]	h_k/h_s	h_c [m]	h_i [m]	Ψ_c
Mean	1.87	0.71	3.0	0.69	0.54	1.45
Std. deviation	0.95	0.46	1.16	0.21	0.25	0.46
Max	3.34	1.65	6.67	1.05	1	2.45

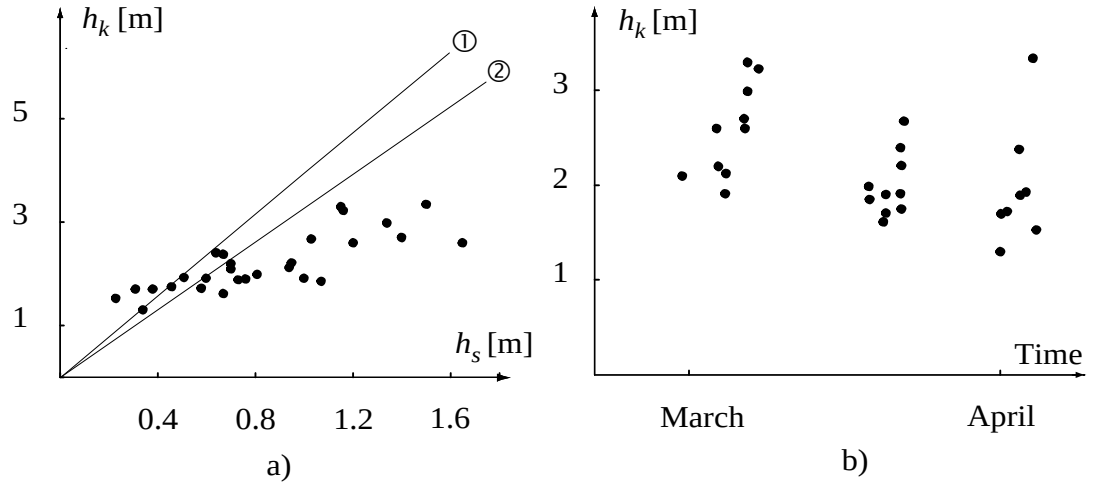

Fig. 2. a) Sail height versus keel depth from the 33 selected ridges and, regression lines by ① Timco and Burden (1997) and ② Evers and Jochmann (1998); b) keel depth versus time in the period 19 February to 11 April, 2002

Fig. 2b shows the ridge keel depth versus time during the measurement period. There is a weak tendency of decreasing keel depths during the season. An explanation for that could be erosion of the keel blocks and/or simply redistribution of ice blocks in the keel.

Ridge ratio Ψ_c

As described by e.g. Høyland (2000), the thickness of the consolidated layer can be estimated in several ways. Regrettably, no corresponding in-situ measurements are available for the 33 selected ridges in this study. Measurements from the vertically segmented load panel are therefore used to estimate the thickness of the consolidated layer (this panel was involved in only 12 of the interactions). The principal scheme of vertical pressure distribution in a ridge/vertical wall interaction shown by Hoikanen (1984) was used. The consolidated layer was estimated as the layer where ice pressures were exceeding 20% of the maximum local pressure. Part II details these calculations. These thickness estimates adjusted for water level fluctuations are also shown in Table 1.

The thickness of the parent ice sheet h_i is determined using video records, Laser/EM measurements and the logbook. When the crushing process is stable and the ice sheet profile looks regular, the parent ice sheet thickness h_i is defined. Høyland (2000) gives a review of ridge measurements and the ratio Ψ_c found by temperature measurements and/or drilling. A scatter from 1.24 (Coon et al., 1995) to 2.13 (Veitch et al., 1991) is found in that review. Ψ_c from the present study scatter as shown in Table 1. The mean value (1.45) is in the lower range of the review. This might indicate a low consolidation of the ridges encountered in 2002. The scatter of the present study is wider than what is reported by Høyland (2000). On one hand, this might be an indication on the accuracy of the method used here. On the other hand, the amount of ridges investigated here (12) is somewhat higher than in previous in-situ investigations. This might be a reason for this wider scatter.

Snow on ice

The presence of snow on the ice will alter the frictional properties of the top surface. This will affect the amount of ice that will accumulate in front of the interaction zone on top of the ice (Määttänen, 1986). The presence of snow on the parent ice sheet was frequently observed. A snow cover was present in 54% of the events. Jammed snow in the ridge sail was not taken into account if the parent ice sheet was uncovered. Remarkably, 93% of the events present no snow cover after 21 March, whereas 100% of the events are covered with 1 to 30 cm snow before 21 March. There seems to be no strong correlation between high loads on the structure and the occurrence of snow cover on the ice.

Surrounding ice

The video records and the log-book were consulted to determine properties of the ice surrounding the selected ridges. It could be a rubble field, rafted ice or simply level ice. Level or rafted ice was present in 74% of the events. In most cases it was not possible from video records to make a serious decision if the ice sheet was rafted or not.

Blanchet (1998) reports that a ridge within a rubble field will not fail by bending in the horizontal plane (around the vertical axis of the structure). Consequently, the failure of a consolidated ridge within a rubble field represent the dominant failure which will result in the highest load during an ice-structure interaction in a first-year ice environment (Blanchet, 1998). The horizontal bending failure of ridges has not been observed during these studies. No significant differences are observed between ridges surrounded by level/rafted ice and ridges surrounded by a rubble field. A reason could be that most of

Blanchet's observations are based on ridges from arctic conditions and the present data are colleted in a temperate/sub arctic region with significantly less consolidation.

FAILURE MODES

Four different failure modes were observed: *crushing*, *splitting*, *bending* failure and failure on a *wedge* formed in front of the structure. Due to the partial coverage of cameras (see Fig 1), there were no possibilities to observe the dodging failure as described by Kärnä and Jochmann (2003).

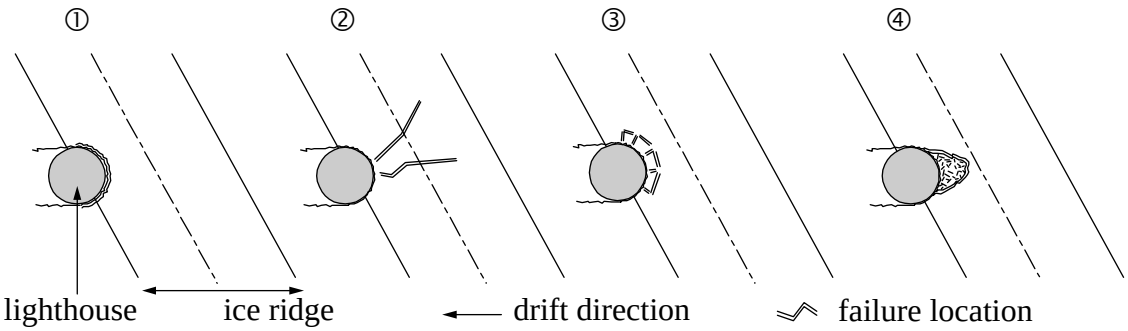

Fig. 3. Failure modes between an ice ridge (lines) and a cylindrical structure (top view);
❶: crushing, ❷: splitting, ❸: bending, ❹: wedge failure

Fig. 3 presents illustrating schemes of the observed failure modes. The lighthouse is a narrow structure compared to the ice ridge length and width. The structure acts as a small indenter; this may explain why neither local or global plug failure of the ridge (Wright and Timco, 2001) nor failure behind the ridge was observed. The relative consolidation of the ridges may explain this also.

Fig. 4a shows a typical ice ridge interaction time series. The upper plot is the ice profile from the EM and Laser devices. The lower plot is the estimated global load on the structure from the load panel measurements. Please note that the axis for the force is not scaled as no physical values are allowed to be shown because of a confidential agreement within the STRICE-Project.

The sequence is the following:

- ①: level ice is crushing against the structure. The forces are relatively low and of a stochastic nature;
- ②: the ridge starts to fail in crushing, the load presents a saw tooth profile;
- α: the load in the interaction zone reaches a maximum. The force necessary to develop splitting failure is reached; there is a change in failure mode;
- ③: the fragments from the splitting failure cannot be evacuated, a wedge builds up in front of the structure. The incoming ice fail on the wedge, the load level on the structure is low. The rubble wedge usually builds up to a max length approximately two times the diameter of the structure. The wedge length varies in time, it usually increases till some collapse appears within the wedge that cause its partial reduction;
- β: the wedge builds up in height and ice accumulates on the lighthouse balcony;

- γ: some higher forces are recorded on one of the panel on the side of the interaction zone; the incoming ice at that point did not meet the wedge and fails in crushing directly on the structure;
- ④: the wedge collapses under the pressure of the incoming ice and the fragments can be cleared around the structure, the ridge event is almost finished;
- δ: the virgin level ice impacts the structure;
- ①: level ice crushing with some local bending failure restarts.

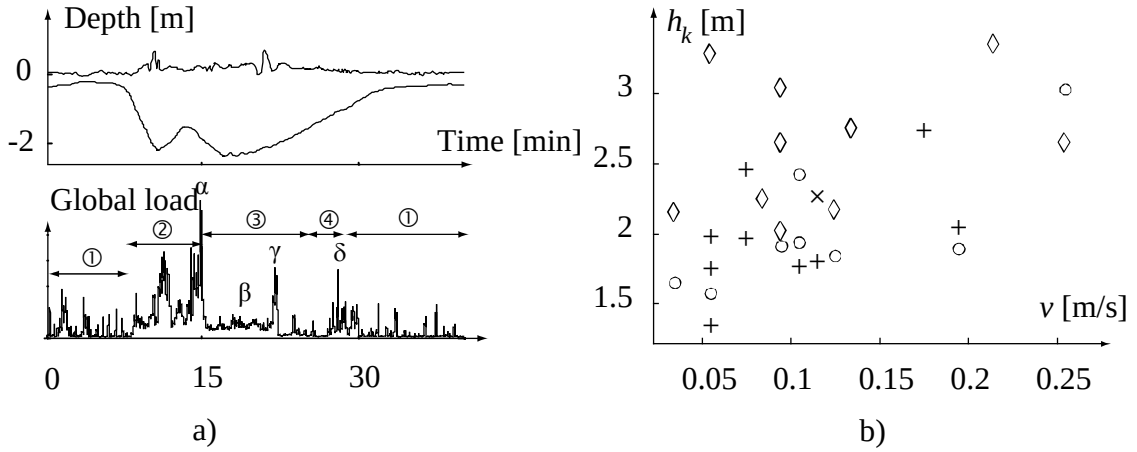

Fig. 4a). Ridge loading event start 11:00, 2 April 2002 at the lighthouse Norströmsgrund, h_i = 0.3 m, h_s = 0.7 m, h_k = 1.9 m, Ψ_c = 1.27., 4b). Failure mode map (◊: crushing and failure on wedge; ○: crushing and bending; ×: crushing and splitting; +: only crushing)

Fig. 4b is a failure mode map in the (h_k – v) plane, where v is the far field drift speed. Crushing failure was observed in all events. It was sometimes associated with other failure modes. Bending (or buckling) and splitting failure was often associated with crushing, these failure modes alternated depending on the homogeneity of the ridge. In 11 cases, failure on a rubble wedge took place. In these cases, crushing failure takes place first followed by splitting or bending that produce a big quantity of rubble in front of the lighthouse. This ice is compacted in a wedge and the incoming ice fails on this wedge. The length of the rubble wedges were in the range of 1-2 lighthouse diameters before they tend to collapse.

The failure modes are rather spread over the failure map. Nevertheless some tendencies are observed. The events with pure crushing concern more shallow and slow drifting ridges whereas wedge failure tends to happen more often with deeper ridges. Unfortunately this mapping is not complete; all the keel depths are not represented at all speeds. Another important factor is the ridge consolidation; it does not appear in that plot. It is believed to play an important role in the selection of the failure mode that will require less energy.

Analysis of all the events showed that the failure mode giving highest forces was pure crushing of the ridge. Nevertheless, the maximum forces in that failure mode are limited, as soon as there is enough force in the ice sheet to trigger bending or splitting failure, the failure mode changes and the load drops. If the fragments cannot be cleared then, wedge failure appears inducing limited loads.

CONCLUSIONS

Part I of this paper addresses the interaction between first-year ice ridges and a lighthouse in brackish water. Altogether 33 relatively small ice ridges were selected and studied in detail. From 12 of the ice ridges, a thickness of the consolidated layer was assumed. Key points from this study are:

1. The deepest keel found is 3.34 m and the highest sail is 1.65 m.
2. From 12 ridge interactions with the vertically segmented panel, the ridge factor based on consolidation is found to be on average 1.45.
3. Snow cover does not seem to influence the ice loads significantly.
4. Ice ridge – structure interaction is complex and the following failure modes were observed: crushing, bending, splitting and failure on a rubble wedges.
5. Crushing failure seems to give the highest loads during interaction with ice ridges.

Further work should be stressed on a more through understanding of the failure modes of first-year ice ridges.

ACKNOWLEDGEMENTS

Discussions with Associated Professor Knut V. Høyland from the University centre on Svalbard (UNIS) are very much appreciated. Likewise is the work of Peter Jochmann, Hamburg Ship model Basin (HSVA), who kindly has sheared data and information from the measurements with the authors. The full-scale measurements were funded by the European Commission DG RESEARCH under the Fifth Framework Programme for Research and Development within the Energy, Environment and Sustainable Development (EESD) Programme under the Key Action RTD activities of a generic nature (Contract No. EVG1-CT-2000-00024).

REFERECNCES

Blanchet, D. (1998), Ice loads from first-year ridges and rubble fields, *Canadian Journal of Civil Eng*. Vol 25, pp. 206-219.

Coon, M.D., Douglas, C.E. and Gerald, S.K. (1995), Force displacement measurements of a first year pressure ridge keel, *ASME Ice Mechanics*, AMD-Vol. 207, pp. 239-254.

Engelbrektson, A., (1977), Dynamic ice loads on a lighthouse structure, *POAC'77*, New Foundland, Canada, pp. 654-663.

Evers, K-U. and Jochmann, P. (1998) Determination of the topography of pressure ice ridges in the Laptev-Sea. IAHR, 98. Potsdam, USA, Vol 1, pp. 331-337.

Haas, C. and Jochmann, P. (2003), Full scale measurements at Lighthouse Norströmsgrund – winter 2002-Annex H1 EM ice thickness measurements, HSVA, Germany, 77 p.

Høyland, K.V. (2000), Measurements and simulations of consolidation in first-year sea ice ridges, and some aspects of mechanical behaviour, Phd. Thesis, NTNU, Trondheim, Norway, 151 p.

Hoikanen, J. (1984), Measuremnets and analysis of ice pressure against a structure in level ice and in pressure ridges. IAHR'84, Hamburg, Germany, pp. 151-160.

Jochmann P. and Schwarz, J. (2000), Ice force measurements at lighthouse Norströmsgrund-Winter 2000. *LOLEIF Report No 9.HSVA*, Germany, 64 p.

Jochmann P. and Schwarz, J. (1999), Ice force measurements at lighthouse Norströmsgrund-Winter 1999. *LOLEIF Report No 5. HSVA*, Germany, 48 p.

Kankaanpää, P. (1997), Distribution, morphology and structure of sea ice pressure ridges in the Baltic Sea, Fennia 175:2, pp. 139-240. Helsinki, ISSN 0015-0010

Kärnä, T. and Jochmann, P. (2003), Field observations on ice failure modes, POAC'03, Trondheim, Norway, pp. 839-848.

Kärnä, T. and Rim, C.W. (1996), Model for global first-year ice loads, VTT Building Technology, Finland, *VTT Internal Report*, RTE39-IR-9/1996.

Krankala, T. and Määttänen, M. (1984), Methods for determining the forces due to first and multi-year ridges, *Proc. of the IAHR'84,* Hamburg, Germany, pp. 263-280.

Leppäranta, M. and Hakala, R. (1992), The structure and strength of first-year ice ridges in the Baltic Sea, *Cold Regions Science and Technology*, 20, pp. 295-311.

Leppäranta, M., Lensu, M., Kosloff, P., and Veitch, B., (1995). The life story of a first- year sea ice ridge. *Cold Regions Science and Technology*, 23, pp. 279-290.

Määttänen, M. (1986), Test Cone Project, Proc. Polartech '86, Technical Research Centre of Finland, *Symposium 71, Espoo,* Finland, Vol II, pp. 749-761.

Timco, G.W. and Burden, R.P. (1997). An analysis of the shape of sea ice ridges. *Cold Regions Science and Technology,* 25: pp. 65-77.

Timco, G.W., Croasdale, K. and Wright, B. (2000). An overview first year sea ice ridges. *Technical report, PERD/CHC Report* 5-112.

Palosuo, E. (1975), Formation and structure of ice ridges in the Baltic, *Winter Navigation Research Board,* Rep. No. 12, Board of Navigation, Helsinki.

Veitch, B., Lensu, M., Riska, K. Kosloff, P, Keiley, P. and Kujala, P. (1991), Field observations of ridges in the Northern Baltic Sea, POAC'91, St. Johns, Canada, pp. 381-400.

Wright, B. and Timco, G.W. (2001), First-year ridge interaction with the Molikpaq in the Beaufort Sea, *Cold Regions Science and Technology*, 32, pp. 27 -44.

17th International Symposium on Ice
Saint Petersburg, Russia, 21 - 25 June 2004
International Association of Hydraulic Engineering and Research

ICE RIDGE-STRUCTURE INTERACTION, PART II: LOADS FROM ICE RIDGES AND THEIR SURROUNDING ICE SHEETS

Morten Bjerkås[1] and Basile Bonnemaire[1]

ABSTRACT

Part II of this paper addresses the ice loads from interactions between first-year ice ridges and a lighthouse in brackish water. Altogether 33 relatively small ice ridges that interacted with the Norströmsgrund Lighthouse were selected and studied in detail. The most significant loads from ice ridges seem to be concentrated in the upper part of the ridge, from the water line and below. From crushing failure of ridges, a concentration of loads is observed parallel to the drift direction. When ice ridges fail on a rubble wedge, loads seem to be concentrated on the two borders of the rubble wedge, usually ±90° to the drift direction. The load levels are usually small. The loads from ridges are 0.5 to 6 times higher than from the surrounding ice sheet. The ridge loads are in the same range as those from level ice crushing events. Loads from ice ridges seem to increase with the sail height. It was found no proof to claim that loads from ice ridges exceed the loads from level ice sheets.

INTRODUCTION

This is Part II of a series of two papers based on analyses of 33 selected interaction events including first-year ice ridges and the lighthouse Norströmsgrund in the Gulf of Bothnia. The selected interactions took place between 19 February and 11 April, 2002. Very little is known about the interaction of first-year ice ridges with offshore structures. The loads from ice ridges are viewed as governing the design ice loads for offshore structures. This paper offers information on how loads form first-year ice ridges are distributed on the structure during ice ridge – structure interactions. A continuance of the discussion from Part I on how loads from ridges differ from loads from the parent ice sheet is given. Ridge factors are calculated based on differences in magnitudes of ice loads between the parent ice sheet and the ice ridge. A discussion is presented on the ridge factor based on the thickness of the consolidated layer as described in Part I and the ridge factor presented herein. Supplementary information on ridge factors is reported by Høyland (2000); VSN (1988) and Wright and Timco (2000).

[1] Norwegian University of Science and Technology Trondheim, Norway

DATA INTERPRETATION

Ice load time series that were obtained from the ice load panels on the lighthouse Norströmsgrund have been used to evaluate first-year ridge load levels and characteristics of failure of selected ridges. As many as 33 discrete relatively small first-year ice ridges were selected. Twelve of the selected ridges were in sufficient contact with a vertically segmented panel facing towards east. A synchronizing tool was developed with the MATLAB™ software to deliver packages with records for further analyses. All events were selected in such a way that the data records contain information from the surrounding ice sheets as well as from the ridges. One data record of information contains time series of load and ice thickness, environmental data, video records, comments from the logbook and several key parameters as snow coverage and height of rubble pile-up.

LOADS FROM ICE RIDGES

Ice ridges are often divided into sail, consolidated layer and keel (Fig. 1b). In the same way, the loads from ice ridges are regularly divided into corresponding parts, sail loads F_s, loads from consolidated layer F_c and keel loads F_k (Fig. 1a). Prediction of ice-ridge loads is not a simple task, the ridge failure process is complex and the real ridge load is not easy to measure. As shown by Timco et al. (2000), an amount of models are presented, however none of the models takes into account 3-dimensional effects and/or velocity effects. This paper shows typical examples of vertical (Fig. 1a) and horizontal (Fig. 1c) distribution of pressure from few selected ice-ridge interaction events which are assumed to be representative. Table 1 shows characteristics of six of the 33 selected events.

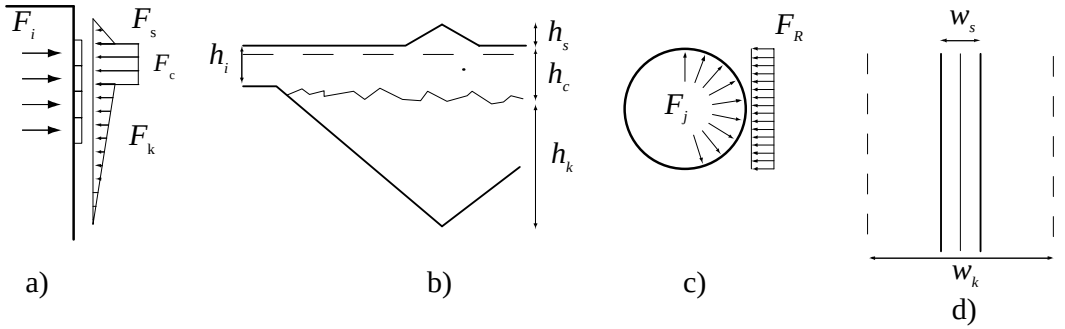

Fig. 1. a) Side view of the base with the segmented panel forces, F_i. Assumed sail loads from: ridge sail F_s, consolidated layer F_c, and ridge keel F_k. (after Hoikanen, 1984 and Krankala and Määttänen, 1984); b) ice ridge with sail height h_s, consolidated layer thickness h_c, and keel depth h_k. (after Leppäranta and Hakala, 1991); c) top view of the lighthouse with the panel forces F_j, ridge load F_R; d) ice ridge with keel width w_k and sail width w_s

Vertical distributed loads

Several ridge load models are formulated as static equivalent load distributions as shown in Fig. 1a. Fig. 2 shows five cases (a – e) of vertical distributed ice loads on the segmented panel during five ice - structure interaction events (details in Table 1).

The sail heights and keel depths are indicated with dashed lines and the water level with a dotted line. Peak loads will most probably occur non-simultaneously through different layers in the ice ridge. Consequently the mean value over time of forces on a segment is

used further. During one ridge passage the mean value reads $\mu_i = E[F_i(t)]$ where $F_i(t)$ is the time varying ice load and i is the name of the segment (1 to 4). A density of the mean value μ_I is defined as:

$$\rho_i = \frac{\mu_i}{\max(\mu_k)_{k=1 \text{ to } 4}}, \quad i = 1 \text{ to } 4 . \tag{1}$$

Table 1. Summary of ridge loading events 2002, LI = Level ice, CR = Consolidated rubble.

#	h_i [m]	h_s [m]	h_k [m]	v [m/s]	ψ_c	ψ_L	Parent ice	Figure
1	0.5	-	-	0.20	1	1	-	3c /2e
6	0.5	1.4	2.7	0.12	1.8	0.5	LI	2a
7	0.5	1.7	2.6	0.13	2.6	1	CR	2b
9	0.6	1.3	3.0	0.25	1.5	0.3	CR	2ab
18	1	0.6	1.9	0.07	0.8	1.5	LI	2c
21	0.2	0.5	1.8	0.11	1.7	0.2	LI	2d

Fig. 2 shows ρ_i projected in the vertical direction with step lengths equal to the height of one segment, 0.38 m.

It can be seen that the foremost part of the load is applied on the panel through the two or sometimes three highest segments. As described in Part I of this paper, a threshold is defined such that the density of average loads on one segment have to reach 20 % of the max density if the segment should be assumed to have loads from the consolidated layer. If the water line is above the top of the upper segment, the distance from the upper segment to the waterline is also assumed to have full load. On the other hand, if the water level is below the top of the panel, the full segment height is assumed to have load. Fig. 2a shows a case where the water level is 0.15 m above the panel and the two uppermost segments have densities of loads higher than 20 %. In this case the consolidated layer is assumed to be $h_c = 2 \times 0.38 + 0.15$ m = 0.91 m. In Fig 2b as many as three panels have densities higher than 20 %. Then h_c is $3 \times 0.38 + 0.15$ m = 1.29 m. In both Figs. 2b and 2c the lower segments have densities in the range of 2 - 10 %. The load is assumed to go to zero at the depth h_k.

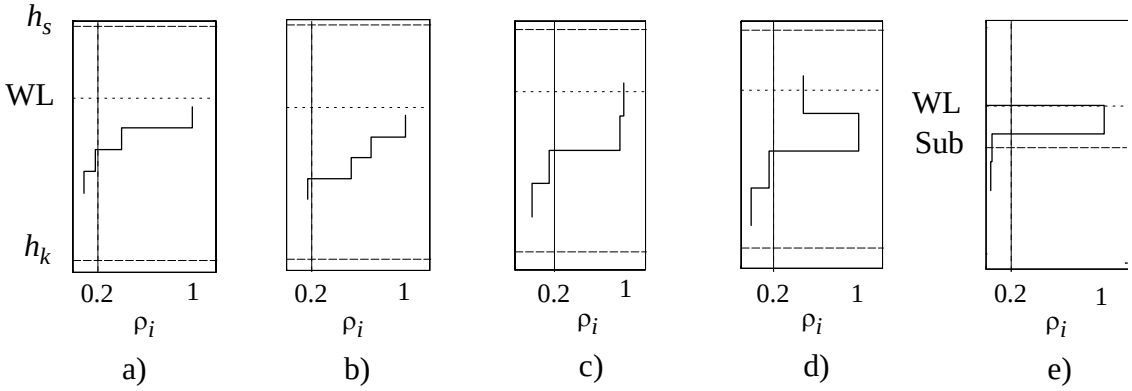

Fig. 2. Density of forces on a segmented panel from ridges (a - d) and level ice (e) interactions

Fig. 2c illustrates a case with a concentrated load on the two upper segments and densities lower than 20 % on both the two lowermost segments. The water line in this case is underneath the top of the panels. The consolidated layer is assumed to be h_c = 2 × 0.38 = 0.76 m. In Fig. 2d parts of the uppermost segments are probably above the consolidated layer and into the sail of the ice ridge. The sail is most probably not consolidated and gives densities of loads in the range of 50 %. However, the consolidated layer is assumed also here to be 0.76 m. Fig. 2d shows that the loads from the sail is significantly lower than the loads from the consolidated layer. Fig. 2e shows a case with a level ice sheet with thickness h_i = 0.5 m and the water level exactly on the top of the panels. The main part of the load (as expected) acts on the uppermost segment.

From studies of the vertical distribution of loads on a segmented panel, it is found that during ice ridge - structure interactions, most of the loads seem to be applied through the two or three uppermost segments. It is believed that the thickness of the layer in ice ridges that gives the most significant contribution to the load is a function of the refreezing/consolidation of ridges. The loads from the partly consolidated and unconsolidated parts of ridges in the keel section could both remain minor or significant. It should be mentioned that peak loads from different levels in the more or less consolidated parts of the ice ridge will occur non-simultaneously; consequently peak loads from single segments should not be added to assume design loads. More studies have to be conducted to predict the loads from the partly consolidated zones of ridges.

Horizontal distributed loads

Uniformly distributed pressure around the structural perimeter is regularly assumed during level ice crushing events. Little is known, but this is most likely not the case for ice ridge interactions. For narrow cylindrical structures, the ice - structure interaction zone is supposed to cover 180° of the structural perimeter. Lighthouse Norströmsgrund is instrumented with nine load panels, covering 162° of the perimeter (Jochmann and Schwarz, 1999, 2000). From one selected interaction with an ice-ridge (no. 9 in Table 1), the distribution of forces around the perimeter will be calculated. Peak values will most probably not occur simultaneously around the perimeter, consequently the mean value of forces through out a ridge passage is used. The average value of the forces in one panel is defined as $\mu_j = E[F_j(t)]$, where F_j is the load from one panel and j is a number from one to nine. A density of the mean values is defined as:

$$\rho_j = \frac{\mu_j}{\max(\mu_k)}, \quad j = 1 \text{ to } 9, \tag{2}$$

where j is the panel number. Fig. 3 shows how the densities in Eq. (2) are distributed around the covered parts of the perimeter from a ridge failing by crushing and with a rubble wedge as described in Part I. For evaluation, a distribution of densities from crushing failure of a level ice sheet is shown. The densities are shown as step functions with step length equal to the width of panel 1.2 m.

In Fig. 3a the density ρ_j is shown on the covered part of the perimeter. The drift direction is 0° and ±90° is the normal to the drift direction. The peak densities are located approximately in the drift direction during the crushing mode. This event

endured one minute. Fig. 3b shows the same event as in Fig. 3a, but now failing on a rubble wedge. During these 50 seconds of failure on the rubble wedge, the densities are distributed less in the drift direction and more normal to the drift direction.

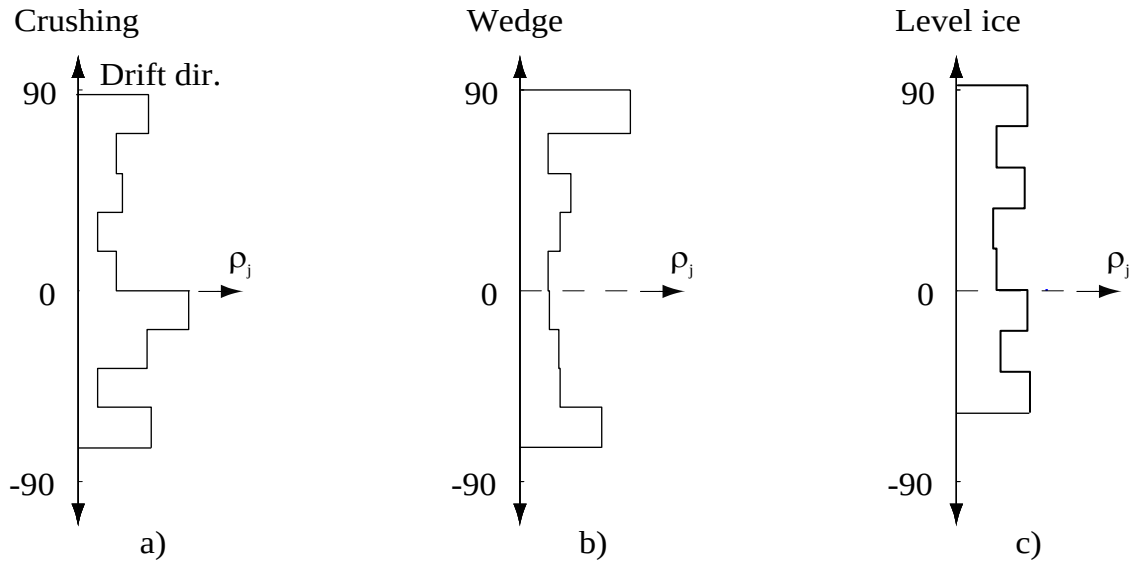

Fig. 3. Density of average values from (a) crushing of an ice ridge, (b) failure on a rubble wedge, (c) failure of a level ice sheet. Please note the axis for the force is not scaled as no physical values are allowed to be shown because of a confidential agreement within the STRICE-Project

Panels located inside the rubble wedge have regularly a low amount of loads. The rubble wedge is covering less than 180° of the interaction zone. Crushing failure is often observed on the border of the rubble wedge, and that could be the reason for the higher intensity of loads in these zones. It should be remarked that the global ice loads to the structure from the wedge failure mode is low (Part I). Fig. 3c shows the densities of forces from a level ice sheet crushing to the structure. The densities are more evenly scattered than in both the ridge events. The event in Fig. 3c endured in 2 minutes. From calculations of densities of mean values of forces, the crushing failure of ridges seems to give more concentrated loads than crushing failure of level ice. A reason could be that the ridge acts as a floating beam hitting the structure and induces high local pressures on a limited part of the structural width. Conversely, no horizontal bending of ridges has been observed, for that reason it could be other explanations for the concentration during crushing failure of ridges.

Ridge factors

Global loads from level ice sheets to structures have been extensively studied the last four decades, and a large amount of data is available (Masterson and Frederking, 1993). The aim of the ridge factor is to have a factor that describes the differences between loads from level ice sheets and loads from ice ridges. In this study, the ridge factor has been calculated in two unlike ways. Part I shows a ridge factor based on the thickness of the most active layers and the thickness of the surrounding ice sheet. In this part the ridge factor is based on the measured global loads from the ridge and the surrounding ice sheet, and are defined as

$$\psi_L = \frac{F_R}{F_{LI}}, \tag{3}$$

where F_R is the ridge load and F_{LI} is the load from the surrounding ice sheet. Ridge factors are regularly reported in the literature by e.g. Høyland (2000) and Timco et al. (2000) based on different approaches. It is noteworthy that the ridge factor value is independent of ridge size (Wright and Timco, 2001). From 33 selected events with ice ridge – structure interaction, loads from the parent ice sheet and the global load from the ridge interaction were selected. It was observed that the max global load from ridges not always occur at the same time as the max keel depth. When the ridge was enclosed by unconsolidated rubble ice, the loads were generally very low from the enclosing ice sheet. On the other hand when a continuous level ice sheet surrounded the ridge, the load was high if the failure mode was pure crushing and low if the failure mode was bending or splitting.

From Eq. (3), it was found that the ridge factors typically ranged from 0.5 to 6, with average 3.15 (Fig. 4a). The lowest values were caused by high loads from the parent ice sheet and low loads from the ridge. It was believed that it was because the ridge was young and little consolidated. The surrounding ice sheet when the low ridge factors occurred was both consolidated rubble fields and continuous level ice floes. The high values were caused by ridges surrounded by little consolidated rubble fields and continuous level ice sheet that failed in bending or splitting failure modes. Fig. 4a shows a correlation plot between the calculated ridge factor $\psi_c = h_c/h_i$ from Part I and the ridge factor determined from the global load calculation as defined in Eq. (3). It shows that the ψ_c have scatter from 0.8 to 2.45 and ψ_L from 0.5 to 6. The magnitudes are notably different but a correlation is to be seen. The values of ψ_c are in the range of the average level reported by e.g. Høyland (2000). The ridge factor based on global load prediction is higher than what have been recommended in codes VSN (1988), and what have been reported elsewhere in the literature. However, Wright and Timco (1999) have reported that ridge factors based on loads from the parent ice sheet and the ice ridge itself seems to be higher than what are suggested in Russian codes. From the present study, it is found that the loads from relatively small first-year ridges are lower than what have been caused by consolidated ridge fields and in the same range as loads from level ice crushing events.

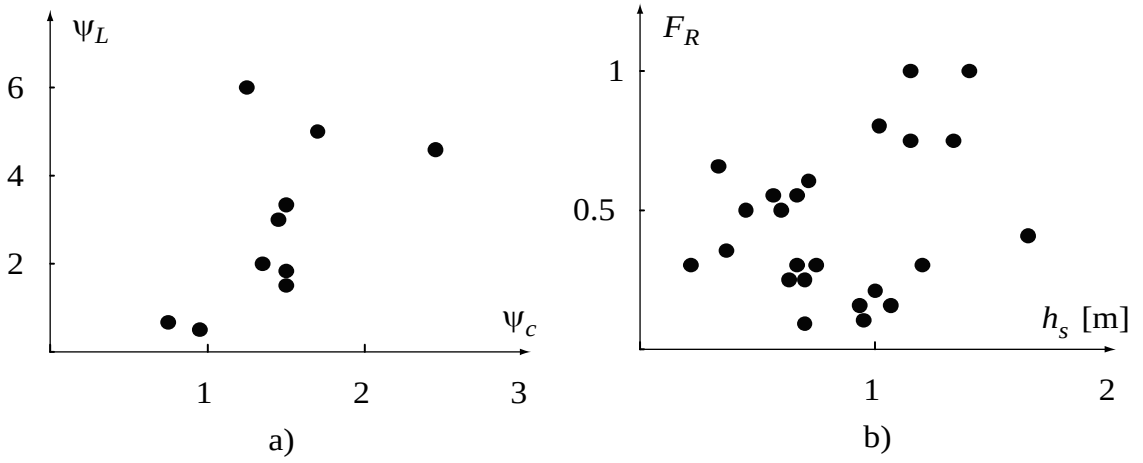

Fig. 4. a) The ridge factor based on measured loads ψ_L versus the ratio between an assumed consolidated layer thickness and the parent ice sheet thickness ψ_c, b) measured sail height h_s versus the peak global ridge load F_R

The ridge sail height h_s is a common measure of the size of ice ridges (Timco and Burden, 1997). Fig. 4b shows the global ridge loads versus the sail heigth h_s. It seems to be an affinity of increasing global load with increasing h_s. The sail heights found in the present study are in the same range as those reported by Leppäranta and Hakala (1991), however smaller than 3.5 m reported by Palosuo (1975).

CONCLUSIONS

Part II of this paper addresses the ice loads from interactions between first-year ice ridges and a lighthouse in brackish water. Altogether 33 relatively small ice ridges were selected and studied in detail. The key points from this part of the study are that:

1. The most significant loads from ice ridges seem to be concentrated in the upper part of the ridge, from the water line and below.
2. From crushing failure of ridges, a concentration of loads is observed parallel to the drift direction.
3. When ice ridges fails on a rubble wedge, loads seems to be concentrated on the two borders of the rubble wedge, usually ±90° to the drift direction. The load levels are usually small.
4. The loads from ridges have been calculated to be 0.5 to 6 times higher than the surrounding ice sheet.
5. The ridge loads are in the same range as those from level ice crushing events.
6. Loads from ice ridges seem to increase with the sail height. It was found no reason to claim that loads from ice ridges exceed the loads form level ice sheets.

Efforts should be offered to detect which ice features gives the highest global loads to structures in sub-arctic regions and how forces are distributed both spatially and temporally.

ACKNOWLEDGEMENTS

Discussions with Associated Professor Knut V. Høyland at the University centre on Svalbard (UNIS) are very much appreciated. Likewise, the work by Peter Jochmann, Hamburg Ship model Basin (HSVA) who kindly has sheared data and information from the measurements with the authors. The full-scale measurements were funded by the European Commission DG RESEARCH under the Fifth Framework Programme for Research and Development within the Energy, Environment and Sustainable Development (EESD) Programme under the Key Action RTD activities of a generic nature (Contract No. EVG1-CT-2000-00024).

REFERECNCES

Frederking, R.M.W., Timco, G.W. and Wright, B.D. (1999), Ice Pressure Distribution from First-Year Sea Ice Features Interacting with the Molikpaq in the Beaufort Sea., ISOPE'99, Brest, France, pp. 541-548.

Haas, C. and Jochmann, P. (2003), Full scale measurements at Lighthouse Norströmsgrund –winter 2002-Annex H1 EM ice thickness measurements, HSVA, Germany, 77 p.

Høyland, K.V. (2000), Measurements and simulations of consolidation in first-year sea ice ridges, and some aspects of mechanical behaviour, Phd. Thesis, NTNU, Trondheim, Norway, 151 p.

Jochmann P. and Schwarz, J. (2000), Ice force measurements at lighthouse Norströmsgrund-Winter 2000. *LOLEIF Report* No 9.HSVA, Germany, 64 p.

Jochmann P. and Schwarz, J. (1999), Ice force measurements at lighthouse Norströmsgrund-Winter 1999. *LOLEIF Report* No 5. HSVA, Germany, 48 p.

Kärnä, T. and Jochmann, P. (2003), Field observations on ice failure modes, POAC'03, Trondheim, Norway, pp. 839-848.

Korzhavin, K.N. (1962), Action of ice on engineering structures, Siberian Department of Academy of Science, Novosibirsk.

Leppäranta, M. and Hakala, R. (1992), The structure and strength of first-year ice ridges in the Baltic Sea, *Cold Regions Science and Technology*, 20, pp. 295-311.

Masterson, D.M. and Frederking, R.M.W. (1993), Local contact pressure in ship and structure/ice interactions, *Cold Regions Science and Technology*, 21, pp. 169-185.

Palosuo, E. (1975), Formation and structure of ice ridges in the Baltic, Winter Navigation Research Board, Rep. No. 12, *Board of Navigation*, Helsinki.

Timco, G.W. and Burden, R.P. (1997). An analysis of the shape of sea ice ridges. *Cold Regions Science and Technology*, 25: pp. 65-77.

Timco, G.W., Croasdale, K. and Wright, B. (2000). An overview first year sea ice ridges. *Technical report, PERD/CHC Report* 5-112.

VSN, (1988), Designing of Stationary Ice-Strengthened Platforms. VSN 41.88, Moscow, Russia.

Wright, B. and Timco, G.W. (2001), First-year ridge interaction with the Molikpaq in the Beaufort Sea, *Cold Regions Science and Technology*, 32, pp. 27 -44.

17th International Symposium on Ice
Saint Petersburg, Russia, 21 - 25 June 2004
International Association of Hydraulic Engineering and Research

EXPERIMENTAL INVESTIGATIONS OF VERTICAL ICE LOADS ON PILES

Frank Weichbrodt[1], Christian Dede[2], Jörg Radomski[3], Sören Kohlhase[4]

ABSTRACT

Within a comprehensive research project aiming at the development of design rules for wooden piles used for coastal engineering purposes, large scale laboratory investigations on vertical ice forces are performed in the Institute for Hydraulic and Coastal Engineering Rostock. Vertical ice forces are effected by an ice cover frozen to the piles. In combination with a rising water level uplift forces on the pile must be expected which may exceed the resistant forces leading to a failure of the coastal structure. In contrast to first assumptions the failure is caused by exceeding ice resistance against bending. In addition the measured vertical ice forces are remarkable higher than calculated by German standard methods (EAU). To dimension the necessary holding forces and to define the necessary ramming depths of (groyne) piles the vertical ice forces on wooden piles are compared to subsoil holding forces measured in field tests on the Baltic coast of Germany.

INTRODUCTION

Wooden groyne piles represent an important part of coastal protection structures against erosion on the Baltic coast of Germany. The German Ministry for Research and Education has initiated a research programme to investigate the loading forces on piles and the respective resistant forces. The aim of the project is the development of scientific rules for the dimensioning of ramming depths of wooden (groyne) piles. In addition to wave forces vertical ice loads on piles are one of the most important loads acting on nearshore piles on the Baltic coast.

Vertical ice loads on piles are effected by an ice cover frozen to the pile and lifted up during water level rise. Piles then can be pulled out of the sea floor, known as ice-jacking. Since cold winters occur only rarely on the German coast and cannot be

[1] Dipl.-Ing., Researcher, Institute for Hydraulic and Coastal Engineering (IWR), University of Rostock, iwr@bau.uni-rostock.de
[2] Dr. rer. nat., Researcher, IWR, University of Rostock
[3] Dipl.-Ing., Researcher, IWR, University of Rostock
[4] Prof. Dr.-Ing. habil., Director, IWR, University of Rostock

predicted ice loads transmitted from an ice cover onto wooden piles need to be investigated in laboratory.

Vertical ice loads on wooden piles depend on ice genesis, ice thickness, temperature, salinity, surface of the pile, pile diameter and velocity of water level rise. Loads increase with increasing loading velocity (water level rise). For the German coast maximum rates of water level rise were measured as 0,5m/h. However under natural conditions the ice sheet is rather flexible. As a consequence, the failure of the system pile-ice does not occur directly at the pile but mostly at a certain distance to the pile. This is also caused by the fact that the thickness of the ice cover is increased in the contact area of the pile which also leads to clamping effects (ice collar at the pile). Generally the ice sheet may fail by exceeding its bending strength as well as its shear strength. Since the main aim of the project was to determine realistic loads on piles, ice thickness in the laboratory tests must not exceed a few centimetres to exclude the influence of the given model boundary. Otherwise the radius of ice deformation would increase beyond the margin of the tank and shear failure would occur between wood surface and ice.

LABORATORY TESTS

The ice tests are performed in the climate chamber of the Rostock University, Department of Civil Engineering. Temperatures down to –25°C can be produced. Tests were conducted in a circular water tank, with 2,5 m in diameter and a depth of 0,7 m. A wooden pile (0,2 m diameter, tropic wood with high modulus of elasticity) was frozen in the middle of the tank (figure 1). In order to produce an ice sheet with only small thickness, the tank was insulated. Air temperature in the climate chamber, water temperature in the tank, temperature in the isolation layer and ice temperature in the ice sheet was controlled by 28 temperature sensors (T 30). Temperature profiles in the ice sheet and water at different places were recorded.

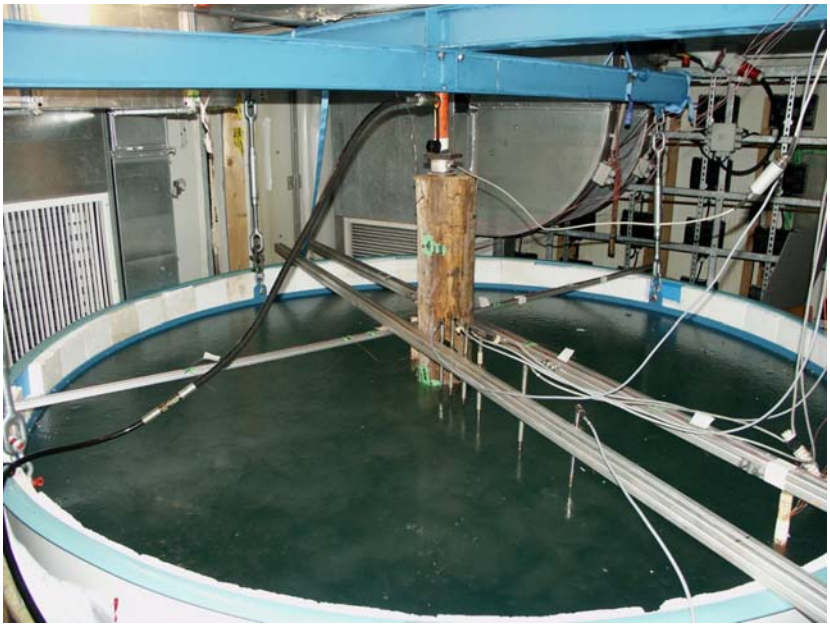

Fig. 1. Test tank with frozen pile in climate chamber

In order to receive reproducible ice properties the water in the tank was mixed during cooling down to a uniform temperature of 3 - 4°C to develop a stable temperature profile in the tank. Air temperature was between –14° C and –17°C. In this manner ice with reproducible mechanical properties was produced. The mechanical ice properties were investigated by testing compression strength of ice cylinders from the ice sheet. PE-pipes were installed in the tank floating at water surface. After ice growth the PE-pipes with ice were taken out of the tank. The ice cylinders can be easily dismantled from the pipes without damage for compression strength tests. Experiments to determine bending strength of the ice are not so successful compared with compression strength determination because undisturbed sampling of ice is difficult.

To investigate the forces transmitted from ice to pile, the pile was hydraulically pressed downwards at defined velocity until failure occurred. Load and deformation of the ice sheet were digitally recorded by a load cell and seven displacement sensors (figure 2). Before pressing the pile downwards, some holes were drilled into the ice sheet to reduce the hydrostatic pressure, which develops by ice volume extension during ice growing. Up to now 12 experiments with different ice thicknesses were performed.

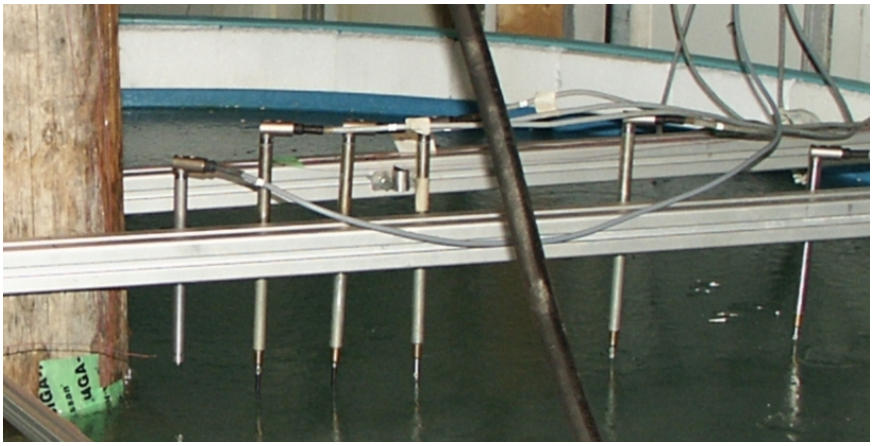

Fig. 2. Measurement of deformation of ice sheet

RESULTS OF EXPERIMENTS

For small ice thickness (<100 mm) failure of the system pile-ice does not occur directly at the pile surface directly but at a certain distance to the pile within the ice cover. Failure is caused by exceeding the bending strength or the shear strength of ice. Figure 3 shows typical deformations of the ice cover for small ice thickness and failure load.

For ice thickness of more than 100 mm only a small deformation of the ice cover is measured. Failure of pile-ice-system occurs directly at the pile surface. The measured forces for shear failure (wood-ice, ice thickness >100 mm) are smaller then measured forces for smaller ice thickness with deformation of the ice cover (failure by exceeding of bending strength). In nature the ice deformation is not restricted. Because of an ice collar at the pile shear failure of this type does not occur on naturally piles.

During the experiment, it was observed that first radial cracks appear after loading of the ice cover and later concentric cracks are formed. In figure 4 a load-deformation diagramme for different ice thickness is presented. The maximum loads transmitted from pile to ice (in nature from ice to pile) are between 4,5 KN and 15,5 KN, with ice thickness from 40 to 100 mm (figure 5).

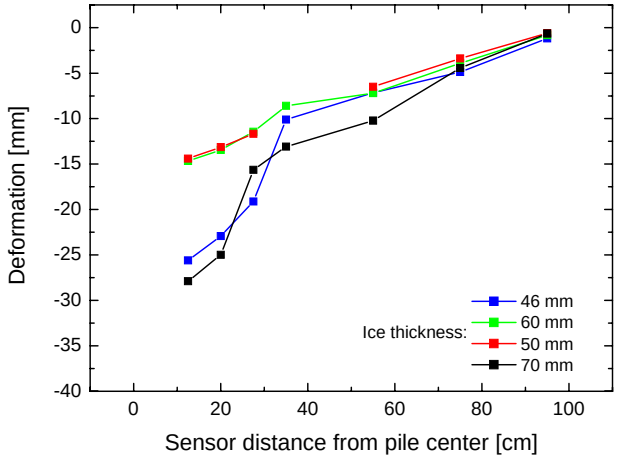

Fig. 3. Deformation of ice surface under maximal load

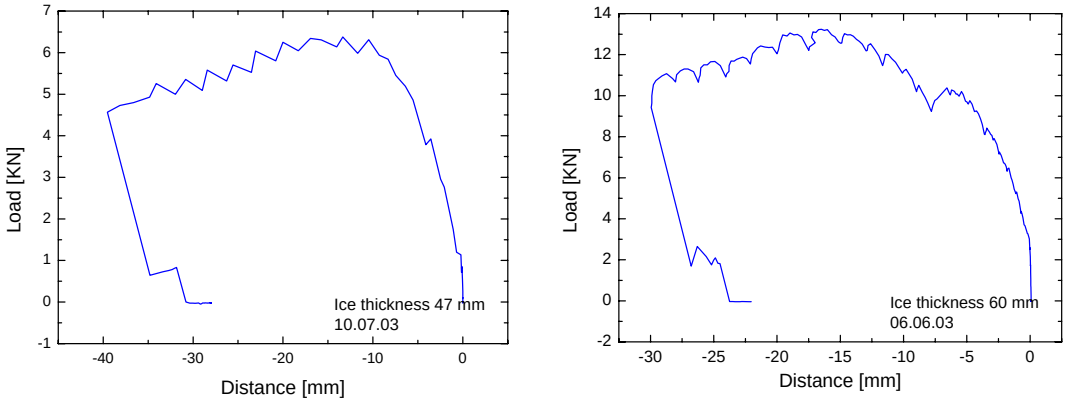

Fig. 4. Typical load deformation curves for different ice thickness

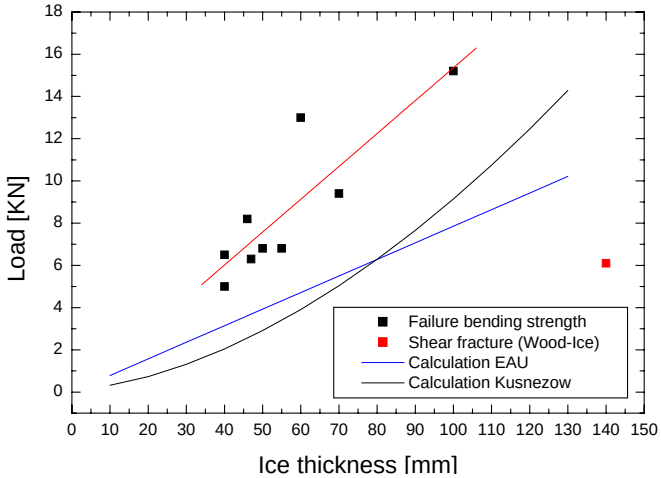

Fig. 5. Measured vertical ice loads compared to EAU / Kusnezow calculation

DISCUSSION OF RESULTS

Measured ice forces transmitted on piles caused by ice-jacking are higher than calculated by German standard methods (EAU) and empirical calculations by

KUSNEZOW (figure 5). This difference seems to be due to the physical assumptions, which were used as basis for EAU calculations. In EAU calculation buoyancy is the main source of uplift forces. The authors assume that uplift forces can be induced by hydrostatic pressure below a closed, deformed ice sheet. The vertical ice lifting forces on piles and other constructions are limited by bending strength or shear strength of the ice sheet at a certain distance of the (pile) surface.

The measured vertical ice forces are not directly transferable to natural ice thicknesses (20-40 cm on the German Baltic coast). A transformation of laboratory experiments is being done by a numerical simulation in ongoing cooperation with the Technical University of Braunschweig.

COMPARISON WITH HOLDING FORCES

To investigate the necessary ramming depth of nearshore (groyne) piles the vertical ice loads are compared to holding forces of groyne piles on the German coast. To investigate holding forces as a function of type of subsoil and ramming depths of piles, pull out tests were performed on numerous piles. Ramming depths of piles and type of subsoil are varied in the tests based on groyne data of the Agency for Nature and Environment Rostock.

Fig. 6. Pull-out-test on the Baltic coast

A test apparatus (figure 6) was constructed, which allows the piles to be pulled with forces up to 100 KN. Pulling load and displacement of the pile are recorded simultaneously. Experiments on 27 piles (ramming depth 3-4 m) under different subsoil conditions show that ice forces (20-40 cm thick) can be an important load for the dimensioning of groyne piles on the Baltic coast against ice-jacking.

REFERENCES

Arbeitsausschuss „Ufereinfassungen“ from HAFENBAUTECHNISCHE GESELLSCHAFT e.V. and from DEUTSCHEN GESELLSCHAFT FÜR GEOTECHNIK e.V. (1996) EMPFEHLUNGEN DES ARBEITSAUSSCHUSSES „UFEREINFASSUNGEN“ (EAU 1996), 593 S., Berlin

Kusnezow, *Werkstandard Lastannahmen im Wasserbau*, WAPRO 3.03, Halle (1969)

Frederking R. and Karri J., Effects of pile material and loading state on adhesive strength of piles in ice, *Canadian Geotechnical Journal* 20, (1983) 673-680

17th International Symposium on Ice
Saint Petersburg, Russia, 21 - 25 June 2004
International Association of Hydraulic Engineering and Research

PRELIMINARY RESULTS OF YIELD CRITERIA OF PACK ICE AND THEIR IMPACT ON THE ORIENTATION OF LINEAR KINEMATIC FEATURES

Keguang Wang[1]

ABSTRACT

The yield criteria of pack ice and their impact on the orientation of linear kinematic features are discussed. Several typical yield curves are investigated whether they are capable to reproduce the observed features in pack ice. The analyses show that the yield curves of diamond and hexagon are unable to provide some of the desired features, while those of ellipse, parabolic lens and teardrop are basically able to offer these characteristics. The ice-cream cone is of very strong capability to consist with the observed kinematic features; however, a final comprehensive observation is needed to support this conclusion.

INTRODUCTION

Linear kinematic features (LKFs) are long, narrow geophysical features with much higher deformation than the surrounding pack ice. These features are generally morphologically distinct from the surrounding ice. In general, they may consist of open water, new ice, young ice, rafted ice, or even ridged ice. Such features are common in the polar oceans, and have long been observed systematically distributed (e.g. Marko and Thompson, 1977; Sodhi, 1977; Pritchard, 1988; Erlingsson, 1988; Overland et al., 1995; Kwok, 2001).

The mechanism for developing LKFs has so far been well agreed due to plasticity, a major mechanical property of pack ice recognized during the Arctic Ice Dynamics Joint Experiment. In a plastic framework, the orientation of LKFs can be related to a yield curve, whenever pack ice is treated as a general plastic material (e.g. Pritchard, 1988) or a granular material (e.g. Sohdi, 1977; Erlingsson, 1988). However, being lack of a well-acknowledged yield curve for pack ice, this problem still remains unresolved.

[1] Department of Physical Sciences, University of Helsinki, Helsinki 00014, Finland

In the present paper, an inversed way is introduced to determine the yield curve, i.e. by examining the orientation of LKFs under certain atmospheric and oceanic forcing, which is much more observable. A theoretical relationship between yield curves and angles of intercrossed LKFs is derived, and six typical yield curves are then examined on how many LKFs they may support at a point and what intercrossed angles they may provide. By comparing with the existing observations, some yield curves, which cannot provide the desired angles and numbers of LKFs, can be primarily excluded.

YIELD CRITERIA FOR PACK ICE

All yield criteria so far proposed for pack ice are two-dimensional. In the present paper, they are reexamined starting from three-dimension. When horizontal isotropic stress is low, e.g. less than the vertical critical stress, the stress state can be solved as a plane strain problem, where the vertical stress is a middle stress. A physically reasonable yield curve for this situation is the Coulomb law, which was first proposed for pack ice by Coon (1974) and later derived from the general Reiner-Rivlin equation by Smith (1983). We here take the form

$$\sigma_{II}^{*} = -\sigma_{I}^{*} \sin\phi\,, \tag{1}$$

where asterisks represent variables in three dimensions, σ_{II}^{*} and σ_{I}^{*} are horizontal shear and isotropic stresses, equal to halves of the sum and difference of the principal stresses, respectively; ϕ is the angle of internal friction. The cohesion in pack ice is generally very small, and is here ignored. If we neglect the vertical variation of stress and strength, then this yield curve can be transformed to two-dimension

$$\sigma_{II} = -\sigma_{I} \sin\phi\,, \tag{2}$$

where σ_{II} and σ_{I} are two-dimensional horizontal shear and isotropic stresses, equal to $h\sigma_{II}^{*}$ and $h\sigma_{I}^{*}$ respectively, h is ice thickness.

When the isotropic stress is high, assuming the failure of pack ice obeying the von Mises criterion, we have the yield condition in terms of principal stresses

$$(\sigma_1^{*} - \sigma_2^{*})^2 + (\sigma_2^{*} - \sigma_3^{*})^2 + (\sigma_3^{*} - \sigma_1^{*})^2 = 2P_c^{*2}\,, \tag{3}$$

where P_c^{*} is ice strength in simple compression. In the case of failure under high isotropic stress, the vertical stress can be assumed to always reach the ice strength, i.e. $\sigma_3^{*} = -P_c^{*}$, thus Equation (3) becomes

$$[(\sigma_1^{*} + \sigma_2^{*})/2P_c^{*} + 1]^2 + 3[(\sigma_1^{*} - \sigma_2^{*})/2P_c^{*}]^2 = 1\,. \tag{4}$$

The critical stress of horizontal uniaxial compression can be achieved by taking $\sigma_1^{*} = 0$ in Equation (4), which leads to $\sigma_2^{*} = -P_c^{*}$, identical to σ_3^{*}. The two-dimensional yield curve can easily be obtained from Equation (4)

$$[(\sigma_1 + \sigma_2)/2hP_c^{*} + 1]^2 + 3[(\sigma_1 - \sigma_2)/2hP_c^{*}]^2 = 1 \tag{5a}$$

or equivalently

$$(\sigma_I / hP_c^* + 1)^2 + 3(\sigma_{II} / hP_c^*)^2 = 1, \qquad (5b)$$

where σ_1 and σ_2 are two-dimensional principal stresses in horizontal plane. When compared with the traditional elliptical yield curve (Hibler, 1979), the ratio of ellipse e is here equal to $\sqrt{3}$ instead of 2, and the ice strength parameter in Hibler (1979) P^* equals to $2P_c^*$.

Combining Equations (2) and (5b) may lead to a possible yield curve for the two-dimensional pack ice. It is an ice-cream cone, consisting of a Coulomb yield curve with an elliptical compressive cutoff, as shown by the thick lines in Figure 1. Only the upside part is illustrated, since we assumed a nonnegative shear stress. Inside the yield curve, pack ice could behave elastically (e.g. Coon et al., 1974) or viscously (e.g. Hibler, 1979). If P_c^* is assumed constant, then during increasing ice thickness, the Coulombic part remains its shape, while the elliptical part continues expanding its shape and shifting its central point leftward. Therefore, in the two-dimensional form, pack ice would experience isotropic hardening during compression when ice thickness increases, although it behaves as a perfect plasticity in three-dimension.

Another yield curve close to the ice-cream cone is the teardrop, as shown by the dotted line in Figure 1. This curve takes the form in two-dimension as

$$\sigma_{II} = -(1 + \sigma_I / 2hP_c^*)^{1/2} \sigma_I \sin\phi . \qquad (6)$$

This curve can be considered as a modified Coulomb yield curve. Smith (1983) argued that this yield curve had a problem of weakening shear strength with increasing isotropic stress in the left part. We now know that his discussion is only valid for a plane strain problem, while here it is a plane stress problem.

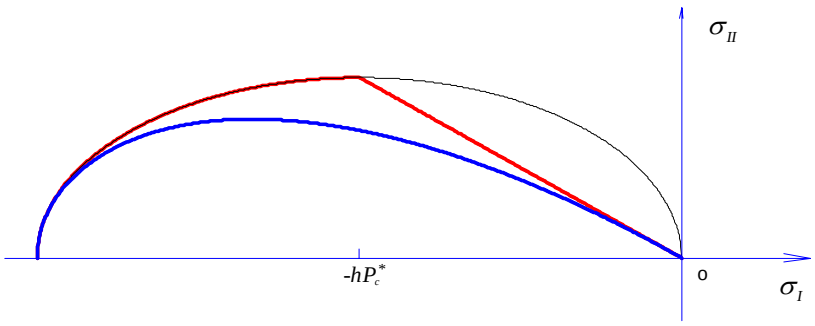

Fig. 1. The yield curves of ellipse ($e = \sqrt{3}$, thin line), ice-cream cone (thick line) and teardrop (dotted line)

The hexagon yield curve (Mckenna et al., 1983) is essentially the Tresca yield criterion when the vertical stress is fixed, as done for the von Mises yield criterion above. It takes the form

$$\sigma_{II} = -\sigma_I, \quad \sigma_{II} = hP_c^*/2, \quad \sigma_{II} = 2hP_c^* - \sigma_I \quad . \qquad (7)$$

It is shown as the thick line in Figure 2.

The parabolic lens (Rothrock, 1975) and diamond (Pritchard, 1981) are effective in numerical simulations of ice movement (e.g. Ip et al., 1991) and open water production (e.g. Stern et al., 1995); hence, they are also included here for further investigation. The equation for parabolic lens takes

$$\sigma_{II} = -(1 + \sigma_I / 2hP_c^*)\sigma_I \tag{8}$$

and for diamond

$$\sigma_{II} = -\sigma_I, \quad \sigma_{II} = \sigma_I + 2hP_c^*. \tag{9}$$

These two yield curves are also illustrated in Figure 2. In addition, each of the figures shows an elliptical yield curve with axial rate of $\sqrt{3}$ (Figure 1) and 2 (Figure 2).

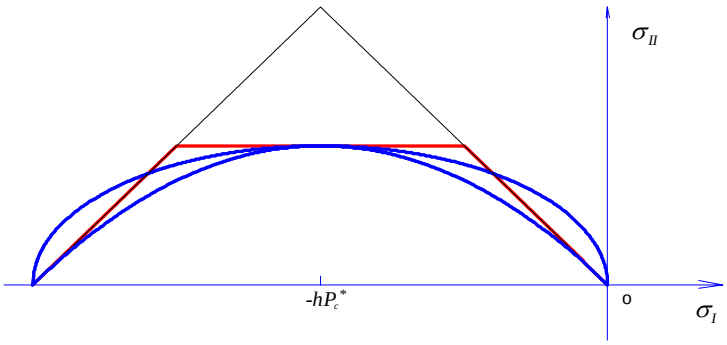

Fig. 2. The yield curves of ellipse (e = 2, dash line), parabolic lens (dotted line), hexagon (thick line) and diamond (thin line)

CHARACTERISTIC LINES AND LINEAR KINEMATIC FEATURES

Characteristic lines and their propagation are well developed in mathematics for one order multi-variable partial differential equations (e.g. Courant and Hilbert, 1962). These lines are failure lines in plastic deformations. In the case of sea ice in large scale, the relation between the slope of yield curves and the orientation of characteristic lines (Pritchard, 1988) is physically reasonable since it started from a yield curve appropriated for problems in plane stress, while mathematically similar result from mechanical analysis based on the Coulomb yield curve (Erlingsson, 1988; 1991) is restricted for problems in plane strain, or for cases when isotropic stress is relatively low as discussed above.

In the present paper, we give a mathematical approach to identification of the orientation of stress field, and further provide a relationship, on LKFs, between the ice stress, the orientation and the external forces. The orientation of the characteristic lines of ice velocity fields can be easily obtained under the associated flow rule, however, these lines have no relation to the external forces.

Following Pritchard (1988), a quasi-steady momentum equation is taken as the starting point,

$$\nabla \cdot \boldsymbol{\sigma} + \mathbf{F} = 0, \tag{10}$$

where $\boldsymbol{\sigma}$ is the two-dimensional stress tensor, $\mathbf{F}$ is the resulting external forces, including wind and water stresses, Coriolis force and sea surface tilt. The stress components are expressed in terms of the invariants σ_I and σ_{II} and the principal direction γ with respect to x-axis

$$\begin{aligned} \sigma_{xx} &= \sigma_I + \sigma_{II} \cos 2\gamma \\ \sigma_{yy} &= \sigma_I - \sigma_{II} \cos 2\gamma \\ \sigma_{xy} &= \sigma_{II} \sin 2\gamma. \end{aligned} \tag{11}$$

When σ_{II} is expressed in terms of σ_I through the yield curves listed above, the three stress components are only functions of σ_I and γ. For convenience, take a general form as the yield curve such that

$$\sigma_{II} = b(\sigma_I, h, P_c^*). \tag{12}$$

Substituting Equations (11, 12) into (10) gives the differential equations with respect to the principal direction

$$(1 + b')\,\partial\sigma_I/\partial\xi + 2b\,\partial\gamma/\partial\eta = G_\xi; \tag{13}$$

$$(1 - b')\,\partial\sigma_I/\partial\eta + 2b\,\partial\gamma/\partial\xi = G_\eta, \tag{14}$$

where ξ and η are tangent and normal to the principal direction, and

$$b' = \tan\beta = \partial\sigma_{II}/\partial\sigma_I; \tag{15}$$

$$G_\xi = -F_\xi - (\partial b/\partial h\,\partial h/\partial\xi + \partial b/\partial P_c^*\,\partial P_c^*/\partial\xi); \tag{16}$$

$$G_\eta = -F_\eta - (\partial b/\partial h\,\partial h/\partial\eta + \partial b/\partial P_c^*\,\partial P_c^*/\partial\eta), \tag{17}$$

where β is the angle of slope of the yield curves. Then introduce two perfect differentials for σ_I and γ

$$\partial\sigma_I/\partial\xi\,d\xi + \partial\sigma_I/\partial\eta\,d\eta = d\sigma_I; \tag{18}$$

$$\partial\gamma/\partial\xi\,d\xi + \partial\gamma/\partial\eta\,d\eta = d\gamma. \tag{19}$$

On the characteristic lines, the determinant of coefficients of Equations (13), (14), (18) and (19) needs to be zero, i.e.

$$\Delta = \begin{vmatrix} 1+b' & 0 & 0 & 2b \\ 0 & 1-b' & 2b & 0 \\ d\xi & d\eta & 0 & 0 \\ 0 & 0 & d\xi & d\eta \end{vmatrix} = 0. \tag{20}$$

Solution to this equation gives the slopes of the characteristic lines

$$d\eta/d\xi = \pm\tan\theta = \pm[(1-b')/(1+b')]^{1/2}\,, \qquad (21)$$

where θ is the angle between the principal direction and the characteristic lines, prescribed within 0 and $\pi/2$. Thus, there are two characteristic lines when $|b'| < 1$ or equivalently $|\beta| < \pi/4$; only one characteristic line when $|b'| = 1$ or equivalently $|\beta| = \pi/4$; and no characteristic line when $|b'| > 1$ or equivalently $|\beta| > \pi/4$. It is clear that 2θ is the angle between the two intercrossed LKFs. From Equation (21) it is easy to know

$$b' = \tan\beta = \cos 2\theta \qquad (22a)$$

or equivalently

$$\beta = \arctan(\cos 2\theta) \quad \text{or} \quad 2\theta = \arccos(\tan\beta)\,. \qquad (22b)$$

One remarkable feature from Equations (22) is that the angle between LKFs, 2θ, is only controlled by the slope of yield curves. Thus, for the diamond yield curve, $b' = -1$ on the right part gives $\theta = -\pi/2$. This leads to LKFs perpendicular to the principal direction, corresponds to a simple tension and results in a uniaxial opening. Similarly, $b' = 1$ on the left part leads to $\theta = 0$, and ridging occurs parallel to the principal direction. Therefore, this yield curve is unlikely to provide an acute angle between LKFs, although the corners on the yield curve may offer some possibility. Similar problem happens for the hexagon yield curve, in which the left and right parts are identical to the diamond yield curve. $b' = 0$ in the central top gives $\theta = \pi/4$ and the two LKFs perpendicular to each other.

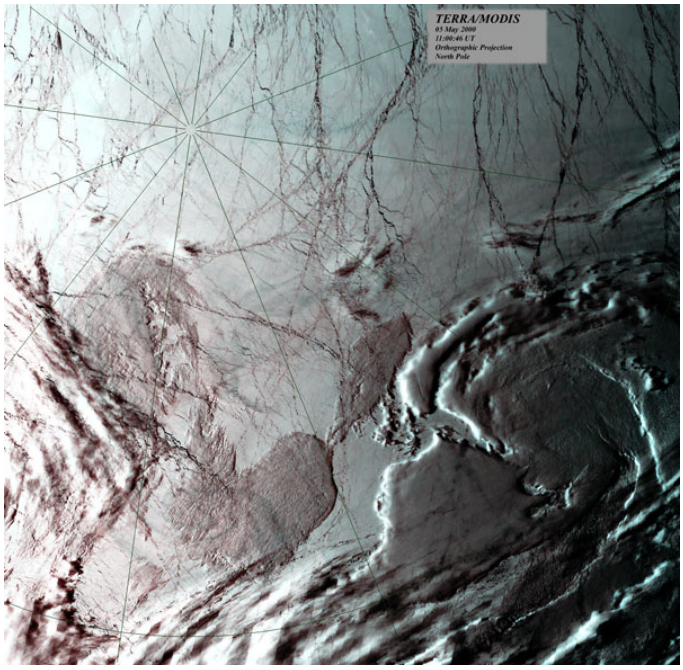

Fig. 3. MODIS bands 1,4,3 RGB true color image
of the North Pole on the 5th of May 2000

A typical pattern of LKFs in the central Arctic is shown in Figure 3. In this image, sea ice

appears white and areas of open water, or recently refrozen sea surface, appear black. The widest dark lines are, in general, active leads, since open water cannot sustain long in the central western Arctic. The angels between these LKFs are normally between 20˚ and 60˚, with the most significant ones of 45˚ and 30˚. This is generally consistent with other observations, for example, 20˚ ~ 40˚ in the Arctic Ocean (Marko and Thompson, 1977), about 60˚ when through channels (Sohdi, 1977) and about 30˚ in coastal slip-line fields (Eringsson, 1988). When LKFs are very close to coast, however, the angles would sometimes be contaminated by the shape of the coast. In this case, care must be cautiously taken of the accuracy of the angles. Since the Coulomb law with a constant angle of internal friction always leads to a single angle between LKFs (if not from singularities), as the deformation field shown by Kwok (2001), this yield curve (together with the ice-cream cone) seems very promising for the production of opening LKFs. However, this implies that the variation of the angle between LKFs is due to the inhomogeneity and anisotropy of the pack ice.

Figure 4 shows the dependence of slopes of the yield curves of ellipse, parabolic lens and teardrop on the isotropic stress. The lower thick line (β = – 45º) shows the slope under simple tension and the upper thick line (β = 45º) under simple compression. Regions between these two lines have two characteristic lines. The thick dotted line (β = 0º) shows the slope under simple shearing. Above this line, pack ice experiences shearing and compression; below this line, pack ice experiences shearing and tension. One considerable difference among the slopes of these curves are that they are of central symmetry when applying yield curves of ellipses and parabolic lens, while the teardrop yield curve possesses a high isotropic stress under simple shearing. Regions out of the thick lines have no characteristic lines. Pack ice experiences isotropic contracting when β > 45º, and experiences isotropic opening when β < – 45º.

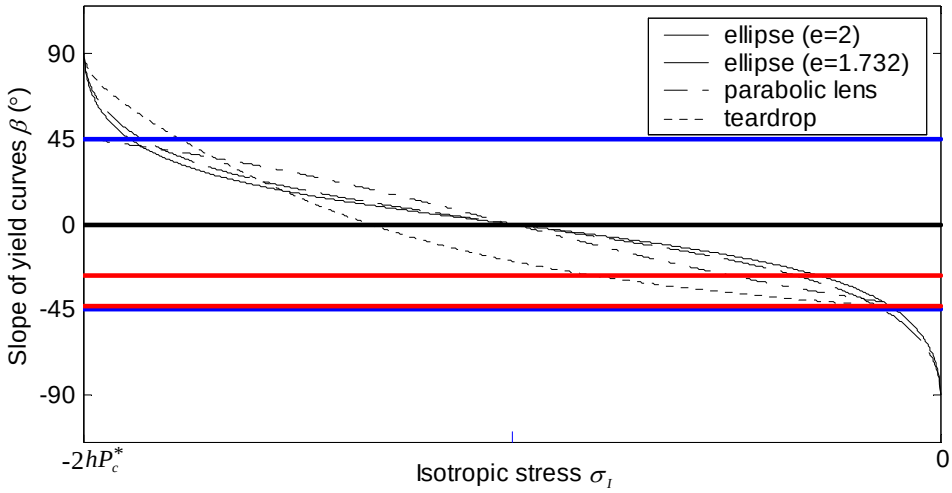

Fig. 4. Slopes of the yield curves dependent on the isotropic stress (see text for a detail description)

In this case, only the elliptical yield curves are able to provide both isotropic opening and

contracting, the teardrop yield curve is only able to offer isotropic contracting, while the parabolic lens always has at least one characteristic line. However, these results could be altered when these yield curves are modified with a certain coefficient. A final assessment of these properties needs more observations. The two thick dash lines show the slopes when 2θ equals 20º (lower line) and 60º (upper line). All of the four yield curves are capable to provide the observed angles between LKFs, however, the teardrop yield curve seems to have more possibility to fall into this region with a varying isotropic stress. The two elliptical yield curves are basically the same in providing the desired features of pack ice.

CONCLUSION

This paper has been devoted to investigate the yield curves for pack ice by examining their impact on the orientation of linear kinematic features. Several different yield curves, which are quite commonly applied in sea ice dynamics, are studied whether they are capable to provide the desired observed features of pack ice under deformation. The analyses show that the yield curves of diamond and hexagon are very difficult to provide an acute/obtuse angle, so they are, in general, inappropriate as a yield curve for pack ice. The ice-cream cone seems to provide a constant angle between LKFs. The parabolic lens is able to provide any angle between LKFs, but it cannot provide any isotropic contracting and opening. The teardrop is capable to provide all the angles between LKFs and also support isotropic contracting, but it does not support isotropic opening. The ellipse is capable to provide any situations. A further study would be needed to finally determine the yield curve for pack ice.

ACKOWLEDGEMENTS

This study was partly supported by the European Commission project ‘Climate and Lake Impacts in Europe’ and the Chinese project of National Natural Science ‘Arctic Sea Ice Physical Processes and Ice-Ocean Modeling’ under contract 40233032.

REFERENCES

Coon, M. D., 1974. Mechanical behavior of compacted Arctic ice floes, *J. Petrol. Tech.*, 26, 466-470.

Coon, M. D., G. A. Maykut, R. S. Pritchard, D. A. Rothrock, and A. S. Thorndike, 1974. Modeling the pack ice as an elastic-plastic material, *AIDJEX Bull.* 24, pp. 1-106, Univ. of Wash., Seattle, Wash.

Courant, R. and D. Hilbert, 1962. *Methods of Mathematical Physics*, Vol. 2, Interscience, New York.

Erlingsson, B., 1988. Two-dimensional deformation patterns in sea ice, *J. Glociol.*, 34, 301-308.

Erlingsson, B., 1991. The propagation of characteristics in sea-ice deformation fields, *Ann. Glaciol.*, 15, 73-80.

Hibler, W. D. III, 1979. A dynamic thermodynamic model of sea ice, *J. Phys. Oceanogr.*, 9, 815-846.

Ip, C. F., W. D. Hibler, and G. M. Flato, 1991. On the effect of rheology on seasonal sea-ice simulations. *Ann. Glaciol*., 15, 17-25.

Kwok, R., 2001. Deformation of the Arctic Ocean sea ice cover between November 1996 and April 1997: A qualitative survey, in *IUTAM Symposium on Scaling Laws in Ice Mechanics and Ice Dynamics*, J. P. Dempsey and H. H. Shen (eds.), pp. 315-322, Kluwer, the Netherlands.

Marko, J. R. and R. E. Thompson, 1977. Rectilinear leads and internal motion in the ice pack of the western Arctic Ocean, *J. Geophys. Res.*, 82, 979-987.

McKenna, R. F., J. F. Sykes, and W. C. Lennox, 1983. The influence of changes in constitutive law on sea ice motion, *The 7th International Conference on Port and Ocean Engineering under Arctic Condition*, pp. 172-179, Helsinki, Finland.

Overland, J. E., B. A. Walter, T. B. Curtin, and P. Turet, 1995. Hierarchy and sea ice mechanics: A case study from the Beaufort Sea, *J. Geophys. Res.*, 100, 4,559-4,571.

Pritchard, R. S., 1981. Mechanical behavior of pack ice, in *Mechanics of Structured Media*, part A, A. P. S. Selvadurai (ed.), pp. 371-405, Elsevier, New York.

Pritchard, R. S., 1988. Mathematical characteristics of sea ice dynamics models, *J. Geophys. Res.*, 93, 15,609-15,618.

Rothrock, D. A., 1975. The energetics of the plastic deformation of pack ice by ridging, *J. Geophys. Res.*, 80, 4,514-4,519.

Smith, R. B., 1983. A note on the constitutive law for sea ice, *J. Glaciol.*, 29, 191-195.

Sodhi, D. S., 1977. Ice arching and the drift of pack ice through restricted channels, *CRREL Rep.* 77-18, Cold Regions Res. and Eng. Lab., Hanover, N. H.

Stern, H. L., D. A. Rothrock, and R. Kwok, 1995. Open water production in Arctic sea ice: Satellite measurements and model parameterizations. *J. Geophys. Res.*, 100, 20,601 -20,612.

17th International Symposium on Ice
Saint Petersburg, Russia, 21 - 25 June 2004
International Association of Hydraulic Engineering and Research

APPLICATION FEA FOR CALCULATION OF LOADING ON AN ISOLATED STRUCTURE FROM AN ICE COVER AT INCREASE OF TEMPERATURE OF ICE

Ivchenko A.B and Vasiliev S.P.[1]

ABSTRACT

The calculation scheme and, accordingly, calculation dependences for a case of interaction of an isolated structure and ice cover which is locate between this structure and a coast is improved.

The case is considered, when the ice cover is between an extended coast and isolated structure. On the other hand structure of an ice cover is not present, that results in temperature displacement free, not contacting with a structure edge of ice. The extent of an ice cover in a direction to perpendicular effort is not limited. The structure impedes with temperature expansion not only opposite of a strip of an ice cover, but also sites, next to it. The scheme of interaction is given a fig. 1. It is obvious, that loading on such structure will be much greater, than on a coastal structure. The mechanical properties of polycrystalline ice are described by the reological model of an elastic-viscous body (Ivchenko, 1990). The ice cover is considered as a plate from a modeling material.

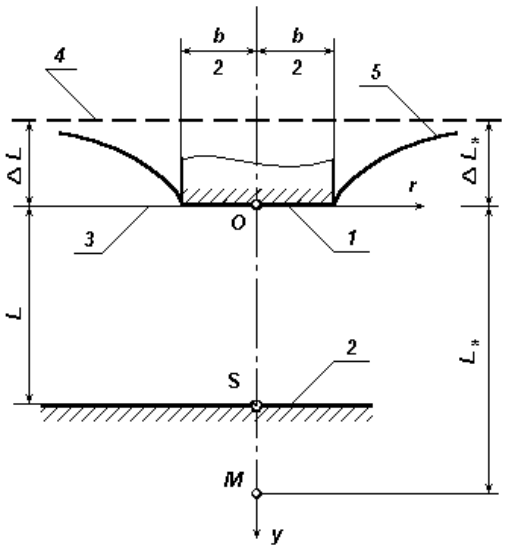

Fig. 1. 1 – structure, 2 – bank – a line actually attachment of an ice cover, 3 – initial location of an ice edge, 4 – possible location of an ice edge after the temperature rise when structure is absent, 5 – ice edge after temperature rise, M – point of equivalent fastening of plate, S – point fastening of plate in the assumption is earlier received

[1] State Siberian University of Transport, Novosibirsk, Russia

The solution for definition of loading on an isolated structure in the assumption is earlier received, that the ice cover is fixed in one point (point S in fig.1) of a coastal line (Ivchenko, 1998). Such fastening in sufficiently strictly corresponds to real conditions, as all other points of a line of contact have an opportunity to be displaced. Actually attachment of a cover is carried out on a line (2 in fig.1). The specification of the accepted before calculation scheme is necessary. Between a separate structure and point of fastening of a plate, in case of increase of temperature there is a line of zero exists on an axis y. (is below shown, that it proves to be true aloes by results of numerical experiment). The valid line of zero displacement can be replaced by a straight line. We accept that this straight line coincides with a coastal line and on it the plate (line 2 on fig. 1) is fixed. Then a point M in fig. 1 – point of equivalent fastening of a plate. The deflections of edge of a plate at fastening on a line under a stamp and in an equivalent point are identical. Distance from a stamp up to a point of equivalent fastening L_* will be determined from a condition of equality of effort of interaction at that and other way of fastening of a plate. Deflection in any point of edge elastic of a plate of unity thickness fixed in a point (fig. 1) on (Michell, 1902)

$$y = \frac{2}{\pi E}\int_{r_{11}}^{r_1+b} q(r)\ln\frac{L_*}{r}dr - \frac{1+\nu}{\pi E}\int_{r_1}^{r_1+b} q(r)dr\,, \qquad (1)$$

where E – module of elasticity; b – extent of the loaded site; y and r – coordinate axes; q(r) – law of distribution of loading; L_* – distance from a structure up to a point of equivalent fastening; ν – factor of elastic cross deformation.

Distribution of loading on contact of a plate and rigid stamp shall accept, as well as in (Sadowsky, 1928) as:

$$q(r) = \frac{q_0 b}{\pi\sqrt{\left(\frac{b}{2}\right)^2 - r^2}}\,, \qquad (2)$$

where q_0 – average on a line of contact the continuous load. We substitute dependence (2) in (1). We pass to a dimensionless coordinate axis. Then, and, having changed borders of integration, we shall receive a deflection under the center of a stamp:

$$\Delta L_* = \frac{4bq_0}{\pi^2 E}\int_0^1 (1-\xi^2)^{-0.5}\ln\frac{2L_*}{b\xi}d\xi - \frac{2(1+\nu)bq_0}{\pi^2 E}\int_0^1 (1-\xi^2)^{-0.5}d\xi\,. \qquad (3)$$

Relative distance from a structure up to a coastline $-m_b = L/b$, and up to a point of equivalent fastening $m_{b*} = L_*/b$. After integration we receive the formula for a deflection under a stamp

$$\Delta L_* = \frac{bq_0}{\pi E}[2\ln(4c_0 m_b) - 1 - \nu], \qquad (4)$$

where $c_0 = L_*/L$ – relative distance up to a point of equivalent fastening. The numerical value should be determined. For the ice cover surrounded with a rigid closed contour, complete absolute temperature deformation of any horizontal layer as the function of time is equal

$$\Delta L_i(t) = \frac{[1-\nu_{di}(t)]c_0 L}{E_{di}(t)dh}q_i(t)\,, \qquad (5)$$

where $\nu_{di}(t)$ – factor of full cross deformation for a considered layer, $q_i(t)$ – a linear continuous load from a layer limited in the plan to a rigid contour, $E_{di}(t)$ – apparent module of elasticity or module of deformation, dh – thickness of a layer.

Loading, as the function of time, is determined on the published method (Ivchenko, 1990). We replace in (4) the module of elasticity variable in time with the module of deformation. We take into account, that for an elementary layer $q_0 = q_{0i}(t)$, $\nu = \nu_{di}(t)$, $\Delta L = \Delta L_i\ (t)$. Received from (4) size from deflection of a layer "i", we equate to the appropriate size from dependence(5). The continuous load from of layer "i" on a separate structure

$$q_{oi}(t) = \frac{\pi c_0 m_b [1 - \nu_{di}(t)]}{2\ln(4 c_0 m_b) - 1 - \nu_{di}(t)} q_i(t)\,. \tag{6}$$

We summarize on thickness of an ice cover of loading from layers determined on (6). We believe factor of full cross deformation by size practically constant. Average on a line of constant variable in time loading on a separate structure

$$q_o(t) = \frac{\pi c_0 m_b [1 - \nu_d]}{2\ln(4 c_0 m_b) - 1 - \nu_d} q(t)\,, \tag{7}$$

where ν_d – average value of complete cross deformation, q(t) – loading from all thickness of an ice cover at the same change of temperature and rigid cloused contour, as function of time (Ivchenko, 1990). Dependence (7) is possible to present as

$$q_o(t) = K_o q(t)\,, \tag{8}$$

where

$$K_0 = \frac{\pi c_0 m_b [1 - \nu_d]}{2\ln(4 c_0 m_b) - 1 - \nu_d}\,. \tag{9}$$

According to (8) relative loadings

$$K_0 = \frac{q_0(t)}{q(t)}\,. \tag{10}$$

From dependences (8) and (9) follows, that change of temperature in a more thickly ice cover, mechanical properties and physical characteristics of ice are taken into account at definition q(t).

From (9) follows, that the influence of mechanical properties and physical characteristics on K_0 is limited to factor ν_d, which is accepted constant. That relative loading, on dependence (9), depends only on a ratio of the geometrical sizes. Then at calculation till (10) relative loadings K_0, the replacements of a plate from visco-elastic of a material by a plate form an elastic material with factor of complete cross deformation as at ice in conditions of a considered problem is possible. In this case loadings $q_0(t)$ and $q(t)$ are determine as for an elastic plate and do not depend on time and the numerical experiment can be carried out on a plate from an elastic material.

By a method of finite elements is considered plane stress a condition of a plate of unity thickness from an elastic material. Proceeding from conditions of symmetry, half of a plate (ice cover) is considered, the least size of a plate in a cross direction is established, the character of fastening of sides of a plate is determined. As a result of account the line of zero displacement for a case of fastening of a plate in one point is received. As is told above we replace such line of straight line and are considered as a line of an attachment of an ice cover a coast.

At a real attachment of an ice cover to a coast (on a line) purpose of account was the definition of relative loading K_0, and relative distance c_0. The values of loading $q_0(t)$ and $q(t)$at change of temperature are determined on a method of finite elements for a plate from an elastic material with factor d, as at ice. The significance $q_0(t)$ are determined for different L, b and m. Relative loading K_0, at various value m_b, is determined on (10) at experimental significance of loadings $q_0(t)$and $q(t)$. Is established, that K_0 depends from m_b and does not depend on absolute value L and b. Experimental dependence $K_0 = f(m_b)$ – line 1 in a fig. 2.

Comparison of calculation dependence (9) with the experimental data (the diagram 1 in a fig. 2) has shown, that it is really possible to consider factor c_0 as value practically constant and equal 1.63 ($m_b \geq 2.5$). The calculation dependence received on (9) at c_0=1.63 (curves 2 on a fig. 2), well coincides with the experimental data (curve 1 in a fig. 2). Recommended above experimental dependences is possible to use at $m_b \geq 2.5$.

At definition of calculation loading on a separate structure on dependence it is possible to count up (8) relative loading K_0, on (9) or to receive under the diagram 1 fig. 2.

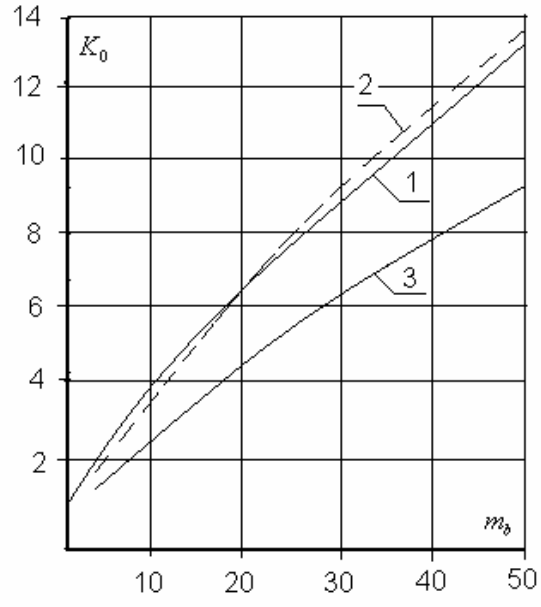

Fig. 2. Dependence $K_0 = f(m_b)$
1 – experimental curve, when the plate is fixed on line; 2 – calculation curve, when the plate is fixed in point M; 3- calculation curve, when the plate is fixed in point S

Calculation dependence $K_0 = f(m_b)$ at the former calculation scheme (Ivchenko, 1998), when the plate is fixed only in one point on a coastal line (point S in a fig. 1), is submitted by a line 3 in a fig. 2. The given research has followed essentially making more precise calculation definition of loading on a separate structure.

It is known, that the mechanical properties fresh-water and sea ice coincide, but the physical characteristics differ essentially. For example, factor of temperature expansion of sea ice strongly depends on temperature and other factors. The considered settlement technique can be distributed to a case of interaction of a separate structure with a sea cover at the known characteristics list.

REFERENCES

Ivchenko, A.B. Rheological Model of Polycrystalline Ice. *Proceedings of the 10th International Symposium on Ice 1.* Espoo (Finland), (1990) 230-237.

Ivchenko, A.B. Investigation of Stress of Ice Cover under Changes of temperature. *Proceedings of the 10th International Symposium on Ice 3.* Espoo (Finland), (1990) 149-157.

Ivchenko, A.B. Ice forces on isolated structures under temperature changes. *Proceeding of the 14th International Symposium on Ice 2.* Potsdam, New York, USA (1998) 907-909.

Michell, J.H. The inversion of plane stress. *Proceedings of the London Mathematical Soc.* 34. London (1902) 134-142.

Sadowsky, M. Zweidimensionale Probleme der Elastiziatatstheorie. *Zeitschrift fur angwandte Mathematik und Mechanik.* Bd.8, H. 2-S (1928) 107-121.

17th International Symposium on Ice
Saint Petersburg, Russia, 21 - 25 June 2004
International Association of Hydraulic Engineering and Research

ICE-RESISTANCE WITHDRAWAL CONSTRUCTION

Zhulenkov V.N.[1]

As far as we know the water supply system for the user must be uninterrupted and have respective quality including the temperature, presence or absence of mechanical or organic impurities and so on depending on economic or industrial activity of the user. However, the special place is taken here by withdrawal constructions situated near rivers with the unfavorable, often extreme, hydrothermal regime, with special shuga formation on the river during freeze-up period and with large ice jams in the period of high water in the spring. These conditions bring to often interruptions of withdrawal construction working.

According to that in the aim to increase the maintenance reliability of the constructions for water withdrawal out of the surfaced reservoirs in Siberia and Far North the author suggested the constructive-technological modification of the known *filtering construction*, considered below, executed as coastal filling of *sorted rock material* with perforated withdrawal pipelines inserted into the filling. The water having been filtered enters the filling body. This water flows along self-flowing pipelines to the pump-house of the first rise [1].

There is also a withdrawal construction including filtering enrockment dam constructed by unsort rock material and using the aid of face filling. This dam protects the allocated section of water area with a particular depth and temperature stratification and also the pump house delivering the water filtered through the dam into the water supply system for the user [2].

In the first case the weak point of the technical decision is the fact that during the withdrawal constructing there appear technical difficulties when it is necessary to carry out the laying and joining under water the collectors and self-flowing pipelines deepened into coastal gulf near which it is necessary to install the water catch construction, laid on the same depth, made of the more expensive sorted by large-size rock material. In the second case the weak point of the decision is the fact that when the construction is situated on the river embankment with high water during the flood in spring and when there is a large ice regime the filtering dam must be sufficiently high to enclose the water area from ice penetrating into it, this will lead to increasing the rock filling in the dam body and construction cost.

[1] The B.E. Vedeneev All-Russian Research Institute of Hydraulic Engineering (VNIIG), Gzhatskaya str., 21, St.Petersburg, Russia.

Constructive-technological simplification of the arrangement and, respectively, decrease of material and financial expenses in the process of building the ice-resistant withdrawal construction can be successfully achieved if, as we suggested in [3], the filtering enrockment fill being a principal constructive element of this ice-resistant water intake construction is constructing to full height by usual means using the method of end face filling from the bank to the river bed. The unsorted rock is the material of the enrockment (Fig. 1). According to the material segregation there occurs the formation of 2 seams: the overhead small permeable seam consisted of fine material and the lower permeable water inflow seam consisted only of coarse material (rock mass).

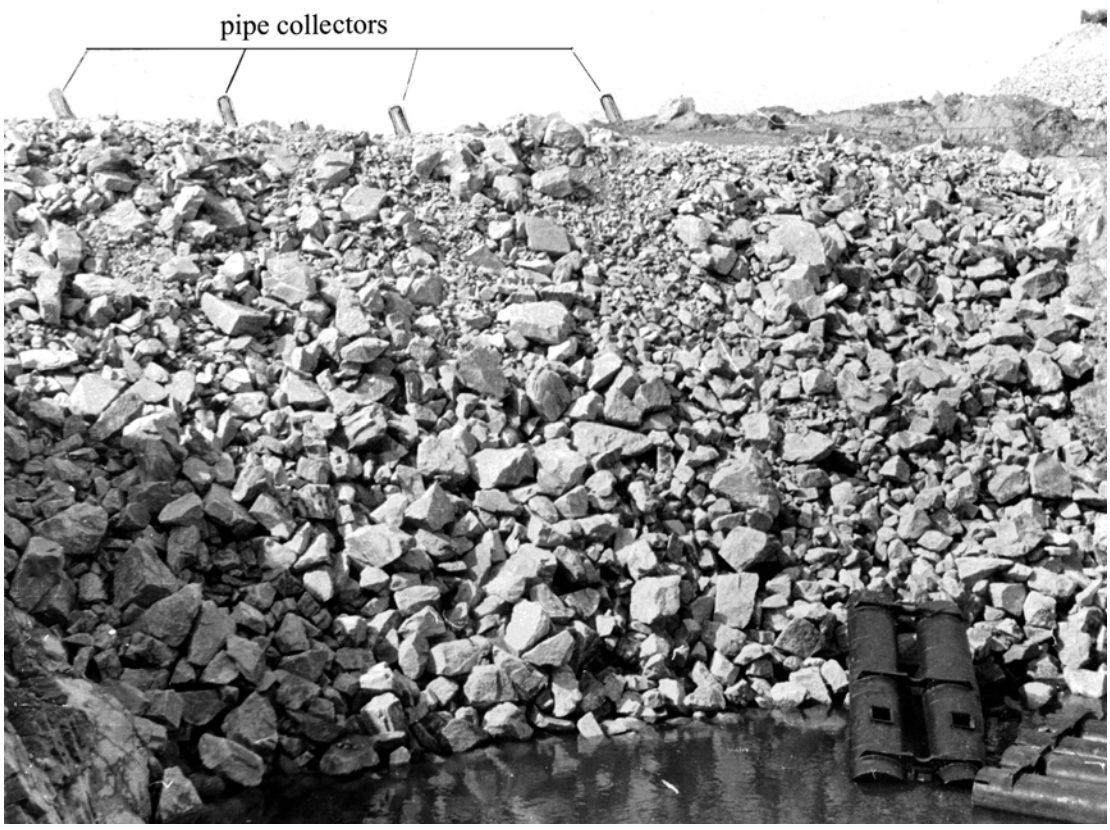

Fig. 1. The end face bank slope of 15 m high on which the segregation of unsorted rock material during its filling into water is visible

In the process of filtering enrockment work the pipe collectors are placed directly on natural slopes with the steepness from 1:1,3 to 1:1,5 and in inclined position perpendicular to the crest of the filling. There is perforation on collector trailer ends placed in the lower water inflow seam of the filling. The diameter, quantity and mutual placement of pipe collectors are preliminary determined by calculation or by seepage simulation depending on water intake discharge, rock material size in the lower seam, depth of the river near the filling and the type of submersible pumps place inside the collectors.

The offered water withdrawal construction is schematically illustrated by means of longitudinal and cross-section cuts given in Fig. 2.

The lower water inflow seam of the filtering enrockment filling is covered with the layer made of different-size material for contamination prevention. In this case there occurs clearing of water filtered from the river into the water inflow seam.

The slopes of the filtering enrockment filling are protected from above by means of a waterbreaking cover, e.g. by means of reinforced concrete slabs joined with the caponier on the crest of this filling. Inside of this caponier there are initial lots of water removing pipe collectors with the locking armature and with the devices regulating submersible pumps operation. In particular, such pumps completed with connection and protection facilities are produced by the German firm GRUNDFOS GMBH 23807 Wahlstedt.

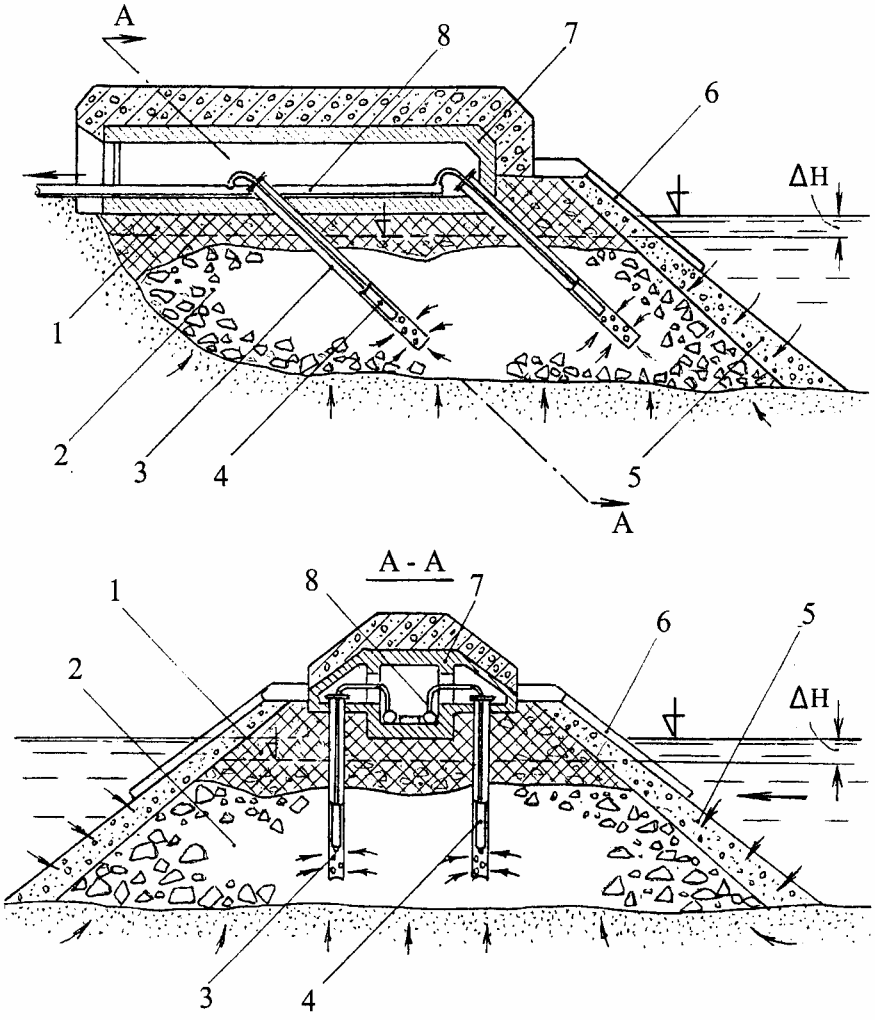

Fig. 2. Schematic explanation of the constructive-technological arrangement of the ice-resistant withdrawal construction, longitudinal (a) and cross-section (b) cuts:
1 – overhead low permeable seam of the filtering enrockment filling; 2 – lower water inflow seam of the filtering enrockment filling; 3 – catch water pipe collectors with perforation on lower trailer end lots; 4 – submersible pumps place inside the catch water pipe collectors; 5 – protected layer made of different – size material on the slopes of the filtering enrockment filling; 6 – waterbreaking cover on the slope of the filtering enrockment filling; 7 – caponier made of reinforced concrete on the crest of the filtering enrockment filling; 8 – pipe collectors removing water

When the submersible pumps achieve the working regime inside the filtering enrockment filling there will occur the decrease of the water level wile it flows stable in the lower seam of this filling both from its lateral face and from the river bed (foundation). If there is no the suffosional protection of the bed, for example, as a covered layer of sand-gravel or geosynthetic material, the admissible difference between the levels inside and outside of the filtering enrockment filling can be determined as a value of the exit head gradient of seepage from the bed. If the bed contains fine-granulated soils this value can be not more than 1.

Due to small speed of seepage which flows into the enrockment filling the withdrawal construction in before winter period is not contaminated with the shuga. Because of the significant mass the rock prism of the filtering construction is stable to the influence of the floe bulk during spring high water.

According to it the following distinctive attribute of the offered withdrawal construction can be noted: the water having been filtered flows to the pumps of the first rise just along the lower inflow seam of the filtering enrockment filling but not along the channel or aquatory. In this seam there are located the pipe collectors with submersible pumps intercepting the seepage. The water removing collectors and armature regulating water delivered discharge are protected outside by means of the caponier made of reinforced concrete; thanked to the specially selected external faces the caponier on the crest of the filtering enrockment filling is stable to the influence of floe.

It is assumed that the given technical decision referred to the engineering means of water supply will be used for uninterrupted water withdrawal out of the surfaced reservoirs in the Siberia and Far North, particularly in the city of Yakutsk.

The capacity of this withdrawal construction must be preliminary estimated by different ways (calculation, simulation). The parameters of the filtering field in the lower water inflow seam of the filling are obtained by using the filtering properties of the enrockment. To determine these properties the author [4] uses the equations shown below.

So, to estimate the water permeability of the coarse grained materials (here – rock materials) first of all there has to be found in which peripheral zone of the water inflow seam of the construction there remains the laminar filtration, when the filtration gradient and the critical gradient are not different or differ a little.

$$i_k = \frac{155}{\sqrt[3]{(\phi \cdot nD_0^2)^4}} \sqrt[9]{\left(\frac{\nu^2}{g}\right)^8}, \qquad (1)$$

where $\phi = 0{,}5$ – morphologic parameter of the rock material; n – porosity of enrockment; $D_0 \approx 0{,}2D_{50}$ – the diameter of porous channels of enrockment; ν – the coefficient of kinematic velocity; g – free fall acceleration.
For exemple, $\nu = 0{,}016$ cm^2/s (t_w = 4° C), $\phi = 0{,}5$, n = 0,45 and D_0, cm,

$$i_k = \frac{3{,}7 \cdot 10^{-4}}{\sqrt[3]{D_0}}, \qquad (2)$$

According to [4], the coefficient of turbulent filtration is

$$k_T = 17{,}9 \cdot n \cdot \sqrt{gD_0} \sqrt[6]{Ji}, \qquad (3)$$

where $Ji = \frac{\rho_W \cdot g}{E_W} \cdot D_0$ – the criteria that characterizes the ratio between the gravity force and the elastic force of water (modulus of elasticity is $E_W = 2{,}06 \cdot 10^3$ MPa and the density is $\rho_W = 1{,}0$ g/cm^3.

The more simple expression for the coefficient of turbulent filtration can be used for engineering estimation of the water inflow

$$k_t = 14{,}5 \cdot \sqrt[3]{D_0}\ , \text{ cm}, \tag{4}$$

where D_0, cm.

If the regime of filtration is not known the Prony-Fohrghmayer's binomial expression will be used for calculations.

$$i = \frac{V}{k_l} + \left(\frac{V}{k_t}\right)^2, \tag{5}$$

where V – filtration velocity;

$k_l = \frac{\phi \cdot n \cdot g}{36 \cdot \nu} \cdot D_0^2$ – coefficient of laminar filtration.

REFERENCE

1. Averkiev A.G., Makarov I.I., Sinotin V.I. Damless withdrawal buildings.- L.O. «Energia», (1999), 107 p.

2. Zhilenkov V.N. Experience of filtered-selective withdrawal development in system of technical water supply Pechorskaya GRES. – Electrical stations, (2002), №8, 25 p.

3. Zhilenkov V.N. et.al. Invention application 2003 103716 priority (07.02.2003). Ice resistant withdrawal buildings.

4. Zhilenkov V.N. The hydraulic resistance to motion of water in cracking and granular medium. – Izvestia VNIIG named after Vedeneeva (1983), p. 59-67

17th International Symposium on Ice
Saint Petersburg, Russia, 21 - 25 June 2004
International Association of Hydraulic Engineering and Research

PAINT COATINGS WITH HIGHER HYDROPHOBICITY FOR PROTECTION AGAINST ICE ACCRETION

Edwad F.Itsko, Andrey S.Drinberg, Lyudmila G.Sidorova, Natalia A.Novoselova[1].

ABSTRACT

The application of hydrophobic paint coatings is one of the ways to reduce the ability to ice accretion. The properties of painted surfaces largely depend on the paint formulation and they are determined by the volume loading of ingredients. The study carried out in this field made it possible to classify the coatings into the surface hydrophobic and volume hydrophobic coatings as well as to elaborate scientific approaches to their development. Some paint coatings were found to increase hydrophobic properties due to the change in their surface polarity with time. The hydrophobic properties of the coatings can also be changed by the use of pigments and extenders with high surface energy in their compositions. The investigations have led to the development of the anti-icing enamel ЭП-439П.

The issues of fighting against icing of ships, waterside structures, oil and gas facilities, especially in connection with the Arctic shelf development attract sound attention of experts engaged in solving this problem.

Of special interest out of many methods used in the fight with ice accretion, i.e. thermal, mechanical, physical and chemical methods [Borisenko et al], is the application of anti-icing paint coatings that must meet a number of specific requirements the main of which is the lower ice adhesion.

The exposure of the ice ships underbody and waterside structures to ice has been well explored [Panushkin et al; Gladkov] as well as the paint products forming the coatings with the properties desired and protecting against its impact have been developed, e.g. the paint "ЭП-437", which is a Russian prototype of well-known Inerta-160. However, the paint products designed for forming weather-resistant anti-icing coatings are practically not available.

Ice deposited on the coatings passes through a liquid state phase, therefore, the theoretical backgrounds to develop anti-icing coatings are to be considered from the viewpoint of the surface phenomena occurring at the liquid-solid interface [Zimon; Jakock]. When such coatings are formulated, the most important matters are the free

[1] NIPROINS, 6 Lisichanskaya st., 197342 St.Petersburg

specific surface energy, which is determined by the surface tension (γ_c, mJ/m^2), the wettability determined by the interfacial angle (θ), the adhesion defined by the adhesion strength (A, kgf/cm) and some others.

Pigment	γ_c, mJ/m^2
Titanium dioxide	
rutile	143
anatase	91
Iron oxide	107
Silicon oxide	123
Carbon black	9

The surface properties of the lacquer films based on hydrophobic filmformers and those of the paint products containing pigments and extenders as a solid phase differ sharply, as the most of solid ingredients specified have high γ_c. Some of their values are given in the left table:
In this connection the study to determine the θ variations depending on the loading degree of epoxy resins by rutile TiO_2 (% by volume) was carried out (see Fig.1).

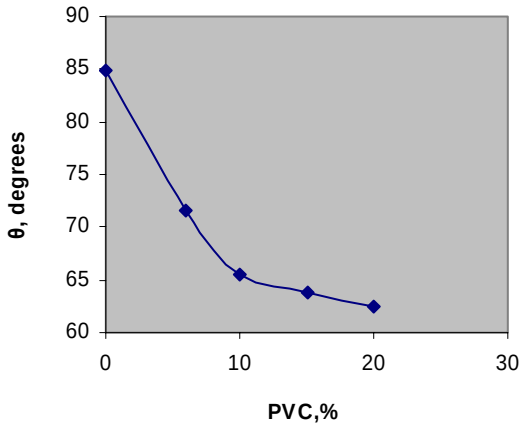

Fig.1.Θ – versus Pigment Volume Concentration

As seen from Fig.1, the loading greatly influences upon the value of the wetting angle, in particular, when up to 10% TiO_2 (by volume) is introduced, thereafter the influence is sufficiently decreased. The loading influence was evaluated by the average degree of change in the wetting angle depending on the 1% by volume change in loading. In a range of 0% to 10% of TiO_2 loading that value amounts to 2°/ % TiO_2, and in a range of 10 to 20% of TiO_2 it accounts for 0.4°/ % TiO_2.

The statistical treatment of the experimental data by the least-squares method has shown that the relationship between the coating wetting angle and the TiO_2 volume content in the coating is described with a polynomial function in the best way.

So, it can be considered that the decrease in the wetting angle is the result of a complex action of the hydrophilic TiO_2 introduction that, being statistically distributed in an epoxy binder, causes in addition the surface energy change as a consequence of its interaction with a binder. Thus, the paint materials designed for anti-icing coatings must comprise of pigments and extenders having low surface energy. In this case the total surface tension of the formulation can be expressed as:

$$\gamma_к = \frac{c_1\gamma_{см} + c_2\gamma_р + c_3\gamma_п}{c_1 + c_2 + c_{31}}, \quad (1)$$

where $\gamma_{см}$ = γ of resin; $\gamma_р$ = that of solvent; $\gamma_п$ = that of a pigment or an extender; c = concentration.

At the same time the additive formula given above is not sufficient to describe a system resulted from the ingredients interaction.

As a result of the coating exposure to atmospheric factors (UV-radiation, moisture, oxygen) and the influence of the mechanical alternating stresses, its surface is destructed and becomes rough. In this case the value of roughness R_a for various coatings can be varied in a range of 1.4 to 4.5 μm [Itsko, Zaporozhets; Itsko et al].

According to the Wenzel-Deryagin equation the link between rough and smooth surfaces is established:

$$\cos \theta_ш = K \cos\theta . \quad (2)$$

The K value shows how much the bonding strength of liquid with a surface is changed, when the roughness increases.

According to the existing concepts [Zimon], the roughness of the hydrophobic surface decreases its wettability, as the liquid is not able to penetrate into the surface cavities, and the θ value becomes higher than that for a smooth surface. On the contrary, the θ value for the hydrophilic surface is decreased. When the hydrophobic coating based on the multi-ingredient paint formulation is being decomposed, the influence of pigments and extenders having high surface energy is enhanced and the surface becomes hydrophilic.

That's why some deviation can be observed between the equation for hydrophobic surfaces:

$$\cos \theta_ш < \cos \theta, \theta_ш > \theta \quad (3)$$

and the equation for multi-component formulations that can be represented as follows:

$$\cos \theta_ш > \cos \theta, \theta_ш < \theta. \quad (4)$$

Thus, the filmformers, which are resistant to mechanical stresses and climatic factors in the Northern latitudes and which do not change the coatings roughness during their service life, should be used in the paint compositions for anti-icing applications.
The epoxy filmformers having the molecular weight of 360 to 20,000 (phenoxy resins) most absolutely comply with these requirements, that allows the coatings with a wide range of properties to be formulated.

The epoxy compounds are polar and have high dissolving power. The solubility parameters of epoxy oligomers (e.g. of ЭД-20 type) have the values, $(mJ/m^3)^{1/2}$ as follows:

Before curing	After curing
δ_d = 17.3	δ_d = 16.72
δ_p = 11.2	δ_p = 6.73
δ_h = 11.2	δ_h = 6.93

Where δ_d, δ_p, δ_h are solubility parameters due to the interaction energies of dispersive, polar and hydrogen bonds.

According to [Van Krevelen], $\gamma_c \sim \delta^{4/3}$, and hence, it can be assumed that a kind of the coating "self-hydrophobization" is taking place in the process of curing.

However, for such coatings θ is equal to 75 - 80^O [Itsko et al] depending on the type of a hardener and the temperature.

So, in this paper silicone adhesion promoters and silazane curing agents were used to enhance the hydrophobicity of epoxy resins.

The compounds having a common formula of X-R-Si$(OR^1)_3$, where X = reactive group; R = aliphatic radical; OR^1 = a hydrolyzable group of C_2H_5O-, have been used as adhesion promoters.

If the moisture is present at the surface of an epoxy coating, silanol groups interact with each other and with hydroxyl groups of the epoxy oligomer located at the surface according to the mechanism as follows:

$$XRSi(OR^1)_3 + 3H_2O \xrightarrow{-2R^1OH} XRSi(OH)_3$$

$$XRSi(OH)_3 + OHOH \longrightarrow XRSi(OH)_2 + XRSi(OH)_2$$

(OHOH: coating; $XRSi(OH)_2$ + $XRSi(OH)_2$: coating)

The ice adhesion strength has been determined by the technique based on the tearing-out of a rod located in a cylinder from the ice mass [Itsko et al].

The cylinder made of stainless steel and having the internal diameter of 39 m is filled with 70 ml of tap water. Afterwards the painted rod is immersed into it and the cylinder is covered with a cylinder head. Then it is placed into a cooling chamber where it is conditioned at (40 ± 2)^O for 1.5 h until firm ice is formed. Thereafter the cylinder is taken out of the cooling chamber, fixed in the clamps of the tearing machine and the force (P) is determined at which the rod is pulled out from the ice thickness. The adhesion strength A (mPa) is calculated by the below formula:

$$A = 0.1\ P/2\pi rl\ , \qquad (5)$$

where P = force to tear out a rod, kg; r = radius of a rod, cm; l = length of a rod in contact with ice.

The results given below show that the addition of the adhesion promoter into the epoxy formulation leads to a sharp decrease in the ice adhesion to the coating.

Substrate	Adhesion strength, mPa
Non-coated rod	2.27
Epoxy coating	2.13
Epoxy coating with an adhesion promoter	0.92

The hydrophobic coatings can be obtained if siliceous curing agents (based on silazane) are used that are capable of interacting with hydroxyl groups of an epoxy filmformer, thus forming a space structure with built-in Si, for instance:

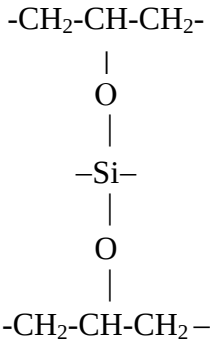

The experiments carried out, while hydrophobic coatings were developed, gave the opportunity to classify the latter into the surface-hydrophobic and volume-hydrophobic coatings according to the principle of imparting the properties required [Itsko, Drinberg]. The surface-hydrophobic coatings are obtained when the surface is treated by water-repellent agents, when hydrophobic filmformers or coatings having the absolute hydrophobicity effect are used [Abramzon]. The volume-hydrophobic coatings are obtained by the usage of hydrophobic modifiers (promoters), chemical modification (the addition of curing agents), completely hydrophobic compositions (see equation 1).

Based on the research carried out the NIPROINS company has developed the enamel ЭП-439П (Specifications 2312-123-05034239-99) designed for anti-icing coatings that is recommended by the Vedeneev VNIIG for application on floodgates of hydropower plants and by CNII KM Prometey for marine structures.

REFERENCES

Abramzon, A.A., *Journal of Applied Chemistry*, 1993, v.66, no.6, pp.1409-1411.

Borisenko, E.P., et al., Means of ships protection from icing. In *Proceedings: The research of the ships ice accretion. Hydrometeorology Publishing House*, Leningrad (1975), v.317, pp.4-12.

Itsko, Ed.F., Zaporozhets, V.D., Ecological problems of the materials and equipment durability. Theory and practice of field tests. In *Proceedings of the Scientific and Applied Research Conference*. Moscow (1997), pp.127-130.

Itsko, Ed.F., et al. *Journal of Coatings Products*, 2003, no.10, pp.10-13.

Itsko, Ed.F., Drinberg, A.S. In *Proceedings of the 3^{d} International Conference "Navy and Shipbuilding in contemporary environment"*. St.Petersburg (2003), pp.238-239.

Gladkov, M.B., Load and influence of ice upon marine waterside structures. *Author's abstract. Dr.thesis.* St.Petersburg (1997), 45 p.

Jakock, M., Prafit, Jh. Surface chemistry of phase separation. *Mir Publishing House*, Moscow, 1984, 269 p.

Panushkin, A.V., et al. Some thermo-dynamical criteria to select materials designed for coatings reducing ice adhesion to structural materials. *In Proceedings: The research on physical nature of ship icing. Hydrometeorology Publishing House,* Leningrad (1972), pp.51-58.

Van Krevelen, D.W., Polymer properties and their chemical structure. *Chemistry Publishing House*, Leningrad, 1976, 414 p.

Zimon, A.D., Liquid adhesion and wetting adhesion. *Chemistry Publishing House*, Moscow, 1974, 416 p.